論文 / 著書情報
Article / Book Information

題目(和文)	光学的に粗く物理的に平坦な薄膜太陽電池用透明導電膜基板の開発
Title(English)	Development of optically-rough and physically-flat transparent conductive oxide substrates for thin-film solar cells
著者(和文)	孟 磊
Author(English)	Lei Meng
出典(和文)	学位:博士(工学), 学位授与機関:東京工業大学, 報告番号:甲第10151号, 授与年月日:2016年3月26日, 学位の種別:課程博士, 審査員:宮島 晋介,岩本 光正,中川 茂樹,山田 明,PHAM NAM HAI,市川 幸美
Citation(English)	Degree:Doctor (Engineering), Conferring organization: Tokyo Institute of Technology, Report number:甲第10151号, Conferred date:2016/3/26, Degree Type:Course doctor, Examiner:,,,,,
学位種別(和文)	博士論文
Type(English)	Doctoral Thesis

DOCTORAL THESIS

Development of optically-rough and physically-flat transparent conductive oxide substrates for thin-film solar cells

March, 2016

Lei Meng

Directed by Associate Professor Shinsuke Miyajima

Department of Physical Electronics

Graduate School of Science and Engineering

Tokyo Institute of Technology

Table of Contents

1 Background and Motivation

1.1 Transparent conductive oxides 1

1.2 TCO in the field of solar cells 2

1.2.1 Photovoltaic technologies and solar cells 2

1.2.2 Thin-film solar cells 6

1.2.3 TCO substrates in thin-film solar cells 8

1.2.4 Effect of the surface morphology of TCO substrates on the performance of thin-film solar cells 10

1.3 Optically-rough and physically-flat TCO substrates 15

1.4 Motivation and Objectives 18

1.5 Outline of this thesis 21

References 24

2 Review of $Zn_{1-x}Mg_xO$ thin film and Sol-Gel process

2.1 Introduction 27

2.2 Basics of $Zn_{1-x}Mg_xO$ 27

2.3 Status of $Zn_{1-x}Mg_xO$ thin film 29

2.3.1 Fabrication methods of $Zn_{1-x}Mg_xO$ thin film 29

2.3.2 Application 32

2.4 Basics of Sol-Gel process 36

2.4.1 Basic concepts 36

2.4.2 Processing Steps 37

2.4.3 Application 42

2.5 Summary 43

Reference 44

3 Development of transparent conductive $Zn_{1-x}Mg_xO$ thin film by sol-gel process on flat glass substrate

3.1 Introduction 49

3.2 Fabrication of $Zn_{1-x}Mg_xO$ thin film by sol-gel process on flat glass substrate . 50

3.2.1 Precursor preparation 50

3.2.2 Film deposition 52

3.2.3 Two-step annealing 52

3.3. Experimental results 54

3.3.1 Effect of precursor preparation condition 54

3.3.1.1 Effect of Mg content 54

3.3.1.2 Effect of solute concentration and solvent 60

3.3.1.3 Effect of dopant and doping concentration 65

3.3.1.4 Effect of aging time of precursor solution 78

3.3.2 Effect of spin-coating parameters 79

3.3.2.1 Effect of spin speed 79

3.3.2.2 Effect of drying time 80

3.3.2.3 Effect of the number of coating layer 80

3.3.3 Effect of two-step annealing 81

3.3.3.1 Effect of the first step annealing 81

3.3.3.2 Effect of the second step annealing 97

3.4 Summary 108

Reference 110

4 Fabrication and characterization of optically-rough and physically-flat TCO substrates

4.1 Introduction 113

4.2 Basics of reactive-ion etching and room-temperature nanoimprinting 113

4.2.1 Basics of reactive-ion etching 113

4.2.2 Basics of nanoimprinting lithography 117
4.3 Roughening surface of glass substrate 119
4.3.1 Etching glass substrate by RIE 119
4.3.2 Wet etching treatment.....120
4.3.3 Patterning glass substrate with room-temperature nanoimprinting 121
4.4 Characteristics of roughened glass substrates 123
4.4.1 Characteristics of RIE etched corning eagle XG glass substrate.....123
4.4.1.1 Effect of etching time 124
4.4.1.2 Effect of RF power of plasma generation.....126
4.4.1.3 Effect of pressure.....128
4.4.1.4 Effect of wet etching treatment 130
4.4.2 Characteristics of RIE etched corning 7059 glass substrate.....133
4.4.3 Characteristics of nanoimprinting patterned glass substrate 137
4.5 Characteristics of sol-gel AZMO/roughened glass substrate.....139
4.5.1 Characteristics of sol-gel AZMO/RIE etched XG glass substrate.....139
4.5.1.1 AZMO sol-gel precursor with EtOH as solvent.....140
4.5.1.2 AZMO sol-gel precursor with 2-Methoxyethanol as solvent 143
4.5.1.3 AZMO sol-gel precursor with 2-M and EtOH as solvent 146
4.5.2 Characteristics of sol-gel AZMO/RIE etched 7059 glass substrate.....149
4.5.3 Characteristics of sol-gel AZMO/imprinting patterned glass substrate 154
4.6 Summary 161
Reference.....164

5 Application of AZMO/glass substrate to hydrogenated amorphous silicon single junction solar cells

5.1 Introduction 167
5.2 Fabrication process of a-Si single junction solar cells.....167
5.2.1 Deposition of antireflection layer.....168
5.2.2 Deposition of photovoltaic active layer 169

5.2.3 Deposition of back reflector layer 172
5.3 Characteristics of a-Si single junction solar cells deposited on flat AZMO/flat glass substrate 173
5.3.1 Effect of bandgap widening of TCO 173
5.3.2 Effect of antireflection layer 176
5.4 Characteristics of a-Si single junction solar cells deposited on rough AZMO/flat glass substrate 181
5.4.1 Experiments 182
5.4.2 Results and discussions 183
5.4.3 Conclusions 188
5.5 Characteristics of a-Si single junction solar cells deposited on optically-rough and physically-flat TCO substrates 190
5.5.1 Characteristics of a-Si single junction solar cells deposited on AZMO/RIE etched glass substrates 190
5.5.2 Characteristics of a-Si single junction solar cells deposited on AZMO /imprinting patterned glass substrates 194
5.6 Summary 198
References 200

6 General conclusions and future prospects

6.1 General conclusions 203
6.2 Future prospects 206
Reference 210

Acknowledgments 211
List of Publications 213

Chapter 1 Background and Motivation

1.1 Transparent conductive oxides

Transparent conductive oxides (TCO) are materials, generally in the form of thin film, which simultaneously possess high transparency and good electrical conductivity. They are usually metal oxides. The most common transparent conductive oxides are binary compounds including tin oxide (SnO_2), indium oxide (In_2O_3) and zinc oxide (ZnO). Ternaries, that is, combination of binaries including Zn_2SnO_4, $Zn_2In_2O_5$ and $In_4Sn_3O_{12}$ have also been developed. The widely used TCOs are n-type compound semiconductor. Table 1.1 shows the overview of the commonly used n-type TCO. This table also shows the deposition method, doping elements usually used for these films, the resistivity range for doped films, and the bandgap of the undoped film. It can be found that low resistivity of around 10^{-4} Ω·cm has been achieved for these TCO. Compared with SnO_2 and In_2O_3, the bandgap of ZnO and TiO_2 (3.2 eV) is narrow.

TCO is a very important part in various optoelectronic devices including liquid-crystal displays, organic light-emitting diodes, touchscreens, and solar cells. It contributes a lot to the development of these optoelectronic devices. The most widely used TCO is fluorine doped tin oxide (SnO_2: F) that is usually used as the heat-reflecting coating on architectural glass and as the transparent electrode of amorphous silicon (a-Si) and cadmium telluride (CdTe) based thin-film solar cells. The next mostly used material is tin doped indium oxide (In_2O_3: Sn). It is widely used in flat-panel displays, thin-film transistor, touch screens and some types of solar cells based on crystalline Si wafers. ZnO has been widely used in the fields of including varistors, gas sensors, lasers, light-emitting diode, surface acoustic wave devices, and spintronic devices.

Table 1.1 Overview of commonly used TCO [1].

TCO	SnO_2	In_2O_3	ZnO	TiO_2
Deposition method	APCVD Spray pyrolysis	Sputtering, PLD	Sputtering, PLD, LPCVD, APCVD	Sputtering，PLD
Bandgap (undoped) (eV)	3.6	3.7	3.3	3.2
Resistivity (10^{-4} Ω·cm)	3-8	1-3	1-8	9-10^6
Dopant	F, Sb, Cl	Sn, Mo, Ti, Nb, Zr	Al, Ga, B, In, F	Nb, N

Note: APCVD refers to atmospheric pressure chemical vapor deposition; PLD refers to pulsed laser deposition; LPCVD refers to low pressure or metalorganic chemical vapor deposition.

1.2 TCO in the field of solar cells

1.2.1 Photovoltaic technologies and solar cells

Human have benefited quite a lot from the energy supply generated by fossil fuel (coal, petroleum, and natural gas) burning and nuclear fission so far. They are the main processes which generate electricity through creating heat to turn water into steam that rotates giant turbines. According to the data from the *International Energy Agency*, as shown in Fig. 1.1, the fossil fuel burning and nuclear fission occupied the top two position of world electricity generation from 1971 to 2013.

However, human have also been suffering from the increasing greenhouse emission generated by the fossil fuel burning so far. Based on the data from IPCC reports, as shown in Fig. 1.2 (c), the greenhouse gas emissions have increased the

concentrations of carbon dioxide (CO_2), methane (CH_4), and nitrous oxide (N_2O) in the atmosphere greatly since 1850. Figure 1.2 (d) shows the global CO_2 emission from 1971 to 2011 generated by fossil fuel burning and other use. It can be found that the CO_2 emission increases significantly in the last 40 years. The cumulative CO_2 emission to the atmosphere were about 2040 ± 310 $GtCO_2$ between 1850 and 2011. This increasing CO_2 emission would result in global climate change, including global warming, sea level rise, and change in rainfall.

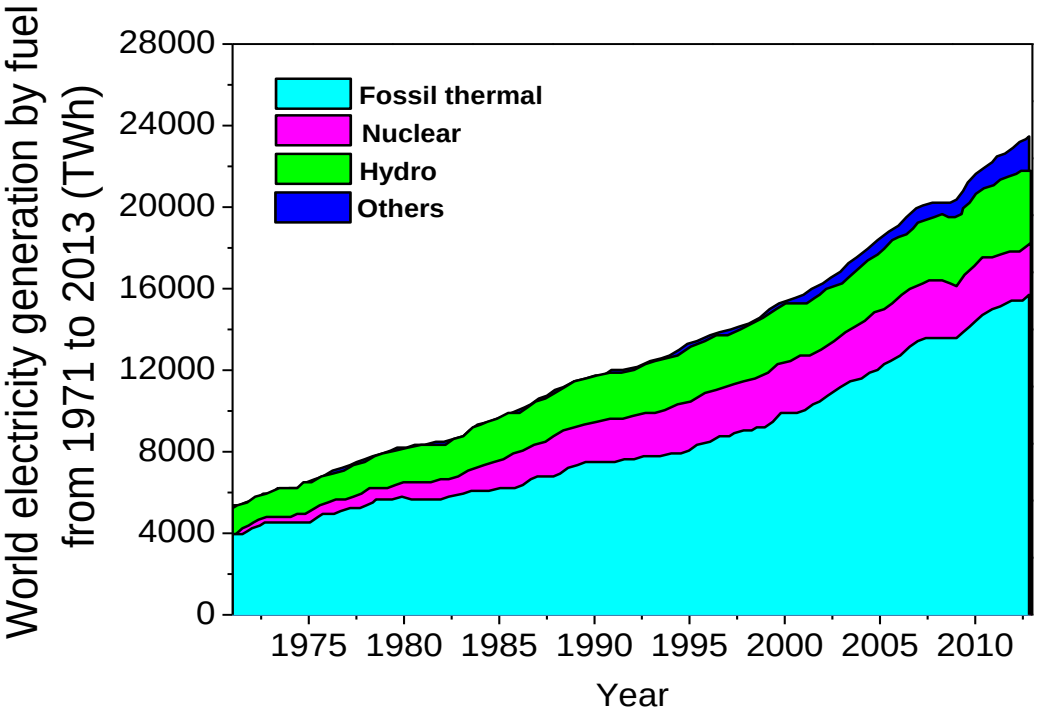

Fig. 1.1 World electricity generation from 1971 to 2013 by fuel (TWh). *Excludes electricity generation from pumped storage; **Includes geothermal, solar, wind heat, etc. (Key World 2015, p.24)[2].

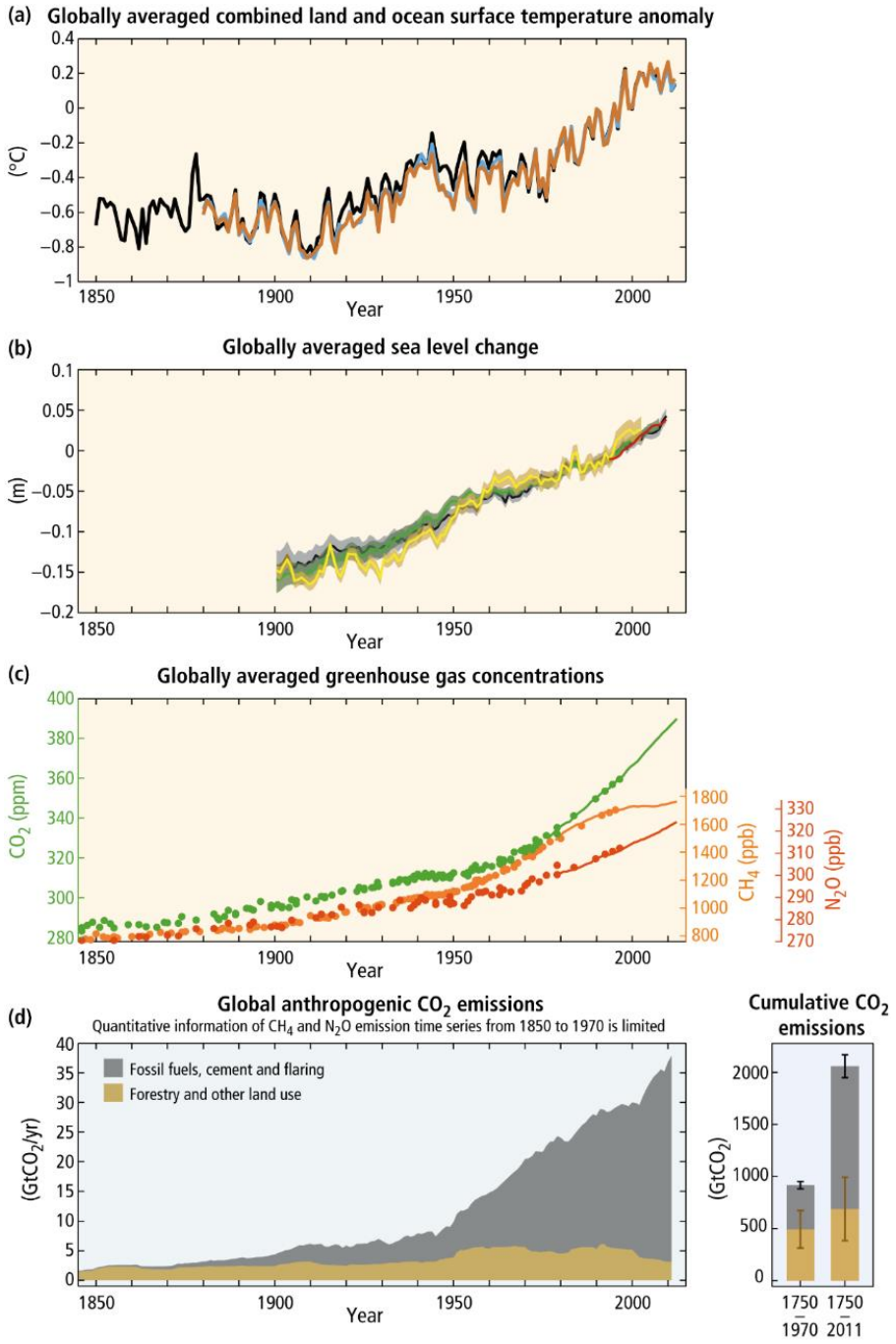

Fig. 1.2 (a) Annually and globally averaged land and surface temperature anomalies relative to the average over the period 1860 to 2005. Colors indicate different date sets. (b) Annually and globally averaged sea level change relative to the average over the period 1986 to 2005 in the longest-running dataset. Colors indicate different data sets. (c) Atmospheric concentrations of the greenhouse gases carbon dioxide (green), methane (orange), and nitrous oxide (red) determined from ice core data (dots) and from direct atmospheric measurements (lines). (d) Global anthropogenic CO_2 emissions from forestry and other land use as well as from burning of fossil fuel, cement production and flaring. Cumulative emissions of CO_2 from these sources and their uncertainties are shown as bars and whiskers, respectively, on the right hand side [3].

Figure 1.2 (a) clearly shows that the globally averaged combined land and ocean surface temperature increases by about 0.85 ^{o}C over the period from 1880 to 2012. Figure 1.2 (b) shows that the global mean sea level increases by 0.19 m over the period from 1901 to 2010 due to the widespread melting of ice and snow. It is also predicted that based on theoretical calculation that the global average temperature will continuously increase and it will increase by about 5 ^{o}C by the end of the 21st century. This would influence agriculture, disease control, and other human activities. In addition, the amount of fossil fuels is finite. The petroleum and natural gas will exhaust within decades, while coal will exhaust within few centuries.

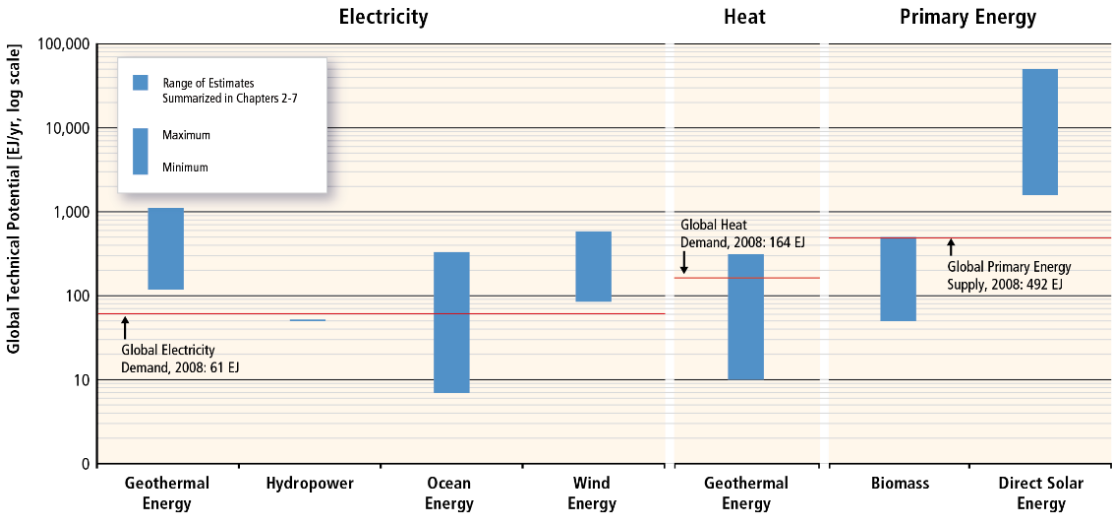

Fig 1.3 Ranges of global technical potentials of renewable energy sources [4].

Human can obtain electrical generation through nuclear plant without CO_2 emission, but nuclear fuel is very dangerous. The leak of highly radioactive wastes or the presence of nuclear accident will influence quite a lot. People have learned lessons from 2011 Japanese Fukushima nuclear disaster and 1986 Chernobyl disaster. These

nuclear accidents evacuated millions of people from their home, costed tens of billions of dollars, and decades to do cleanup job.

Consequently, with the continuous upgrade of ecological deterioration and energy crisis, the development of clean renewable energy has become the top issue for the whole world. Clean renewable energy mainly includes hydroelectric power, wind energy, sun energy, geothermal energy, and biomass energy. According to the data shown in Fig. 1.3, solar energy possesses the highest technical potential among these renewable sources.

Solar cells based photovoltaics (PV) technology helps human to collect electrical power from solar power directly. It generates electrical power simply if the light shines on the solar cells. According to the data from Green peace, PV can reduce the CO_2 emission by about 4 billion tonnes of CO_2 equivalent in the year 2050 [5]. As a result, many kinds of solar cells are being developed to increase the photoelectric conversion efficiency as high as possible to reduce the cost. Most of the solar modules today in the market are made of crystalline silicon (c-Si) solar cells. About 10 % of the solar module today are made of thin-film solar cells, including amorphous silicon (a-Si), copper indium gallium diselenide (CIGS), cadmium telluride (CdTe), and others. Others includes organic solar cells and emerging PV techniques.

1.2.2 Thin-film solar cells

The global production of PV devices is dominated by c-Si and poly-Si solar cells. The c-Si is usually produced in the form of an ingot which is subsequently mechanically sawn into slices. The thickness of the Si-wafers used is in the range of 150-300 μm. Thin-film solar cells occupies a special place in the field of solar cells, because they has light weigh, they enable flexible module, and they can be fabricated

by large area deposition method. The thickness of thin-film solar cells is in the range of 0.3~2 μm. This reduces greatly the cost of raw materials, compared to c-Si and poly-Si solar cells. They also need simple device processing and manufacturing technology, which result in low production cost and better price performance ratio. Thin film solar cells are usually deposited at low temperatures of 150-300 ^{o}C. Therefore, these types of solar cells also can be deposited on substrates of low cost, such as glass and even some plastics. In addition, thin-film solar cells have light weight due to thin thickness. This can reduce the installation cost of solar cell modules. Furthermore, flexible solar cells can be fabricated by depositing the solar cells on a flexible substrate, such as metal film or plastic foil, since the solar cells are very thin.

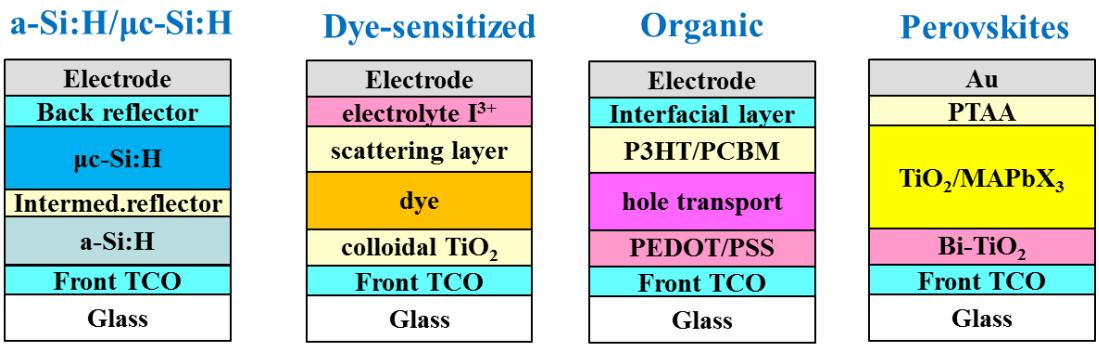

Fig 1.4 Schematics of thin-film solar cells with superstrate configuration.

There are many members in the family of the thin-film solar cells. Figure 1.4 exhibits the four kinds of thin-film solar cells with superstrate configuration, including a-Si:H/μc-Si:H tandem solar cells, dye-sensitized solar cells, organic solar cells, and perovskites solar cells. They have different device structure, but they have one thing in common. That is the TCO substrate.

1.2.3 TCO substrates in thin-film solar cells

In the photovoltaic field, TCO substrate is an integral part of thin-film solar cell devices, which is usually used as a front electrode or as part of the back reflector. The TCO substrate has a decisive influence on the conversion efficiencies of state-of-the-art thin-film solar cells. Figure 1.5 shows the schematic of the cross section of the conventional TCO substrates and the photograph of SnO_2: F coated glass substrate. As shown in Fig. 1.5(a), TCO substrate is defined as the glass substrate that is coated by one thin film of transparent conductive oxides on the top. Currently, the most widely used TCO includes ZnO: Al (AZO) or ZnO: B (BZO), SnO_2: F (FTO), and In_2O_3: Sn (ITO). The widely used glass substrates include Corning, Soda-lime, and fused quartz.

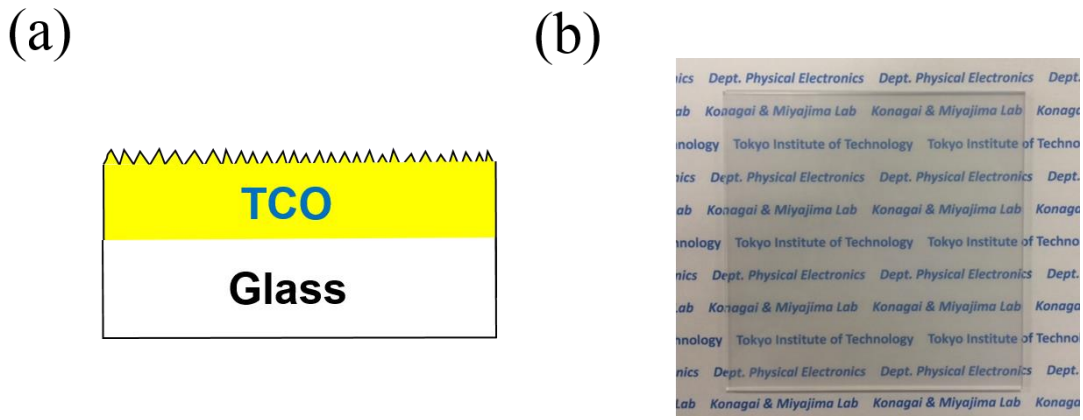

Fig 1.5 (a) Schematics of the cross section of the conventional TCO substrates (b) the photograph of SnO_2: F coated glass substrate.

For the TCO substrates in superstrate-type thin-film solar cells, there are mainly three essential requirements: high transmittance, low sheet resistance, and moderate surface morphology. Firstly, the transmittance of TCO substrate is usually required to be higher than 85% for visible and near infrared light region. This high transmittance of TCO substrate would reduce the optical loss in the transparent conductive layer and let much more light go into the absorption layer. Secondly, the sheet resistance of TCO

should be less than 10 *Ω/sq*. Low sheet resistance would minimum the power dissipation, that is, Joule heating (I^2R losses), in the film and collect much more power from the solar cells. Thirdly, moderate surface morphology of TCO substrate is required to improve the performance of solar cells.

Both amorphous silicon (a-Si) and cadmium telluride (CdTe) superstrate thin-film PV technologies typically use FTO as the TCO, although next-generation a-Si/nc-Si cells tend to use AZO or BZO. The dye-sensitized TiO_2 type cells also use FTO. The Panasonic heterojunction with intrinsic thin layer (HIT) cell uses ITO and a metal grid on top of the p-type a-Si/n-type c-Si base for current collection [6].

At present, ITO and FTO are the most commercially available TCO substrates when applied in solar cells. However, both of them suffered drawbacks which would prevent their use in next-generation thin-film silicon modules. The cost of ITO is very high and tends to increase continuously with time. The availability of indium deposits, the principal material of ITO, is rapidly decreased, by growing production of liquid crystal displays (LCDs) and solar cells (the main applications of this material). It is believed that a shortage of indium will be evident around 2020. Because of increasing demand, the price of indium has risen from about $100/kg in 2002 to about $600/kg in 2010 [7]. For the FTO, it suffers two severe drawbacks. One drawback is that the exposure of FTO to atomic hydrogen (H) produced during plasma enhanced chemical vapor deposition (PECVD) can chemically reduce the film, thereby creating elemental tin (Sn) that cause optical absorption and film darkening. It also has been reported that Sn can diffuse into the solar cell p-layer, thereby reducing its bandgap [8]. ITO also undergoes a similar reduction in the presence of H. Another drawback is that FTO has an inappropriate morphology for effective light-trapping for wavelengths (~1000 nm) near the band edge of the nc-Si:H, i.e. for wavelengths longer than those near the band

edge of a-Si:H (~700 nm). Consequently, ZnO becomes one promising candidate as the TCO layer for thin-film Si solar cell, because of high stability in hydrogen-rich plasma, ease in modifying surface morphology, and abundance in nature.

1.2.4 Effect of the surface morphology of TCO substrates on the performance of thin-film solar cells

Surface morphology and roughness of TCO substrate is very important for thin-film solar cells. For thin-film solar cells, based on the mainstream standpoints, roughening surface morphology, that is, increasing surface roughness would enhance light-scattering and contributes to the light-confinement in the solar cells, because the photoactive layers are not thick enough to sufficiently absorb light in a single pass. This would improve the performance of solar cells by increasing short circuit current. At present, FTO or BZO substrate with growth induced pyramidal surface textures, which are deposited by chemical vapor deposition, can scatter light effectively and were widely used as the front electrode of thin-film Si solar cells. Figure 1.6 and 1.7 show the surface and cross section SEM micrographs of BZO and FTO, respectively.

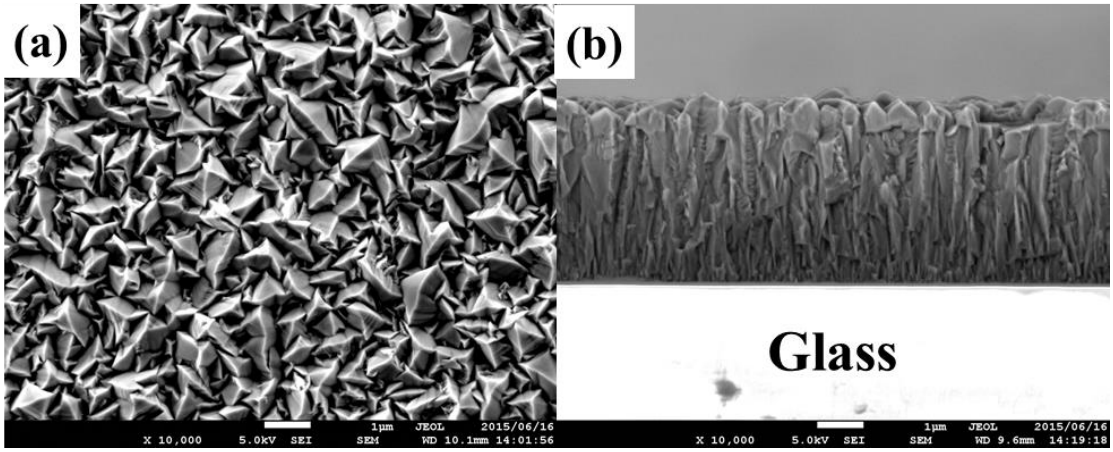

Fig 1.6 SEM (a) surface and (b) cross section micrograph of the BZO substrate.

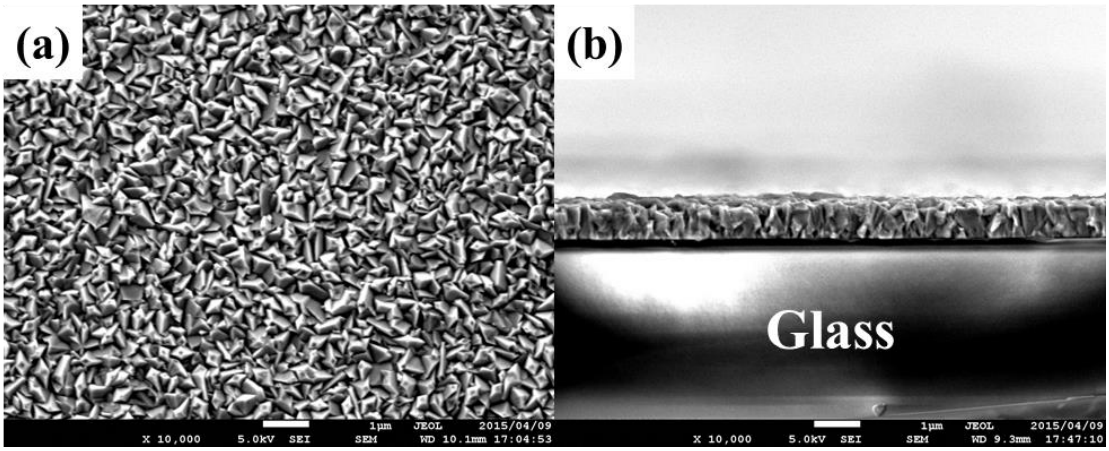

Fig 1.7 SEM (a) surface and (b) cross section micrograph of the FTO substrate.

Based on the published literatures, the relationship between the surface roughness of TCO substrate and the performance of thin-film solar cells was briefly reviewed as following.

(a) Effect of substrate surface roughness on the short-circuit current density

Increasing substrate surface roughness can increase the short-circuit current by enhancing the light-scattering. However, too large surface roughness would reversely decrease the short-circuit current density because increasing substrate surface roughness would also influence the microstructure of absorption layer. Matsui et al. [9] reported that the short-circuit current density of polycrystalline silicon (poly-Si) solar cells would decrease if the Root Mean Square (RMS) roughness of textured substrate is larger than 38 nm. This is attributed to the enhanced recombination current due to the increased defect density. It is related to the change in poly-Si (220) preferential growth caused by the increased roughness of substrate surface. It is well known that the poly-Si films with (220) preferential orientation basically possess columnar structure. The growth direction of poly-Si film should be perpendicular to the local surface of substrate.

The decrease in I(220)/I(111) implies that poly-Si film tends to grow perpendicularly to slanting texture surface but not to substrate itself. Such diagonally oriented columnar growth may result in the collision with other grains, and then create many grain-boundary and related defects. These defects would increase the recombination current, resulting in the decrease in short-circuit current density. Sobajima et al. [10] also mentioned that the short-circuit current density of microcrystalline silicon (μc-Si: H) solar cells would decrease gradually with increasing the surface roughness of TCO substrate. It is resulted from the deteriorated microstructure of photovoltaic i-layer caused by the roughened surface. Rough TCO surface would cause the formation of growth-induced micro-cracks in the μc-Si layer and decrease the degree of (220) preferential orientation and the crystalline volume fraction. These changes in microstructures induce the reduction in the short-circuit current density. Ma et al. [11] confirmed that a smoother ZnO interlayer enabled the increase in short-circuit current density. The smooth surface of ZnO interlayer would facilitate the exciton dissociation through increasing the donor/acceptor interfacial area in the active layer. In addition, based on the work of Eperon et al. [12], it is reasonable to conclude that TCO substrate with small surface roughness could contribute to the increase in short-circuit current density of solution-processed $CH_3NH_3PbI_{3-x}Cl_x$ planar heterojunction perovskite solar cells. In addition, TCO substrate with large surface roughness is quite likely to induce the incomplete coverage of the perovskite. This poor coverage would lead to the decrease in photo-generated current, because light would pass straight through without absorption at the regions of no perovskite coverage. Moreover, Hishikawa et al. [13] revealed that the electric fields in the a-Si layer would become weak locally above the V-shape surface texture of substrate. It would degrade the photocarrier collections.

(b) Effect of substrate surface roughness on the open-circuit voltage

Sakai et al. [14] systematically investigated the effect of surface morphology of transparent electrode on the open-circuit voltage of a-Si:H solar cells. It was found that increasing haze value with enhancing the surface roughness of TCO substrate would decrease the open-circuit voltage, regardless of the i-layer thickness. It is caused by the formation of white stripelike defective regions in the absorption layer deposited on highly textured transparent electrodes. The white stripes appearing in the i-layer would act as recombination centers which enhance the dark current and this leads to the drop in open-circuit voltage of a-Si-based p-i-n solar cells.

Nasuno et al. [15] reported that the crystal growth of μc-Si: H on steep texture would result in the decrease in open-circuit voltage. The reduction in open-circuit voltage with increasing the substrate surface roughness is ascribed to the increased carrier recombination at the grain-boundary defect. In the solar cell deposited on the TCO substrate with large surface roughness, the columnar grow is limited by collision of the columns and a lot of grain boundaries are formed. On the other hand, on smoother substrates, the collision of the columns is suppressed and the density of grain boundaries is reduced. The degree of preferential orientation I(220)/I(111) was correspondingly suppressed with increasing surface roughness. Sobajima et al. [10] mentioned the open-circuit voltage of μc-Si:H solar cells also tend to increase from 0.43V to 0.45V if the surface roughness of TCO substrate increases from RMS 59 nm to RMS 19 nm.

Ma et al. [11] studied the influence of the surface roughness of ZnO electron transport layer on the open-circuit voltage of the inverted organic solar cells (ISCs). It was found that the open-circuit voltage of the ISCs based on rough ZnO electron transport layer is lower than that based on smooth ZnO electron transport layer. It is

caused by the enhanced trap-assisted recombination due to the increased surface roughness of ZnO electron transport layer. The surface roughness of ZnO determines the effective ZnO/active layer interfacial area and then the amount of interface traps at the ZnO/active layer interface. Thus, increasing surface roughness of ZnO electron transport layer would increase the amount of interface traps, causing the increase in trap-assisted recombination. In the case of the solution-processed $CH_3NH_3PbI_{3-x}Cl_x$ planar heterojunction perovskite solar cells. Eperon et al.[12] reported that insufficient coverage of perovskite active layer on TCO substrate with large surface roughness would cause the drop in open-circuit voltage. This poor coverage results in the formation of "shunt paths" allowing contact between spiro-OMeTAD and the TiO_2 compact layer. Any such contact will play as a parallel diode in the solar cell equivalent circuit, causing the reduction in open-circuit voltage.

(c) Effect of substrate surface roughness on the fill factor

The substrate surface roughness would influence the fill factor as it affects the open-circuit voltage in the field of μc-Si: H [15] and solution-processed $CH_3NH_3PbI_{3-x}Cl_x$ planar heterojunction perovskite solar cells [12]. In the case of inverted organic solar cells (ISCs) [11], ZnO surface with large roughness could reduce the FF of the solar cell due to the increased trap-assisted recombination. ZnO surface roughness determines the effective interfacial area between the ZnO layer. Increasing ZnO surface roughness would enhance the ZnO/active layer interfacial area, resulting in more interface traps. The interface traps, resulting in an undesired trap-assisted recombination, would decrease the FF of the solar cells.

1.3 Optically-rough and physically-flat TCO substrates

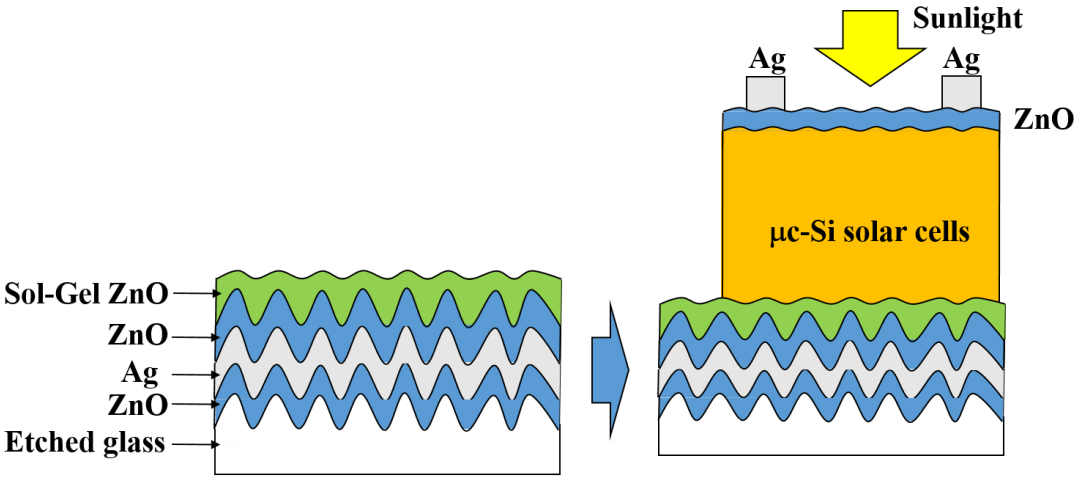

Fig. 1.8 Schematics of OR-PF TCO substrate with Type-T structure and its application in μc-Si solar cells.

As mentioned in section 1.2.4, the surface morphology of TCO substrates influences greatly the performance of thin-film solar cells. Roughening surface morphology of TCO substrate enables an effective light-trapping in absorption layer through enhancing light-scattering or diffusing reflection. However, the TCO substrate with rough surface texture would reversely deteriorate the performance of thin-film solar cells through influencing the growth of absorption layer. Consequently, this trade-off between effective light-trapping and growth of high quality absorption layer limits the improving the performance of thin-film solar cells by modifying the surface morphology of TCO substrates. New kind of TCO substrate is very expected to enable effective light-trapping and growth of high quality absorption layer simultaneously. Therefore, optically-rough and physically-flat (OR-PF) TCO substrate is being developed to meet this issue. The unique strategy of OR-PF TCO substrate is to fulfill effective light-trapping and growth of high quality absorption layer simultaneously by using two different interfaces. It utilizes the rough interface between the substrate and

TCO for enhancing light-trapping, and uses the flat surface of TCO substrate for the growth of high quality absorption layer. Up to now, three kinds of concepts or structure have been developed in the field of OR-PF TCO substrate.

Sobajima et al. [11] developed a OR-PF TCO substrate with Type-T structure. As shown in Fig. 1.8, it was fabricated by depositing sol-gel derived ZnO film on chemically etched glass substrate. The roughened interface between TCO and glass substrate enhanced light-trapping with RMS roughness of 57 nm, and the plarnarized surface of ZnO film with RMS roughness of 12 nm prompted the growth of high quality absorption layer. When this Type-T substrate was used as the back reflectors in microcrystalline silicon (μc-Si:H) solar cells, an increase in short-circuit current (J_{sc}) by about 25% due to the improved quantum efficiencies for the long-wavelength light as well as a slight increase in open-circuit voltage (V_{oc}) in accordance with the planarization, resulting in an improved conversion efficiency.

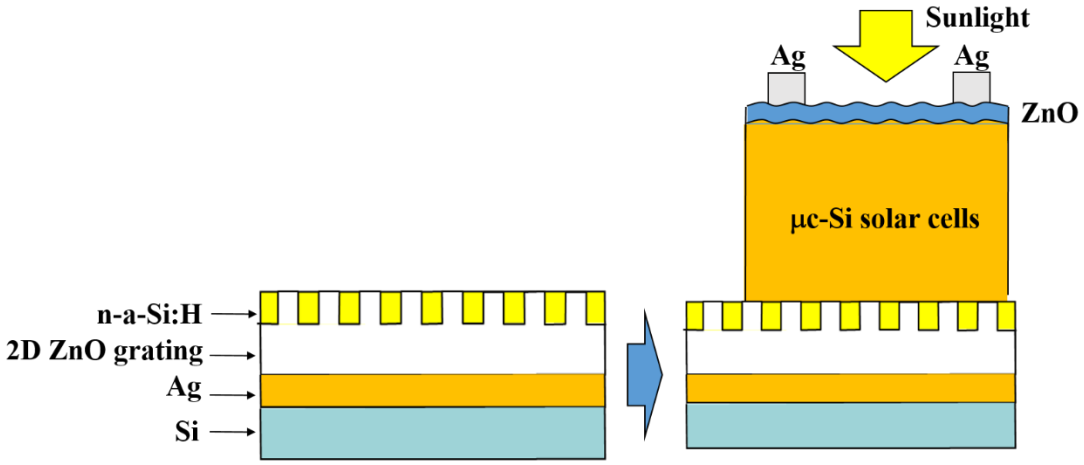

Fig. 1.9 Schematics of OR-PF TCO substrate with grating structure and its application in μc-Si solar cells.

Sai et al. [16] proposed a flattened light-scattering substrate. As shown in Fig. 1.9, it composed of a two-dimensional (2D) ZnO grating layer, n-type amorphous

silicon (n-a-Si:H) and Ag reflector. A stacked layer of Ag and Ga doped ZnO is deposited on a supporting substrate (Si wafer) by magnetron sputtering. Then, a 2D ZnO grating was formed by photolithography and dry etching techniques. The trenches of the ZnO grating were filled by an n-a-Si:H bury layer deposited by plasma-enhanced chemical vapor deposition method. Finally, the substrate surface was flattened by chemical mechanical polishing method and the ZnO parts were exposed. The period and depth of the ZnO grating are 1000 nm and 300 nm, respectively. It substantially improved the spectral response of μc-Si:H solar cells in the infrared region while maintaining a high V_{oc} and fill factor (*FF*), which are almost equal to those of cells deposited on a flat substrate. The key point of this concept is an appropriate distribution of the refractive indices on the plane.

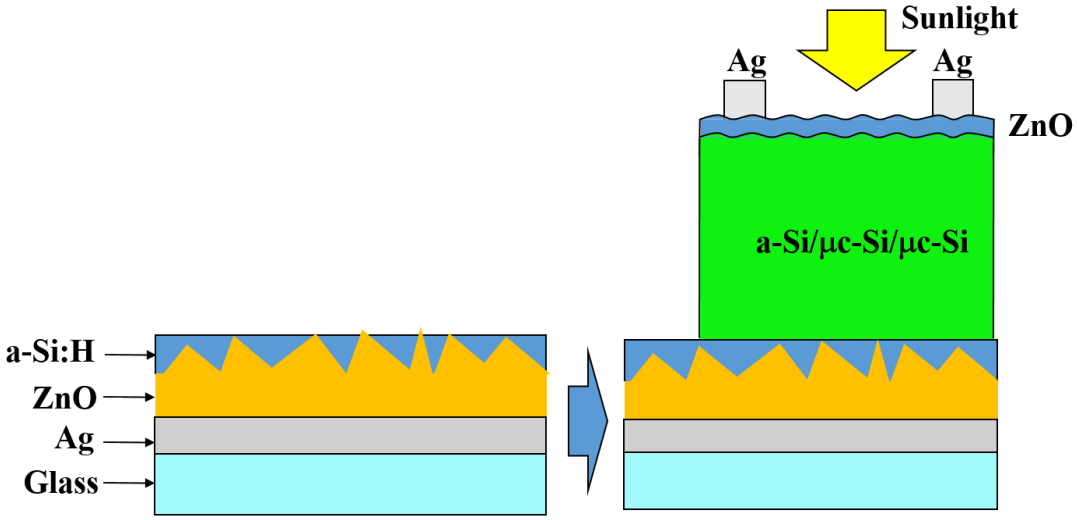

Fig. 1.10 Schematics OR-PF TCO substrate with a polished flat surface and its application in a-Si/μc-Si/μc-Si three junction thin-film solar cells.

Söderström et al. [17, 18] designed a novel substrate that decouples the growth interface from the light-scattering interface. As shown in Fig. 1.10, it consists of a flat Ag layer covered with 20 nm of sputtered ZnO: Al and untreated 2.5 or 5 μm-thick layer of non intentionally doped ZnO deposited by low pressure chemical vapor deposition. The optically rough interface was created by growing a dummy undoped a-

Si:H layer that buries the pyramidal ZnO features. The light-scattering at the pyramidal features is ensured by the difference in refractive index of the a-Si:H (~ 4) and ZnO (~ 2). The final flat interface on which cells were grown was subsequently obtained by chemical mechanical polishing. This kind substrate could combined efficient light management and an interface suitable for the growth of high-quality materials. When applied to triple-junction a-Si:H/μc-Si:H/μc-Si:H solar cells, it not only enabled a gain in J_{sc} relative to conventional textured substrate through improving the light-management for wavelength of larger than 700 nm, but also get similar V_{oc} and FF as flat substrate by decreasing the formation of defective porous areas in the μc-Si:H layer.

1.4 Motivation and Objectives

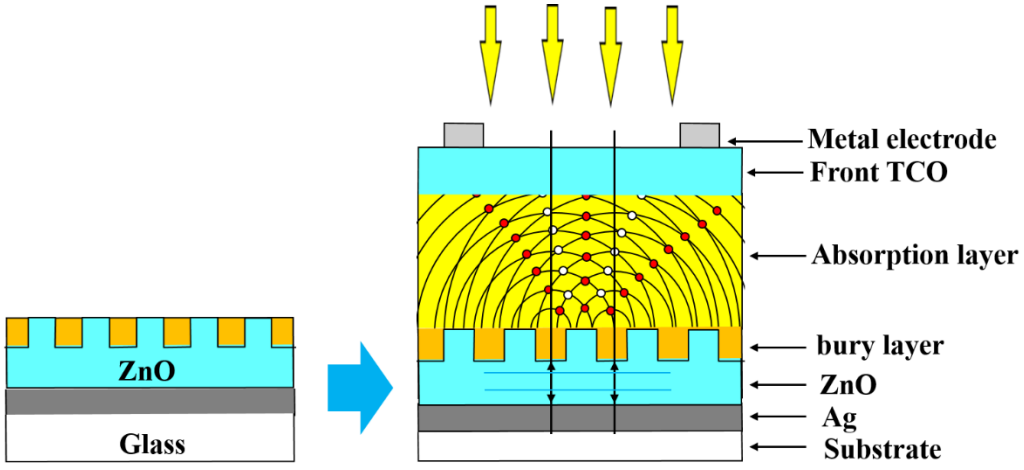

Fig. 1.11 Schematics of the conventional OR-PF TCO substrate and its application in substrate type thin-film solar cells.

Figure 1.11 shows the schematics of the conventional OR-RF TCO substrate. At present, all of these developed OR-PF TCO substrates are utilized as back reflector in thin-film solar cells with substrate configuration and contribute to the light-confinement in the absorption layer. The conventional OR-RF TCO substrates have achieved flat surface by using spin-coating and chemical mechanical polishing

techniques, but they have several disadvantages. Firstly, the light-scattering ability is limited. According to the research of Haase et al.[19], the light-scattering behavior of a grating structure at the rear surface shows strong dependence on the scattering properties of the front contact. Secondly, the sheet resistance of these substrates is usually very high due to the deposition of bury material of a-Si on the top. This is quite probably the reason why there is no application of these substrates as front electrode in the thin-film solar cells with superstrate configuration.

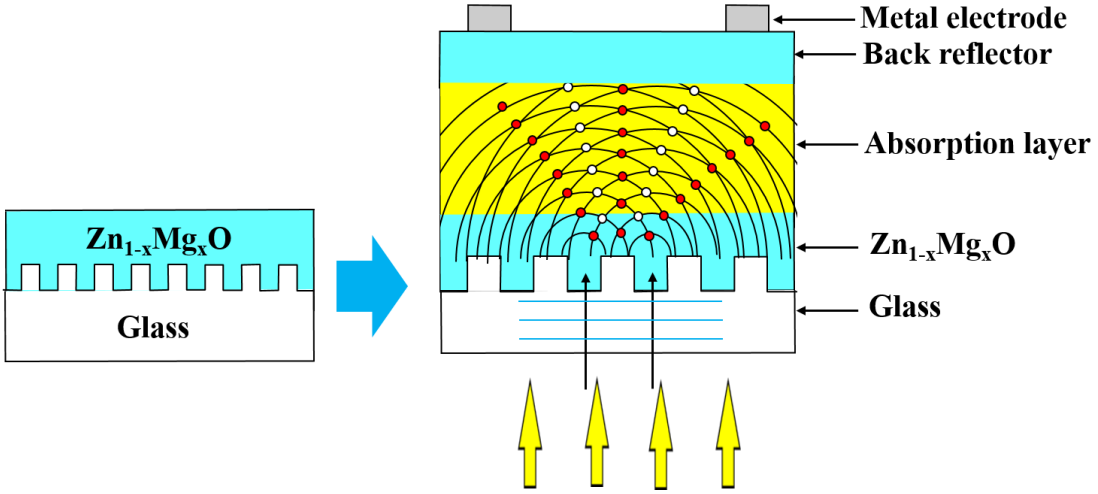

Fig. 1.12 Schematics of the novel OR-PF TCO substrate and its application in superstrate type thin-film solar cells.

Therefore, novel OR-PF TCO substrates were developed in this thesis to overcome these problems. Figure 1.12 shows the schematics of the novel OR-PF TCO substrate and its application in thin-film solar cells. This novel OR-PF TCO substrate would be fabricated with spin-coating widegap $Zn_{1-x}Mg_xO$ transparent conductive thin film on reactive ion etched glass substrates or imprinting patterned glass substrates. The concept of "optically rough" will be achieved by using the rough interface between TCO and surface of reactive ion etched glass substrates or imprinting patterned glass substrates. The concept of "physically flat" will be achieved by depositing $Zn_{1-x}Mg_xO$

thin film with sol-gel based spin-coating method.

These novel OR-PF TCO substrates were developed to be used as front electrode in thin-film solar cells with superstrate configuration. This is the first proposal of development of OR-PF TCO substrate for thin-film solar cells with superstrate configuration. They have several advantages. Firstly, they can scatter the incident light more effectively than the conventional ones that were used as the back reflector in substrate type thin-film solar cells. The simulation results for p-i-n μc-Si: H cells with diffractive grating structure demonstrates that the application of a grating structure at the front surface is more beneficial than at the rear surface [19]. Secondly, the rough interface between the TCO and the roughed substrate has antireflection effect and enhance the light transmittance [20]. Thirdly, they can reduce the optical loss in the TCO layer through the bandgap widening of TCO layer.

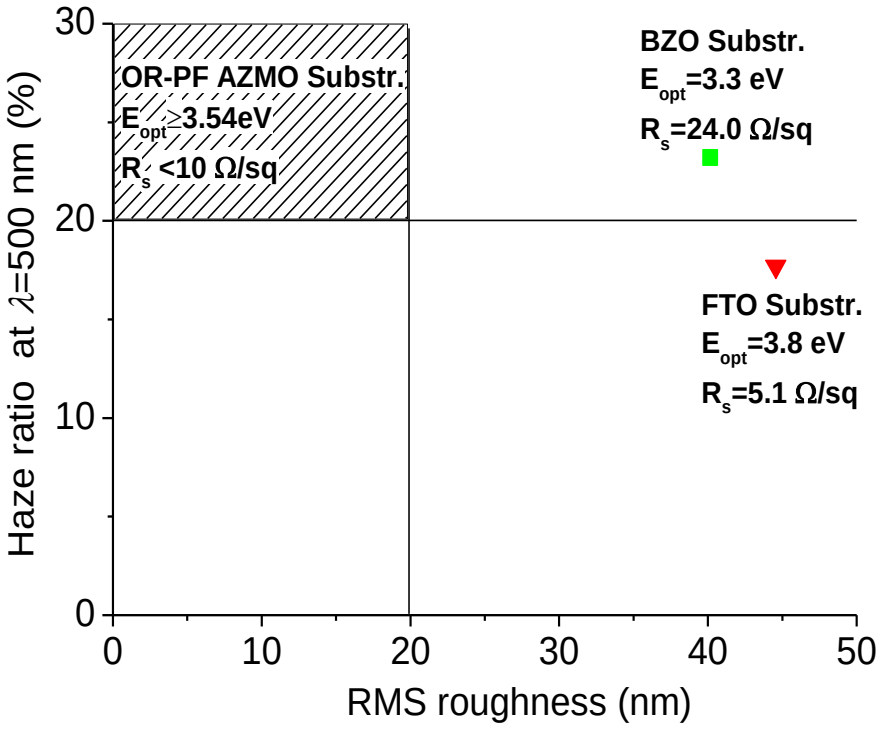

Fig. 1.13 Schematics of the development target for OR-PF AZMO substrate in this work.

The objectives of this thesis are to create one novel TCO substrate that can fulfill

low optical absorption, strong light-scattering and low surface roughness simultaneously. Figure 1.13 shows the development target for OR-PF AZMO substrate in this work. (1) Development of widegap $Zn_{1-x}Mg_xO$ thin film (E_{opt} > 3.54 eV) with low sheet resistance (R_s < 10 *Ω/sq*). (2) Achievement of high haze ratio (H_T >20 %) at λ=500 nm. (3) Flat surface with low surface roughness (RMS roughness < 20 nm). These can improve the performance of thin-film solar cells with superstrate configuration by improving the values of J_{sc}, V_{oc} and *FF* simultaneously.

1.5 Outline of this thesis

The organization of this thesis is shown in Fig. 1.14. This thesis consists six chapters. Chapter 1 introduces the background, motivation and objectives of this study.

In Chapter 2, the review of $Zn_{1-x}Mg_xO$ thin film and sol-gel process will be done in order to show the basics and research status of $Zn_{1-x}Mg_xO$ thin film. Moreover, the advantage of developing $Zn_{1-x}Mg_xO$ thin film with sol-gel process will be explained.

Chapter 3 describes the development of $Zn_{1-x}Mg_xO$ thin film by sol-gel process on flat glass substrate in details. Effect of preparation condition of sol-gel precursor, parameters of spin-coating, and two-step annealing on the electrical, optical and structural properties of $Zn_{1-x}Mg_xO$ thin film will be discussed. Focus is on the reducing the resistivity of $Zn_{1-x}Mg_xO$ thin film.

In Chapter 4, the fabrication and characterization of optically-rough and physically-flat TCO substrates will be conducted. Firstly, roughening the surface of glass substrates will be conducted by reactive-ion etching and room-temperature nanoimprinting technique. In one hand, two kinds of glass commercial substrates (Cor-

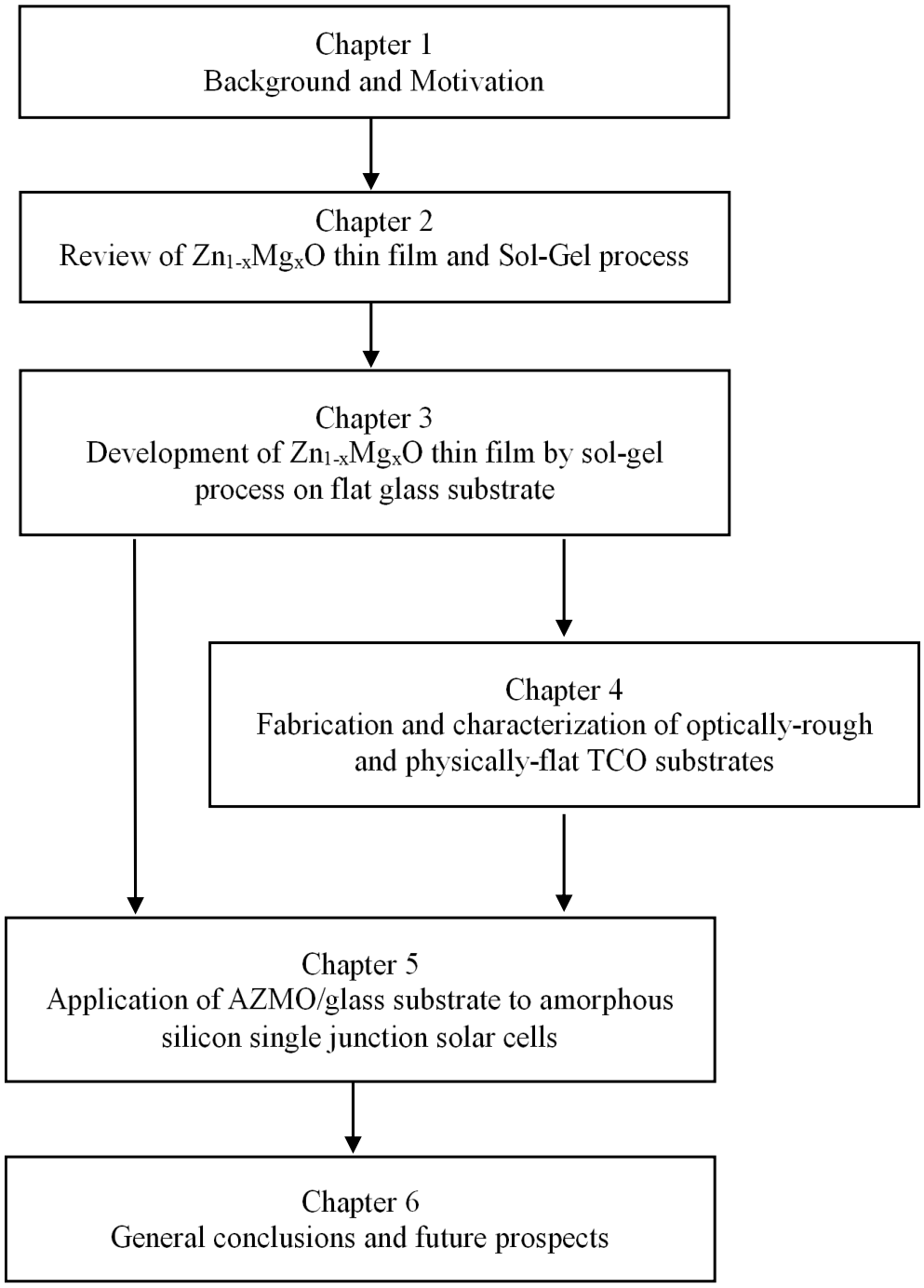

Fig. 1.14 Organization of this thesis.

ning Eagle XG and Corning 7059) will be etched by reactive-ion etching method. The effect of etching time, plasma generation power, pressure and wet etching treatment on the characteristics of etched glass substrate will be investigated. On the other hand, a variety of nanoscale feature sizes are formed on the glass substrate by using room-

temperature nanoimprinting with different mold patterns. The effect of various feature size on the optical properties of patterned glass substrates will be studied. Subsequently, coating sol-gel AZMO thin film on these etched or patterned glass substrates will be carried out. The electrical, optical and surface characteristics of the sol-gel AZMO/etched glass substrate will be studied.

In Chapter 6, these sol-gel AZMO/flat glass, etched glass or patterned glass substrate will be applied as the transparent conductive layer in hydrogenated amorphous silicon single junction solar cells. Firstly, the effect of bandgap widening and roughening surface morphology on the performance of solar cells will be studied. After that, the device performance of solar cells deposited on the optically-rough and physically-flat TCO substrates will be presented.

Finally, Chapter 7 concludes this study and introduces future prospects.

References

[1] A. Luque, S. Hegedus, Handbook of Photovoltaic Science and Engineering, Second Edition, John Wiley & Sons, Ltd., 2011.
[2] Key World Energy Statistics, International Energy Agency, 2015, p-24.
[3] Moomaw, W., F. Yamba, M. Kamimoto, L. Maurice, J. Nyboer, K. Urama, T. Weir, 2011: Introduction. In IPCC Special Report on Renewable Energy Sources and Climate Change Mitigation [O. Edenhofer, R. Pichs-Madruga, Y. Sokona, K. Seyboth, P. Matschoss, S. Kadner, T. Zwickel, P. Eickemeier, G. Hansen, S. Schlomer, C.von Stechow (eds)], Cambridge University Press, Cambridge, United Kingdom and New York, NY, USA.
[4] Climate Change 2014: Synthesis Report. Contribution of Working Groups I, II and III to the Fifth Assessment Report of the Intergovernmental Panel on Climate Change. [Core Writing Team, Pachauri, R.K. and Meyer, L. (eds.)]. IPCC, Geneva, Switzerland.
[5] Solar generation 6, solar photovoltaic electricity empowering the world, European Photovoltaic Industry Association, 2011, p-78.
[6] http://panasonic.net/energy/solar/hit/.
[7] J. Goladsmith, J. Riggle, A.C.L. Yu, The Handbook of Phonological Theory, Second Edition, Wiley-Blackwell, 2011.
[8] H. Schade, Z. Smith, A. Catalano, Thin Solid Films 117 (1984) 149-155.
[9] T. Matsui, M. Tsukiji, H. Saika, T. Toyama, H. Okamoto, Influence of substrate texture on microstructure and photovoltaic performances of thin film polycrystalline silicon solar cells, J. Non-Cryst. Solids 299-302 (2002) 1152-1156.
[10] Y. Sobajima, T. Matsuura, T. Higuchi, T. Kawabe, N. Haruta, T. Toyama, H. Okamoto, Novel light-trapping structure having smooth surface for silicon thin-film solar cell, Proc. 33th IEEE Photovoltaic Specialists Conf., 2008, p-1.
[11] Z. Ma, Z. Tang, E. Wang, M.R. Andersson, O. Inganas, F. Zhang, Influences of surface roughness of ZnO electron transport layer on the photovoltaic performance of organic inverted solar cells J. Phys. Chem. C 116 (2012) 24462-24468.
[12] G.E. Eperon, V.M. Burlakov, P. Docampo, A. Goriely, H.J. Snaith, Morphological Control for High Performance, Solution-Processed Planar Heterojunction Perovskite Solar Cells, Adv. Funct. Mater. 24 (2014) 151-157.
[13] Y. Hishikawa, Tech. Digest of the Int. PVSEC-11, Sapporo, Japan, 1999, p-219.
[14] H. Sakai, T. Yoshida, T. Hama, Y. Ichikawa, Effect of surface morphology of transparent electrode on the open-circuit voltage in a-Si:H solar cells, Jpn. J. Appl. Phys. 29 (1990) 630-635.
[15] Y. Nasuno, M. Kondo, A. Matsuda, Effects of Substrate Surface Morphology on Microcrystalline Silicon Solar Cells, Jpn. J. Appl. Phys. 40 (2001) L303-L305.
[16] H. Sai, Y. Kanamori, M. Kondo, Flattened light-scattering substrate in thin film silicon solar cells for improved infrared response, Appl. Phys. Lett. 98 (2011) 1135021-1135023.
[17] K. Soderstrom, G. Bugnon, R. Biron, C. Pahud, F. Meillaud, F.J. Haug, C. Ballif, Thin-film silicon triple-junction solar cell with 12.5% stable efficiency on innovative

flat light-scattering substrate, J. Appl. Phys. 112 (2012) 1145031-1145033.
[18]K. Soderstrom, G. Bugnon, F.J. Haug, S. Nicolay, C. Ballif, Experimental study of flat light-scattering substrates in thin-film silicon solar cells, Sol. Energ. Mat.& Sol. Cell 101 (2012) 193-199.
[19]C. Haase and H. Stiebig, Optical propeties of thin-film silicon solar cells with grating couplers, Prof. Photovolt: Res. Appl.14 (2006) 629-641.
[20]M. Kambe, N. Taneda, A. Takahashi, T. Oyama, Res. Reports Asahi Glass Co., Ltd., 60(2010) 7-12.

Chapter 2 Review of $Zn_{1-x}Mg_xO$ thin film and Sol-Gel process

2.1 Introduction

$Zn_{1-x}Mg_xO$ thin film becomes a very promising wide bandgap semiconductor due to non-toxicity, low-cost of raw materials, tunable bandgap [1, 2, 3]. It is very expected to replace ZnO as the front transparent conductive layer in thin-film solar cells, for decreasing the optical loss in the transparent conductive layer. This chapter will introduce the basics and status of $Zn_{1-x}Mg_xO$ thin film. Then, the deposition methods and main applications of $Zn_{1-x}Mg_xO$ thin film will be presented. After that, sol-gel process will be introduced. The basic concepts, processing steps and its main applications will be reviewed.

2.2 Basics of $Zn_{1-x}Mg_xO$

$Zn_{1-x}Mg_xO$ is an II-VI widegap semiconductor alloy of ZnO (3.3 eV) and MgO (7.8 eV). The bandgap energy of $Zn_{1-x}Mg_xO$ can be tuned from 3.3 eV to 7.5 eV by varying the content of MgO. Based on the phase diagram of ZnO-MgO binary system, the thermodynamic solid solubility of MgO in ZnO is less than 4 mol % [4]. ZnO shows a wurtzite, hexagonal structure (a= 3.24 Å and b=5.20 Å), while MgO shows a NaCl type cubic structure (a= 4.24 Å). Although there is a large structural dissimilarity between ZnO and MgO, Ohtomo et al. [5] concluded that the solid solubility of MgO in ZnO is 33 mol % for thin-film alloys grown by pulsed laser deposition under metastable conditions. MgO would segregate from the wurtzite $Zn_{1-x}Mg_xO$ lattice when

the content of MgO is larger than 33 mol %. At the same time, the crystal structure of $Zn_{1-x}Mg_xO$ would change from hexagonal ($0 < x < 0.33$) to cubic ($x > 0.45$) phase. As shown in Fig. 2.1, wurtzite $Zn_{1-x}Mg_xO$ is reasonably regarded as a substitutional solid solution because Mg^{2+} (0.57 Å) tends to substitute Zn^{2+} (0.60 Å) due to their similar tetrahedral ionic radius.

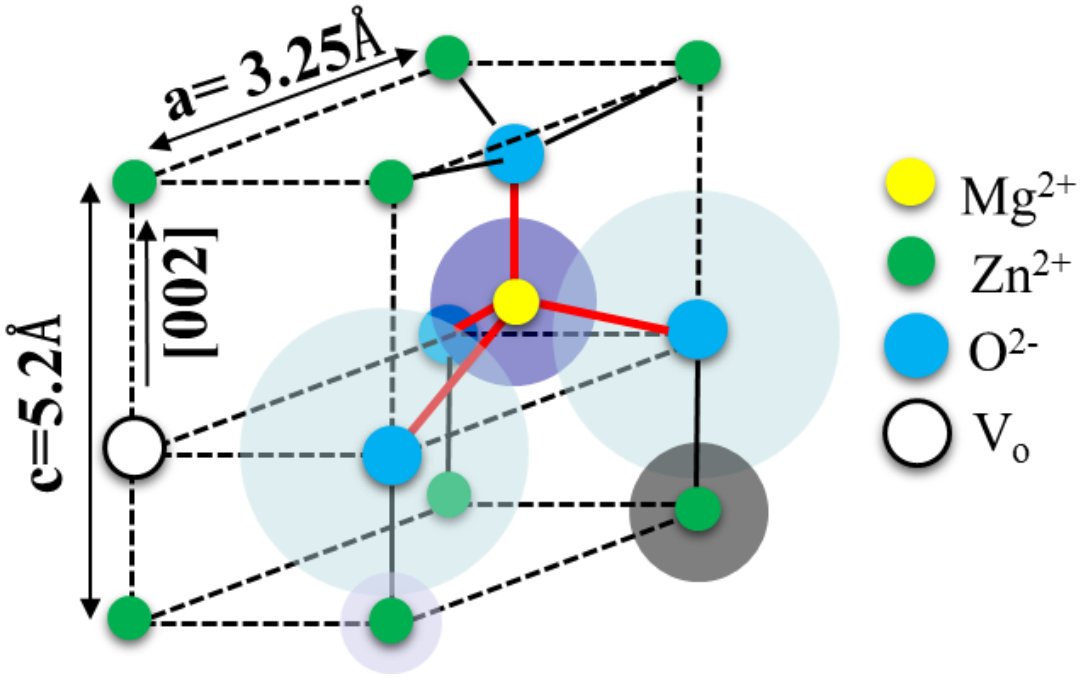

Fig. 2.1 Lattice structure of wurtzite $Zn_{1-x}Mg_xO$.

Figure 2.2 shows the bandgap widening mechanism of $Zn_{1-x}Mg_xO$ thin film. In one hand, the Zn^{2+} site substitution with Mg^{2+} would increase the bond length between metal cation and oxygen anion. This enhanced binding energy would decrease the lattice interatomic distance in the [002] direction [6]. In the other hand, it would also increase the reduced effective mass and then influence the bottom of the conduction band [7]. These two factors results in the bandgap widening of $Zn_{1-x}Mg_xO$ relative to ZnO.

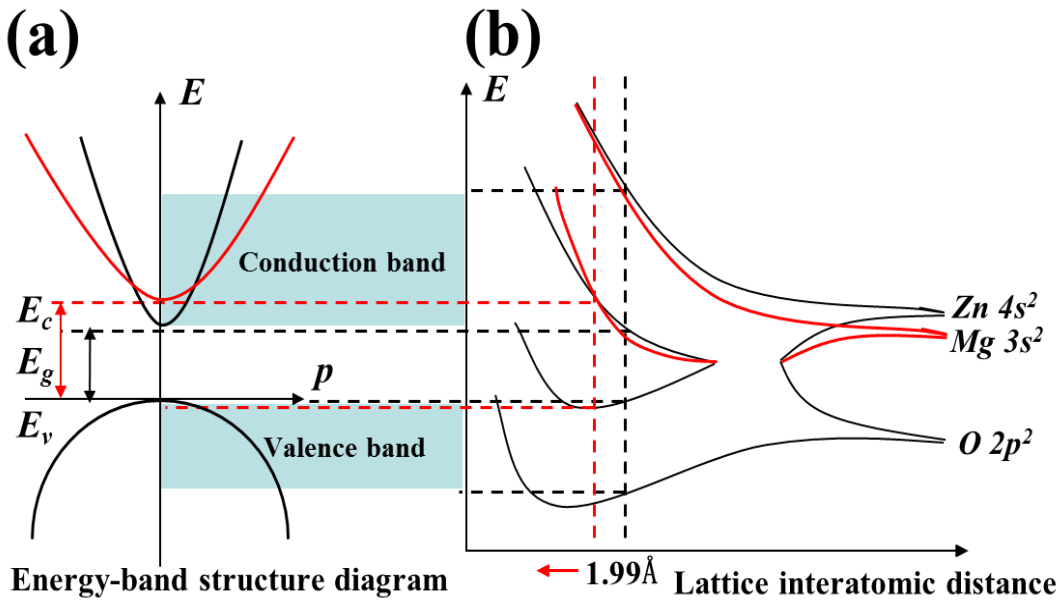

Fig. 2.2 Bandgap widening mechanism of $Zn_{1-x}Mg_xO$
(a) energy-band structure diagram and (b) energy lever splitting diagram

2.3 Status of $Zn_{1-x}Mg_xO$ thin film

2.3.1 Fabrication methods of $Zn_{1-x}Mg_xO$ thin film

$Zn_{1-x}Mg_xO$ thin film have been developed by many different methods. A brief review on the main deposition methods is shown below.

(a) Magnetron Sputtering

Minemoto et al. [8] reported the deposition of $Zn_{1-x}Mg_xO$ thin film by radio frequency (RF) magnetron co-sputtering on fused silica substrates at room temperature. The deposited $Zn_{1-x}Mg_xO$ had bandgap energy from 3.24 eV at x=0 to 4.20 eV at x=0.46. The transmittance of $Zn_{1-x}Mg_xO$ films were nearly equivalent to those of ZnO for a visible, near infrared light. The absorption edge shifted to a short wavelength as the Mg content increased. Ma et al. [9] developed gallium doped ZnMgO ($Zn_{1-x}Mg_xO$:Ga)

films with Mg content from 0 to 10 % that were deposited on glass substrate by DC reactive magnetron sputtering. The resistivity of these films increases with increasing Mg concentration. The transmittance of $Zn_{1-x}Mg_xO$: Ga thin film is over 90% in the visible range. Maejima et al. [10] studied the characterization of $Zn_{1-x}Mg_xO$: Ga or Al transparent conductive thin films fabricated by multi-cathode RF magnetron sputtering. The $Zn_{1-x}Mg_xO$: Ga thin-film is more electrically conductive than $Zn_{1-x}Mg_xO$: Al thin film, because the former generated larger carrier concentration than the latter. A resistivity as low as 8×10^{-4} Ω·cm was achieved for $Zn_{0.9}Mg_{0.1}O$: Ga thin film.

(b) Metalorganic chemical vapor deposition

Park et al. [11] reported that high quality $Zn_{1-x}Mg_xO$ ($0.00\leq x\leq0.49$) thin-film were fabricated by metalorganic vapor-phase epitaxy method at 500-650 ^oC on Al_2O_3 (001) substrates. Increasing the Mg content in the films up to 49 at. % resulted in that the c-axis constant of the films decreased from 5.21 to 5.14 Å and no significant phase separation was observed. Chiba et al. [12] investigated the phase transition of $Zn_{1-x}Mg_xO$ thin films grown by metalorganic chemical vapor deposition (MOCVD) process. It was found that the structure of $Zn_{1-x}Mg_xO$ thin film shows strong dependence on the Mg/(Zn+Mg) molar flow rate ratio and substrate temperature during growth. Higher growth temperature was needed for the growth of wurtzite $Zn_{1-x}Mg_xO$ with high Mg content. Li et al. [13] reported the effect of Mg content and B doping on the structural, electrical, and optical properties of $Zn_{1-x}Mg_xO$ thin films prepared by MOCVD. It was illustrated that the resistivity of $Zn_{1-x}Mg_xO$:B thin film can be reduced to about 10^{-5} Ω·cm by varying the B doping concentration. It was achieved that a blue shift of the absorption edge and a high transmittance of about 90% in visible regions.

(c) Pulse laser deposition

Ohtomo et al. [14] developed the $Zn_{1-x}Mg_xO$ thin films by pulse laser deposition

(PLD) method on sapphire (0001) for the fabrication heteroepitaxial ultraviolet light emitting devices based on ZnO. In that work, solid solution films were prepared with Mg content up to x=0.33, achieving a bandgap of 3.99 eV at room termperature. MgO impurity phase segregated at $x \geq 0.36$. These films showed ultraviolet photoluminescence at energies from 3.36 (x=0) to 3.87 eV (x=0.33) at 4.2 K. Ryoken et al. [15] investigated the thermal stability and defect structure of $Zn_{1-x}Mg_xO$ thin films deposited by PLD on substrate of cubic zirconia stabilized by addition of yttria with well-polished (111) face. It was found that the equilibrium state is likely in the range of $0.12<x<0.18$. The lattice constants of the alloy film with $x < 0.12$ varied with annealing temperature. The films with $x \geq 0.18$ decomposed into a rocksalt-type and a wurtzite-type phase. These behaviors indicated the highly non-quilibrium nature of this $Zn_{1-x}Mg_xO$ alloy film grown by PLD. Matsubara et al. [2] achieved the Al doped $Zn_{1-x}Mg_xO$ thin film with resistivity of about 3×10^{-4} Ω·cm by PLD method. It was deposited on glass substrate at a substrate temperature of 200 ^oC. It demonstrated the band-gap engineering possibilities in the range of E_g=3.5-3.97 eV with a resistivity of less than 1×10^{-3} Ω·cm.

(d) Molecular beam epitaxial deposition

Vashaei et al. [16] reported the growth of $Zn_{1-x}Mg_xO$ thin film on MgO (111)/c-sapphire by plasma-assisted molecular-beam epitaxy (MBE) method. The dependence of the cation-anion bond length to Mg content was studied. A virtual crystal model of MgZnO was proposed to interpret the bond-length variation. High-resolution transmission electron microscopy results indicated that the initial stage of the $Zn_{1-x}Mg_xO$ growth on a MgO buffer layer strarted with a cubic structure. Koike et al. [17] conducted the research on the growth of ZnMgO alloy films on (111)-oriented Si substrate toward UV-detector applications. It was found that the solid solubility limit of

MgO in ZnO lattice is about x=0.45 at low growth temperature. The photoresponse measurement for $Zn_{1-x}Mg_xO$/Si photoconduction cells exhibited visible-blind characteristics with specific cutoff wavelengths.

(e) Sol-Gel process

Wei et al. [18] reported that amorphous $Zn_{1-x}Mg_xO$ thin films were synthesized by a low-cost sol-gel method on quartz substrates. It was found that the synthesized film showed high transmittance of more than 90% in the visible and near infrared regions, with optical bandgap tenability from 3.3 eV to more than 6.5 eV. Singh et al. devoted much efforts on the research of $Zn_{1-x}Mg_xO$ film deposited by sol-gel method. It was found that the resistivity, carrier concentration, work function, and bandgap increased with the post annealing increased from 300℃ to 700℃. As the sample were further annealed above 700 ºC, the degradation was observed in the above mentioned properties [19]. Furthermore, in their investigation of phase segregation, it was found that the single-phase wurtzite thin films start showing phase segregation for Mg content of x=0.25 [20]. The derived samples are highly transparent (85-95 %) in the visible region (400-700 nm) and have a sharp absorption edge in the ultraviolet region, but their resistivity is higher than 10^3 Ω cm due to high porosity. Ahmad et al [21] investigated the effect of aging and Mg content on the structure and resistivity of $Zn_{1-x}Mg_xO$ thin film. It was found that the electrical resistivity increased with aging time. One resistivity of 12.6 Ω·cm was achieved for $Zn_{1-x}Mg_xO$ with Mg content of 10 at. %.

2.3.2 Application

$Zn_{1-x}Mg_xO$ thin film have been widely used in many fields. It enables novel heterostructures and quantum wells with combining with ZnO thin film. It also contributes a lot to the development in the field of transparent conductive oxides (TCO),

bulk acoustic wave devices, thin-film transistors, optoelectronic devices such as UV light detectors, UV light emitting diodes, and thin film solar cells. These application will be introduced in order.

(a) Heterostructures and quantum wells

Ye et al. [22] reported the formation of two-dimensional electron gas (2DEG) with the Zn-polar $Zn_{1-x}Mg_xO$/ZnO heterostructure. The $Zn_{1-x}Mg_xO$ thin film was grown by MOCVD method. The $Zn_{0.8}Mg_{0.2}O$/ZnO heterostructure showed a high Hall mobility of 2138 cm^2/Vs and a carrier sheet density of 3.51×10^{12} cm^{-2} at temperature of 1.4 K. It is the donor states on ZnMgO surface that causes the formation of 2DEG. The carrier density of 2DEG also depends on the thickness and Mg composition of ZnMgO layer. Gruber et al [23] developed ZnO-ZnMgO quauntum well structure with different well widths through using ZnMgO as barrier material. The quantum well luminescence showed a quantization behavior and an enhancement of exciton binding energy up to 96 meV can be inferred from the results. It would enable an even higher stability of excitons in ZnO quantum well structures above room temperature and enhanced the performance of ZnO based excitonic devices.

(b) Transparent conductive oxides

Transparent conductive oxide applications require low resistivity and transparency. As mentioned in section 2.3.1, transparent conductive $Zn_{1-x}Mg_xO$ thin films have been developed by many methods. The optical bandgap energy and resistivity of representive $Zn_{1-x}Mg_xO$ thin film fabricated by different methods are shown in Table 2.1. It can be found that $Zn_{1-x}Mg_xO$ thin film with wide bandgap and low resistivity has been achieved by PLD, radio frequency magnetron sputtering, MOCVD, and atomic layer deposition (ALD) method. The sol-gel derived $Zn_{1-x}Mg_xO$ thin film has wide bandgap, but its resistivity is still too large compared to the Zn_{1-}

$_xMg_xO$ thin film fabricated by other methods.

Table 2.1 Transparent conductive $Zn_{1-x}Mg_xO$ thin film deposited by different methods.

Deposition process	E_{opt} (eV)	Dopant	Resistivity (Ω·cm)
PLD[2]	3.97	Al	$\leq 1\times10^{-3}$
Sputtering[10]	3.82	Al	8×10^{-4}
MOCVD[24]	3.88	B	9×10^{-4}
ALD[25]	3.81	Al	4.5×10^{-3}
Sol-Gel[20]	3.54	none	1×10^{3}

(c) Bulk acoustic wave devices

$Zn_{1-x}Mg_xO$ is also a new piezoelectric material. It allows for flexibility in thin film multilayer surface acoustic wave, because its piezoelectric properties can be tailored by controlling the Mg composition as well as the $Zn_{1-x}Mg_xO$/ZnO multilayer structures. Emanetoglu et al. [26] reported the analysis of the piezoelectric properties of MOCVD deposited $Zn_{1-x}Mg_xO$/sapphire material system with different Mg compositions, based on a transfer matrix method. It was found that in-plane anisotropy in piezoelectric properties resulted in the excitation of Rayleigh and Love wave modes parallel and perpendicular to the $Zn_{1-x}Mg_xO$ c-axis, respectively. It was also found that the acoustic velocity increases, whereas the piezoelectric coupling decreases with increasing Mg composition in piezoelectric $Zn_{1-x}Mg_xO$ films.

(d) Thin-film transistors

Lee et al. [27] developed one thin-film transistor with sol-gel derived Zn_{1-}

$_xMg_xO$ thin film as the active channel layer. The depletion region in the grains increased with the amount of Mg addition and resulted in almost depleted grains in the active channel layers at x=0.2. This enabled one TFT with an enhancement mode and an on/off ratio of 10^6. Wu et al. [28] reported transparent thin-film transistors using ZnMgO as dielectrics and channel. They used cubic-phase ZnMgO as gate insulator and hexagonal-phase ZnMgO as channel. It was found that the cubic-phase isolating layer demonstrated low leakage current characteristics, i.e., 4×10^{-7} A/cm^2, at a bias of 10V. It enabled one transparent thin-film transistor with a channel mobility of 1.5 $cm^2 \cdot V^{-1} \cdot s^{-1}$ and an on/off ratio of 10^4.

(e) Optoelectronic devices

Kamada et al. [29] reported the fabrication of ZnMgO thin films by linear-source ultrasonic spray chemcical vapor deposition method and its application to ultraviolet photodetectors. A UV photodetector fabricated with using the ZnMgO thin film showed high photoresponsivity and suggested the promising optoelectronic characteristics of the ZnMgO thin films. Chawla et al. [30] developed a series of ZnMgO thin-film nanophosphors with varied Zn/Mg by chemical bath deposition method. It was found that the luminescence in the visible region increases significantly with changing Mg content, reaching a maximum with 25% Mg. This ZnMgO thin-film nanophosphors have a photoluminescence (PL) exciation band in the range of 330-400 nm, while the commercially available UV LEDs cover the wavelength range of 275-390 nm. It would make an efficient single pc-LED for white-light generation feasible. Meng et al. [31] reported the application of MOCVD derived $Zn_{1-x}Mg_xO$ thin film to $Cu(InGa)(SSe)_2$ solar cells as one buffer layer. It was mentioned that $Zn_{1-x}Mg_xO$ thin film is superior to CdS or ZnO films as buffer and window layers mainly due to its controllable bandgap enery and safety.

2.4 Basics of Sol-Gel process

2.4.1 Basic concepts

In materials science, the sol-gel process is defined as a method for producing solid materials from small molecules [32]. It is also defined as the preparation of ceramic materials and organically modified materials by preparation of a sol, gelation of the sol, and removal of the solvent [33]. The sol-gel process is usually utilized for the fabrication of metal oxides, especially the oxides of silicon and titanium. Sol-gel process requires considerably less equipment and is potentially less expensive, compared to conventional thin film forming process such as chemical vapor deposition, evaporation, or sputtering. The advantages of sol-gel process are the precise control of stoichiometry and film growth with preferential orientation. It has the ability to control precisely the microstructure of the deposited film, i.e., the pore volume, pore size and surface area. However, the disadvantages of sol-gel process are (1) thick film (>1 μm) is difficult to make without cracking; (2) relatively high annealing temperature is must procedure for good properties; (3) long processing time is needed to repeat coating and drying procedure, which not only increases cost but also increase the possibility of contamination [33].

A sol refers to a stable dispersion of colloidal particles or polymers in a solvent. The colloid particles are so small (~1-1000 nm) that gravitational forces are negligible and interactions are dominated by short-range forces, like van der Waals attraction. A gel is made up of an interconnected, rigid network with pores of submicrometer dimensions and polymeric chains whose average length is greater than a micrometer [34]. A gel is made up of a three dimensional continuous network, which encloses a liquid phase. A gel may also be prepared from particulate sols, when attractive

dispersion forces cause them to stick together in a way to form a network.

2.4.2 Processing Steps

The sol-gel process usually comprises mixing, gelation, drying, and sintering. Here we take the sol-gel process for preparation of ZnO thin film for example. As shown in Fig 2.3, the process includes three parts: the preparation of the precursor solution, the deposition of the sol-gel precursor on the substrate, and the heat treatment of the xerogel film. The xerogel refers to the dried gel at ambient pressure. At each step, there are many physical and chemical factors that influence the final property of materials. The details of each step will be introduced in order.

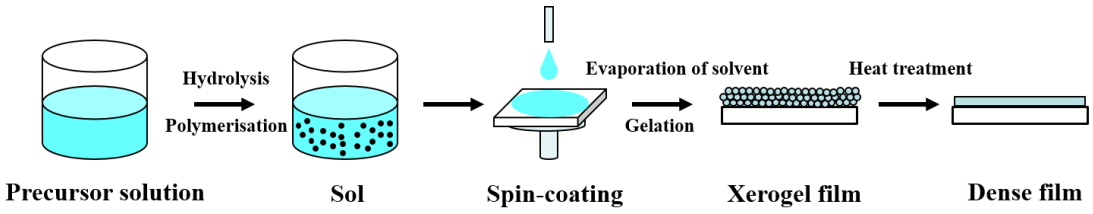

Fig. 2.3 Schematics of sol-gel process for film preparation [35].

(a) Preparation of the sol-gel precursor

First of all, the precursor (starting compound) solution is prepared by dissolving the raw materials in a solvent. The raw materials are usually metal salts, including nitrate, chloride, perchlorate, acetylacetonate, alkoxides such as ethoxide and propoxide, and acetate dehydrate. The most often used one is the acetate dehydrate. The solvent must have a relatively high dielectric constant in order to dissolve the inorganic salts [36]. The commonly used solvents are methanol, ethanol, 1-propanol, 2-propanol, 1-butanol, and 2-methoxyethanol. The most used ones are ethanol and 2-propanol.

Except metal salts and solvent, additives are indispensable for preparing precursor solution. Additives (stabilizer) are chemical species possessing at least one functional group, which enables these species to act as several roles. They play as basic or acid and chelating agent. For znic salt, the best stabilizer is mono- to tri- ethanolamines or lactic asid. Ohyama et al. [37] proposed that monoethanolamine (MEA) coordinates the zinc atoms as a bidentate ligand in two ways: one is to act as a chelating ligand and the other is to bridge two zinc atoms. Briefly, the precursor nature and its concentration, solvent, additive, and aging time influence the finial properties of oxide films.

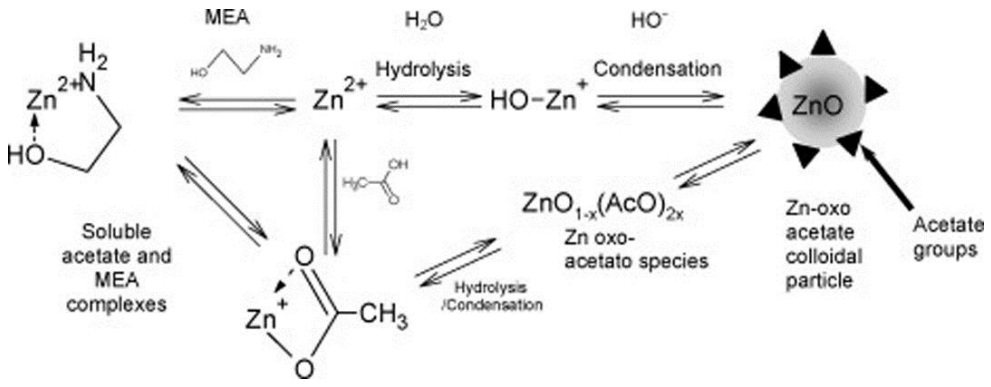

Fig. 2.4 Sketch of the chemical equilibria taking place in the initial solution of sol-gel precursor [38].

Complex chemical equilibria occurs in the initial solution of sol-gel precursor, as shown in Fig. 2.4. A molecular precursor in a homogeneous solution undergoes a succession of transformations [35]: the hydrolysis of the molecular precursor, the polymerization via successive bimolecular additions of ions, the formation of oxo-, hydroxyl, or aquabridges, the condensation by dehydration, the nucleation and growth. Znaidi et al. [39] described the mechanism for the reaction between the main species in the precursor solutions containing znic acetate dehydrate, ethanol, and MEA. In the initial solution, small znic-oxo-acetate oligomers are formed through interaction between the nucleophilic (MEA, HO^- and CH_3COO^-) species and the Zn^{2+} Lewis acid

center. Stable acetate-capped colloidal nanometric to sub-micronic particles are formed in the solution through gradual forced hydrolysis of Zn-MEA or Zn-AcO soluble complexes during aging and progressive condensation of the hydrolyzed moieties. Tokumoto et al. [40] mentioned that the formation of ZnO colloidal particles in an alcoholic solvent contains two stages. Small oligomers are continuously formed at the early stage of phase transformation, and the oligomers aggregate to form wurtzite, the primary colloidal particles. After that, the primary particles aggregate and form a third family, the secondary colloidal particles. Subsequently, these particles undergo nucleation and growth. The growth of the colloidal particles is a stepped, discontinuous process. Spanhel et al. [41] reported the way in which ZnO colloidal particle grows. Firstly, some small stable molecular clusters are formed, and they would rapidly combine to undergo the next stable aggregate. The primary aggregates would further rapidly combine to give the next most stable secondary aggregate and so on. Meulenkamp [42] suggested that large particles grow at the expense of smaller particles. The rate of particle growth is related to the concentration of precursors or dissolved species and their reactivity, which depends on the number of particles surface atoms and the solution composition.

(b) Deposition of the prepared sol on substrates

Generally, films can be prepared by dip coating, spin-coating or spraying the aged sols on substrates. ZnO thin films have already elaborated by spin-coating [43], dip-coating [44], and spray pyrolysis [45]. In this thesis, we just focus on spin-coating method. Spin coating is a well-developed lab-scale thin film deposition method and it is simple to operate. A spin coater is usually used to do film deposition. The process of spin-coating is divided into four stages: deposition, spin-up, spin-off and evaporation [33], as shown in Fig. 2.5. At the beginning, a small amount of sol-gel precursor is

applied on the center of the substrate, which is either spinning at low speed or not spinning at all. In the spin-up state, the liquid flows radially outward, driven by centrifugal force. Factors such as final rotation speed, acceleration, and evaporation influence the properties of the coated films. In the spin-off stage, excess liquid flows to the edge of the substrate and leaves as droplets, leaving a thin film of material on the surface. In the fourth stage, evaporation removes the solvent and xerogel film is formed on the substrate.

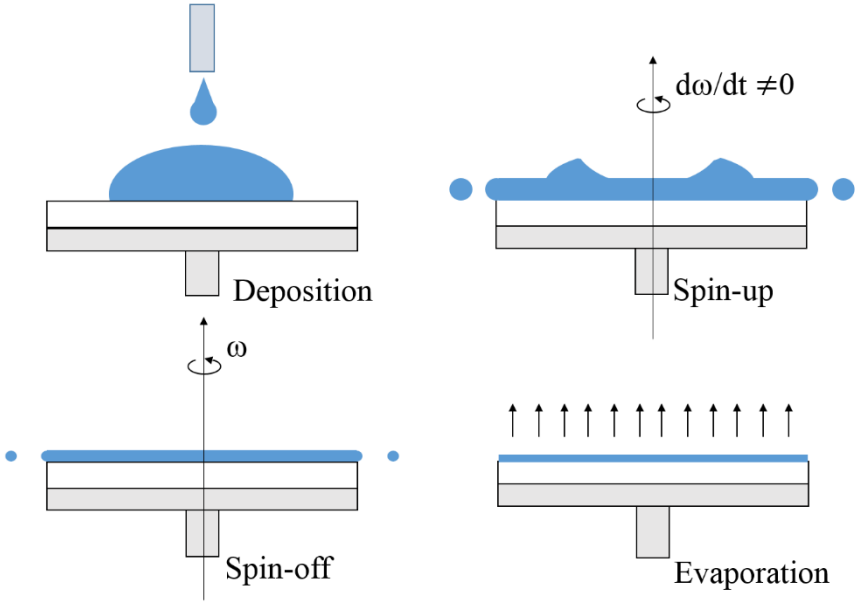

Fig. 2.5 Schematics of stages of the spin-coating process.

The thickness of the film depends on the viscosity and concentration of the solution and the solvent. The thickness of an initially uniform film during spin-off is described by Eq. 2.1 [46],

$$h(t) = h_0 / (1 + 4\rho\omega^2 h_0^2 t / 3\eta)^{1/2} \qquad (2.1)$$

where h_0 is the initial thickness, ρ is the density of the liquid, η is the viscosity, t is time, and ω is the angular velocity. The ρ and ω are assumed constant. Based on the mode of spin-coating proposed by Meyerhofer [47], which separates the spin-off and evaporation stages, the final thickness and total elapsed time to achieve this thickness are represented by following equations,

$$h_{final} = (1 - \rho_{A_0} / \rho_A)(\frac{3\eta m}{2\rho_A \omega^2})^{1/3} \quad (2.2)$$

$$t_{final} = t_{spin-off} + h_{spin-off}\rho_{A_0} / m\rho_A \quad (2.3)$$

where ρ_A is the mass of volatile solvent per unit volume, ρ_{A0} is its initial value and e is the evaporation rate that depends on the mass transfer coefficient. Equations 2.1-2.3 apply to Newtonian liquids that do not show a shear rate dependence of the viscosity during the spin-off stage.

(c) heat treatment of the coated film

After coating, heat treatment (annealing or sintering) is subsequently carried out for enhancing structural and electrical properties through densification and grain growth. It is a process of network densification, which is driven by interfacial energy. Materials moves by viscous flow or diffusion to eliminate porosity and thereby reduce the solid-vapor interfacial area [33].

The heat treatment of the deposited films is usually conducted in two steps. At the first step, a pre-heat treatment (drying) (40-500 ^oC) is performed during a short time for solvent evaporation and organic compounds removal. A xerogel film is formed on

the substrate after drying with unhindered shrinkage. When solvent removal occurs under supercritical conditions, the network does not shrink and a highly porous, low-density material is formed. The second step, that is, a post-heat treatment (annealing) is carried out in order to obtain a well-crystallized film and the decomposition of organic by-products. It effectively transforms the porous gel into a dense film.

2.4.3 Application

The sol-gel process has been widely utilized in many fields. The early applications for sol-gel films were optical coating. Optical coatings change the optical behavior of the substrate. TiO_2/Pd coated architectural glass [48] utilizes TiO_2 to control the reflectivity and Pd content to control the absorption. Buildings covered with TiO_2/Pd coated architectural glass appear outwardly uniformly reflective and the light transmission is controlled in accordance with sun exposure to minimize summer cooling cost. In addition, the refractive index SiO_2-TiO_2 binary films decrease continuously with SiO_2 content from about 2.2 to 1.4. They are used as the optical oxide coatings on glass for antireflective and self-cleaning purpose. Moreover, it was reported that the absorption of thin film could be modified through the incorporation of transition metals for producing a variety of colored coatings on different substrates [49]. Then, oxide coatings on glass and silicon substrates have also been applied as antireflective (AR) layer in solar cells to improve device performance [50] and as laser-damage-resistant AR coating for laser optics [51].

After that, sol-gel films began to be used in electronic, membrane, and sensor application. It is used intensively in photolithography, to deposit layers of photoresist about 1 μm thick. Electronic films include high temperature superconductors [52],

conductive indium tin oxide [53], and vanadium pentoxide [54] are also developed by sol-gel process. Furthermore, sol-gel process is used to prepare protective films to increase strength of oxide glasses [55], or provide passivation or planarization [56].

2.5 Summary

Brief review of $Zn_{1-x}Mg_xO$ thin film and sol-gel process was conducted. $Zn_{1-x}Mg_xO$ thin film has widely tunable bandgap and achievable low resistivity. It shows promising potentials in many fields. The sol-gel process holds potentials in fabrication of optical coatings, electronic films and protective films due to purity and homogeneity. In order to fabricate optically-rough and physically-flat TCO substrates, development of $Zn_{1-x}Mg_xO$ transparent conductive thin film by sol-gel process becomes a very important topic.

Reference

[1] A. K. Sharma, J. Narayan, J. F. Muth, C. W. Teng, C. W. Teng, C. Jin, A. Kvit, R. M. Kolbas, and O. W. Holland, Optical and structural properties of epitaxial $Mg_xZn_{1-x}O$ alloys, Appl. Phys. Lett. 75 (1999) 3327-3329.

[2] K. Matsubara, H. Tampo, H. Shibata, A. Yamada, P. Fons, K. Iwata, S. Niki, Band-gap modified Al-doped $Zn_{1-x}Mg_xO$ transparent conducting films deposited by pulsed laser deposition, Appl. Phys. Lett. 85 (2004) 1374-1376.

[3] R. Ghosh, D. Basak, Composition dependence of electrical and optical properties in sol-gel $Mg_xZn_{1-x}O$ thin films, J. Appl. Phys. 101 (2007) 0235071-0235075.

[4] J.F. Sarver, F.L. Katnack, F.A. Hummel, Phase Equilibria and Manganese–Activated Fluorescence in the System $Zn_3(PO_4)_2$-$Mg_3(PO_4)_2$, J. Electrochem. Soc. 106 (1959) 960-963.

[5] A. Ohtomo, M. Kawasaki, T. Koida, K. Masubuchi, H. Koinuma, Y. Sakurai, Y. Yoshida, T. Yasuda, Y. Segawa, $Mg_xZn_{1-x}O$ as a Ⅱ-Ⅵ widegap semiconductor alloy, Appl. Phys. Lett. 72 (1988) 2466-2468.

[6] A. Boonchun, W.R.L. Lambrecht, Bond lengths, phase stability, and bandgaps in $Mg_xZn_{1-x}O$ alloys, J. Vac. Sci. Technol. B 27 (2009) 1717-1721.

[7] J.G. Lu, S. Fujita, T. Kawaharamura, H. Nishinaka, Y. Kamada, Carrier concentration induced band-gap shift in Al-doped $Zn_{1-x}Mg_xO$ thin films, Appl. Phys. Lett. 89 (2006) 2621071-2621073.

[8] T. Minemoto, T. Negami, S. Nishiwaki, Preparation of $Zn_{1-x}Mg_xO$ films by radio frequency magnetron sputtering, Thin Solid Films 372 (2000) 173-176.

[9] Q.B. Ma, H.P. He, Z.Z. Ye, Sixfold self-assembled hierarchical structures synthesized by direct annealing of Zn microtips, Journal of Solid State Chemistry 181 (2008) 673-678.

[10] K. Maejima, H. Shibata, H. Tampo, K. Matsubara, S. Niki, Characterization of $Zn_{1-x}Mg_xO$ transparent conducting thin films fabricated by multi-cathode RF-magnetron sputtering, Thin Solid Films 518 (2010) 2949-2952.

[11] W.I. Park, G.Yi, H.M. Jang, Metalorganic vapor-phase epitaxial growth and photoluminescent properties of $Zn_{1-x}Mg_xO$ thin films, Appl. Phys. Lett. 79 (2001) 2022-2024.

[12] Y. Chiba, F.Y. Meng, A. Yamada, M. Konagai, Study of phase transition of $Zn_{1-x}Mg_xO$ thin films grown by MOCVD process, IEEE 4th World Conference on Photovoltaic Energy Conversion 1 (2006) 567-570.

[13] C. Li, F.Y. Meng, S. Zhang, J.Q. Wang, Effects of Mg content and B doping on structural, electrical and optical properties of $Zn_{1-x}Mg_xO$ thin films prepared by MOCVD, J Cryst Growth (2010) 1929-1934.

[14] M. Ohyama, H. Kozuka, T. Yobo, Sol-Gel Preparation of Transparent and Conductive Aluminum-Doped Zinc Oxide Films with Highly Preferential Crystal Orientation, J. Am. Ceram. Soc. 81 (1998) 1622-1632.

[15] H. Ryoken, N. Ohashi, I. Sakaguhi, Y. Adachi, S. Hishita, H. Haneda, Structures and properties of (Zn, Mg)O films studied from the aspect of phase equilibria, Journal

of Crystal Growth 287 (2006) 134-138.
[16]Z. Vashaei, T. Minegishi, H. Suzuki, T. Hanada, M.W. Cho, T. Yao, A. Setiawan, Structural variation of cubic and hexagonal $Zn_{1-x}Mg_xO$ layers grown on MgO (111)/c-sapphire, J. Appl. Phys. 98 (2005) 0549111-0549113.
[17]K. Koike, K. Hama, I. Nakashima, G. Takada, K. Ogata, S. Sasa, M. Inoue, M. Yano, Molecular beam epitaxial growth of wide bandgap ZnMgO alloy films on (1 1 1)-oriented Si substrate toward UV-detector applications, J. Crys. Growth 278 (2005) 288-292.
[18]M. Wei, R.C. Boutwell, J.W. Mares, A. Scheurer, W.V. Schoenfeld, Bandgap engineering of sol-gel synthesized amorphous $Zn_{1-x}Mg_xO$ films, Appl. Phys. Lett. 98 (2011) 2619131-2619133.
[19]A. Singha, D. Kumara, P.K. Khannab, A. Kumara, M. Kumara, M. Kumarc, Anomalous behavior in ZnMgO thin films deposited by sol-gel method, Thin Solid Films 519 (2011) 5826-5830.
[20]A. Singh, A. Vij, D. Kumar, P.K. Khanna, M. Kumar, S. Gautam, K.H. Chae, Investigation of phase segregation in sol-gel derived ZnMgO thin films, Semicond. Sci. Technol. 28 (2013) 0250041-0250048.
[21]R. Ahmad, M. Salina, M.H. Mamat, A.A. Teh, M. Kara, M. Rusop, Z. Awang, Aging effects on physical and electrical properties of nano-structured MgZnO thin films for carbon nanotube applications, Journal of nanoscience and nanotechnology 12 (2012) 8153-8157.
[22]J.D. Ye, S. Pannirselvam, S.T. Lim, J.F. Bi, X.W. Sun, G.Q. Lo, K.L. Teo, Two-dimensional electron gas in Zn-polar ZnMgO/ZnO heterostructure grown by metal-organic vapor phase epitaxy, Appl. Phys. Lett. 97 (2010) 111908-111910.
[23]T. Gruber, C. Kirchner, R. Kling, F. Reuss, A. Waag, ZnMgO epilayers and ZnO-ZnMgO quantum wells for optoelectronic applications in the blue and UV spectral region, Appl. Phys. Lett. 84 (2004) 5359-5361.
[24]C. Li, F.Y. Meng, S. Zhang, J.Q. Wang, Effects of Mg content and B doping on structural, electrical and optical properties of $Zn_{1-x}Mg_xO$ thin films prepared by MOCVD, J. Cryst. Growth 312 (2010) 1929-1934.
[25]G. Luka, B.S. Witkowski, L. Wachnicki, K. Goscinski, R. Jakiela, E. Guziewicz, M. Godlewski, E. Zielony, P. Bieganski, E. Placzek-Popko, W. Lisowski, J.W. Sobczak, A. Jablonski, Atomic layer deposition of $Zn_{1-x}Mg_xO$:Al transparent conducting films, J. Mater. Sci. 49 (2014) 1512-1518.
[26]N.W. Emanetoglu, P. Wu, R.H. Wittstruck, Y. Chen, Y. Lu, $Mg_xZn_{1-x}O$: A New Piezoelectric Material, IEEE Trans. Ultrason. Ferroelectr. Freq. Control 50 (2003) 537-543.
[27]J.H. Lee, P. Lin, C.C. Lee, J.C. Ho, Y.W. Wang, Sol-gel-derived $Zn_{1-x}Mg_xO$ thin films used as active channel layer of thin-flim transistors, Jpn. J. Appl. Phys. 44 (2005) 4784-4789.
[28]H. Wu, J. Liang, G. Jin, Y. Lao, T. Xu, Transparent thin-film transistors using ZnMgO as dielectrics and channel, IEEE Trans. Electron Dev. 54 (2007) 2856-2859.
[29]Y. Kamada, T. Kawaharamura, H. Nishinaka, S. Fujita, Linear-Source Ultrasonic Spray Chemical Vapor Deposition Method for Fabrication of ZnMgO Films and

Ultraviolet Photodetectors Jpn. J. Appl. Phys. 45 (2006) L857-L857.
[30] S. Chawla, K. Jayanthi, H. Chander, Enhancement of luminescence in ZnMgO thin-film nanophosphors and application for white light generation, Phys. Stat. Sol. (a) 205 (2008) 271-274.
[31] F.Y. Meng, Y. Chiba, A. Yamada, M. Konagai, Growth of $Zn_{1-x}Mg_xO$ films with single wurtzite structure by MOCVD process and their application to $Cu(InGa)(SSe)_2$ solar cells, Sol. Energ. Mat. Sol. Cells 91 (2007) 1887-1891.
[32] Wikipedia, https://en.wikipedia.org/wiki/Sol-.
[33] C.J. Brinker, G.W. Scherer, SOL-GEL SCIENCE The Phsics and Chemistry of Sol-Gel Processing, ACADEMIC PRESS, INC., 1990.
[34] L.L. Hench, J.K. West, The Sol-Gel Process, Chem. Rev. 90 (1990) 33-72.
[35] L. Znaidi, Sol-gel-deposited ZnO thin films: A review, Materials Science and Engineering B 174 (2010) 18-30.
[36] E. Hosono, S. Fujihara, T. Kimura, H. Imai, Non-Basic Solution Routes to Prepare ZnO Nanoparticles, J. Sol-Gel Sci. Techno. 29 (2004) 71-79.
[37] M. Ohyama, H. Kozuka, T. Yoko, S. Sakka, Preparation of ZnO Films with Preferential Orientation by Sol-Gel Method, Journal of the Ceramic Society of Japan 104 (1996) 296-300.
[38] L. Znaidi, G.J.A.A.S. ILLIA, S. Benyahia, C. Sanchez, A.V. Kanaev, Oriented ZnO thin films synthesis by sol-gel process for laser application, Thin Solid Films 428 (2003) 257-262.
[39] L. Znaidi, G.J.A.A.S. Illia, R.L. Guennic, C. Sanchez, A. Kanaev, Elaboration of ZnO Thin Films with Preferential Orientation by a Soft Chemistry Route, J. Sol-Gel Sci. Techno. 26 (2003) 817-821.
[40] M.S. Tokumoto, S.H. Pulcinelli, C.V. Santilli, A.F. Craievich, SAXS study of the kinetics of formation of ZnO colloidal suspensions, J. Non-Cryst. Solids 247 (1999) 176-182.
[41] L. Spanhel, M.A. Anderson, Semiconductor clusters in the sol-gel process: quantized aggregation, gelation, and crystal growth in concentrated zinc oxide colloids, J. Am. Chem. Soc. 113 (1991) 2826-2833.
[42] E.A. Meulenkamp, Synthesis and Growth of ZnO Nanoparticles, J. Phys. Chem. B 102 (1998) 5566-5572.
[43] S. Ilican, Y. Caglar, M. Caglar, Preparation and characterization of ZnO thin films depostited by sol-gel spin-coating method, Journal optoelectronics and advanced materials 10 (2008) 2578-2583.
[44] G.G. Valle, P. Hammer, S.H. Pulcinelli, C.V. Santilli, Transparent and conductive ZnO:Al thin films prepared by sol-gel dip-coating, Journal of the European Ceramic Society 24 (2004) 1009-1013.
[45] F.P. D., W.E. La., D.R.A. N., E. Andradeb, M. Miki-Yoshida, Growth, structure and optical characterization of high quality ZnO thin films obtained by spray pyrolysis, Thin Solid Films 350 (1999) 192-202.
[46] A.G. Emslie, F.T. Bonner, L.G. Peck, Flow of a Viscous Liquid on a Rotating Disk, J. Appl. Phys. 29 (1958) 858-862.
[47] D. Meyerhofer, Characteristics of resist films produced by spinning, J. Appl. Phys.

49 (1978) 3993-3997.
[48] H. Dislich, E. Hussmann, Amorphous and crystalline dip coatings obtained from organometallic solutions: Procedures, chemical processes and products, Thin Solid Films 77 (1981) 129-140.
[49] A. Duran, J.M.F. Navarro, P. Casariego, A. Joglar, Optical properties of glass coatings containing Fe and Co, J. Non-Cryst. Solids 82 (1986) 82-391.
[50] R.B. Pettit, C.J. Brinker, Use of sol-gel thin films in solar energy applications, Sol. Energ. Mat. 14 (1986) 269-287.
[51] K. Hara, T. Inazumi, T. Izumitani, Application of sol-gel derived silica films containing a methyl radical to a slab laser, J. Non-Cryst. Solids 100 (490) 490-493.
[52] S.A. Kramer, G. Kordas, J. McMillan, G.C. Hilton, D.J.V. Harligen, Highly oriented superconducting thin films derived from the sol–gel process, Appl. Phys. Lett. 53 (1988) 156-158.
[53] N.J. Arfsten, Sol-gel derived transparent IR-reflecting ITO semiconductor coatings and future applications, J. Non-Cryst. Solids 63 (1984) 243-249.
[54] C. Sancheza, F. Babonneaua, R. Morineaua, J. Livagea, J. Bullotb, Semiconducting properties of V_2O_5 gels, Philosophical Magazine Part B 47 (1983) 279-290.
[55] B.D. Fabes, W.F. Doyle, B.J.J. Zelinski, L.A. Silverman, D.R. Uhlmann, Strengthening of silica glass by gel-derived coatings, J. Non-Cryst. Solids 82 (1986) 349-355.
[56] Y.W. Lam, H.C. Lam, Dielectric and interface-state measurements of metal-spin-on-oxide-silicon capacitors, J. Phys. D. Appl. Phys. 9 (1976) 1477-1487.

Chapter 3 Development of transparent conductive $Zn_{1-x}Mg_xO$ thin film by sol-gel process on flat glass substrate

3.1 Introduction

This chapter introduces the development of $Zn_{1-x}Mg_xO$ thin film by sol-gel process on flat glass substrate. Firstly, the detailed fabrication process will be presented. After that, the effect of preparation condition of sol-gel precursor, spin-coating parameters, and two-step annealing on the electrical, optical and structural properties of $Zn_{1-x}Mg_xO$ thin film will be investigated in order.

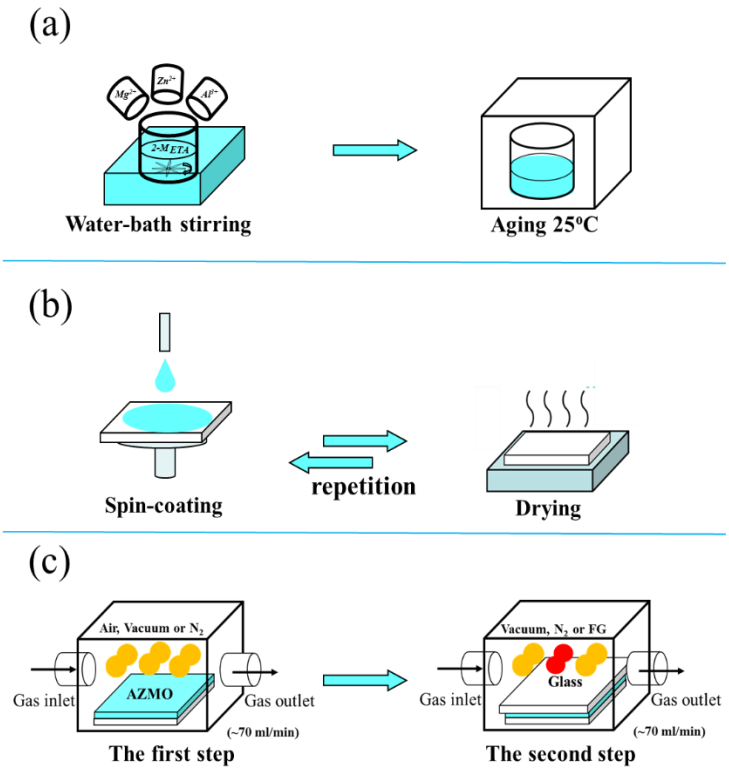

Fig. 3.1 Fabrication process of sol-gel derived $Zn_{1-x}Mg_xO$ thin film (a) precursor preparation (b) spin-coating, and (c) two-step annealing.

3.2 Fabrication of $Zn_{1-x}Mg_xO$ thin film by sol-gel process on flat glass substrate

The fabrication process of sol-gel derived Al doped $Zn_{1-x}Mg_xO$ (AZMO) thin film is shown in Fig. 3.1. It concludes three parts. The first part is the preparation of sol-gel precursor, the second part is the film deposition, and the third part is two-step annealing. Details of each part will be introduced in order.

3.2.1 Precursor preparation

Table 3.1 Raw materials used in this work.

Materials	State	Purity	Manufacturer
$Zn(CH_3COO)_2{\cdot}2H_2O$	solid	Min. 99.0%	KANTO CHMICAL CO. INC.
$Mg(CH3COO)_2{\cdot}4H_2O$	solid	Min. 99.3%	KANTO CHMICAL CO., INC.
$AlCl_3{\cdot}6H_2O$	solid	Min. 98.0%	KANTO CHMICAL CO., INC.
$Al(NO)_3{\cdot}9H_2O$	solid	Min. 98.0%	KANTO CHMICAL CO., INC.
NH_4F	solid	Min. 99.99%	SIGMA-ALDRICH CO. LLC.
2-Methoxyethanol	liquid	Min. 99.0%	KANTO CHMICAL CO. INC.
Ethanol	liquid	Min. 99.5%	KANTO CHMICAL CO. INC.
2-Aminoethanol	liquid	Min. 99.0%	KANTO CHMICAL CO. INC.

The information of raw materials used in precursor preparation are listed in Table 3.1. Zinc acetate dehydrate and magnesium acetate tetrahydrate are used as the source of znic and magnesium, respectively. Aluminium chloride hexahydrate, aluminium nitrate nonahydrate, and ammonium fluoride were used as the dopant. 2-

Methoxyethanol (2-M) and ethanol (EtOH) were used as solvent. Monoethanolamine (MEA) was used as stabilizer.

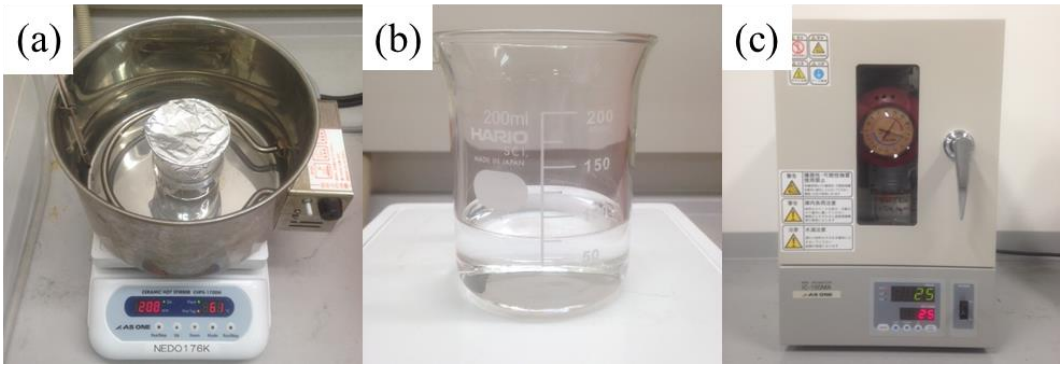

Fig. 3.2 Preparation process of sol-gel precursor.
(a) isothermal water-bath stirring (b) filtration, and (c) aging.

Table 3.2 Preparation condition commonly used in this chapter.

Raw materials	Mg/Zn=14 mol. % Al/Zn=0.8 mol. % ($AlCl_3 \cdot 6H_2O$)
Solvent	2-Methoxyethanol
Solute concentration	0.75 M (Zn^{2+})
Water-bath stirring	1h (60^oC)
Aging	24h (25 ^oC)

The precursor was prepared as following. Firstly, certain amount of zinc acetate dehydrate, magnesium acetate tetrahydrate and aluminium chloride hexahydrate were weighted and put into a beaker. Then, solvent and stabilizer were dropped into the beaker. After that, the beaker was put into a water-bath pot for isothermal stirring, as shown in Fig. 3.2 (a). The temperature of water-bath pot could be tuned continuously. After stirring of certain time, a clear and homogeneous solution was formed, as shown

in Fig. 3.2 (b). Then, this precursor solution was filtrated with a 0.2 μm syringe filter. Finally, the precursor is put into incubator for aging, as shown in Fig. 3.2 (c). Unless otherwise mentioned, the preparation condition of AZMO sol-gel precursor commonly used in this chapter is shown in Table 3.2.

3.2.2 Film deposition

A spin coater (MS-A100, MIKASA CO., LTD) was used to deposit AZMO thin film. A holder was used for holding a glass substrate of 5 cm ×5 cm. Each film coating was conducted by dropping the sol-gel precursor on the glass substrate, spreading out sol-gel precursor on the glass substrate through spinning, and drying the film on a hot plate. Important parameters includes spin-speed, drying temperature and coating layers. Film thickness increases with increasing circles of coating. Unless otherwise mentioned, the spin-coating process commonly used in this chapter is exhibited in Table 3.3.

Table 3.3 Spin-coating process commonly used in this chapter

Spin coating	2000 rpm (5 s)
drying	300^{o}C (10 min)
Circles	10

3.2.3 Two-step annealing

Two-step annealing process was conducted to improve the properties of AZMO thin film. An infrared lamp furnace (MILA3000, ULVAC) was used. Figure 3.3 shows the schematic diagram of cross section of the infrared lamp furnace. Figure 3.4 shows

the annealing program. The two-step annealing was done separately. At each step, different annealing temperature, atmosphere, and holding time are used. During annealing, the film crystallinity is improved and the activation of doping process occurs. At each step, the effect of annealing atmosphere, annealing temperature, and holding time on the properties of AZMO thin film was systematically investigated. Unless otherwise mentioned, the annealing process used in this chapter is shown in Table 3.4.

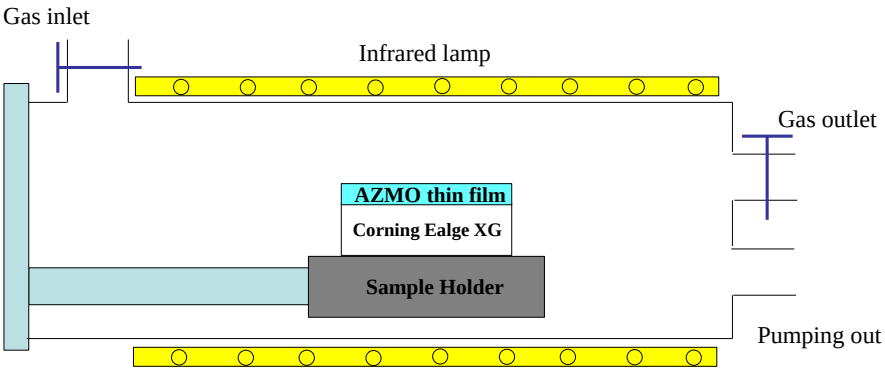

Fig. 3.3 Schematics of cross section of infrared lamp furnace.

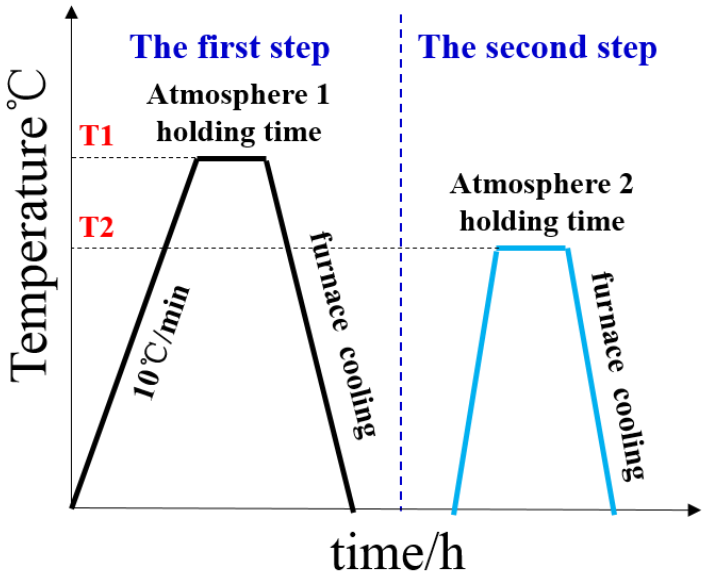

Fig. 3.4 Schematics of annealing program of two-step annealing.

Table 3.4 Two-step annealing process commonly used in this chapter

	The first step	The second step
Atmosphere	Nitrogen	Forming gas (97%N_2+3%H_2)
Temperature	650ºC	500 ºC
Holding time	60 min	5 min

3.3. Experimental results

3.3.1 Effect of precursor preparation condition

3.3.1.1 Effect of Mg content

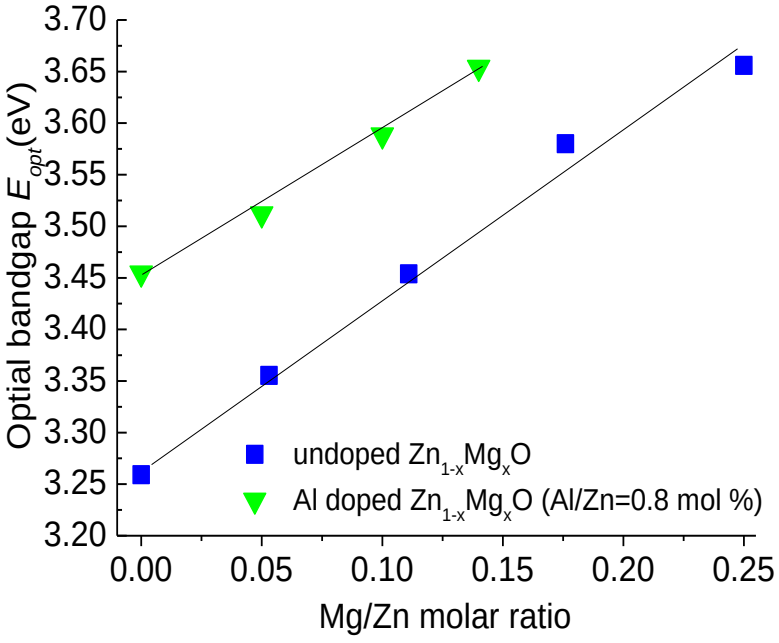

Fig. 3.5 Effect of Mg content on the optical bandgap of AZMO thin film.

Firstly, bandgap widening of AZMO thin film was conducted through controlling Mg content. Figure 3.5 shows the dependence of the optical bandgap (E_{opt}) of AZMO thin film on the Mg content. The optical bandgap energy (E_{opt}) was evaluated by extrapolating the linear portion of the $(\alpha h\upsilon)^2$ versus $h\upsilon$ plot onto the energy axis, according to equation $(\alpha h\upsilon)^2=C(h\upsilon-E_{opt})$ [1]. The absorption coefficient α was calculated from equation $\alpha=ln((1-R(\lambda))^2/T(\lambda))/t$ [2], where $T(\lambda)$ is transmittance, $R(\lambda)$ is reflectance, and t is film thickness. The Mg content was controlled by changing the Mg/Zn molar ratio in the sol-gel precursor. It is clear that the optical bandgap increases linearly with increasing the Mg content, regardless of Al doping or not.

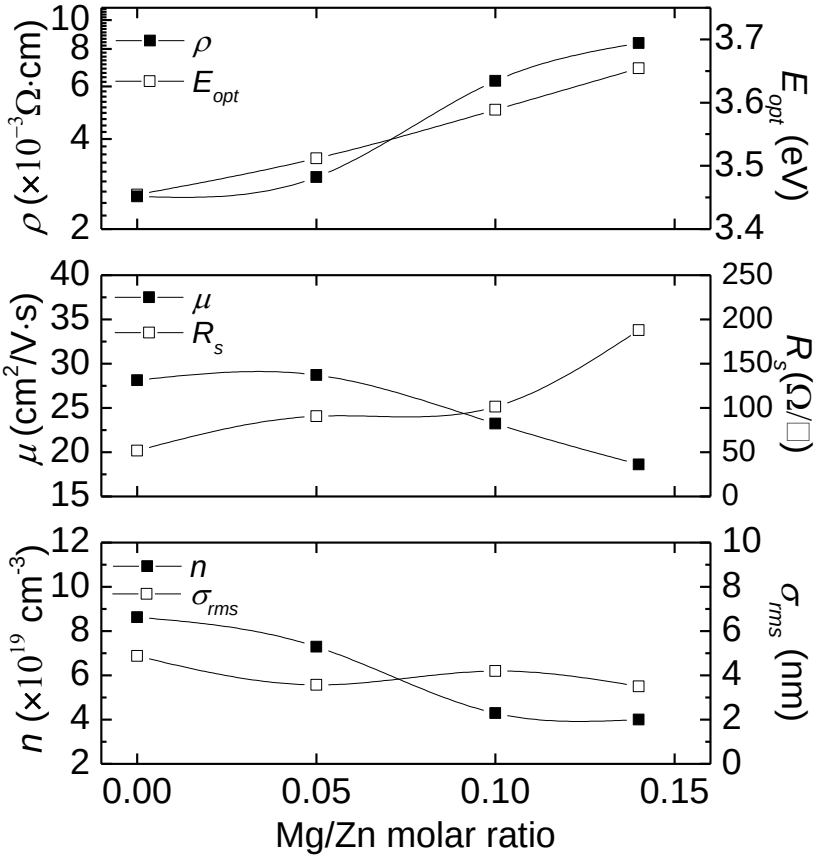

Fig. 3.6 Effect of Mg content on the electrical properties and surface roughness of AZMO thin film. All films have a same thickness of about 400 nm.

Figure 3.6 shows the effect of Mg content on the electrical properties and root-mean-square surface roughness (σ_{rms}) of AZMO thin film. Electrical properties were characterized by using Hall measurement system (Toyo, 8400 series and Ecopia, HMS3000) in van-der-Pauw 4 point probe configuration. The σ_{rms} was measured by a dynamic force microscope (DFM) (Seiko, SPA400/SPI3800N).Although Mg addition contributes to the enhancement of E_{opt}, the resistivity and sheet resistance (R_s) increases gradually with increasing Mg content, because the Hall mobility and carrier concentration decreases gradually with the increase in Mg content. The decrease in carrier concentration is probably caused by the change in band structure due to Mg addition induced bandgap widening. The decrease in Hall mobility is probably attributed to Mg addition induced enhancement of impurity scattering [3]. In addition, Mg addition seldom influences the σ_{rms} of AZMO thin film, and all AZMO thin films show σ_{rms} of less than 10 nm.

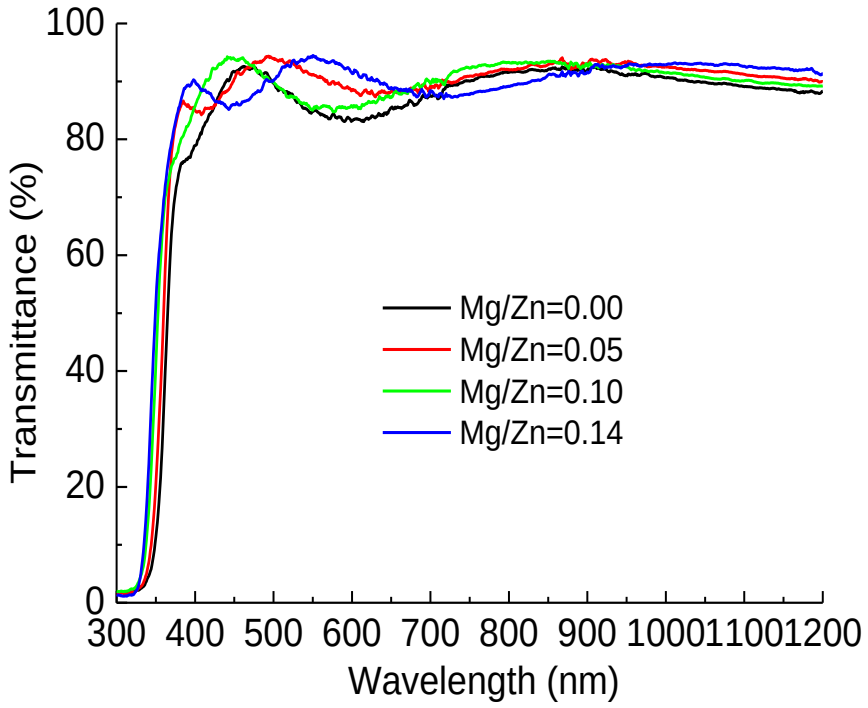

Fig. 3.7 Effect of Mg content on the transmittance of AZMO thin film.

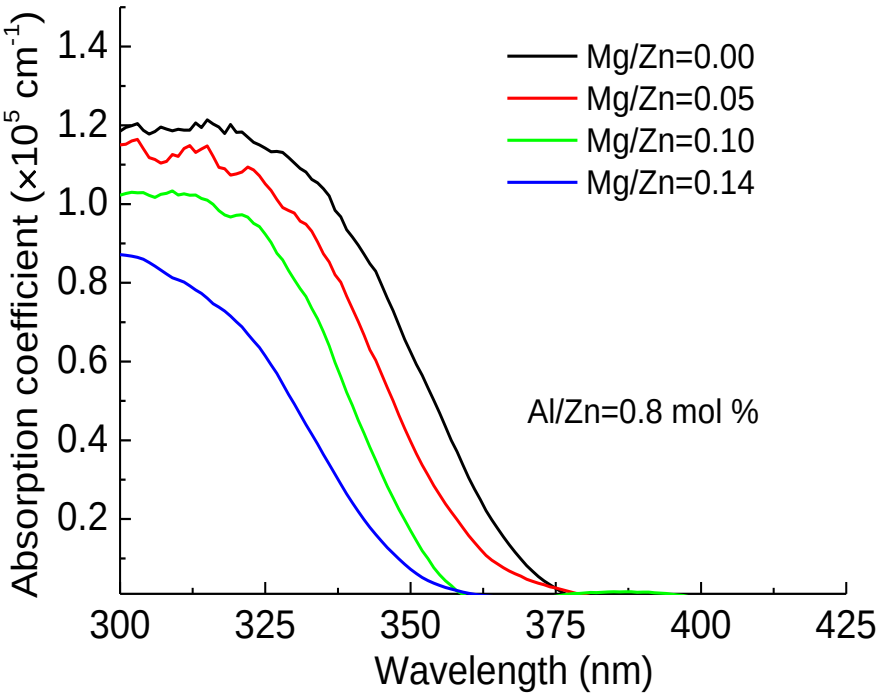

Fig. 3.8 Effect of Mg content on the absorption coefficient of AZMO thin film.

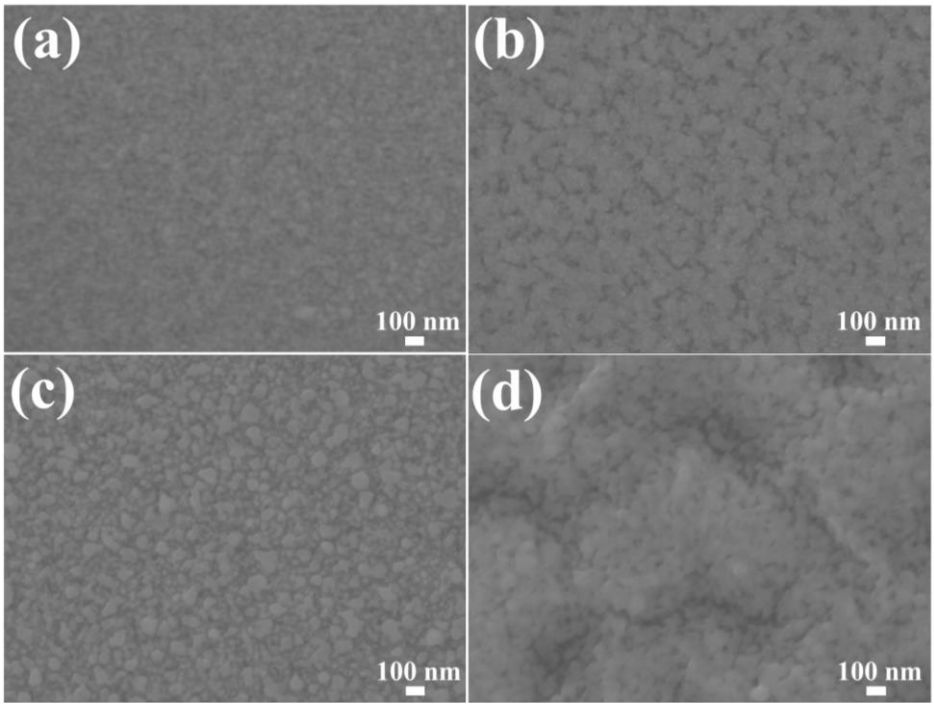

Fig. 3.9 SEM surface micrograph of AZMO thin films with Mg/Zn molar ratio of (a) 0.00 (b) 0.05 (c) 0.10 and (d) 0.15. These films were deposited with 0.5 M sol-gel precursor with EtOH as solvent. All films have same thickness of about 650 nm.

Figure 3.7 exhibits the effect of Mg content on the transmittance of AZMO thin film. The transmittance was measured by using a UV-VIS-NIR spectrophotometer (Shimadzu, Solidspec3700). All films show high transmittance of over 85% at wavelength region from 380 nm to 1200 nm. The transmittance at short wavelength obviously increases with increasing Mg content. The effect of Mg content on the absorption coefficient of AZMO thin film is shown in Fig. 3.8. An obvious blue-shift of absorption edge is observed. The absorption coefficient of AZMO thin film at short wavelength decreases apparently with increasing Mg content.

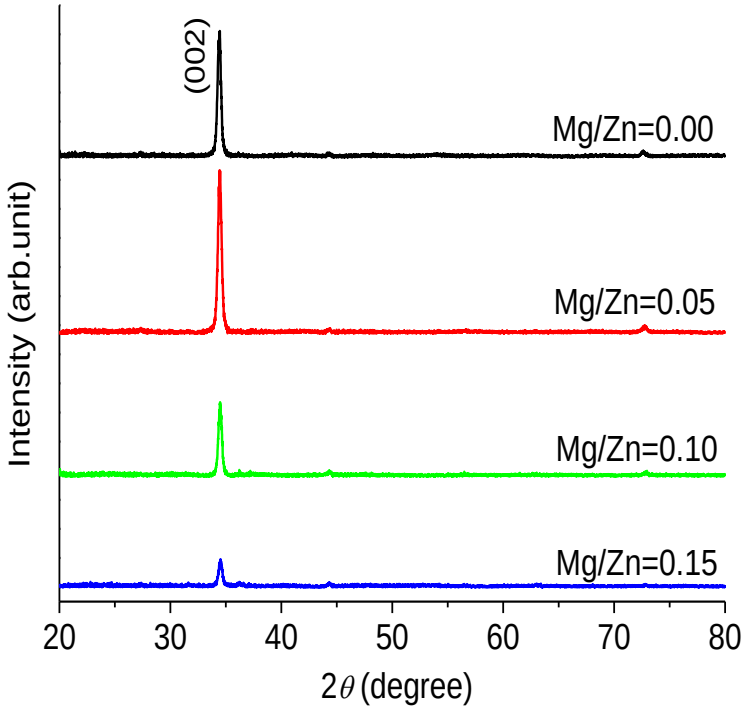

Fig. 3.10 XRD patterns of AZMO thin films with different Mg/Zn molar ratio.

Figure 3.9 shows the SEM surface micrographs of AZMO thin films with different Mg content. The morphology micrographs were determined by a field emission scanning electron microscopy (SEM) (JEOL, JSM-7001F). The Mg addition

influences the surface morphology of AZMO thin film obviously. All samples show nano-spherical grains. These grains tend to agglomerate with increasing Mg/Zn ratio. Some large grains appear in the samples with Mg/Zn ratio of 0.10 and 0.15.

Figure 3.10 shows the XRD patterns of AZMO thin films with different Mg/Zn molar ratio. The crystal phase of samples was identified by X-ray diffraction (XRD) (Philips, X'Pert-MPD) using Cu *Kα* radiation generated at 40kV-55mA. All samples show wurzite (002) preferential orientation. However, the peak intensity of (002) decreases gradually with increasing Mg/Zn molar ratio, indicating that increasing Mg content would deteriorate the film crystallinity of AZMO thin film. This might be the reason why increasing Mg content reduced Hall mobility.

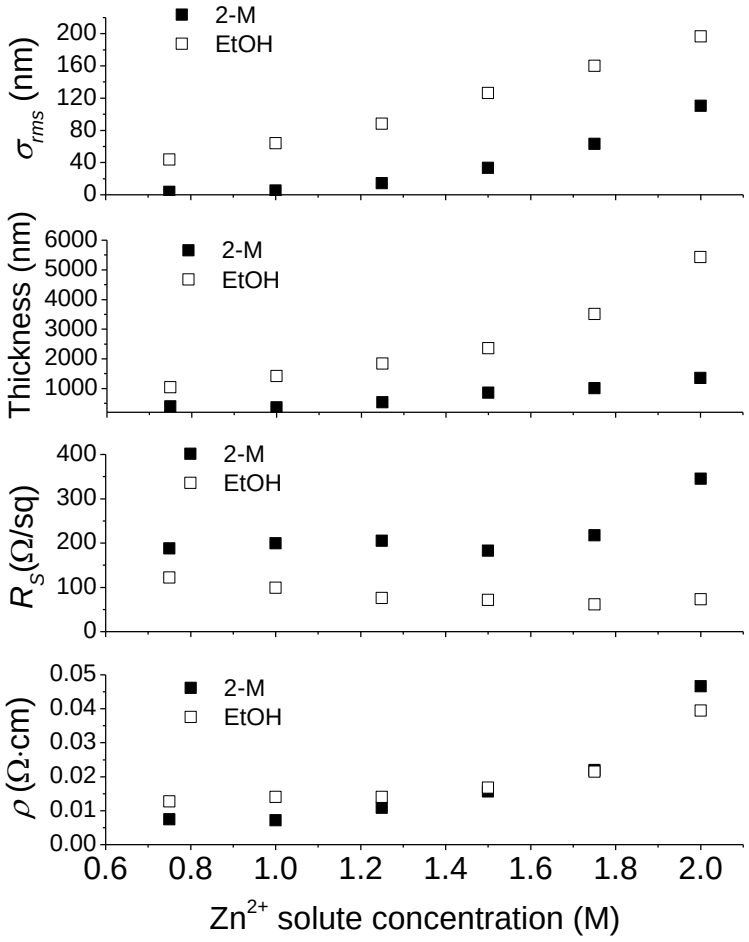

Fig. 3.11 Dependence of surface roughness, thickness, sheet resistance, and resistivity of AZMO thin film on the Zn^{2+} solute concentration in sol-gel precursor.

3.3.1.2 Effect of solute concentration and solvent

Figure 3.11 shows the dependence of surface roughness, thickness, sheet resistance, and resistivity of AZMO thin film on the Zn^{2+} solute concentration and solvent. With increasing Zn^{2+} solute concentration, the σ_{rms} increases obviously due to the increase in film thickness, regardless of solvent. Furthermore, with the same Zn^{2+} solute concentration, using EtOH as solvent enables larger σ_{rms} than using 2-M as solvent.

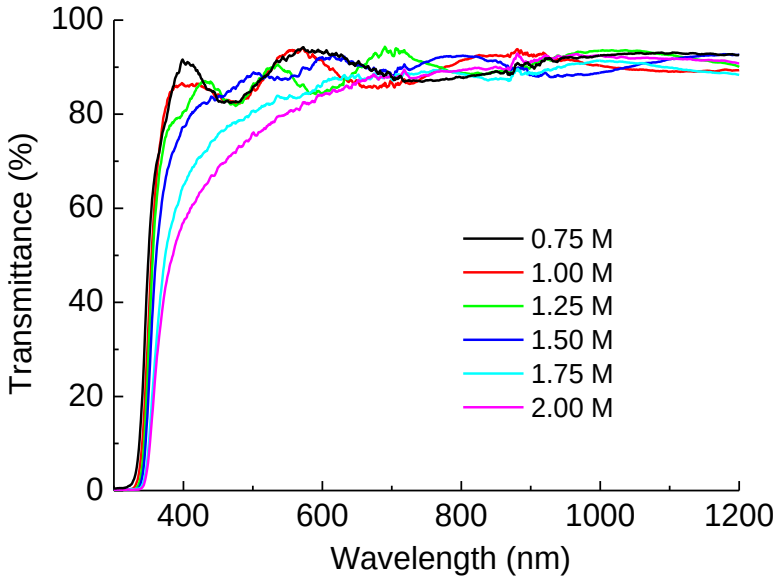

Fig. 3.12 Effect of Zn^{2+} solute concentration (in 2-M) on the transmittance of AZMO thin film.

In addition, with the increase in Zn^{2+} solute concentration, in the case of using EtOH as solvent, the R_s decreases gradually due to the increase in film thickness. However, if 2-M was used as the solvent, the R_s keeps almost constant and even increases when the Zn^{2+} solute concentration is larger than 1.75 M, although the film thickness increased greatly. In addition, the film resistivity increases gradually, regardless of solvent. The resistivity increases greatly when the Zn^{2+} solute concentration is larger than 1.75 M. This is quite probably the reason why the sheet

resistance increases with increasing film thickness as mentioned above.

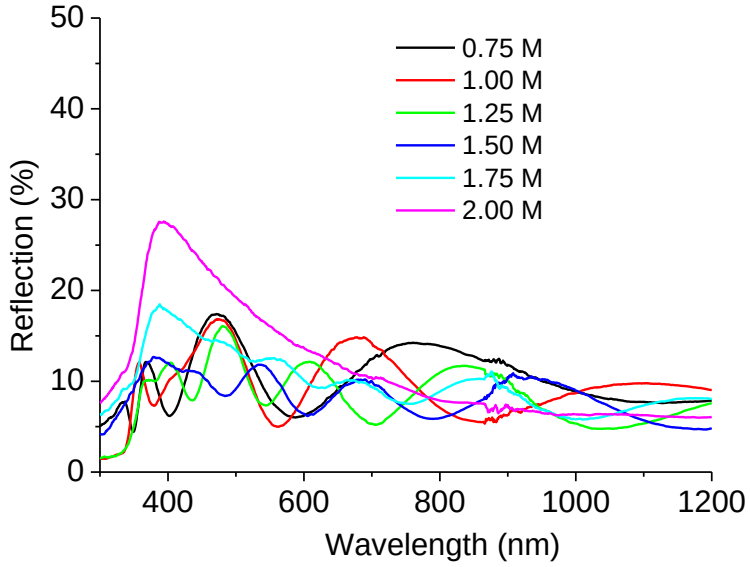

Fig. 3.13 Effect of Zn^{2+} solute concentration (in 2-M) on the reflection of AZMO thin film.

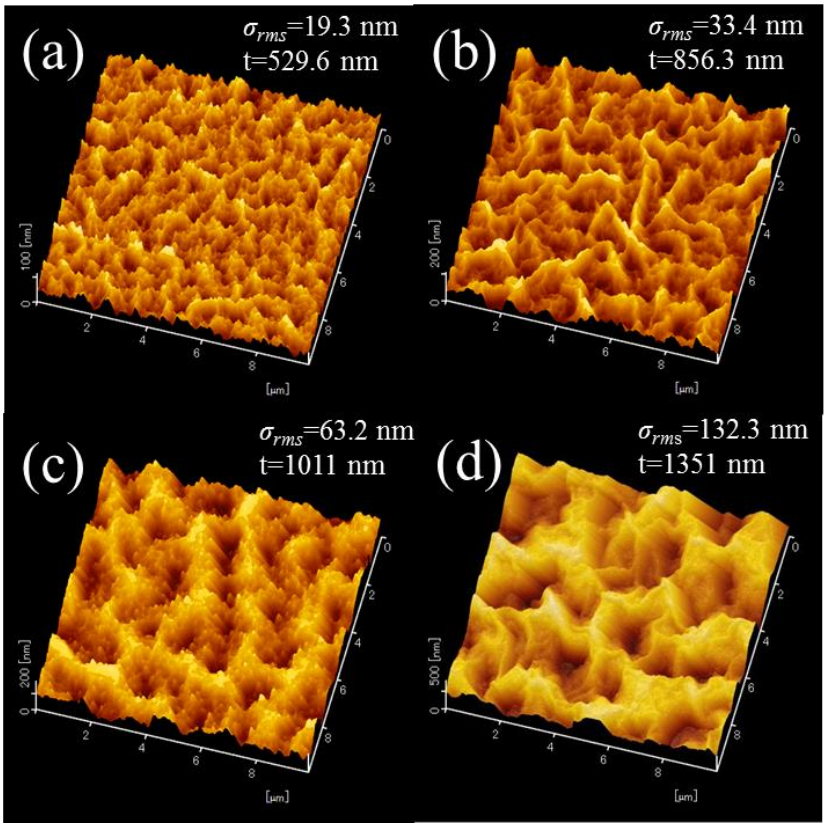

Fig. 3.14 DFM surface morphology of AZMO thin films with Zn^{2+} solute concentration (in 2-M) of (a) 1.25 M (b) 1.50 M (c) 1.75 M (d) 2.00 M. The σ_{rms} and film thickness are also indicated.

Figures 3.12 and 3.13 show the effect of Zn^{2+} solute concentration in 2-M on the transmittance and reflection of AZMO thin film, respectively. Increasing Zn^{2+} solute concentration shows little influence on the transmittance at wavelength of 600 nm-1200 nm, however, it decreases the transmittance at wavelength region of 350-600 nm with the increase in Zn^{2+} solute concentration. The reason is, as shown in Fig. 3.13, that increasing Zn^{2+} solute concentration enhanced the reflection at short wavelength region, especially when the Zn^{2+} solute concentration is larger than 1.25 M.

The DFM surface morphology of AZMO thin films with different Zn^{2+} solute concentration (in 2-M) is shown in Fig. 3.14. It is clear that the Zn^{2+} solute concentration influences the surface morphology significantly. The surface morphology gradually turns to be wrinkle-like morphology from flat surface, with increasing Zn^{2+} solute concentration. The σ_{rms} increases obviously at the same time. When the Zn^{2+} solute concentration is larger than 1.75 M, this wrinkle-like morphology gets very irregular and random. This increased the diffuse reflection in the film and then caused the increase in reflection (Fig. 3.13).

Figure 3.15 shows the transmittance of AZMO thin with different Zn^{2+} solute concentration in EtOH. It can be found that the transmittance decreases apparently with increasing Zn^{2+} solute concentration. Compared to AZMO thin film with the same Zn^{2+} solute concentration in 2-M (Fig. 3.12), using EtOH as solvent decreases the transmittance more significantly than using 2-M. Figure 3.16 shows the reflection of AZMO thin with different Zn^{2+} solute concentrations in EtOH. All AZMO thin films show very large reflection and the reflection increases greatly with increasing Zn^{2+} solute concentration. Compared to AZMO thin film with the same Zn^{2+} solute concentration in 2-M (Fig. 3.13), using EtOH as solvent increases the reflection more

significantly than using 2-M.

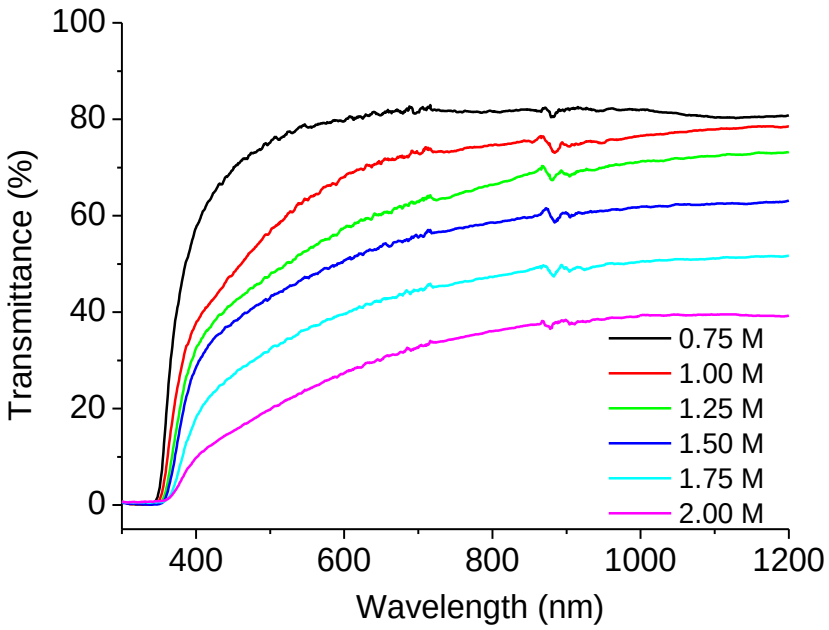

Fig. 3.15 Effect of Zn^{2+} solute concentration (in EtOH) on the transmittance of AZMO thin film.

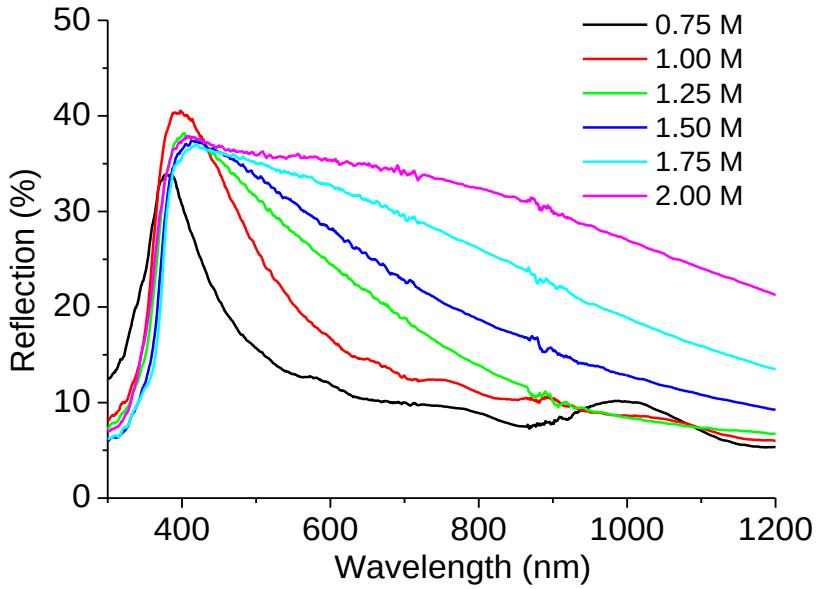

Fig. 3.16 Effect of Zn^{2+} solute concentration (in EtOH) on the reflection of AZMO thin film.

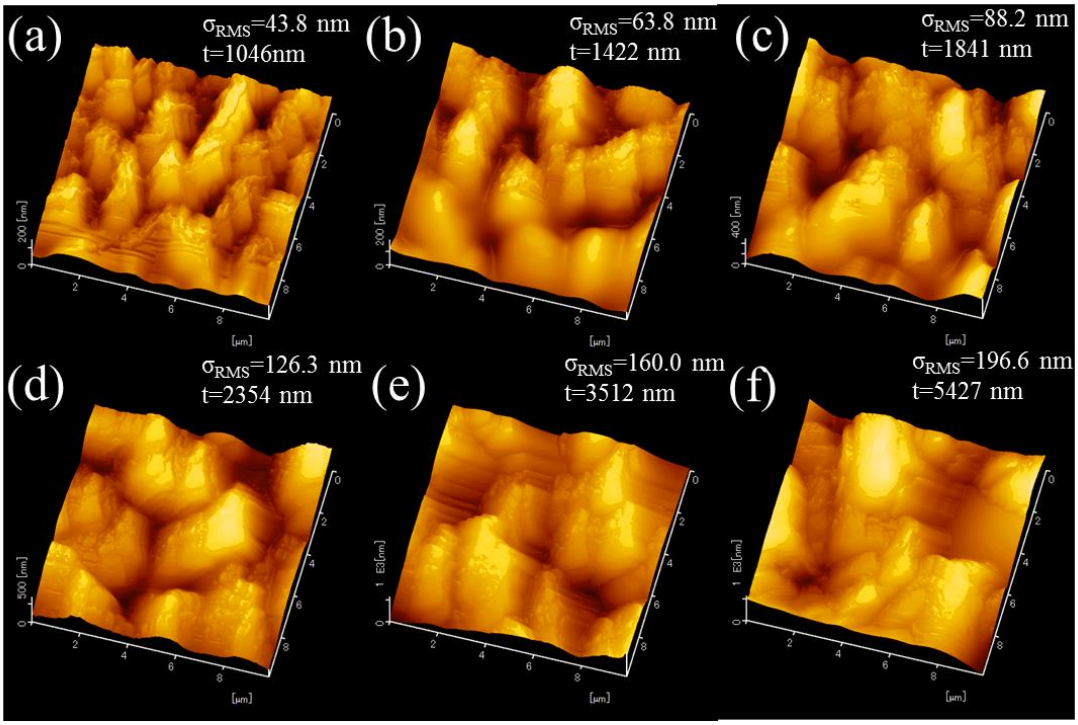

Fig. 3.17 DFM surface morphology of AZMO thin films with Zn^{2+} solute concentration (in EtOH) of (a) 0.75 M (b) 1.00 M (c) 1.25 M (d) 1.50 M (e) 1.75 M (f) 2.00 M. The σ_{rms} and film thickness are also indicated.

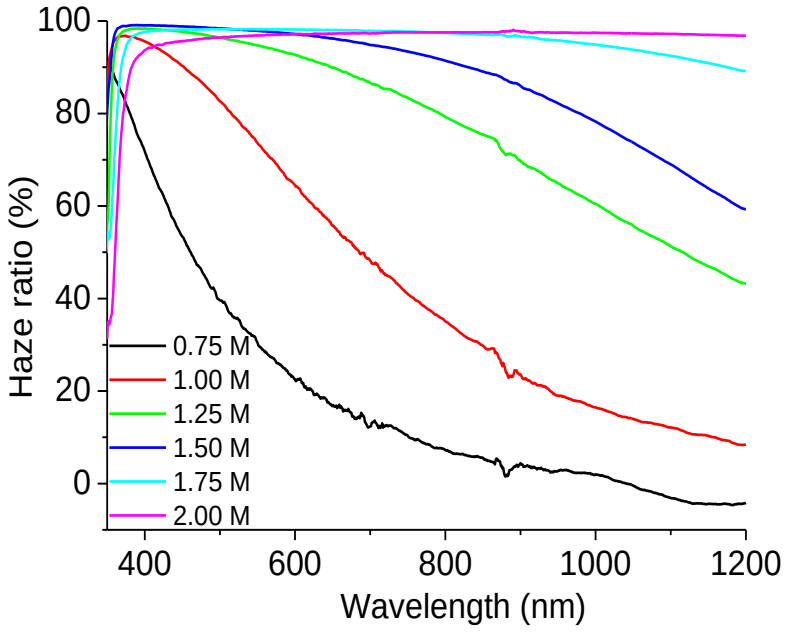

Fig. 3.18 Effect of Zn^{2+} solute concentration (in EtOH) on the haze ratio in transmission of AZMO thin film.

Figure 3.17 shows the DFM surface morphology of AZMO thin films with different Zn^{2+} solute concentration in EtOH. Compared to AZMO thin film with the same Zn^{2+} solute concentration in 2-M (Fig. 3.14), using EtOH as solvent generates much larger σ_{rms} than using 2-M. When the Zn^{2+} solute concentration is larger than 1.25 M, the surface morphology gets much rougher and irregular than that shown in Fig. 3.14. This causes the increase in reflection and decrease in transmittance.

Effect of Zn^{2+} solute concentration (in EtOH) on the haze ratio in transmission of AZMO thin film is shown in Fig. 3.18. The haze ratio in transmission (H_T) is defined as the ratio of the diffuse transmittance to the total transmittance. The diffuse transmittance and the total transmittance were measured by using UV-VIS-NIR spectrophotometer (Shimadzu, Solidspec3700). It can be found that the haze ratio increases significantly greatly with increasing Zn^{2+} solute concentration. It should be related to the increase in diffuse transmittance in film, which is caused by the increase in surface roughness as shown in Fig. 3.17. When the Zn^{2+} solute concentration is larger than 1.00 M in EtOH, the film shows haze ratio of over 60 % at wavelength region from 400 nm to 1000 nm.

3.3.1.3 Effect of dopant and doping concentration

Doping to AZMO thin film was conducted by using dopants including $AlCl_3 \cdot 6H_2O$, $Al(NO_3)_3 \cdot 9H_2O$, NH_4F as well as a mixture of $AlCl_3 \cdot 6H_2O$ and NH_4F, for further decreasing the resistivity of AZMO thin film. The effect of doping on the electrical, optical, and structural properties of AZMO thin film was investigated and will be introduced in order.

(a) Al doping

Firstly, $AlCl_3 \cdot 6H_2O$ was used as the cation doping. The doping concentration was defined by the molar ratio of Al/Zn as a percentage in the sol-gel precursor. It was changed from 0.0 mol. % to 2.0 mol. % at an interval of 0.2 mol. %. The ratio of Mg/Zn was fixed at 14 mol. %. The relationship between the Al/Zn molar ratio in sol-gel precursor and Al content in thin film is shown in Fig. 3.19. The Al content in thin film increases in proportion to the Al/Zn molar ratio in sol-gel precursor when the Al/Zn molar ratio is larger than 0.8 mol. %.

Figure 3.20 exhibits the X-ray photoelectron spectroscopy (XPS) of AZMO thin film with different Al doping concentration. The XPS was measured by using a surface analysis equipment (PHI Quantera SXM) using monochromatic Al *Kα* radiation (*hυ*=1486.6 eV). All samples show a peak centered around 74.4 eV. The peak intensity increases obviously with increasing Al/Zn molar ratio, confirming the increase in the Al content in film. The peak position of Al 2p shows a slight shift towards low energy with increasing Al content, implying the change in Al-O bonding energy due to the increase in Al content.

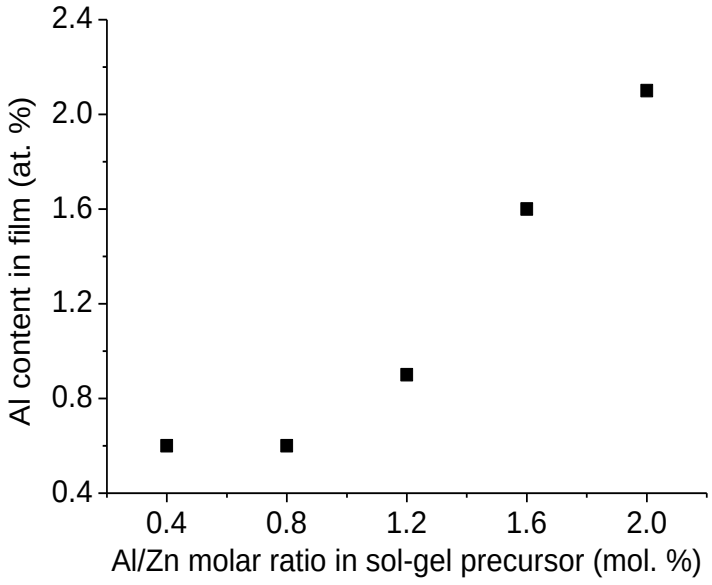

Fig. 3.19 Relationship between the Al content in sol-gel precursor and film.

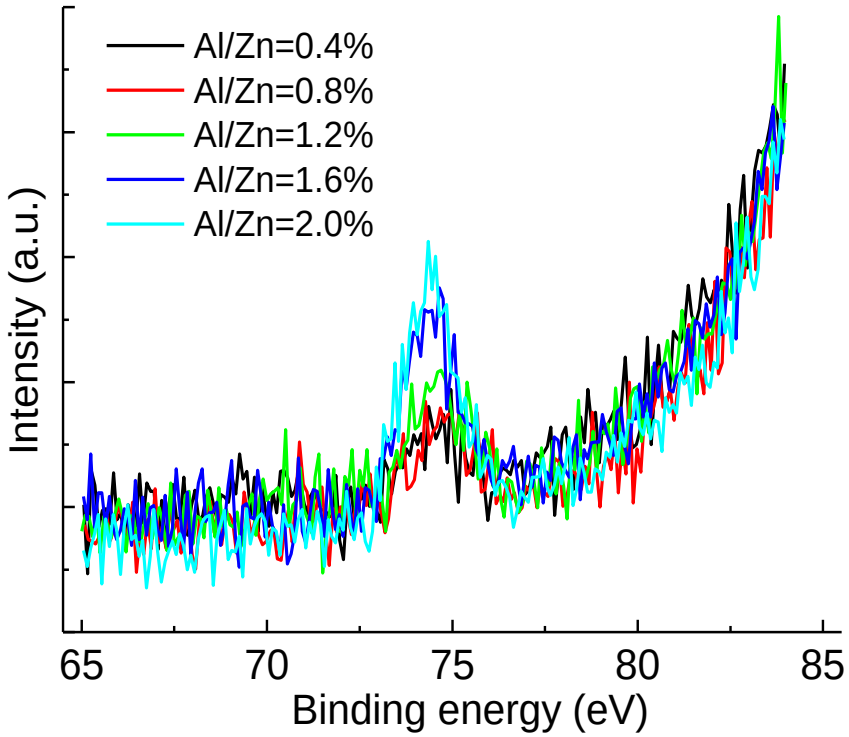

Fig. 3.20 XPS spectra of AZMO samples with different Al doping concentration.

Figure 3.21 shows the Hall measurement results of ZMO thin films with different Al doping concentration. Regardless of the annealing condition, resistivity decreases obviously firstly with increasing Al doping concentration and reaches the minimum value at doping concentration of around 0.8 mol. %. When the doping concentration is larger than 0.8 mol. %, resistivity increases slowly, especially if the sample was firstly annealed in air. It reaches the minimum value of 7.96×10^{-3} Ω·cm with the first step annealing in nitrogen. With increasing Al doping concentration, the carrier concentration increases sharply at first and then keeps constant or even decreases gradually. The Hall mobility decreases slowly with the increase in Al doping concentration.

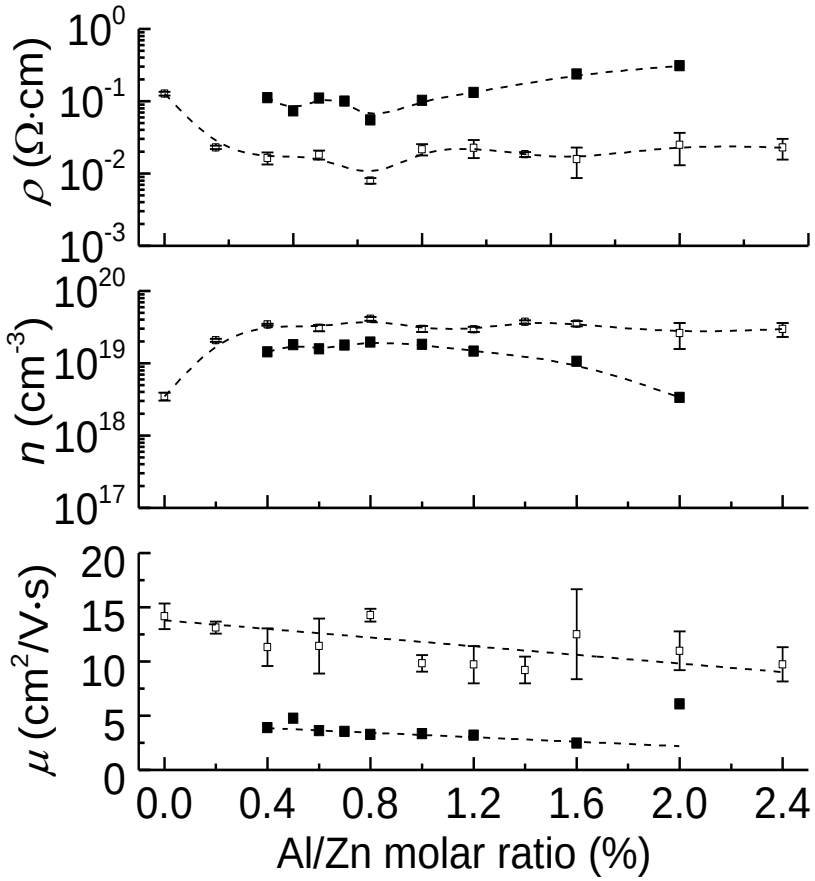

Fig 3.21 Effect of Al doping concentration on the electrical properties of $Zn_{0.87}Mg_{0.13}O$ thin film. The void points refer to the sample that firstly annealed in nitrogen at 650 ºC and secondly annealed in forming gas at 500 ºC, while the filled points refer to the sample that firstly annealed in air at 500 ºC and secondly annealed in forming gas at 450 ºC.

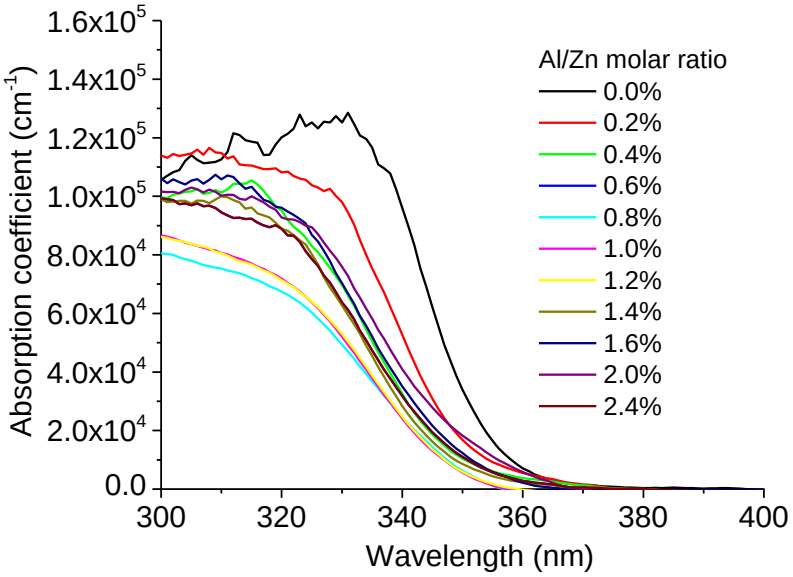

Fig 3.22 Effect of Al doping concentration on the absorption coefficient of $Zn_{0.87}Mg_{0.13}O$ thin film.

The effect of Al doping concentration on absorption coefficient of ZMO thin film is illustrated in Fig. 3.22. It can be found that Al doped samples show an obvious blue-shift of absorption edge at short wavelength range relative to that of undoped sample. The shift extent increases with the increases in Al doping concentration and reaches the maximum at doping concentration of 0.8 mol. %. When doping concentration gets larger than 0.8 mol. %, the shift extent decreases instead.

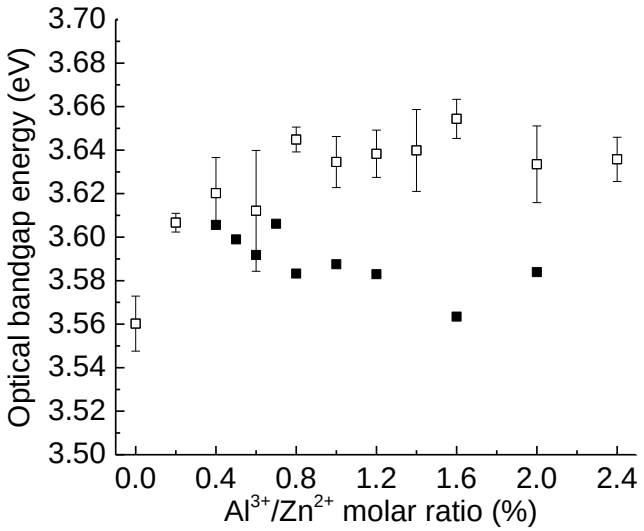

Fig. 3.23 Effect of Al doping concentration on the optical bandgap energy of $Zn_{0.87}Mg_{0.13}O$ thin film. The void points refer to the sample that firstly annealed in nitrogen at 650 °C and secondly annealed in forming gas at 500 °C, while the filled points refer to the sample that firstly annealed in air at 500 °C and secondly annealed in forming gas at 450 °C.

Figure 3.23 presents the effect of Al doping concentration on the optical bandgap energy of ZMO thin film. If the sample was first annealed in nitrogen, with the increase in Al doping concentration, the E_{opt} increases gradually until the doping concentration reaches 0.8 mol. % and then remains almost constant. If the sample was firstly annealed in air, the E_{opt} decreases slowly with the increase in Al doping concentration. Thus, the relationship between the E_{opt} and doping concentration is strongly influenced by annealing condition.

The effect of Al doping concentration on the XRD patterns of ZMO thin film is indicated in Fig. 3.24. In Fig. 3.24 (a), all of the films show wurzite (002) preferential orientation. With the increase in Al doping concentration, the intensity of (002) peak keeps almost unchanged at Al doping concentration of less than 0.8 mol. %, while it gradually decreases when it is larger than 0.8 mol. %. Figure 3.24 (b) shows that the intensity of (002) peak presents a clear decline trend with increasing Al doping concentration, especially when Al doping concentration is larger than 0.8 mol. %. It reflects that heavy Al doping deteriorates the film crystallinity of ZMO thin film.

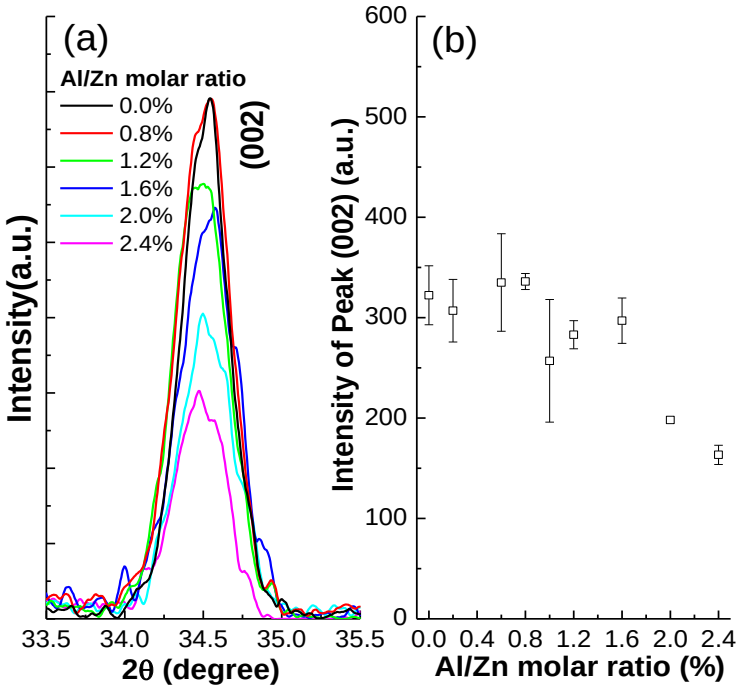

Fig. 3.24 Effect of Al doping concentration on the XRD patterns of $Zn_{0.87}Mg_{0.13}O$ thin film. The samples were firstly annealed in nitrogen at 650 ºC and secondly annealed in forming gas at 500 ºC.

Al doping could decreases the resistivity of ZMO thin film in the sol-gel process at moderate doping concentration. The resistivity decreases sharply and the E_{opt} increases with the increase in Al doping concentration at low doping concentration. The lowest resistivity of 7.96×10^{-3} Ω·cm with an E_{opt} =3.64 eV was obtained at doping

concentration of 0.8 mol. %. It is mainly due to the formation of the maximum carrier concentration.

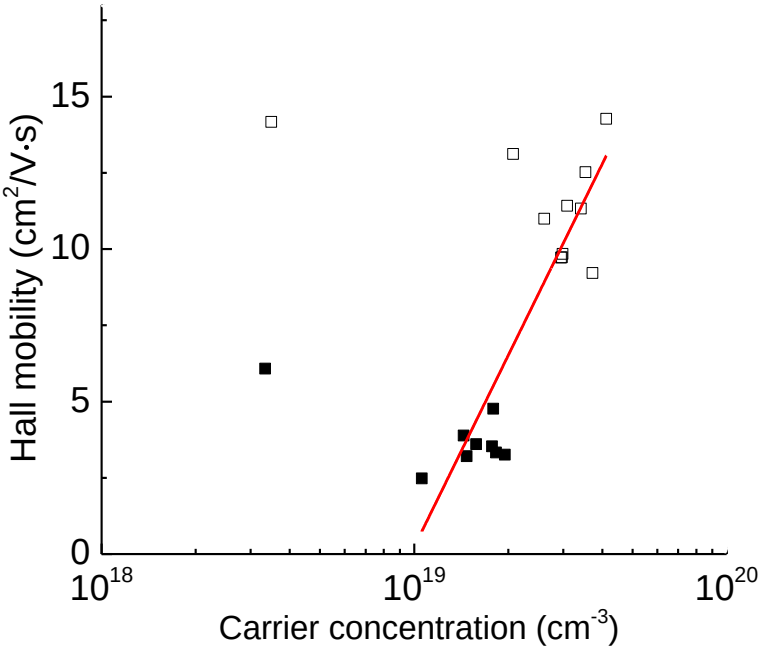

Fig. 3.25 Measured Hall mobility versus carrier concentration of Al doped $Zn_{0.87}Mg_{0.13}O$ thin film. The red line is linear fitting to the data. The void points refer to the sample that firstly annealed in nitrogen at 650 °C and secondly annealed in forming gas at 500 °C, while the filled points refer to the sample that firstly annealed in air at 500 °C and secondly annealed in forming gas at 450 °C.

The scattering mechanism needs to be clarified. Figure 3.25 shows the relationship between the measured Hall mobility and carrier concentration. It can be found that Hall mobility increases almost linearly with the increase in carrier concentration regardless of the annealing condition. Data in this work shows the same tendency as that of Minami [4] It can be concluded that the mobility is dominated by grain-boundary scattering in this work.

The doping concentration that gives the maximum carrier concentration is noticeable. In this work, the carrier concentration of AZMO thin film reached the maximum valve of 4.12×10^{19} cm^{-3} at doping concentration of 0.8 mol. % with the first

step annealing in nitrogen. However, in the case of ZnO thin film, Al doping concentration of around 1.2 mol. % showed the maximum carrier concentration of about 1.2×10^{20} cm^{-3}. Tang et al. also reported that the maximum carrier concentration of about 7×10^{20} cm^{-3} was formed at Al doping concentration of around 1.2 mol. % for sol-gel derived ZnO thin film [5]. The reason why Al doping concentration in AZMO thin film that gives the maximum carrier concentration gets low, relative to that in AZO thin film, should be related to the competition between Mg^{2+} and Al^{3+} for substituting Zn^{2+} lattice site. It is well known that the increase in carrier concentration is caused by the substitutional doping of Al^{3+} at the Zn^{2+} site, creating one extra free carrier in the process. However, the substitution of Al^{3+} on Zn^{2+} site is finite. There is no widely recognized conclusion on the exact saturation of Al substitutional doping in ZnO wurtize lattice up to now. In the case of Al_2O_3 doped ZnO sintered body, the Al solubility limit in ZnO grains was concluded to be approximately 0.3 at. % with SIMS maping technique [6]. Katsuyama et al. reported the solubility limit of Al in the $Zn_{1-x}Al_xO$ system is about x=0.01 through analyzing Seebeck coefficient and electrical resistivity [7]. Tsubota et al. estimated the solubility limit of Al into ZnO is smaller than 0.52 at. % by using ^{27}Al NMR spectroscopy [8]. In the case of ZMO, the saturation of Al substitutional doping in ZnO wurtize lattice would be reduced because some Zn^{2+} lattice sites are occupied by the Mg^{2+} ions.

As to the widening of E_{opt}, it should be caused by the Burstein-Moss effect [9]. The enhancement of E_{opt} is closely related to the doping-induced increase in carrier concentration. The obvious blue-shift of absorption edge with increasing doping concentration is observed in Fig. 3.22. The measured E_{opt} can be presented by Eq. (2.1) [10]. The reduced effective mass can be evaluated by plotting the change in optical bandgap energy with *n*. Based on parabolic energy bands and a spherical Fermi surface,

the Burstein-Moss shift ΔE_g^{BM} can be expressed as Eq. (2.2) [3],

$$E_{opt} = E_{g0} + \Delta E_g^{BM}, \qquad (2.1)$$

$$\Delta E_g^{BM} = \frac{\hbar^2 (3\pi^2 n)^{2/3}}{2m_r^*}, \qquad (2.2)$$

where E_{g0} is the fundamental energy gap, m_r^* is the reduced effective mass, and $\hbar$ is Planck's constant divided by 2π. Figure 3.26 shows a plot of E_{opt} versus $n^{2/3}$. Two different annealing way show same tendency that E_{opt} increases almost linearly with carrier concentration. By using Eqs. (2.1) and (2.2), m_r^* can be derived by using the slope of fitting line and E_{g0} can be obtained through the y intercept. The deduced m_r^* is about $0.41m_e$ and E_{g0} is 3.54 eV, where m_e is the free electron mass. The calculated value of E_{g0} fits well with the E_{opt} of undoped ZMO (3.56 eV). The maximum ΔE_{BM} is about 0.10 eV.

In high doping scope, with increasing Al doping concentration, the resistivity increases little by little due to the slow decrease in mobility (Fig. 3.21) and the E_{opt} keeps almost unchanged or even reduces due to the non-increasing carrier concentration (Fig. 3.23). The non-increasing carrier concentration with increasing Al doping reveals that Al substitutional doping reaches saturation. The excess Al that can't substitute Zn^{2+} lattice site tends to form magnesium aluminate (MgAl) clusters that act as neutral scattering center [11] or may segregate to the grain boundaries in the form of Al_2O_3 which increases the grain-boundary barrier [12]. The decrease in mobility is probably caused by the enhanced neutral impurity scattering and grain-boundary barrier. The MgAl cluster would prevent Al from acting as an electron donor. As shown in Fig. 3.21, if the samples were firstly annealed in air, carrier concentration decreases with further

increasing doping concentration. Figure 3.24 (a) shows that heavy Al doping would also deteriorates the film crystallinity of AZMO thin film. The distortion of crystal structure is probably caused by the occupation of excess Al on interstitial positions or the formation of MgAl clusters.

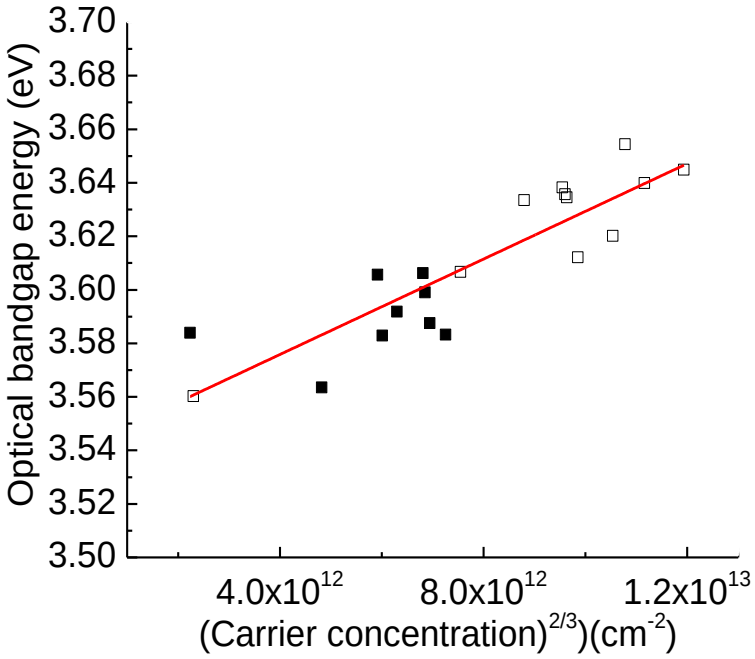

Fig. 3.26 Dependence of E_{opt} of Al doped $Zn_{0.87}Mg_{0.13}O$ thin film on carrier concentration. The red line is linear fitting to the data. The void points refer to the sample that firstly annealed in nitrogen at 650 °C and secondly annealed in forming gas at 500 °C, while the filled points refer to the sample that firstly annealed in air at 500 °C and secondly annealed in forming gas at 450 °C.

Al doping with $Al(NO_3)_3 \cdot 9H_2O$ as the source of cation dopant was also conducted using the same process as $AlCl_3 \cdot 6H_2O$. Table 3.5 shows the Hall measurement results of AZMO thin film with $AlCl_3 \cdot 6H_2O$ and $Al(NO_3)_3 \cdot 9H_2O$ as dopant. It can be found these two dopants result in similar electrical properties of AZMO thin film, although using $Al(NO_3)_3 \cdot 9H_2O$ make a thinner film than using $AlCl_3 \cdot 6H_2O$. In this experiment, the Zn^{2+} solute concentration is 2 M, so resistivity gets

low, as shown in Fig. 3.11.

Table 3.5 Electrical properties of AZMO thin film with $AlCl_3 \cdot 6H_2O$ and $Al(NO_3)_3 \cdot 9H_2O$ as dopant.

Dopant	t (nm)	ρ (Ω·cm)	n (cm^{-3})	μ ($cm^2/(V \cdot s)$)
$AlCl_3 \cdot 6H_2O$	1351	1.8×10^{-2}	3.4×10^{19}	10.0
$Al(NO_3)_3 \cdot 9H_2O$	1144	1.6×10^{-2}	4.2×10^{19}	9.2

Note: 2-M was used as solvent and the Zn^{2+} solute concentration is 2 M.

(b) F doping

Secondly, NH_4F was used as anion dopant to ZMO thin film. The dopant was dissolved into methanol in advance and then added into the solution when preparing sol-gel precursor. The doping concentration was defined by the molar ratio of F/O as a percentage in the sol-gel precursor. It was changed from 0.4 mol. % to 2.8 mol. % at an interval of 0.4 mol. %. The ratio of Mg/Zn was fixed at 14 mol. %.

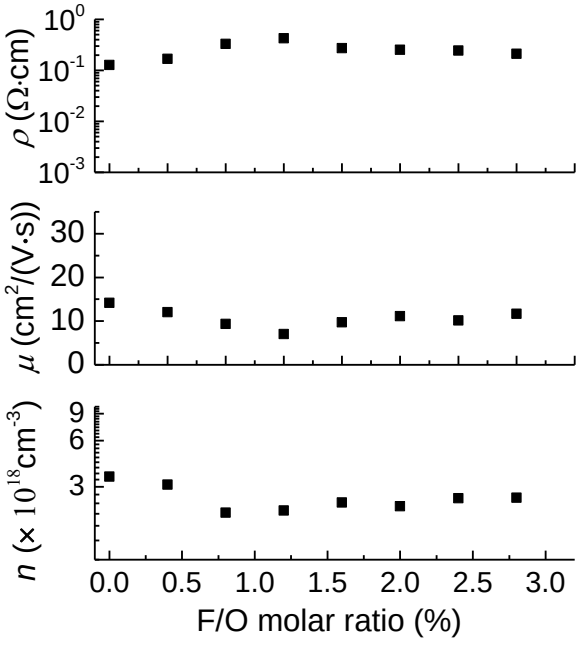

Fig. 3.27 Dependence of electrical properties of ZMO thin film on F doping.

Figure 3.27 shows the influence of F doping concentration on the electrical properties of AZMO thin film. No obvious change in resistivity with increasing F doping concentration is found. It can be found that the carrier concentration hardly change, even if increasing the F doping concentration. There is also little change in Hall mobility with the increase in F doping concentration. Figure 3.28 exhibits the transmittance of AZMO thin film with different F/O molar ratio. No obvious blue-shift of absorption edge is observed due to the ineffective doping effect, although all films show high transmittance of over 85% at wavelength region from 300 nm to 1200 nm. These results suggest that the F doping with NH_4F as the source is ineffective for decreasing the resistivity of ZMO thin film.

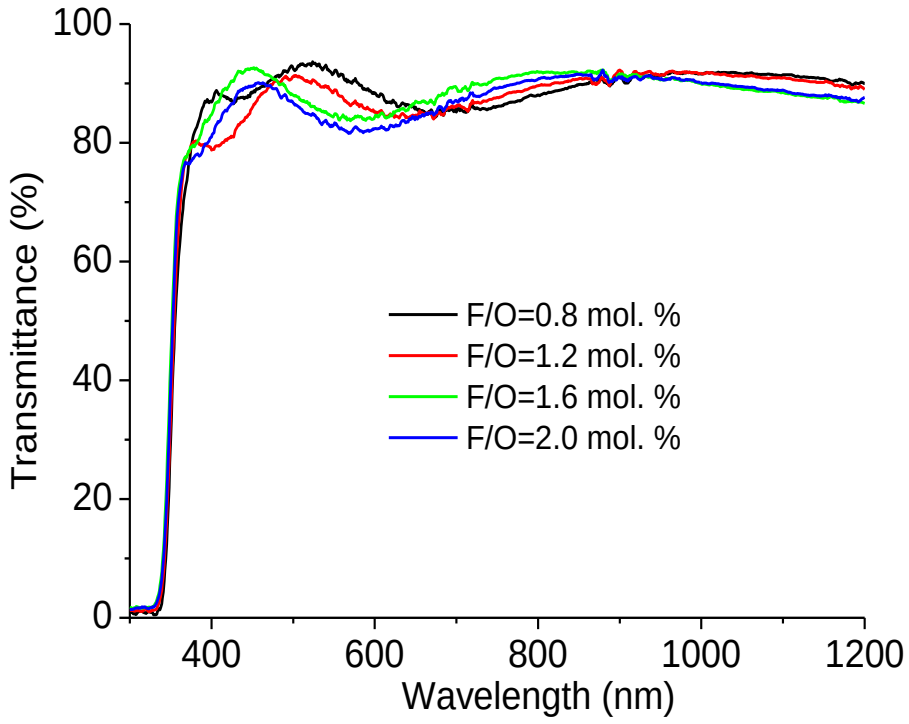

Fig. 3.28 Transmittance of AZMO thin film with different F/O molar ratio.

(b) Co-doping of Al and F

Further efforts were made to investigate the effect of Al and F co-doping on the electrical properties of ZMO thin film. $AlCl_3 \cdot 6H_2O$ was used as the source of cation doping, and NH_4F was used as the source of anion doping. The Al/Zn mole ratio is fixed at 0.8 mol. %, while the F/O mole ratio is changed from 0.4 to 2.0 mol. % at an interval of 0.4 mol. %.

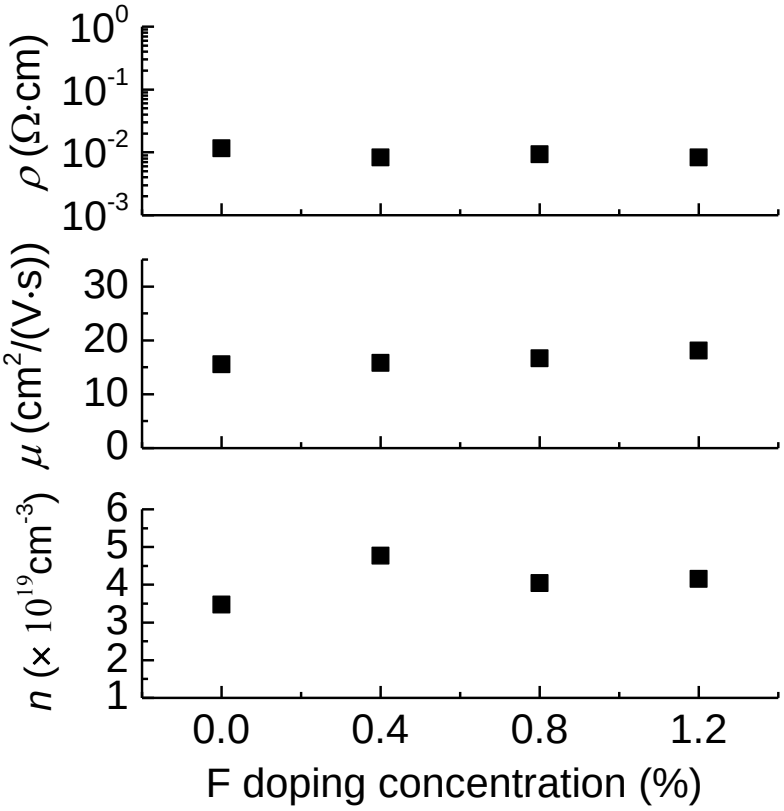

Fig. 3.29 Dependence of electrical properties of AZMO thin film on Al-F co-doping.

Figure 3.29 shows the effect of Al and F co-doping on the electrical properties of ZMO thin film. In this case, little contribution of F doping to decreasing the resistivity of AZMO thin film is found. With changing the F doping concentration, resistivity, carrier concentration and Hall mobility keep almost constant. These results also confirmed that F doping with NH_4F as the source is ineffective for decreasing the resistivity of ZMO thin film.

3.3.1.4 Effect of aging time of precursor solution

The aging time of sol-gel precursor has a significant influence on the properties of annealed AZMO thin film. So the effect of time and temperature of aging on the properties of AZMO thin film was investigated. Two aging temperature (-24°C and 25 °C) was selected. The aging time was changed from 24 h to 720 h.

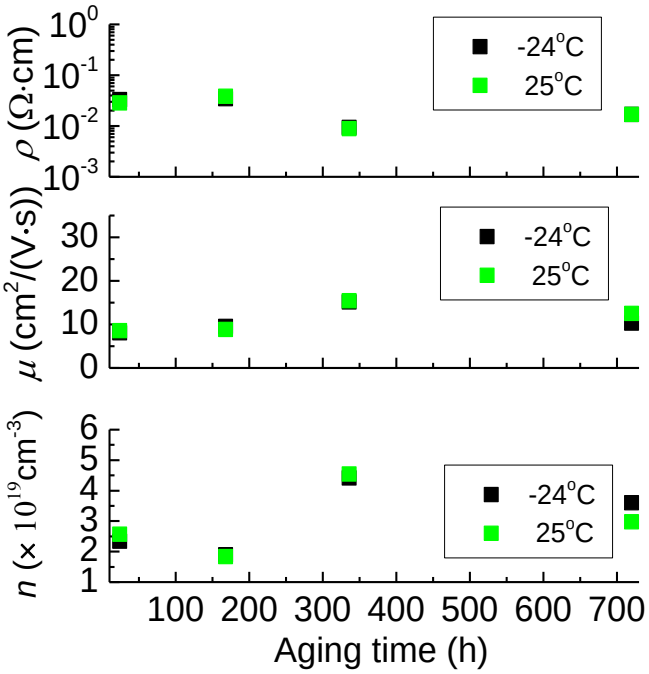

Fig. 3.30 Effect of aging time and temperature on the electrical properties of AZMO thin film.

Figure 3.30 shows the dependence of electrical properties of AZMO thin film on the aging time and temperature of sol-gel precursor. It can be found that the aging time shows much greater effect on the electrical properties than aging temperature. The resistivity decreases with increasing aging time firstly, then gets the minimum at the aging time of 336 h, and then increases. With increasing aging time, both of Hall mobility and carrier concentration increases firstly and then decreases. The lowest resistivity was obtained at the aging time of 336 h, because it enabled the highest carrier

concentration and Hall mobility.

3.3.2 Effect of spin-coating parameters

3.3.2.1 Effect of spin speed

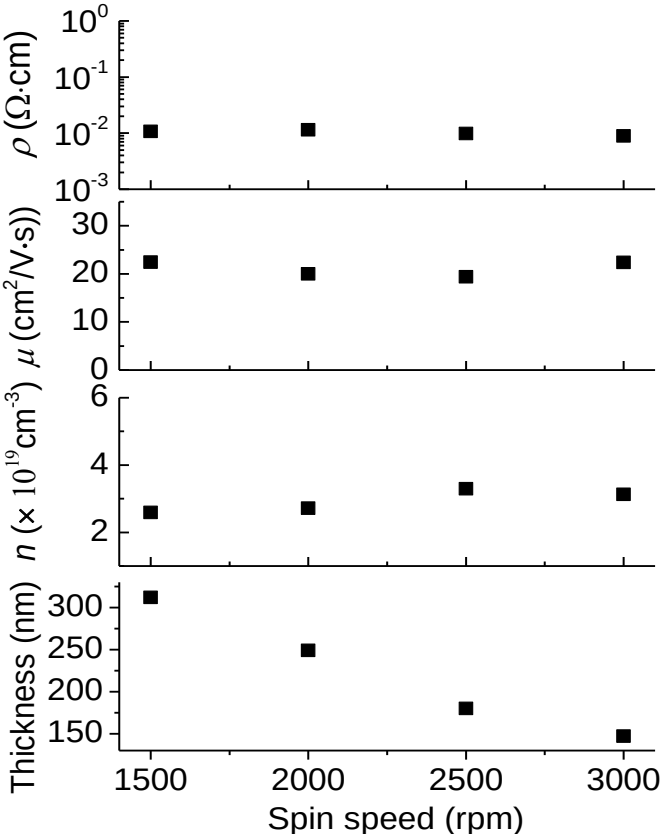

Fig. 3.31 Effect of spin speed of spin coating on the electrical properties of AZMO thin film.

The effect of spin speed of spin-coating on the electrical properties of AZMO thin film was investigated. Figure 3.31 shows the dependence of electrical properties of AZMO thin film on the spin speed of spin-coating. It can be found that spin speed influences the film thickness significantly. The film thickness decreases almost linearly with increasing spin speed. The carrier concentration increases slightly with increasing spin speed, resulting in the decrease in resistivity. The spin speed shows little influence on the Hall mobility.

3.3.2.2 Effect of drying time

The effect of drying time during spin-coating on the electrical property of AZMO thin film was investigated. The drying temperature was fixed at 300 ºC. The drying time is changed from 5 min to 10 min. Table 3.6 shows the result of Hall measurement. The sample dried with 10 min shows a little lower resistivity than that dried with 5 min, because the former one shows a bit larger carrier concentration and Hall mobility than latter one.

Table 3.6 Electrical properties of AZMO thin film with different drying time

Drying time	t (nm)	ρ (Ω·cm)	n (cm^{-3})	μ ($cm^2/(V·s)$)
5 min	396	1.7×10^{-2}	3.4×10^{19}	10.7
10 min	388	1.4×10^{-2}	3.8×10^{19}	11.6

3.3.2.3 Effect of the number of coating layer

The effect of the number of coating layer on the electrical properties of AZMO thin film was investigated. The times of spin coating was changed from 5 to 20 at an interval of 5. Figure 3.32 shows the dependence of electrical properties of AZMO thin film on the circles of spin coating. It is clear that the thickness increases almost linearly with increasing the times of spin coating. With increasing coating layer, the resistivity decreases gradually, because Hall mobility and carrier concentration increase little by little.

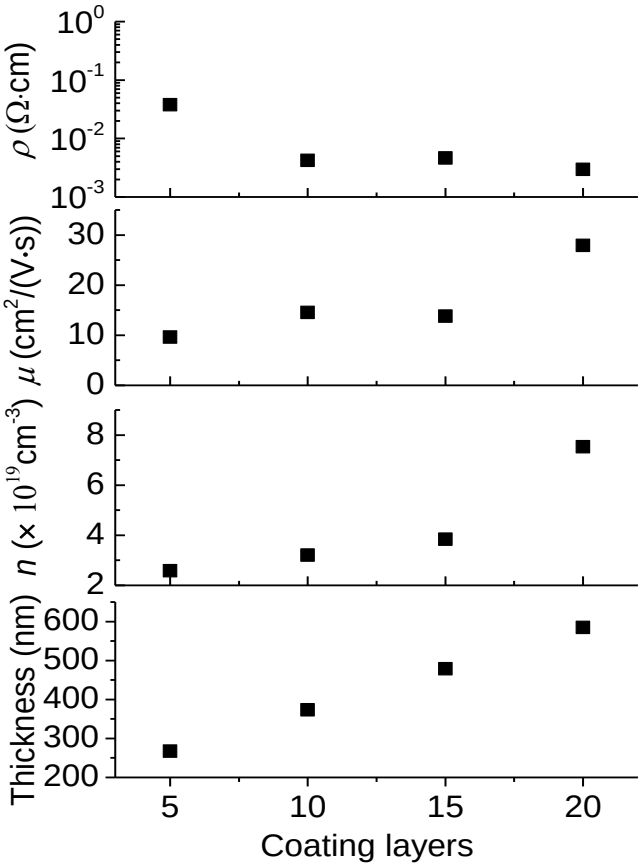

Fig. 3.32 Effect of coating layers on the electrical properties of AZMO thin film (Mg/Zn=0.10).

3.3.3 Effect of two-step annealing

3.3.3.1 Effect of the first step annealing

(1) Effect of annealing temperature

Firstly, the effect of temperature of the first step annealing on the properties of AZMO thin film was investigated. The samples were firstly annealed in air and secondly annealed in forming gas. The temperature of the first step annealing was changed from 400ºC to 600ºC at an interval of 100ºC, while the temperature of second annealing was fixed at 450ºC. Figure 3.33 shows the results of Hall measurement. The film resistivity decreases gradually with increasing annealing temperature. With the increase in temperature, the Hall mobility increases almost linearly, but the carrier

concentration decreases obviously.

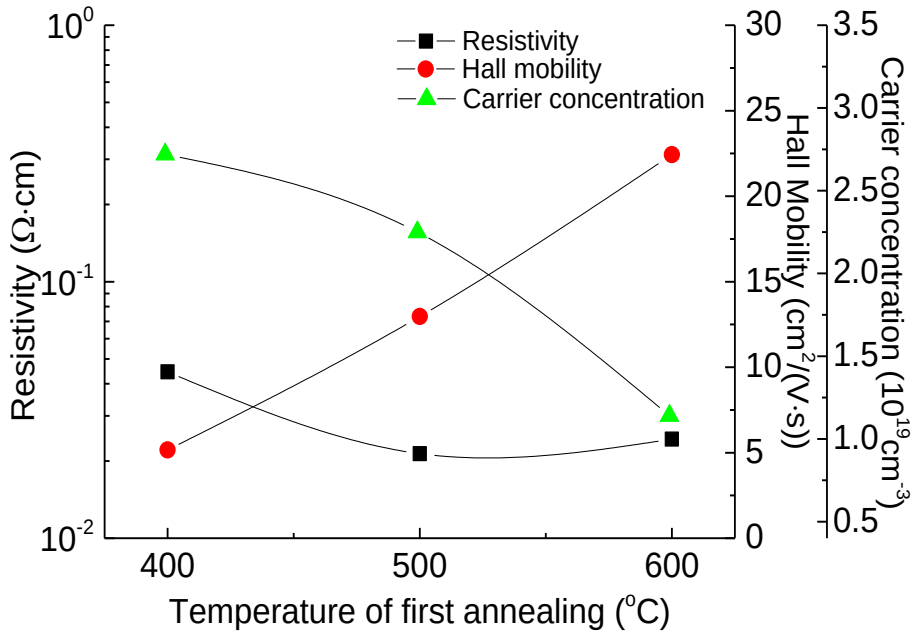

Fig. 3.33 Effect of annealing temperature on the electrical properties of AZMO thin film. The annealing atmosphere is ambient air.

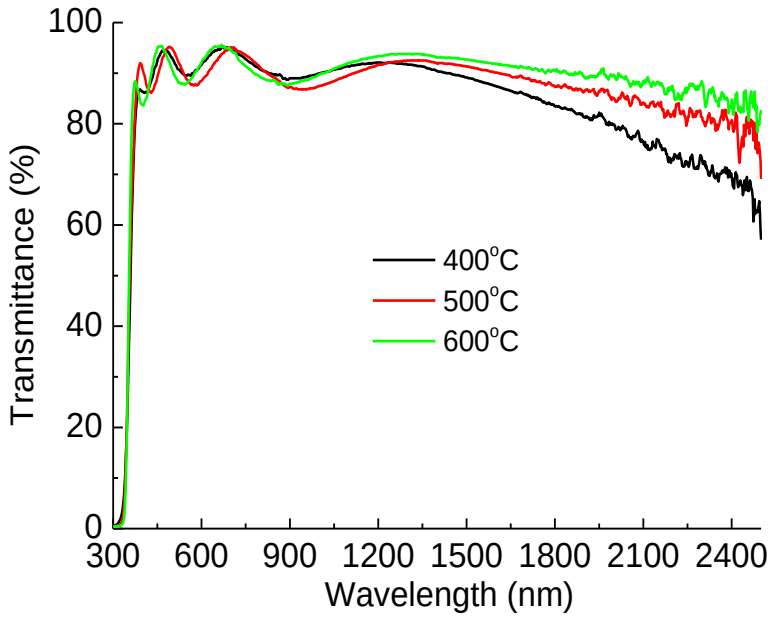

Fig. 3.34 Effect of annealing temperature on the transmittance of AZMO thin film. The annealing atmosphere is ambient air.

The transmittance of AZMO thin film measured after the first annealing with

different temperature is shown in Fig. 3.34. All samples show high transmittance over 85 % at wavelength region from 400 nm to 1800 nm. The transmittance tends to decrease at wavelength of larger than 1800 nm. This is caused by the free carrier absorption. This absorption decreases with increasing temperature. This also indicates that increasing temperature of the first annealing would decrease the carrier concentration.

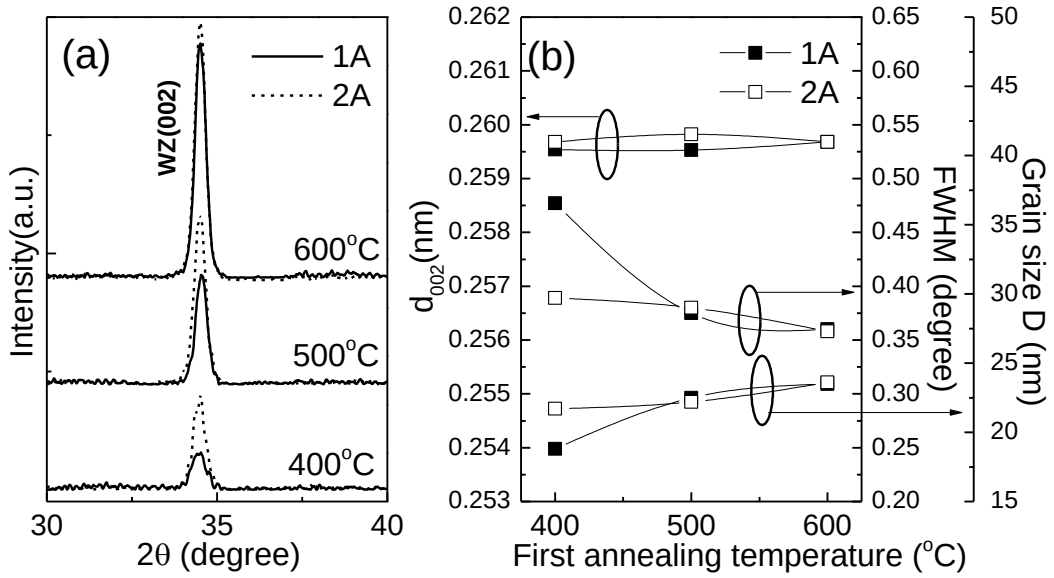

Fig. 3.35 Effect of annealing temperature on the (a) XRD patterns of AZMO thin film and (b) their relevant parameters. The annealing atmosphere is ambient air. 1A and 2A refers to the value obtained after the first and second annealing respectively.

Figure 3.35 (a) exhibits the effect of temperature of the first annealing on XRD patterns of AZMO thin films. All samples show obvious wurtzite (002) preferential orientation. With increasing the first annealing temperature, increase in (002) peak intensity and decrease in full width at half maximum (FWHM) was observed. It indicates that increasing temperature improves film crystallinity. Furthermore, the film crystallinity gets further improved after the second annealing, if the first annealing temperature is lower than 600°C. The grain size calculated using Scherrer's equation is

shown in Fig. 3.35 (b). The grain size increases slightly with the increase in the first annealing temperature. No obvious change in distance of crystal plane (002) (d_{002}) is found among the samples annealed with different temperature. In addition, d_{002} changes a little after the second annealing.

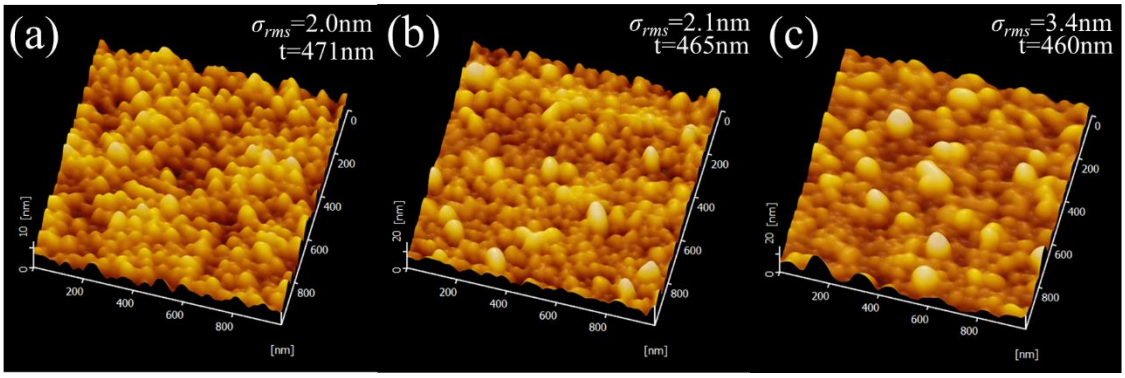

Fig. 3.36 DFM surface morphology micrograph of AZMO thin film taken after the first annealing with different temperature. The annealing atmosphere is ambient air.

DFM surface morphology of AZMO thin film taken after the first annealing with different temperature is shown in Fig. 3.36. All samples show very flat surface with σ_{rms} of about 2 nm. Increasing temperature results in the slight increase in grain size.

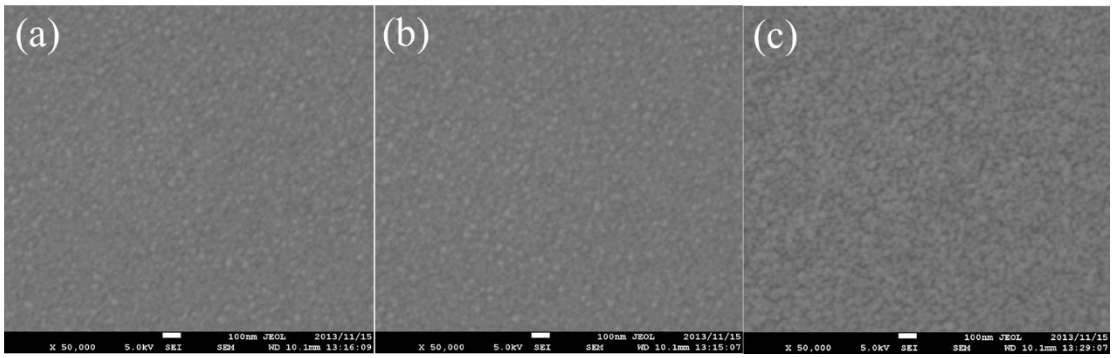

Fig. 3.37 SEM surface micrographs of AZMO thin film taken after the first annealing with annealing temperature (a) 400°C (b) 500°C and (c) 600°C. The annealing

atmosphere is ambient air.

Figure 3.37 shows the SEM surface micrographs of AZMO thin film taken after the first annealing with different temperature. It is clear that all samples show grain size of less than 50 nm. The grain size increases slightly with increasing annealing temperature.

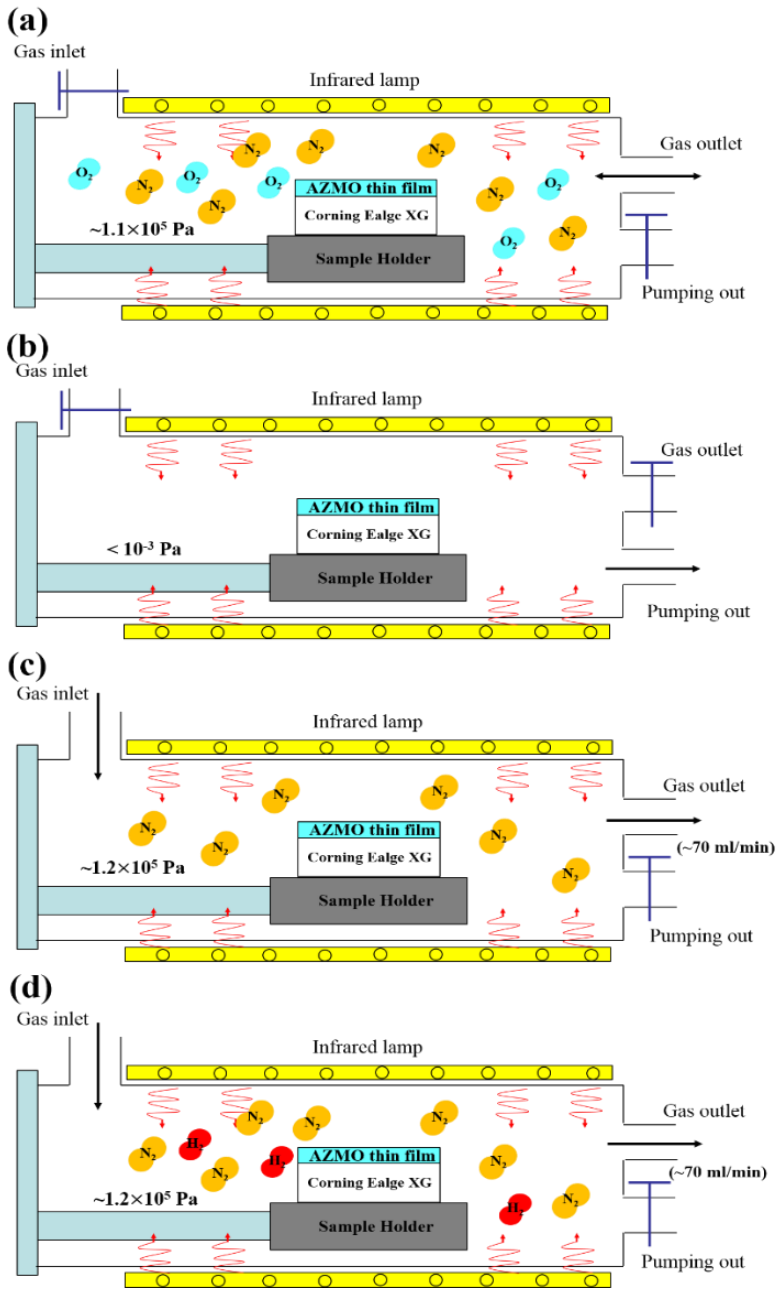

Fig. 3.38 the schematics of first annealing with atmosphere of (a) air (b) vacuum (c) nitrogen and (d) forming gas.

(2) Effect of annealing atmosphere

Annealing atmospheres including nitrogen [13], vacuum [5] or forming gas [14] play a very important role in improving the electrical and optical properties of sol-gel derived AZO thin film. There are few reports about the effect of annealing atmosphere on the properties of sol-gel derived AZMO thin film with two-step annealing. Consequently, the effect of annealing atmosphere on the properties of AZMO thin film is systematically investigated. Firstly, at the first step, four kinds of atmosphere were selected. They are ambient air, vacuum, nitrogen and forming gas. The experimental details is illustrated in Fig. 3.38. The gas flow rate was fixed at 70 ml/min. The pressure in the furnace chamber is about 1.2×10^{5} Pa during annealing with atmosphere of air, N_2 and forming gas. It is less than 10^{-3} Pa during vacuum annealing.

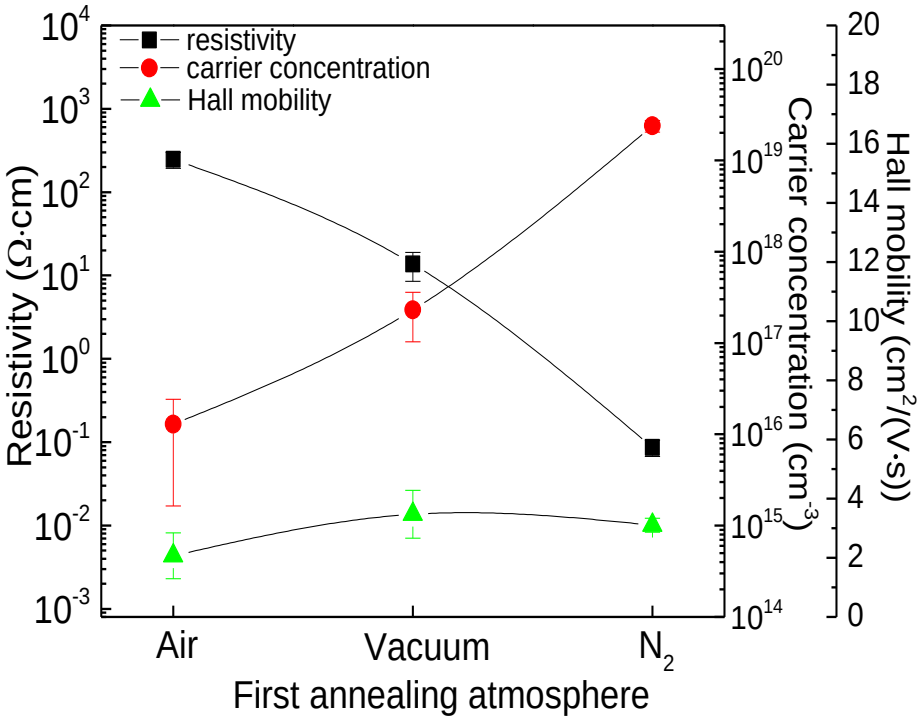

Fig. 3.39 Effect of the first annealing atmosphere on the electrical properties of AZMO thin films. The lines are drawn as a guide for the eyes.

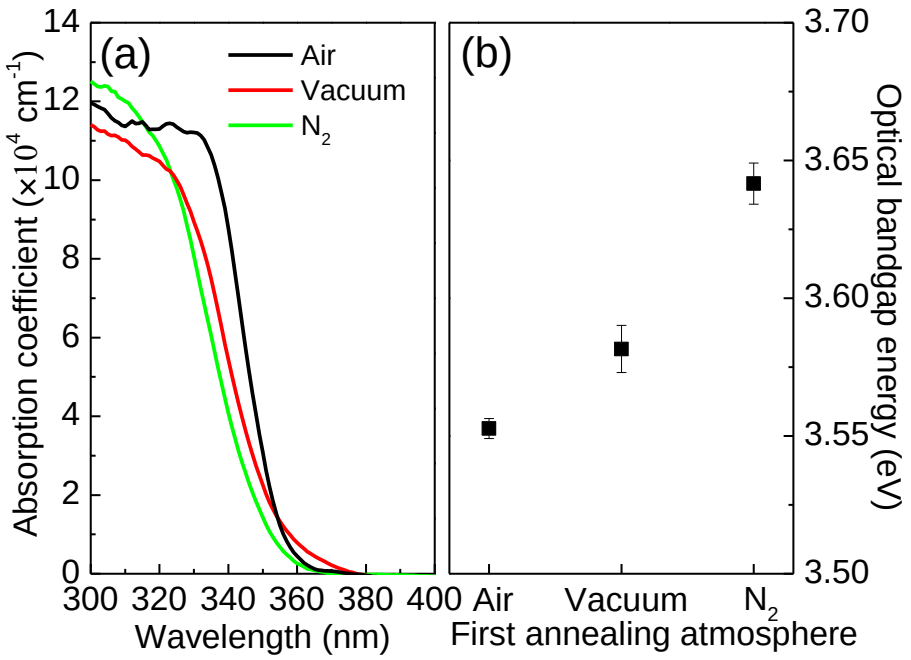

Fig. 3.40 Effect of the first annealing atmosphere on (a) absorption coefficient and (b) optical bandgap energy of AZMO thin films.

Figure 3.39 shows Hall measurement results of AZMO thin films measured after the first annealing in different atmospheres. N_2 and vacuum annealing reduce the resistivity relative to air annealing. The decrease in resistivity is mainly due to the increase in the carrier concentration. The N_2 annealed sample shows the largest carrier concentration of about 2×10^{19} cm^{-3}. Compared with the drastic change in the carrier concentration, Hall mobility was not influenced by the first annealing atmosphere. All samples show low Hall mobilities of less than 4 $cm^2/V\cdot s$. The electrical properties of sample annealed in forming gas were not available because its resistivity was too large to measure.

Effect of the first annealing atmosphere on absorption coefficient (α) and E_{opt} of AZMO thin films is presented in Fig. 3.40. It was found that all samples show high transmittance of over 85% at the wavelength region from 400 to 1600 nm. In Fig. 3.40

(a), only the wavelength region from 300 to 400 nm was illustrated. Compared with the sample annealed in air, the samples annealed in N_2 and vacuum show a clear blue-shift of the spectrum. The samples with N_2 and vacuum annealing show larger E_{opt} than that of the sample with air annealing. The data of FG annealed sample is not shown here, because we found that transmittance of the sample with FG annealing is so similar to that of a bare Eagle XG glass substrate that correct α and E_{opt} of FG annealed sample cannot be obtained.

Table 3.7. Chemical composition in the AZMO thin films determined by XPS after the first annealing in different atmospheres.

Atmosphere	Chemical composition (at. %)				
	Al	Zn	Mg	O	Si
Air	0.8	42	7.6	49.6	0.0
Vacuum	1.1	38.2	10.5	50.3	0.0
N_2	0.5	41.8	8.1	49.6	0.0
FG	5.1	0.6	36.7	55.5	2.2

Table 3.7 shows the effect of the first annealing atmosphere on the chemical composition of AZMO thin films. N_2 and air annealing lead to similar chemical compositions, however, Zn content obviously decreases after annealing in vacuum and FG atmosphere. Especially for FG annealed sample, almost all Zn related phase disappears and Mg related phase is dominant. Trace of Si also appears in FG annealed sample. XPS spectra of the samples are presented in Fig. 3.41. Similar peak intensities at binding energy of Al 2p (74.4 eV), Zn 3p 3/2 (89.0 eV), Mg 2p (50.2 eV) and O 1s

(530.7 eV) were observed for the samples with N_2, air, and vacuum annealing. However, the sample annealed in FG showed a very different spectrum, which indicates that the combination of MgO and Al_2O_3 is dominant.

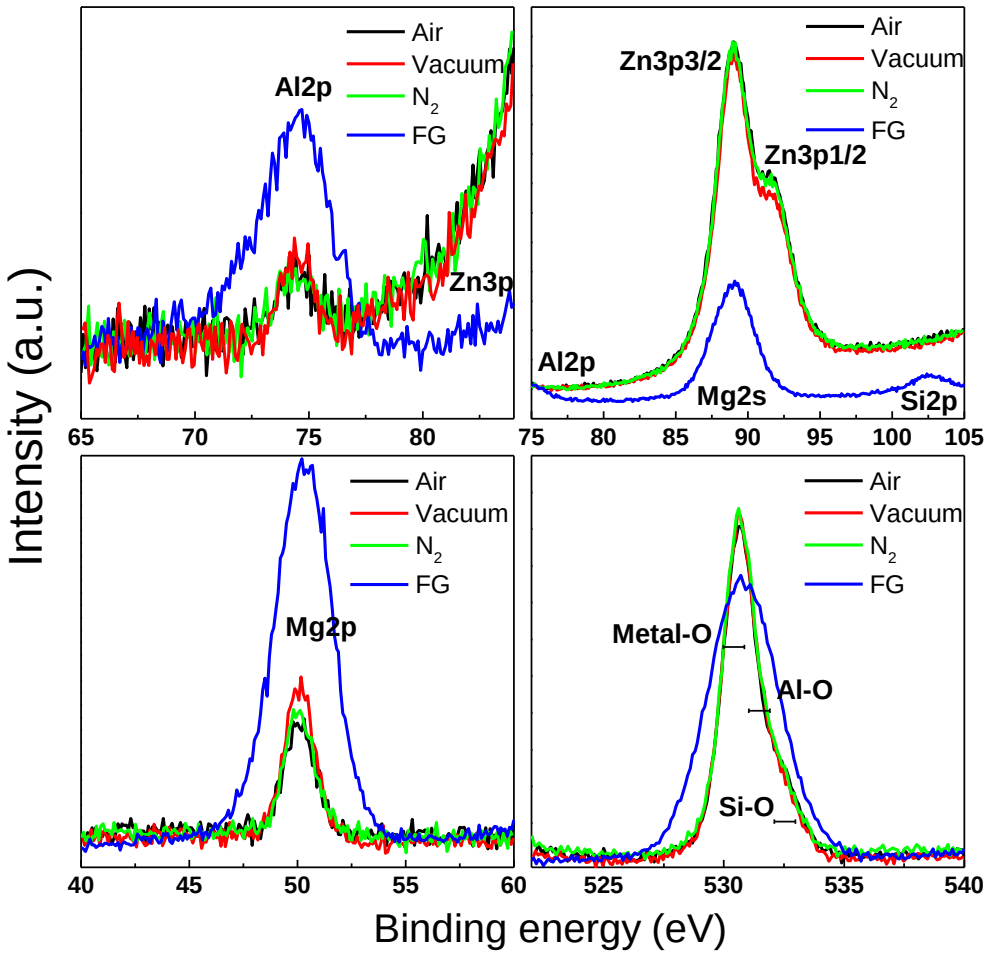

Fig. 3.41 Effect of the first annealing atmosphere on XPS spectra of AZMO thin films. The graph presents effective count.

Effect of the first annealing atmosphere on XRD patterns of AZMO thin films is illustrated in Fig. 3.42. Except for the sample with annealing in FG, the samples show wurzite (002) preferential orientation. Air annealing shows the best film crystallinity. N_2 annealing makes better film crystallinity than vacuum annealing. There was no detectable phase from the sample with FG annealing. This means that the MgO phase

detected by XPS measurement is an amorphous state.

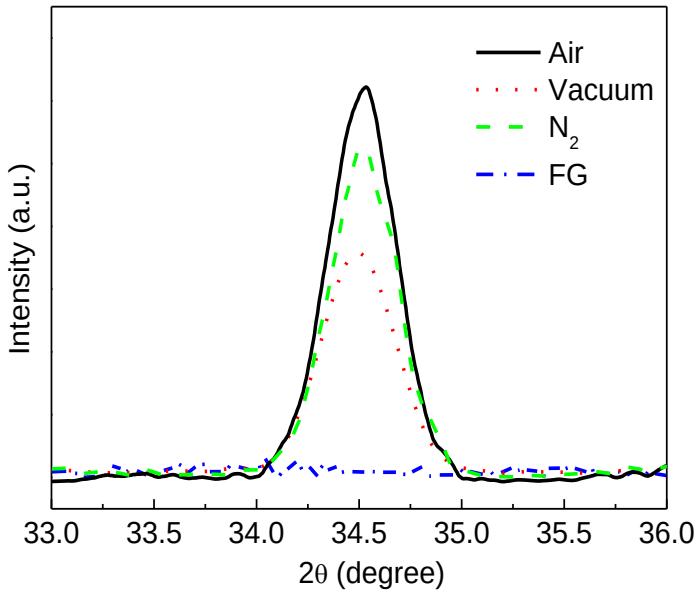

Fig. 3.42 XRD patterns of AZMO thin films measured after the the first annealing in different atmospheres.

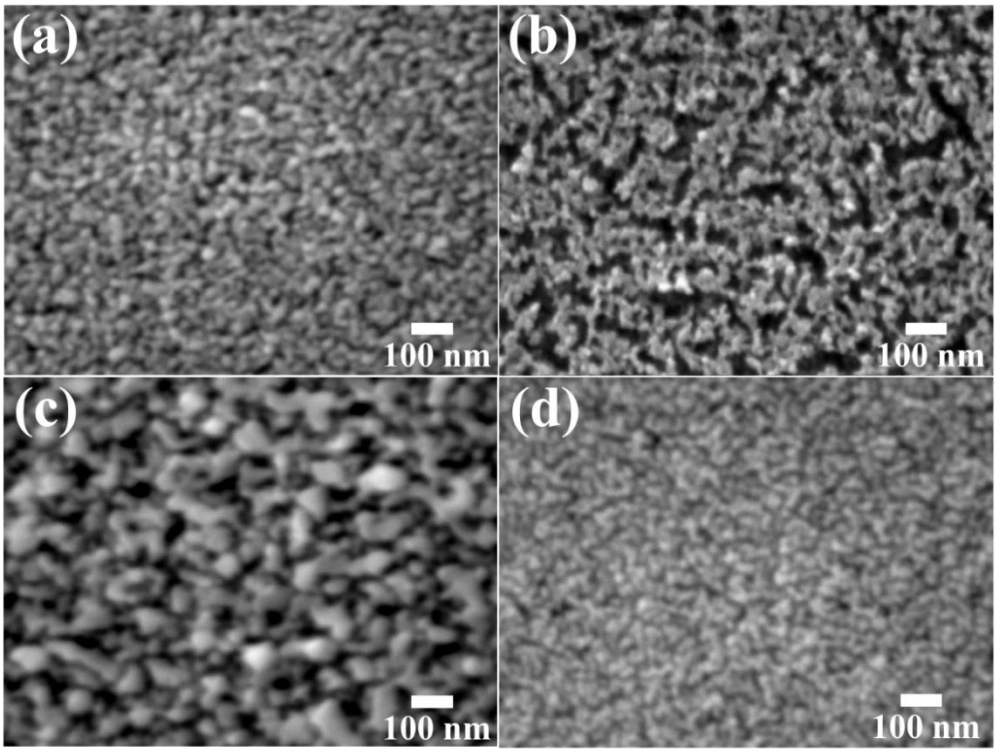

Fig. 3.43 SEM surface micrographs of AZMO thin films taken after the first annealing in (a) air, (b) FG, (c) N_2 and (d) vacuum.

Figure 3.43 shows the SEM surface micrographs of the samples taken after the first annealing in different atmospheres. Nano-spherical grains were formed in all samples. The annealing atmosphere influenced the grain size significantly. N_2 annealed sample shows the largest grain size, while FG annealed sample shows the smallest grain size. The vacuum annealed sample shows a similar grain size as that of air annealed sample. Furthermore, the structure of the FG annealed sample was found to be porous relative to that of the other samples.

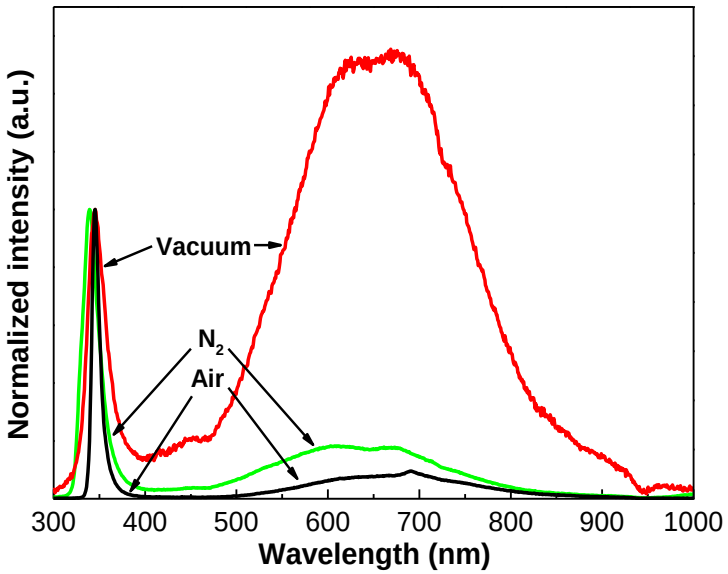

Fig. 3.44 Normalized CL spectra of AZMO thin films measured after the first annealing in different atmospheres. The absolute intensity of the ultraviolet emission peak for vacuum, N_2 and air annealed samples is 80, 943, and 13715, respectively.

Effect of the first annealing atmosphere on the cathodoluminescence (CL) spectra of the samples is shown in Fig. 3.44. All samples exhibit an ultraviolet emission peak at around 340 nm and a red emission peak at around 650 nm. The former is caused by near-band-edge (NBE) emission and the latter probably arises from the transition of electrons between the band edges and the deep level of oxygen vacancy [15, 16, 17]. The N_2 annealed sample shows an obvious blue-shift of ultraviolet emission peak

relative to the vacuum and air annealed sample. This is caused by the enhanced NBE emission due to the increase in carrier concentration. The full width at half maximum (FWHM) of ultraviolet emission peak has an inverse relationship with the film crystallinity. In the order of air, N_2 and vacuum annealing, the FWHM increases, implying film crystallinity decreases. In addition, N_2 and vacuum annealed samples present stronger intensity of red emission peak than that of air annealed sample. It indicates that N_2 and vacuum annealing would generate larger amount of oxygen vacancy than air annealing. Vacuum annealing also exhibits a weak violet emission peak at around 450 nm, which is assigned to a recombination of electrons from conduction band with holes trapped at Zn vacancy state [15]. The annealing atmosphere also influences the peak intensity of the spectra. Air annealed sample shows much stronger peak intensity than that of the other two samples. This reflects the sample was oxidized by the oxygen in the air.

Optimum annealing atmosphere at the first annealing step is N_2 because it realized the lowest resistivity and the largest E_{opt}, taking no account of FG. These are associated with the creation of large carrier concentration in N_2 atmosphere. Ohya et al. [13] mentioned that annealing in an inert atmosphere could decrease the resistivity of AZO thin film and demonstrated that annealing in N_2 at temperature from 500 ^oC to 700 ^oC could effectively decrease the resistivity. The cause of the N_2 annealing-induced high carrier concentration should be the reduced oxygen partial pressure in doping process. According to Kroger-Vink notation [18], the doping process in this work can be expressed by the following equation,

$$Al_2O_3 \xrightarrow{ZnO} 2Al_{Zn}^{\bullet} + 2O_O^{\times} + \frac{1}{2}O_2(g) + 2e^{'} + \Delta E \qquad (2.3)$$

where ΔE is reaction heat. It is well known that this doping process occurs during annealing for sol-gel derived semiconducting materials. N_2 annealing can decrease the oxygen partial pressure and then prompt the equilibrium of reaction to move towards right. It contributes to the increase in carrier concentration. The rise in E_{opt} should be caused by Burstein–Moss effect [9]. Fujihara et al. [19] demonstrated that N_2 annealing at 600 ^oC could make larger E_{opt} of sol-gel derived ZMO thin film (Mg/Zn=10 at.%) than air annealing.

FG was also widely recognized as annealing atmosphere that can effectively reduce the resistivity of AZO thin film [14, 20]. The ineffective function of FG annealing at the first step in this work is probably caused by the high annealing temperature. When annealed in FG which contains H_2, ZnO can be reduced to Zn as illustrated by Eq. (2.4). It is well known that Zn has high vapor pressure. The vapor pressure of Zn at 650 ^oC is about 28 Torr [21]. Then, the gaseous Zn tends to form gaseous ZnH_2 through a reaction with H_2 as shown by Eq. (2.5). Therefore, Zn content is greatly reduced after the first annealing in FG, as shown in Table I. After FG annealing, the film is almost MgO and the porous structure is formed as shown in Fig. 3.43 (b). We also found that only the FG annealed sample showed Si 2p peak in XPS spectrum. The porous structure enabled the detection of Si 2p signal of the Eagle XG substrate underneath the film. This porous MgO film shows very low optical absorption.

$$ZnO + H_2(g) \longrightarrow Zn_{Zn}^{\times} + V_O^{\bullet} + e^{'} + H_2O(g) \tag{2.4}$$

$$Zn(g) + H_2(g) \longrightarrow ZnH_2(g) \tag{2.5}$$

Vacuum annealing could make lower resistivity and larger E_{opt} than annealing

in air because it showed larger carrier concentration than air annealing. It is caused by the formation of ionized oxygen vacancy in the film due to the oxygen-poor atmosphere [5]. The strongest intensity of red emission peak centered at 655 nm in CL spectrum of vacuum annealed sample indicates the production of the largest amount of oxygen vacancy. However, excessive oxygen vacancy would deteriorate film crystallinity, as confirmed by the FWHM widening of ultraviolet emission peak in CL spectrum and (002) peak in XRD patterns. The reason why vacuum annealing makes lower carrier concentration than N_2 annealing is associated with the deficiency of Zn in the film. As mentioned above, the vapor pressure of Zn is high. Vacuum atmosphere would enhance the evaporation of Zn at high temperature so that Zn content is slightly reduced after annealing in vacuum. The Zn 3p1/2 peak intensity in XPS spectrum of vacuum annealed sample decreased due to the deficiency of Zn, compared with that of nitrogen annealed sample. Relatively, Al and Mg becomes a bit excessive so that carrier concentration decreased due to the change in band structure. The unique violet emission at around 450 nm in CL spectrum also confirms the presence of Zn vacancy.

(3) Effect of temperature and holding time in N_2 atmosphere

In view of the improvement on electrical properties of AZMO by using N_2 as annealing atmosphere, the effect of annealing temperature in N_2 on the electrical properties of AZMO thin film was investigated. The samples were firstly annealed in N_2 for 60 min and secondly annealed in forming gas (97% N_2 + 3% H_2) for 60 min. The temperature of the first annealing was changed from 500^{o}C to 650^{o}C at an interval of 50 ^{o}C, while the temperature of the second annealing was fixed at 500^{o}C. Figure 3.45 shows the Hall measurement results. With increasing annealing temperature, the resistivity decreases gradually, because both of carrier concentration and Hall mobility

increases obviously. This is probably caused by the improved film crystallinity. The absorption coefficient at 350 nm decreases obviously due to the increased E_{opt}. The increase in E_{opt} is quite probably caused by the enhanced Burstein-Moss effect due to the increased carrier concentration.

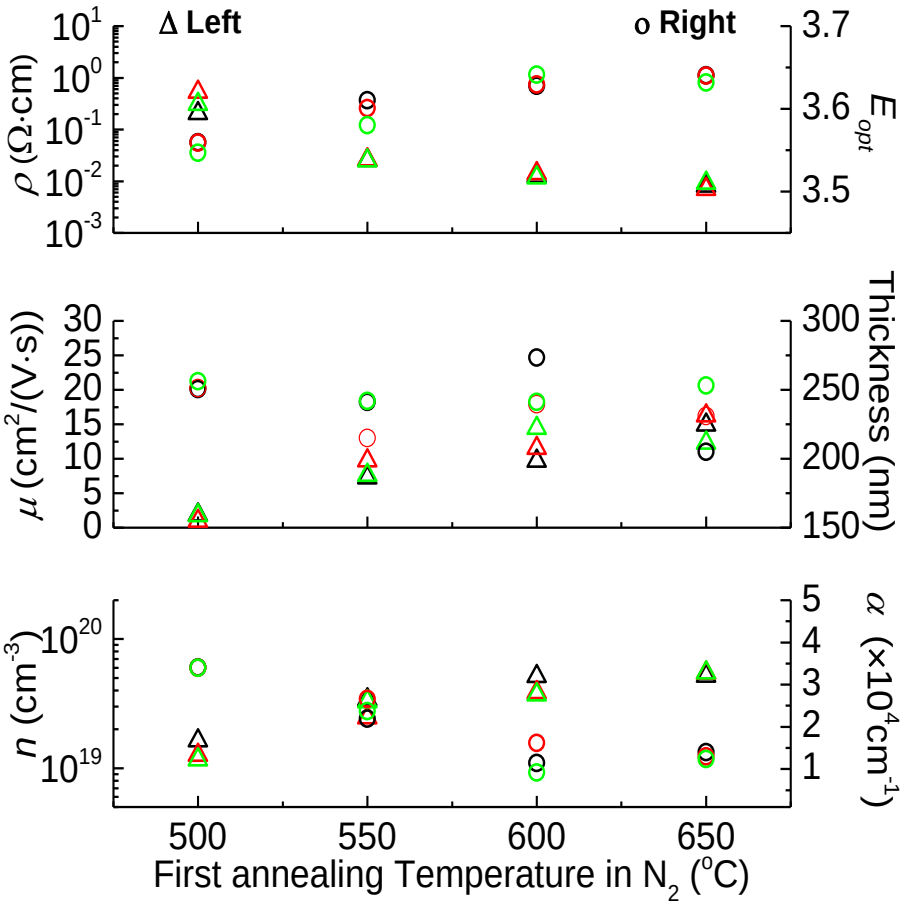

Fig. 3.45 Effect of annealing temperature on the electrical properties of AZMO thin film during the first annealing in N_2. The absorption coefficient refers to the value at 350 nm.

Figure 3.46 shows that the XRD patterns of AZMO thin film measured after the first annealing in N_2 with different annealing temperature. It can be found that all films show wurtzite (002) preferential orientation and the peak intensity of (002) increases obviously with increasing temperature, confirming the improvement on film

crystallinity.

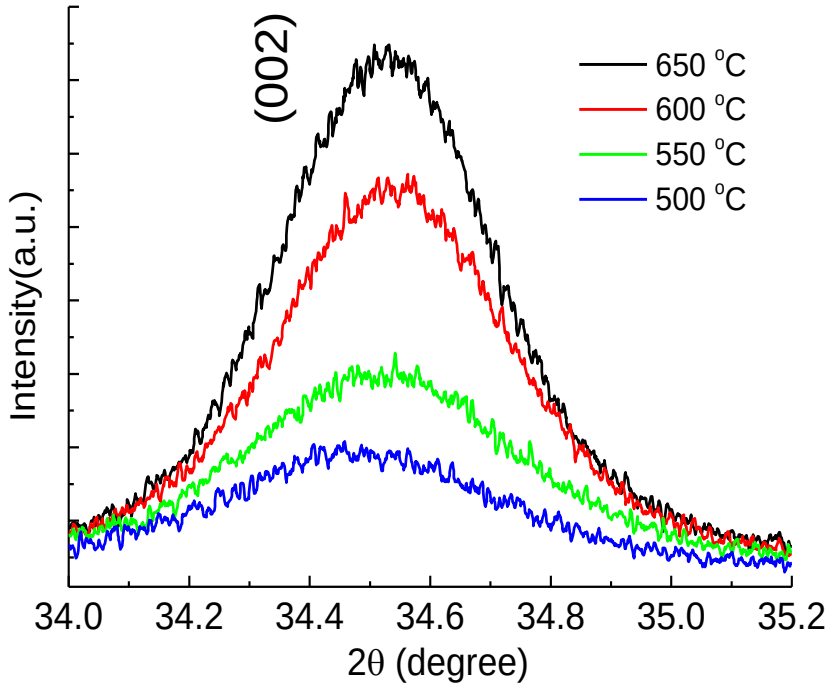

Fig. 3.46 Effect of annealing temperature on the XRD patterns of AZMO thin film during the first annealing in N_2.

Figure 3.47 exhibits the dependence of electrical properties of AZMO thin film on the holding time during N_2 annealing. The first annealing temperature is fixed at 650°C and the holding time is changed from 0.5 h to 4 h. With increasing holding time, the resistivity decreases slowly, get the minimum value and then increases. The minimum value is obtained with holding time of 2 h, because it enabled the largest carrier concentration. The Hall mobility increases slightly due to the improved film crystallinity. The E_{opt} shows a same change tendency with time as carrier concentration. The absorption coefficient shows an opposite change tendency with time relative to the E_{opt}.

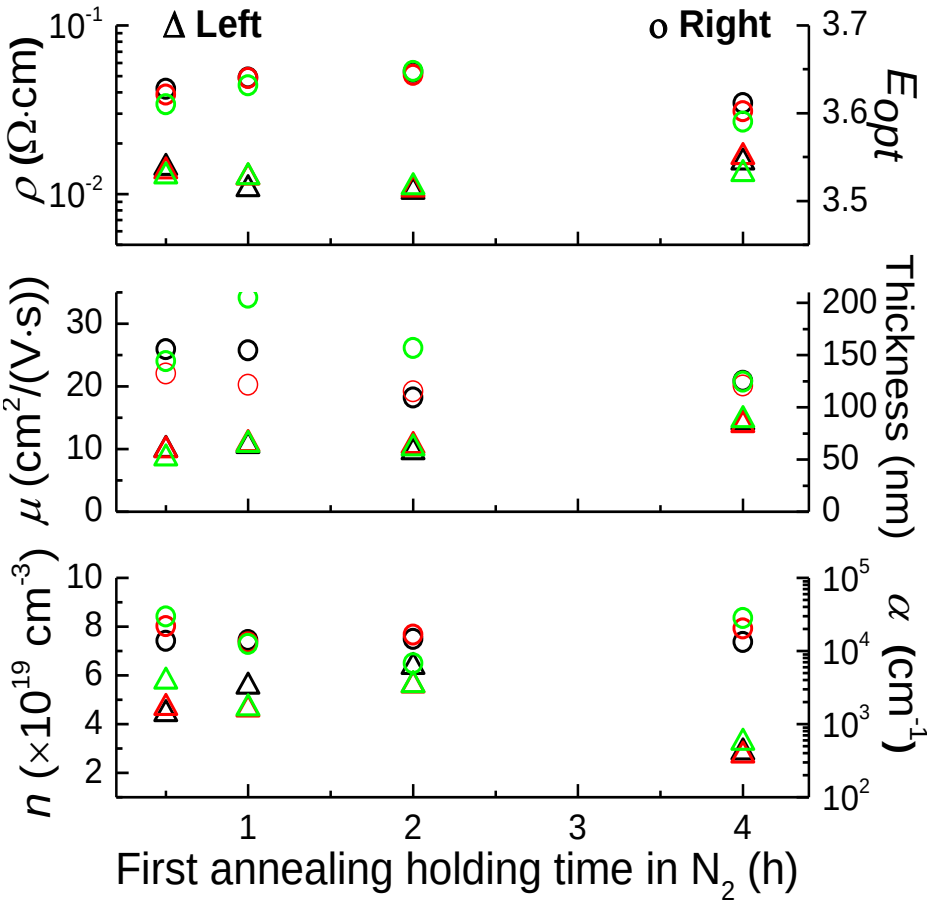

Fig. 3.47 Efect of holding time on the electrical properties of AZMO thin film during the first annealing in N_2. The absorption coefficient refers to the value at 350 nm. The samples were firstly annealed in N_2 and secondly annealed in forming gas (97% N_2 + 3% H_2) at 500 °C for 60 min.

3.3.3.2 Effect of the second step annealing

Based on the above experiments, it was found that the lowest resistivity of AZMO thin film after the first annealing is about 1.1×10^{-2} Ω·cm. It is not good enough to act as electrode. So the second step annealing was conducted to further improve the resistivity. At the second step, films were annealed in N_2, vacuum and FG at 500 °C for

1 h, respectively. In order to evaluate the effect of the second annealing atmosphere, all of these films were firstly annealed in N_2. The gas flow rate was fixed at 70 ml/min. The pressure in the furnace chamber is about 1.2×10^5 Pa during annealing with atmosphere of air, N_2 and forming gas. It is less than 10^{-3} Pa during vacuum annealing.

(1) Effect of annealing atmosphere

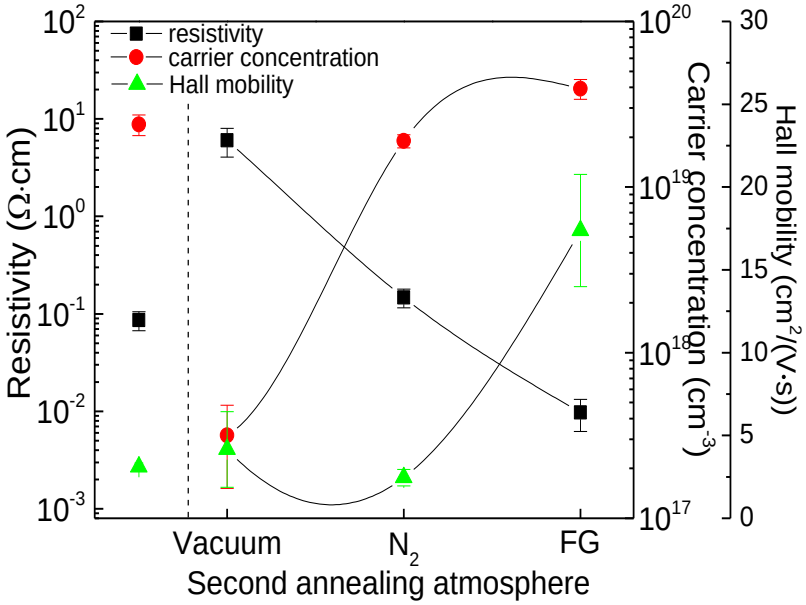

Fig. 3.48 Effect of the second annealing atmosphere on the electrical properties of AZMO thin films firstly annealed in N_2. The points at the left are values measured just after the first annealing in N_2. A piece of glass (Eagle XG, 0.7-mm-thick) was put on the top of samples during annealing. The lines are drawn as a guide for the eyes.

The effect of the second annealing atmosphere on the electrical properties of AZMO thin film firstly annealed in N_2 is shown in Fig. 3.48. Compared with the resistivity measured just after the first annealing in N_2, the resistivity is decreased after the second annealing in FG while it is increased after the second annealing in vacuum. The decrease in resistivity after FG annealing is caused by the obvious enhancement of Hall mobility and slight increase in carrier concentration. The increase in resistivity after vacuum annealing is resulted from the decrease in carrier concentration. The

second annealing in N_2 seldom affect the electrical properties of sample just firstly annealed in N_2. A resistivity of 8.4×10^{-3} Ω·cm (carrier concentration of 4.0×10^{19} cm^{-3} and a Hall mobility of 18.6 $cm^2/V\cdot s$) was achieved after the first annealing in N_2 and the second annealing in FG.

Figure 3.49 shows the effect of the second annealing atmosphere on absorption coefficient and optical bandgap energy of AZMO thin films. In Fig. 3.49 (a), only FG annealed sample shows a slight blue-shift of absorption edge relative to that measured just after the first annealing in N_2. In Fig. 3.49 (b), the E_{opt} increases in the order of vacuum, N_2, and FG after the second annealing. Only FG annealed sample shows a bit larger E_{opt} than that measured just after the first annealing in N_2. The increase in E_{opt} is caused by the enhanced Burstein-Moss effect due to the slightly increased carrier concentration.

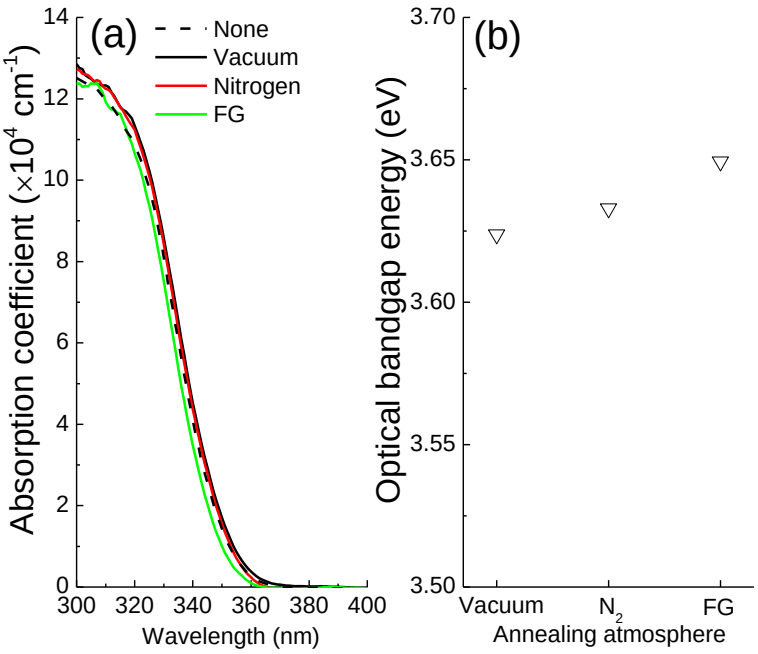

Fig 3.49 Effect of the second annealing atmosphere on (a) absorption coefficient and (b) optical bandgap energy of AZMO thin films.

The effect of the second annealing atmosphere on the XRD patterns of AZMO thin films firstly annealed in N_2 is presented by Fig. 3.50. It can be found that the second

annealing atmosphere seldom affects the (002) preferential orientation of AZMO thin film. The second annealing in FG and vacuum slightly decrease the (002) peak intensity relative to that measured just after the first annealing in N_2. The second annealing in N_2 seldom affects film crystallinity.

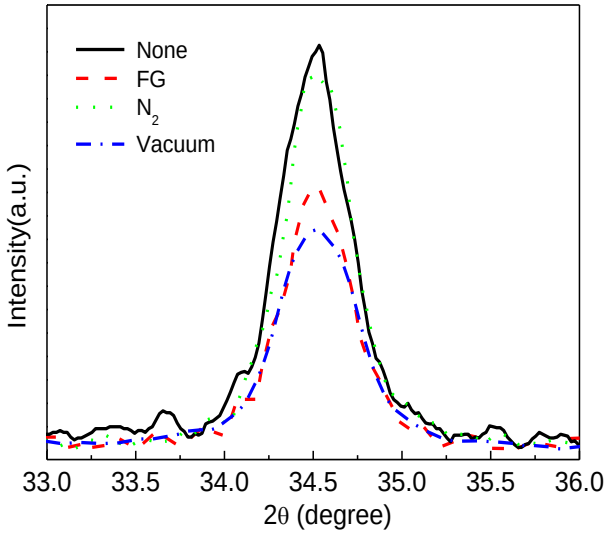

Fig. 3.50 Effect of the second annealing atmosphere on the XRD patterns of AZMO thin films firstly annealed in N_2. The samples were annealed with a Glass Cover in the second annealing. The pattern marked with "None" was measured just after the first annealing in N_2.

(2) Effect of H_2 concentration in FG and glass cover

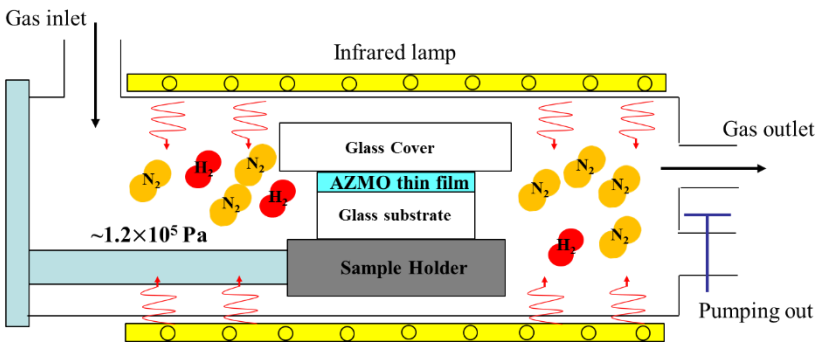

Fig. 3.51 Schematics of FG annealing with GC.

Interestingly, putting a glass substrate on the top of samples (Glass Cover: GC) plays a very important role in the second FG annealing. The FG annealing cannot realize low resistivity films without GC. The schematic of FG annealing with GC is shown in the Fig. 3.51. Figure 3.52 shows how GC affects the resistivity and optical bandgap of the samples. In Fig. 3.52 (a), it is clearly shown that GC significantly contributes to the decrease in resistivity during FG annealing. On the contrary, GC slightly increases the resistivity in N_2 and vacuum annealing. Figure 3.52 (b) shows the E_{opt} of the samples. It is clear that the second FG annealing increases the E_{opt}. The XPS spectra of AZMO samples after the second annealing is shown in Fig. 3.53. It also revealed that the second annealing in FG significantly changed the chemical composition of the sample if the GC was not employed. The sample annealed in FG without GC showed weaker Zn 3p peak intensity and stronger Mg 2p peak intensity than that of the other samples.

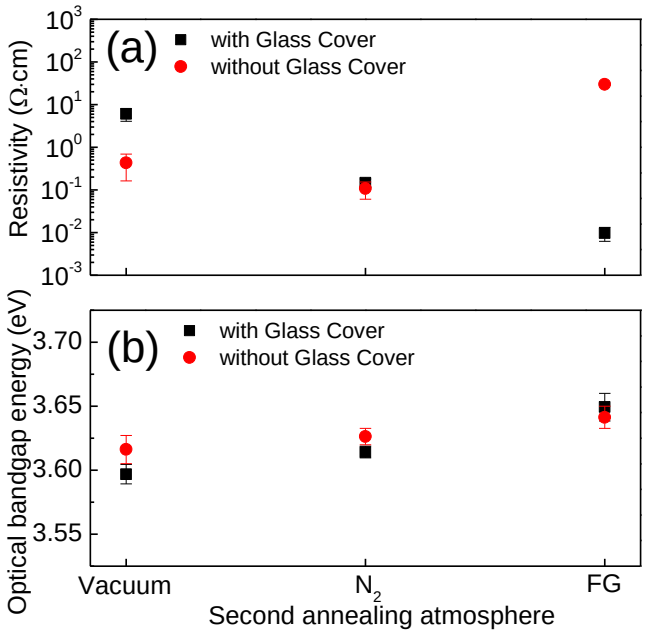

Fig. 3.52 Effect of Glass Cover in the second annealing on the (a) resistivity and (b) E_{opt} of AZMO thin films firstly annealed in N_2.

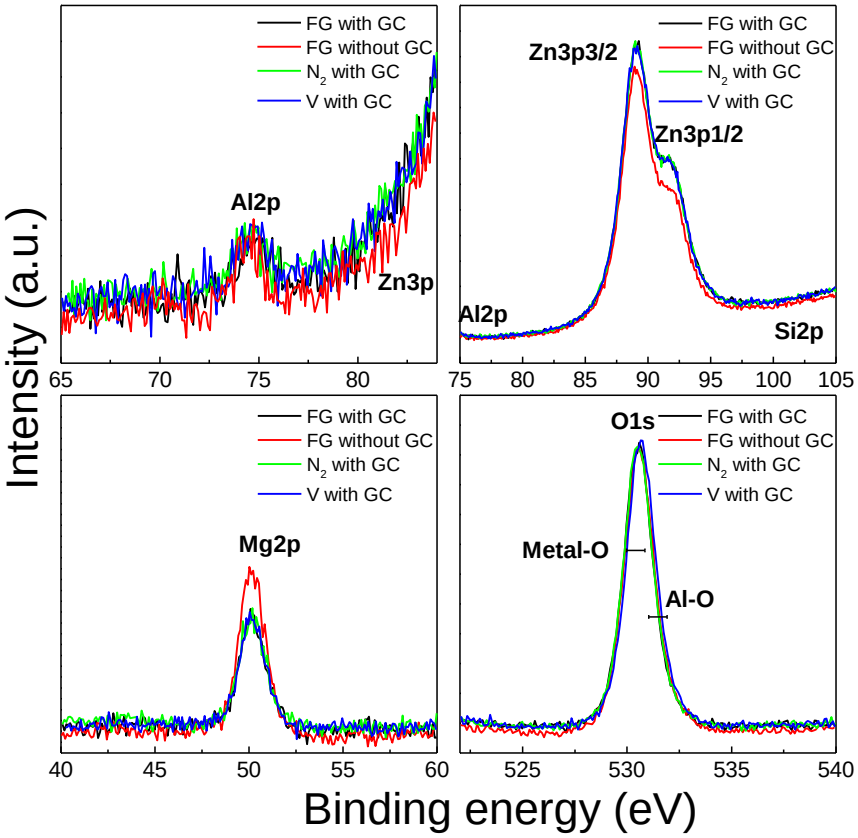

Fig. 3.53 Effect of the second annealing atmosphere on XPS spectra of AZMO thin films. The graph presents effective count.

Table 3.8. Chemical composition in the AZMO thin films determined by XPS after the first annealing in N_2 and the second annealing in different atmosphere.

Atmosphere	Chemical composition (at. %)			
	Al	Zn	Mg	O
FG with glass cover	0.8	41.8	9.4	48.0
FG without glass cover	1.0	35.6	13.6	49.8
N_2 with glass cover	0.6	42.2	8.9	48.2
Vacuum with glass cover	0.6	42.5	8.5	48.5

Table 3.8 summarizes the chemical composition of the samples after the second

annealing. Regardless of atmosphere, samples with GC show similar chemical composition to that measured just after the first annealing in N_2. However, Zn content deceases slightly in FG annealing without GC. These reflect that H_2 in the FG would reduce ZnO during the second annealing without GC.

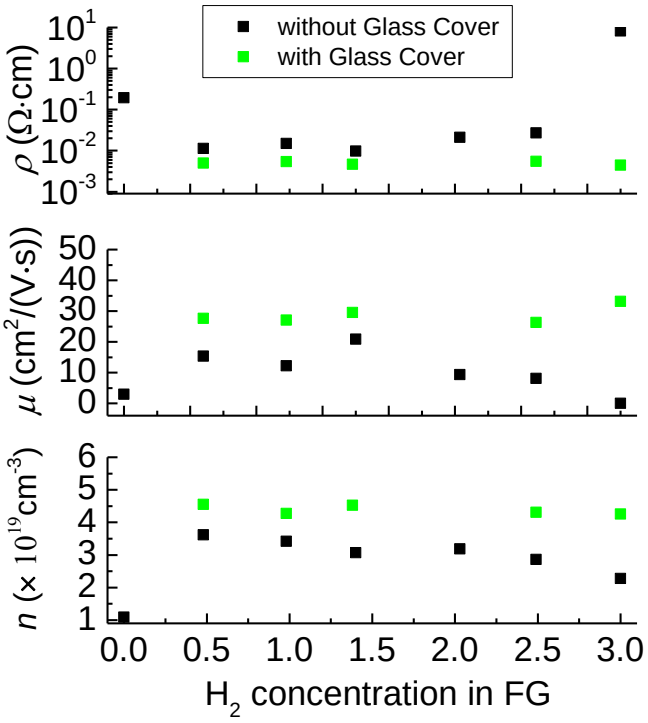

Fig. 3.54 Dependence of the electrical property of AZMO thin film on the H_2 concentration in FG and Glass Cover during the second annealing with FG.

Further experiments were done to clarify the effect of H_2 concentration in FG and GC on the electrical properties of AZMO thin film during FG annealing. The dependence of electrical property of AZMO thin film on the H_2 concentration in FG and GC is shown in Fig. 3.54. Firstly, an optimum H_2 concentration in FG exists for decreasing the resistivity of AZMO thin film when the second annealing in FG was conducted without GC. In this work, the optimum H_2 concentration in FG is approximate 1.5%. At low H_2 concentration that is less than 1.5%, with increasing H_2 concentration, FG annealing decreased the resistivity by increasing the Hall mobility.

At high H_2 concentration that is larger than 1.5%, with increasing H_2 concentration, FG annealing increased the resistivity by decreasing the Hall mobility and carrier concentration. Furthermore, GC can further decrease the resistivity of AZMO thin film through improving the Hall mobility and carrier concentration simultaneously, during FG annealing with any H_2 concentration. GC enabled the lowest resistivity of AZMO thin film with a H_2 concentration of 3% in the FG.

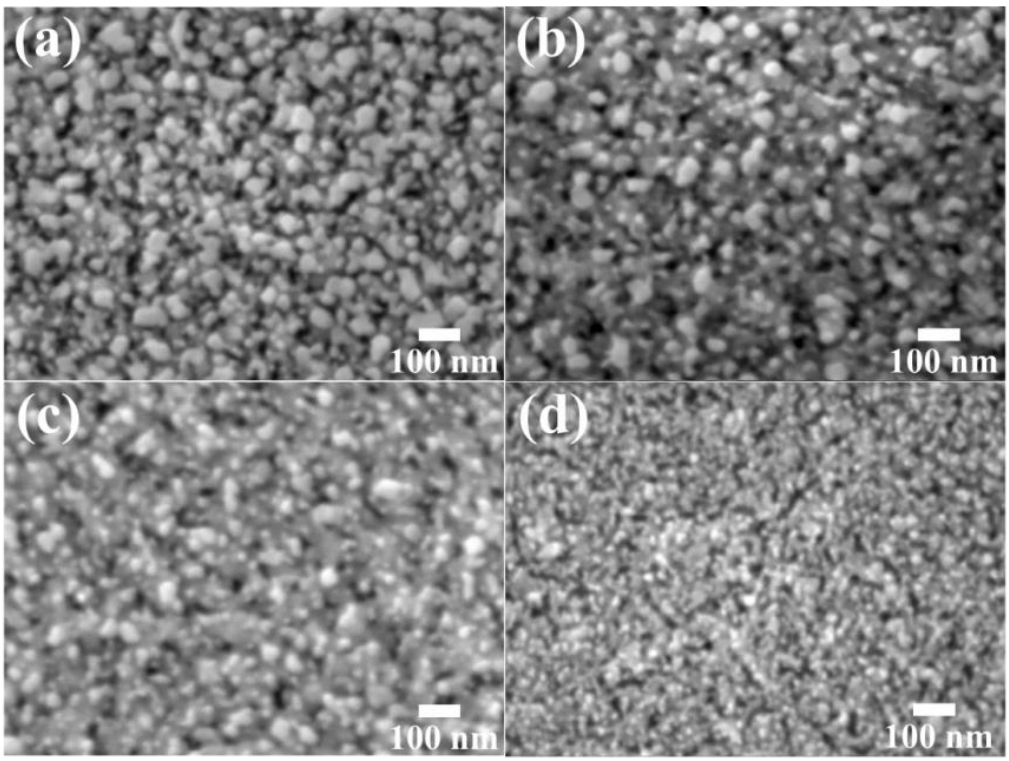

Fig. 3.55 SEM surface micrographs of AZMO thin films taken after the first annealing in N_2 and the second annealing in (a) vacuum with Glass Cover, (b) N_2 with Glass Cover, (c) FG with Glass Cover and (d) FG without Glass Cover.

FG annealing with GC contributed to the improvement of electrical and optical properties. H_2 in the FG and GC played very important roles in this process. It is very important to clarify the functions of H_2 and GC during the FG annealing. The H_2 in the second annealing was thought to have two functions. First, H_2 can promotes the oxygen

desorption from AZMO thin film through reacting with the absorbed oxygen at the grain-boundary. It would decrease the height of potential barrier at the grain-boundary [22, 23]. This contributes to the increase in Hall mobility by decreasing the grain-boundary scattering. Second, H_2 can reduce ZnO. This would deteriorate the electrical properties of AZMO thin film. In this work, at low H_2 concentration that is less than 1.5%, H_2 would preferentially react with the absorbed oxygen at the grain-boundary, because the oxygen is absorbed on the surface of ZnO grain. This is the reason why the Hall mobility increased with increasing H_2 concentration. However, at high H_2 concentration that is larger than 1.5%, the reduction of ZnO with H_2 would dominate because it has lower activation energy (24 kJ/mol) [24] than that of oxygen desorption (96 kJ/mol) [25]. The reduction of Zn content after FG annealing with high H_2 concentration was confirmed in the Table. 3.8.

The SEM surface images of AZMO thin films taken after the first annealing in N_2 and the second annealing in different atmospheres is shown in Fig. 3.55. There is little change of film morphology among the samples. No porous structure was formed. The clear difference was observed only from the sample that annealed in FG without GC. The sample annealed in FG without GC shows smaller ZnO grain than the other samples. It confirmed that FG annealing with high H_2 concentration (3%) decreased obviously the size of grains relative to the annealing with other atmosphere.

The GC used in FG annealing played a very important role in inhibiting the reaction between the H_2 and ZnO. It significantly reduces the contact area between the H_2 and ZnO. This prevents the ZnO from being reduced by H_2 in FG, especially at high H_2 concentration. Table 3.8 shows that the Zn content is apparently reduced after FG annealing without GC. Thus, GC can improves the electrical properties of AZMO thin film during FG annealing with high H_2 concentration. In addition, it can also make a

more stable temperature field at the interface between the GC and AZMO thin film by reducing the influence of gas flow. This probably prompt the process of oxygen desorption from ZnO. Consequently, FG annealing with GC shows a better electrical property than that without GC, regardless of the H_2 concentration.

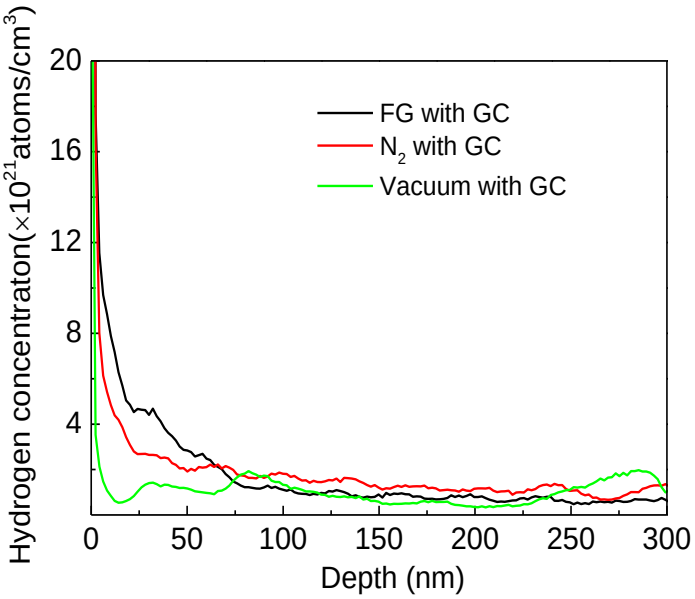

Fig. 3.56 SIMS depth profile of H_2 concentration in the AZMO thin film after the second annealing with different atmospheres.

FG annealing with GC can also improve the E_{opt}. This increase in the E_{opt} is associated with the slight increase in carrier concentration. This increase in carrier concentration is probably caused by the desorption of negatively charged oxygen species [26] or the formation of shallow donors produced by hydrogen incorporation [27, 28]. Figure 3.56 shows the SIMS depth profile of H_2 concentration in the AZMO thin film after the second annealing with different atmospheres. It detected no obvious increase in hydrogen concentration in the film after the second annealing in FG, relative to the second annealing in other annealing atmospheres. This implies that hydrogen in FG just reacts with oxygen in the samples and forms water vapor, resulting in the oxygen-desorption from the samples. Further investigation is required to clarify the role of hydrogen in the second annealing.

(3) Effect of annealing temperature in the second FG annealing

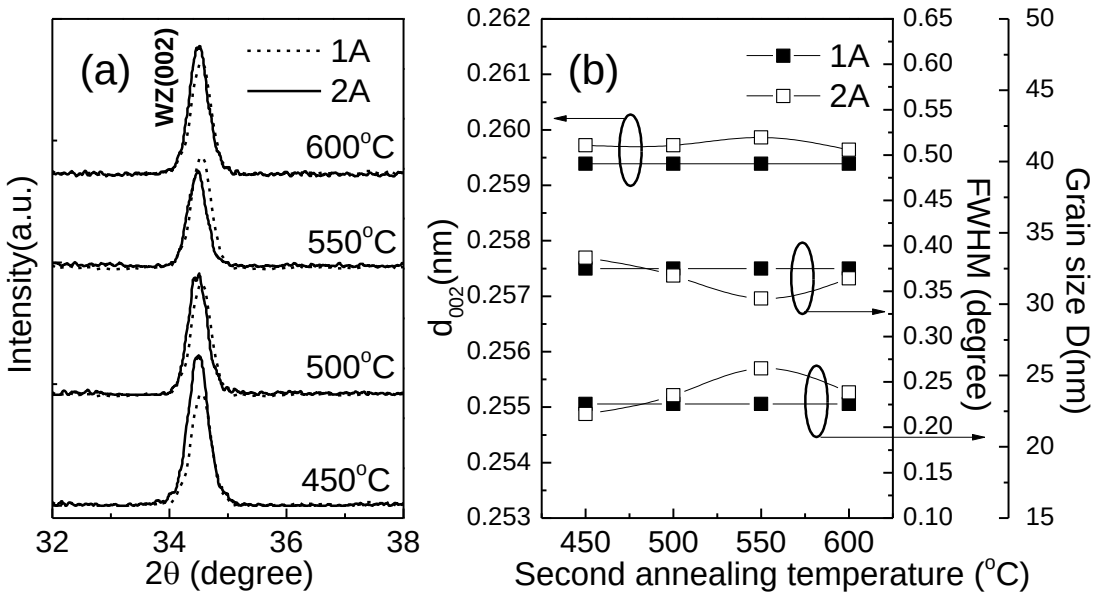

Fig. 3.57 Effect of the second annealing temperature on the XRD patterns. (a) XRD patterns and (b) their relevant parameters. 1A and 2A refers to the value obtained after the first and second annealing respectively. In these experiments, the first annealing temperature was kept constant at 500 ºC, while the second annealing temperature was changed.

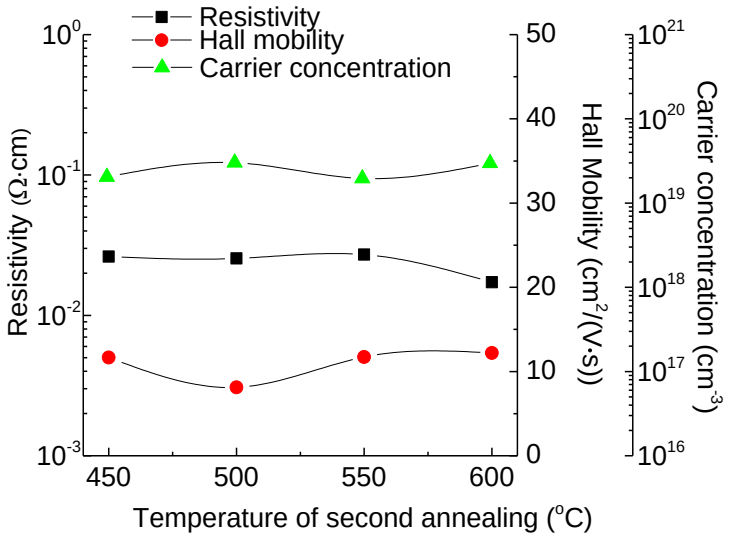

Fig. 3.58 Hall measurement results of AZMO films after the first annealing in air and the second annealing in FG with GC. The first annealing temperature was fixed at 500℃, while the second annealing temperature was changed.

Fig. 3.57 shows the effect of annealing temperature in the second FG annealing on the XRD patterns of AZMO thin film. In Fig. 3.57 (a), it is clear that the position of (002) peak shifts towards low angle after second annealing. In Fig. 3.57 (b), the crystal plane (002) distance increases obviously after second annealing regardless of the temperature. The $Zn_{1-x}Mg_xO$ grain size increases if the second annealing temperature is higher than the first annealing temperature.

Fig. 3.58 shows the effect of temperature of the second annealing with FG atmosphere. With increasing the second annealing temperature, the resistivity decreases, and the carrier concentration increases slightly. The mobility shows a little change. Although low resistivity was obtained at high annealing temperature in the second step, it was found that when the temperature is higher than 500 ^oC the film color changes apparently, and the resistance at the edge of sample is very large. It should be related to the hydrogen in the FG. As mentioned above, H_2 in FG contributes to the decrease in resistivity by prompting the oxygen-desorption process at the grain-boundaries. Increasing the annealing temperature in FG promotes this oxygen-desorption process. However, too high temperature (> 500 ^oC) can also promote the reduction of ZnO, resulting in the high resistance at the edge of GC covered AZMO sample. Consequently, the optimum of second annealing temperature is concluded to be about 500℃.

3.4 Summary

Al doped $Zn_{1-x}Mg_xO$ thin film with low resistivity and low surface roughness was developed by the sol-gel process with two-step annealing. An AZMO thin film with ρ=3.9×10^{-3} Ω·cm and E_{opt}= 3.61 eV was achieved with Mg/Zn=10 mol. % and

Al/Zn=0.8 mol. % (thickness=681 nm). This enabled sol-gel AZMO thin film to be applied as the TCO in solar cells. Increasing Mg content increased the optical bandgap, but it decreased the resistivity. Employing ethanol as the solvent or increasing the Zn^{2+} solute concentration changed the surface morphology and increased the surface roughness. Al doping contributed to the decrease in resistivity and the increase in optical bandgap energy, whereas heavy doping of greater than 0.8 mol % showed detrimental effects on the resistivity and film crystallinity. The mobility was dominated by grain-boundary scattering. In terms of decreasing the sheet resistance through increasing film thickness, increasing the number of coating layer was demonstrated as the best way. Two-step annealing proved to be an effective way to improve the electrical properties. Annealing atmosphere played an important role in improving the electrical and optical properties of AZMO thin film at each step. It was found that the first annealing in nitrogen increased carrier concentration, and the second annealing in forming gas with a glass cover contributed to the improvement of Hall mobility. An optimum H_2 concentration in forming gas existed for decreasing the resistivity of AZMO thin film when the second annealing in forming gas was conducted without glass cover. Increasing the first annealing temperature and/or increasing holding time increased Hall mobility through improving film crystallinity.

Reference

[1] T. Minemoto, T. Negami, S. Nishiwaki, H. Takakura, Y. Hamakawa, Preparation of $Zn_{1-x}Mg_xO$ films by radio frequency magnetron sputtering, Thin Solid Films 372 (2000) 173-176.

[2] Q. Yu, H. Yang, W. Fu, L. Chang, J. Xu, C. Yu, R. Wei, K. Du, H. Zhu, M. Li, G. Zou, Transparent conducting yttrium-doped ZnO thin films deposited by sol-gel method, Thin Solid Films 515 (2007) 3840-3843.

[3] D.J. Cohen, K.C. Ruthe, S.A. Barnett, Transparent conducting $Zn_{1-x}Mg_xO$:(Al, In) thin films, J. Appl. Phys. 96 (2004) 459-467.

[4] T. Minami, New n-Type Transparent Conducting Oxides, MRS Bulletin 25 (2000) 38-44.

[5] W. Tang, D.C. Cameron, Aluminum-doped zinc oxide transparent conductors deposited by the sol-gel process, Thin Solid Films 238 (1994) 83-87.

[6] K. Shirouzu, T. Ohkusa, M. Hotta, N. Enomoto, J. Hojo, Distribution and Solubility Limit of Al in Al_2O_3-Doped ZnO Sintered Body, Journal of the Ceramic Society of Japan 115 (2007) 254-258.

[7] S. Katsuyama, Y. Takagi, M. Ito, K. Majima, H. Nagai, H. Sakai, K. Yoshimura, K. Kosuge, Thermoelectric properties of $(Zn_{1-y}Mg_y)_{1-x}Al_xO$ ceramics prepared by the polymerized complex method J. Appl. Phys. 92 (2002) 1391-1398.

[8] T. Tsubota, M. Ohtaki, K. Eguchi, H. Arai, Thermoelectric properties of Al-doped ZnO as a promising oxidematerial for high-temperature thermoelectric conversion J. Mater. Chem. (1997) 85-90.

[9] E. Burstein, Anomalous Optical Absorption Limit in InSb, Phys. Rev. 93 (1954) 632-633.

[10] A. Luque, S. Hegedus, Handbook of Photovoltaic Science and Engineering, 2nd ed., Wiley, New York, 2011.

[11] J.G. Lu, S. Fujita, T. Kawaharamura, H. Nishinaka, Y. Kamada, Carrier concentration induced band-gap shift in Al-doped $Zn_{1-x}Mg_xO$ thin films, Appl. Phys. Lett. 89 (2006) 2621071-2621073.

[12] J. Wang, L. Meng, Y. Qi, M. Li, G. Shi, M. Liu, The Al-doping contents dependence of the crystal growth and energy band structure in Al:ZnO thin films, J. Crys. Growth 311 (2009) 2305-2308.

[13] Y. Ohya, H. Saiki, Y. Takahashi, Preparation of transparent, electrically conducting ZnO thin film from zinc acetate and alkoxide, J. Mater. Sci. 29 (1994) 4099-4103.

[14] T. Schuler, M.A. Aegerter, Optical, electrical and structural properties of sol gel ZnO:Al coatings, Thin Solid Films 351 (1999) 125-131.

[15] M. Trunk, V. Venkatachalapathy, A. Galeckas, A.Y. Kuznetsov, Deep level related photoluminescence in ZnMgO, Appl. Phys. Lett. 97 (2010) 2119011-2119011.

[16] R.E. Marotti, J.A. Badan, E. Quagliata, E.A. Dalchiele, Red photoluminescence and band edge shift from ZnO thin films, Physica B 398 (2007) 337-340.

[17] V. Kumar, H.C. Swart, O.M. Ntwaeaborwa, R.E. Kroon, J.J. Terblans, S.K.K. Shaat, A. Yousif, M.M. Duvenhage, Origin of the red emission in zinc oxide nanophosphors,

Mater. Lett. 101 (2013) 57-60.
[18]F.A. Kroger, H.J. Vink, Relations between the Concentrations of Imperfections in Crystalline Solids, Solid State Phys. 3 (1956) 307-435.
[19]S. Fujihara, Y. Ogawa, A. Kasai, Tunable Visible Photoluminescence from ZnO Thin Films through Mg-Doping and Annealing, Chem. Mater. 16 (2004) 2965-2968.
[20]V. Musat, B. Teixeira, E. Fortunato, R.C.C. Monteiro, Effect of post-heat treatment on the electrical and optical properties of ZnO:Al thin films, Thin Solid Films 502 (2006) 219-222.
[21]K.I. Hagemark, L.C. Chacka, Electrical transport properties of Zn doped ZnO, Journal of Solid State Chemistry 15 (1975) 261-270.
[22]S.J. Baik, J.H. Jang, C.H. Lee, W.Y. Cho, K.S. Lim, Highly textured and conductive undoped ZnO film using hydrogen post-treatment Appl. Phys. Lett. 70 (1997) 3516-3518.
[23]B.D. Ahn, S.H. Oh, C.H. Lee, G.H. Kim, H.J. Kim, S.Y. Lee, Influence of thermal annealing ambient on Ga-doped ZnO thin films, J. Cryst. Growth 309 (2007) 128-133.
[24]S. Lew, A.F. Sarofilm, M. Flytzani-stephanopoulos, The reduction of znic titanate and zinc oxide solids, Chemical Engineering Science 47 (1992) 1421-1431.
[25]H. Watanebe, M. Wada, T. Takahashi, The activation energy for oxygen desorption from zinc oxide surfaces, Jpn. J. Appl. Phys. 4 (1965) 945-947.
[26]F.H. Wang, H.P. Chang, C.C. Tseng, C.C. Huang, Effects fo H_2 plasma treatment on properties of ZnO: Al thin films prepared by RF magnetron sputtering, Surf. Coat. Tech. 205 (2011) 5269-5277.
[27]C.G.V.d. Walle, Hydrogen as a Cause of Doping in Zinc Oxide, Phys. Rev. Lett. 85 (2000) 1012-1015.
[28]D.M. Hofmann, A. Hofstaetter, F. Leiter, H. Zhou, F. Henecker, B.K. Meyer, S.B. Orlinskii, J. Schmidt, P.G. Baranov, Hydrogen: a relevant shallow donor in zinc oxide, Phys. Rev. Lett. 88 (2002) 0455041-0455044.

Chapter 4 Fabrication and characterization of optically-rough and physically-flat TCO substrates

4.1 Introduction

This chapter introduces the fabrication of optically-rough and physically-flat TCO substrate through spin-coating sol-gel derived AZMO thin film on glass substrates with roughened surface. Techniques of reactive-ion etching (RIE) and room-temperature nanoimprinting (RTNI) will be used to roughen the surface of glass substrates, for making an interface for scattering incident light, that is, a scattering interface. Reactive-ion etching proves to be an effective method to etch glass substrate for getting a variety of rough surface morphology. RTNI is an emerging method to make various high-resolution patterns on glass substrate. The feature size on the roughened glass substrate can be controlled by adjusting RIE condition or designing RTNI pattern, for enhancing light-scattering. In this chapter, at the beginning, the basics of RIE and RTNI as well as their application to roughening glass substrate will be introduced. Then, the fabrication and characteristics of AZMO/roughened glass substrate will be presented.

4.2 Basics of reactive-ion etching and room-temperature nanoimprinting

4.2.1 Basics of reactive-ion etching

Reactive-ion etching (RIE) is a dry etching technique, which was used in microfabrication. Figure 4.1 shows the simple mechanism of RIE effect. The main part

of a RIE system is parallel-plate reactor. Samples are set on a platter situated in the bottom portion of the chamber. The sample platter is electrically isolated from the rest of the chamber. Certain gas is used to generate plasma. Gas pressure is usually maintained in a range between a few militorr and a few hundred militorr. Plasma is produced in the system by applying a strong radio frequency (RF) electromagnetic field to the electrode. The field frequency is usually 13.56 Megahertz, which is applied at a few hundred watts. This oscillating electric field ionizes the gas molecules, resulting in the formation of plasma. The electrons deposited on the platter cause the platter to build up charge due to its DC isolation. This charge forms a large negative voltage on the platter. At the same time, the plasma itself develops a slightly positive charge due to the higher concentration of positive ions compared to free electrons [1]. Because of the large voltage difference, the positive ions would move toward the sample platter where they collide with the samples to be etched. Figure 4.2 shows the schematic of the main processes that occurs during the RIE.

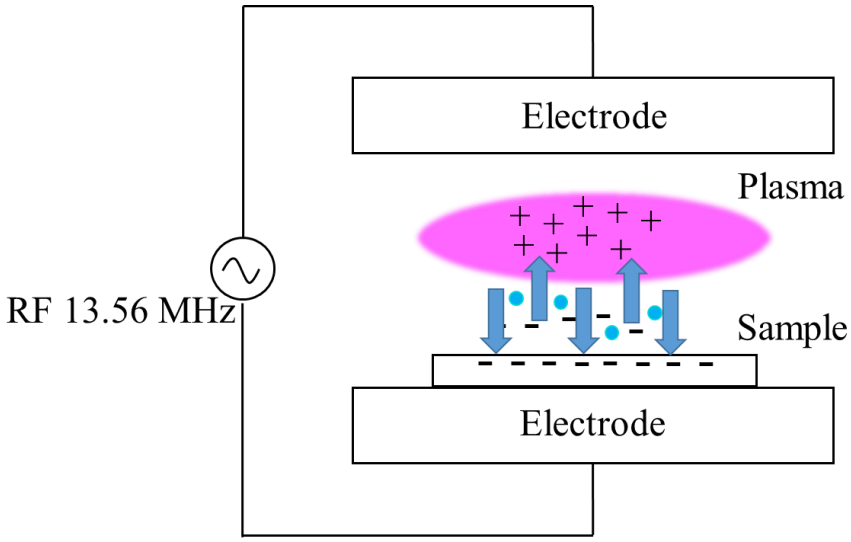

Fig. 4.1 Schematics of RIE effect

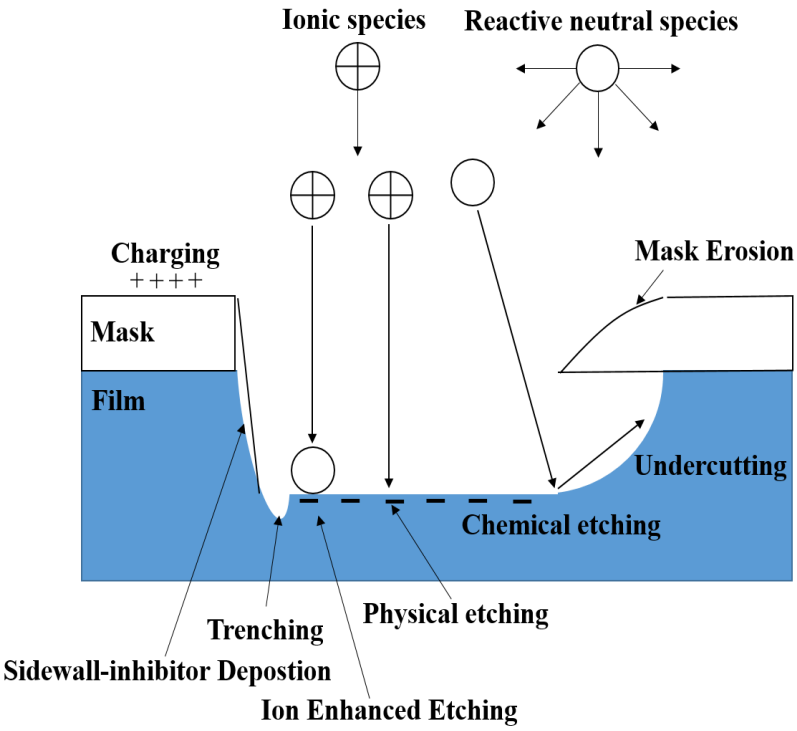

Fig. 4.2 Schematics of processes occurring in RIE etching.

The main processes are physical and chemical etching. The physical etching is highly anisotropic and it has a very low selectivity. During physical etching, the layer molecules are stripped away by the impact of ions on the substrate. On the contrary, the chemical etching is very isotropic and very selective. The ions react chemically with the materials on the surface of the samples. RIE can produce very anisotropic etch profiles due to the mostly vertical delivery of reactive ions. Etching conditions in an RIE system depend strongly on the many process parameters, such as pressure, gas flows, and RF power. RIE is a relatively complicated process. Characteristics such selectivity, anisotropy, and etch rate are influenced by a lot of parameters such as gas species, pressure, dc bias substrate materials and so on.

Recently, much efforts were made to etch glass substrate for the fabrication of

electrophoresis capillary chips [2], diffractive optical elements [3], gratings [4] and waveguides [5], for fabricating nanometer-scale features in the pattern. In these fields, RIE is a preferred etching process, because it can make a good selectivity, anisotropy, ultimate resolution even in a few tens angstroms and exact control on the pattern's profile. One may find great interests from this to make a controllable morphology on the surface of glass substrate. The ingredient of glass substrate is main SiO_2 and other metal oxides. Strainbrüchel et al. [6] concluded that in SiO_2 etching by CF_4 plasma, ions are the chief reactants, and the etching mechanism is shown as following,

$$CF_4 + e^- \leftrightarrow CF_3^+ + F + 2e^-$$

$$CF_3^+ + e^- \leftrightarrow CF_2^{2+} + F + 2e^-$$

$$4CF_3^+ + 3SiO_2 \rightarrow 2CO + 2CO_2 + 3SiF_4 + 4e^- (Y = 2.25),$$

$$2CF_3^+ + SiO_2 \rightarrow COF_2 + CO + SiF + 2e^- (Y = 1.5),$$

$$2CF_3^+ + 3SiO_2 \rightarrow O_2 + 2CO_2 + CO + 3SiF_2 + 2e^- (Y = 4.5),$$

$$2CF_3^+ + 3SiO_2 \rightarrow COF_2 + CO + O_2 + 2SiF_2 + 2e^- (Y = 3),$$

$$2CF_2^+ + SiO_2 \rightarrow 2CO + H_2 + SiF_4 + 2e^- (Y = 1.5),$$

where Y is the etch yields in atoms per ion. Furthermore, the addition of the gas of Ar, O_2, or N_2 can significantly suppress polymerization on grounded surfaces. Consequently, the chemically non-etchable components would stay on the surface of glass substrate and act as the feature on the roughened substrate. As a result, the rough surface morphology is formed.

Shen et al. [4] reported the characterization of RIE of soda-lime glass under various conditions of CHF_3/Ar, CF_4/O_2, and CF_4/Ar gas mixtures and their applications

in integrated optics. In most cases, the etch rate of soda-lime glass is relatively low, about 60 Å/min. Leech et al. [7] investigated the RIE of quartz and silica-based glass in CF_4/CHF_3 plasma for application to grating patterns. It was found that the etching rate reduced strongly with an increasing percentage of non-volatile elements in the composition of the glass. It was also found that the etching rate was dependent on the square root of bias voltage and on the CHF_3/CF_4 ratio, for quartz, suprasil 2 and herasil 2. Li et al. [8] reported the deep RIE of Pyres glass in sulfur hexafluoride plasma. It was found that physical sputter-etching helps to remove nonvolatile etch products during the etching, and a novel etching technique "scoop-out etching" was proposed. Hongsingtong et al. [9] and Wada et al. [10] studied the RIE of Corning 7059 glass substrate in carbon tetrafluoride plasma and its application to fabrication of double textured TCO substrate. This ZnO/etched 7059 glass substrate showed larger haze ratio than single textured ZnO: B substrate.

4.2.2 Basics of nanoimprinting lithography

Nanoimprint lithography (NIL) is a technique that can produce nanometer scale patterns. It is a simple nanolithography process that shows low cost, high throughput and high resolution. It has enabled 25 nm feature size, 70 nm pitch, vertical and smooth sidewalls, and nearly 90°C corners [11]. It can pattern sub-25 nm structures over a large area. Some studies indicate that the ultimate resolution of NIL could be sub-10 nm. The principle of nanoimprinting is very simple. It creates patterns by mechanical deformation of imprint resist and subsequent processes. The usual NIL process includes three basic steps. The first step is the imprinting step that uses a mold to create a thickness contrast in a resist on a substrate. The second step is the pattern transfer. The third step is demolding [11].

The important elements required for NIL are a mold with predefined surface nanostructures, and a suitable resist material that can be deformed and hardened to preserve the shape of the impression [12]. The molds or stamps are normally made in silicon, dielectric materials such as silicon dioxide or silicon nitride, metals such as nickel, or polymeric materials that have a sufficient Young modulus. Polydimethylsiloxane (PDMS) is commonly used as a stamp resin in the procedure of NIL process. The widely used resist material is polymethylmethacrylate (PMMA).

Battaglia et al [13, 14] took the lead in applying ultraviolet nanoimprint lithography to enhance the light harvesting in thin-film silicon solar cells. By replicating the morphology of state-of-the-art nanotextured znic oxide front electrodes, excellent light incoupling was achieved and it results in a remarkable summed short-circuit current density of 25.9 mA/cm^2 for amorphous top cell and microcrystalline bottom cell of only 250 and 1100 nm, respectively.

Room-temperature nanoimprinting (RTNI) lithography technology has been developed to overcome critical dimensions and pattern critical dimensions and pattern placement error due to thermal expansion in the conventional nanoimprint lithography process. Igaku and Matsui et al [15, 16] proposed a RTNI technique using hydrogen silsequioxane (HSQ) instead of PMMA used in conventional NIL, and demonstrated HSQ replicated patterns with 90 nm hole diameter and 50 nm linewidth realized by room temperature replications. Therefore, this RTNI technique would blaze a way in making a scattering interface for OR-PF type substrate, because it enables a variety of high-resolution patterning on glass substrate. These patterns with periodic feature size can be regarded as diffraction grating, which can splits and diffracts light into several beams travelling in different directions.

4.3 Roughening surface of glass substrate

4.3.1 Etching glass substrate by RIE

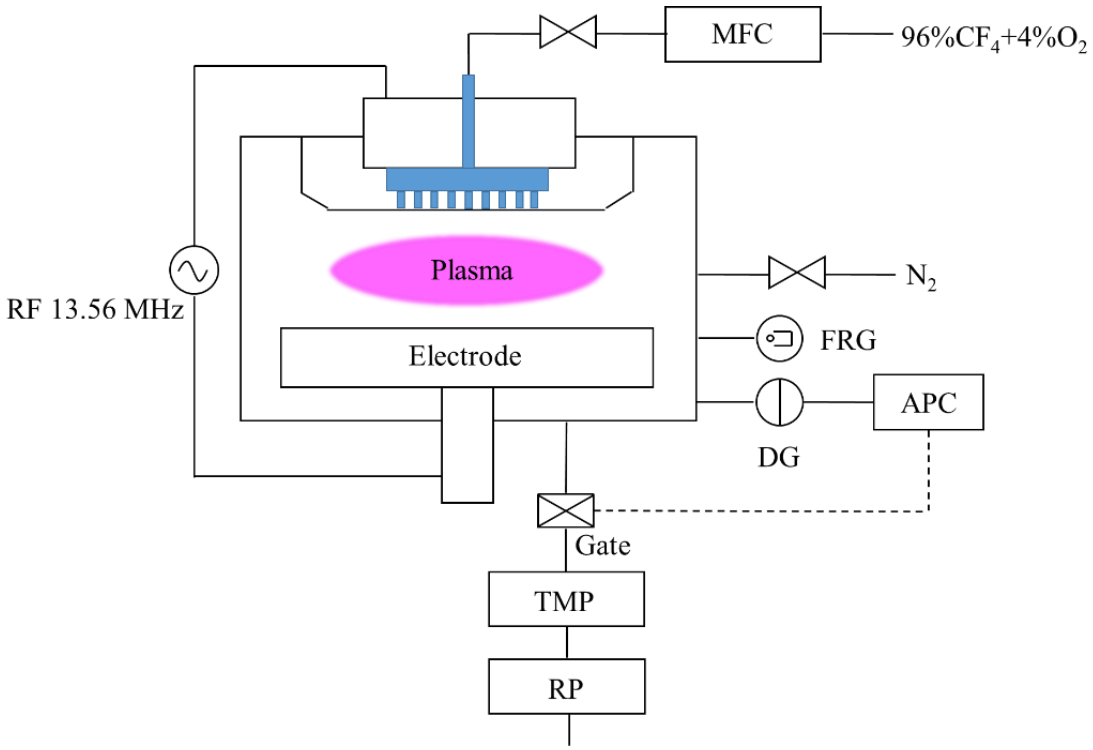

Fig 4.3 Schematics of the reactive-ion etching system (SAMCO RIE-10NR) used in this work. In the figure, MFC is mass flow controllers and APC is automatic pressure controller.

Firstly, etching glass substrate would be conducted with a RIE system (SAMCO RIE-10NR). SAMCO RIE-10NR is a high precision reactive ion etching system which can anisotropically etch a wide variety of semiconductor, insulating, and other materials. Figure 4.3 shows the schematics of cross section of the RIE system. Gas enters through small inlets in the top of the chamber, and exits to the vacuum pump system through the bottom. A mixture gas of 96% carbon tetrafluoride (CF_4) and 4% oxygen was used. It has touch screen interface. The operation can be done automatically with manual option. The radio frequency (RF) power can be tuned continuously from 0 to 300 W.

The field frequency is 13.56 MHz. The gap between electrodes is fixed at 55 mm. The upper electrode (anode) is made up of an aluminum plate with a diameter of 240 mm. The lower electrode (cathode) is an aluminum plate (240 mm diameter) with ground shield and anti-sputter quartz cover. The chamber is evacuated by a set of compound turbo molecular pump (TMP) and rotary pump (RP). The chamber pressure is measured by a full range gauge (FRG) (Purabu/Cold-cathode) and a diaphragm gauge (DG) (Capacitance manometer).The diaphragm gauge is linked to a control gate value, monitoring a deposition pressure.

The influence of etching time, RF power and pressure on the optical properties and surface morphology of glass substrates will be investigated. Two kinds of commercial glass substrates (Corning eagle XG and Corning 7059) are used to do RIE treatment.

4.3.2 Wet etching treatment

The shape of feature formed on the surface of RIE etched glass is too sharp to be used for TCO coating. Therefore, extra treatment must be done to reduce the sharpness of the feature shape after RIE etching. In this work, wet etching treatment is conducted with HCl and HF diluent after RIE etching in this work, for making a suitable surface for the subsequent TCO coating. The detailed experimental procedures of wet etching treatment is shown in Fig. 4.4. Firstly, the substrate is immersed into a 10% diluted HCl solution for 2 h. Then, the substrate is cleaned by ultrapure water for six times. After that, the substrate is immersed into 5% diluted HF solution for 40s with a slow stir. Then, the substrate is rinsed by ultrapure water. Finally, the substrate is put into a drying oven for drying. The purpose of HCl treatment is to remove the polymer formed on the surface of glass substrate, while the purpose of HF treatment is to reduce

the feature sharpness of RIE etched glass substrate.

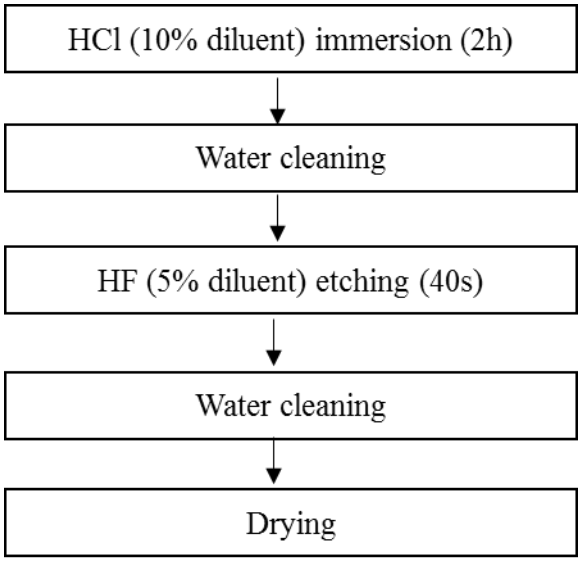

Fig. 4.4 Flow chart of wet etching treatment

4.3.3 Patterning glass substrate with room-temperature nanoimprinting

Table 4.1 Dimension of feature size on the patterns of cone, hole, and pillar.

pattern	period (μm)	height or depth (μm)	diameter (μm)
cone a	4	1.3	4
cone b	2	1.3	2
hole a	2.2	1	2
hole b	1.7	1	1.5
pillar a	2.5	2	0.5
pillar b	2	2	0.5

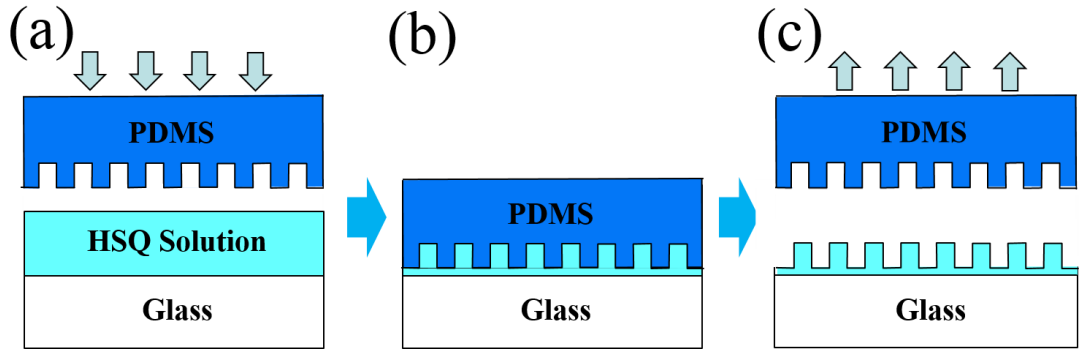

Fig. 4.5 Schematics of the room-temperature nanoimprinting process (a) imprinting (b) pressing (c) demolding.

Room-temperature nanoimprinting technique was used to form various patterns on glass substrate. Figure 4.5 shows the schematic of the process. Firstly, a liquid-phase hydrogen silsesquioxane (HSQ) solution (OCNL 103 T-2, 13000, Tokyo Ohka Kogyo Co., Ltd.) was spin-coated onto a flat glass substrate (0.7 mm thick, Corning Eagle XG). After post coating delay of 15-55 min, PDMS molds (X-32-3095, Shin-Etsu Chemical Co., Ltd.) holding different patterns were pressed onto the HSQ coated glass substrate. Four types of patterns were transferred on the glass substrate: random pyramid, periodic cone array, periodic hole array and periodic pillar array. The pattern of random pyramid was replicated from the surface morphology of undoped ZnO thin film deposited by metalorganic chemical vapor deposition. The detailed information about the dimension of feature size on the patterns of cone, hole, and pillar is listed in Table 4.1. The period (P) feature size on the substrate was changed. During the HSQ curing, a 4.3 kPa imprinting pressure was maintained for 5 min at room temperature. Then, demolding was done and pattern was replicated on the substrate. After baking on a hot plate at 80, 150, 200^{o}C in each 1 min, the patterned substrates were annealed with N_2 atmosphere at 650 ^{o}C in 30 min for hardening pattern.

4.4 Characteristics of roughened glass substrates

4.4.1 Characteristics of RIE etched corning eagle XG glass substrate

In this section, the commercial Corning Eagle XG (abbreviated as XG) glass substrate is used for RIE etching. XG glass is a borosilicate glass, which is designed for high performance LCD. It is environmentally friendly, because it contains no heavy metals (arsenic, antimony, barium, or halides). The glass shows high surface quality, excellent thermal properties, low density, and high resistance to chemicals. Table 4.2 shows the properties of XG glass. It can be found that the advantage of XG glass substrate is the high strain point of 669 ^{o}C, indicating that it can endure high temperature annealing.

Table 4.2 Properties of Corning Eagle XG glass substrate [17]

Chemical composition	55.0% SiO_2, 7.0% B_2O_3, 10.4% Al_2O_3, 21.0% CaO, and 1.0% Na_2O
Density (g/cm^3) at 20^{o}C	2.38
Strain point (^{o}C)	669
Annealing point (^{o}C)	722
Softening point (^{o}C)	971
Hardness	640 (vickers hardness)
Volume resistivity	12.9 (Ω·cm) (250^{o}C)
Transmittance (thickness 0.7 mm)	> 90% (380-2200 nm)
Refractive index	1.5119 (546.1 nm) 1.5078 (643.8 nm)

4.4.1.1 Effect of etching time

The effect of etching time on the surface morphology of etched glass substrate is investigated. The experimental condition is shown in Table 4.3. The etching time is changed from 5 min to 20 min. Figure 4.6 shows the SEM surface morphology of etched XG glass substrate with different etching time. It can be found that crater-like surface morphology is formed. The diameter of crater increases gradually with increasing etching time. However, the uniformity of crater size gets bad when the etching time is less than 10 min.

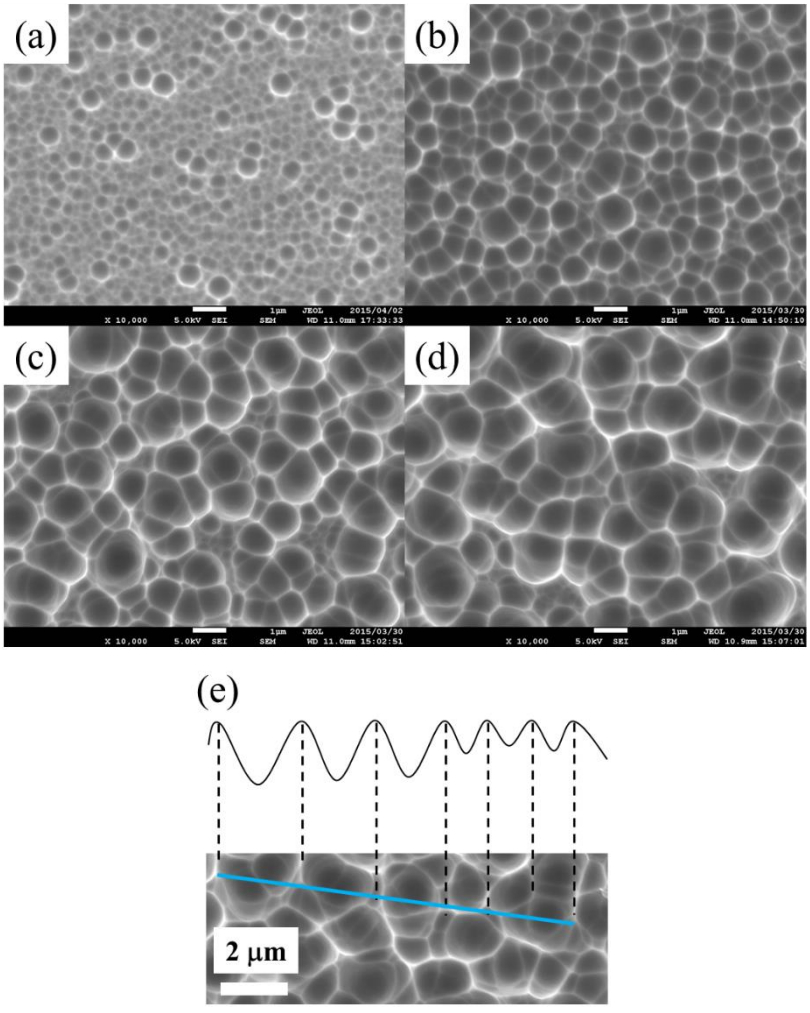

Fig 4.6 Surface morphology of etched XG glass substrate with etching time of (a) 5 min (b) 10 min (c) 15 min and (d) 20 min (e) Schematic of the cross section of etched XG glass substrate.

Table 4.3 Experimental condition of glass substrate etching with different etching time.

Pressure (Pa)	**7**
Gas	CF_4 (96%)+O_2 (4%)
Flow rate (sccm)	15
Power (W)	200
Etching time (min)	5, 10, 15 or 20

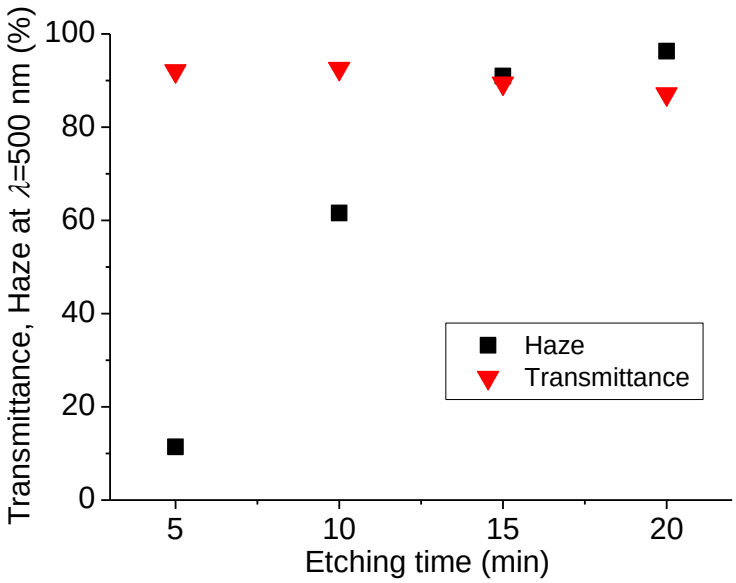

Fig. 4.7 Transmittance and haze of RIE etched XG glass substrate with different etching time.

Figure 4.7 shows the transmittance and haze ratio at λ=500 nm of glass substrate etched with different etching time. The haze ratio increases greatly with increasing etching time. At the same time, all substrates show high transmittance of over 87 %.

4.4.1.2 Effect of RF power of plasma generation

Table 4.4 Experimental condition of glass substrate etching with different RF power of plasma generation.

Pressure (Pa)	**7**
Gas	CF_4 (96%)+O_2 (4%)
Flow rate (sccm)	15
Power (W)	100, 150, 200, 250
Etching time (min)	10

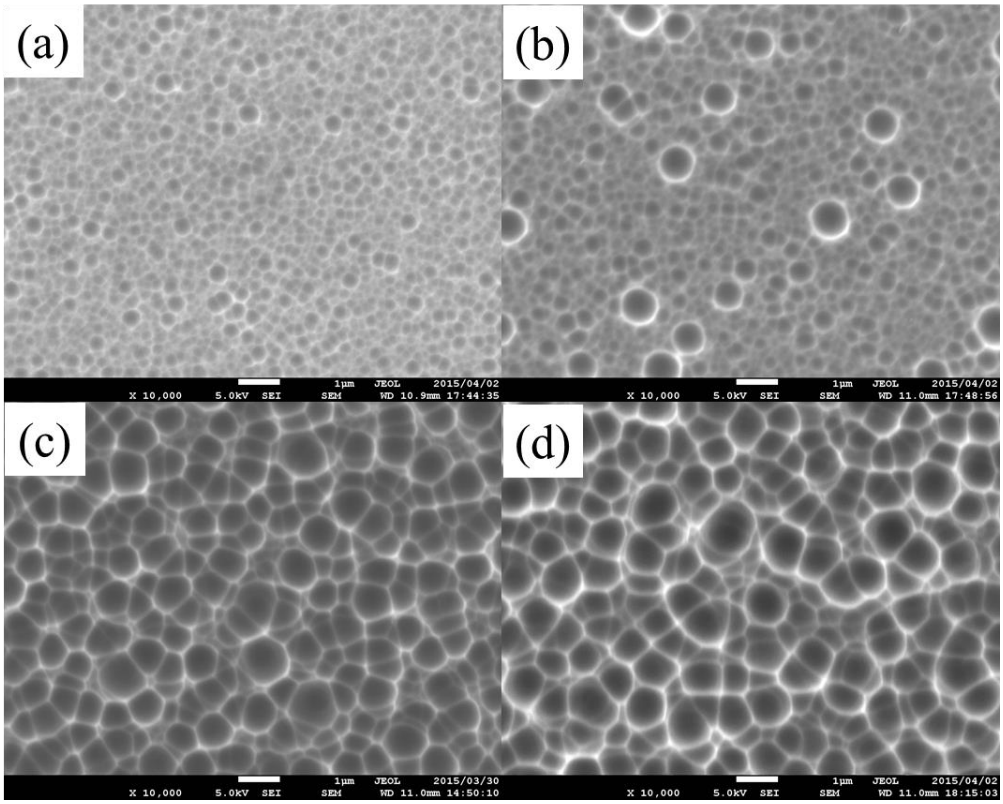

Fig 4.8 Surface morphology of XG glass substrate etched with RF power of (a) 100 W (b) 150 W (c) 200 W and (d) 250 W.

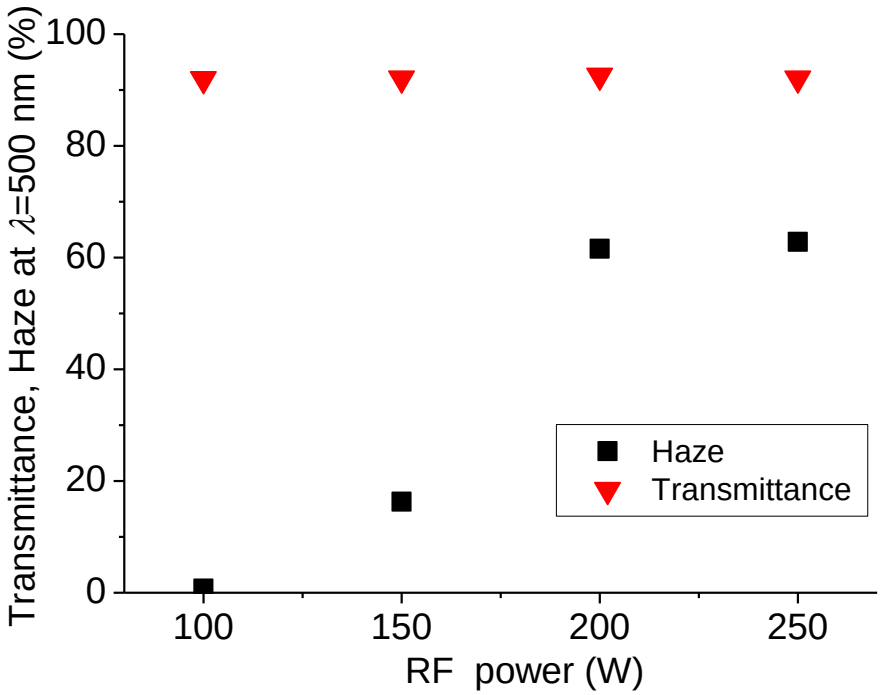

Fig. 4.9 Transmittance and haze of XG glass substrate etched with different RF power.

The effect of RF power of plasma generation on the surface morphology of etched glass substrate is investigated. The experimental condition is shown in Table 4.4. The RF power is changed from 100 W to 250 W. Figure 4.8 shows the SEM surface morphology of etched XG glass substrate with different RF power. All samples show crater-like surface morphology. The diameter of crater also increases gradually with increasing RF power. The uniformity of crater size gets bad when the RF power is 150 W. Figure 4.9 shows the transmittance and haze ratio at λ=500 nm of glass substrate etched with different RF power. The haze ratio increases greatly with increasing RF power. However, the haze ratio increase slowly when the RF power is larger than 200 W. All substrates show high transmittance of over 87 %.

4.4.1.3 Effect of pressure

Table 4.5 Experimental condition of glass substrate etching with different pressure

Pressure (Pa)	4, 7, 10 or 15
Gas	CF_4 (96%)+O_2 (4%)
Flow rate (sccm)	15
Power (W)	200
Etching time (min)	10

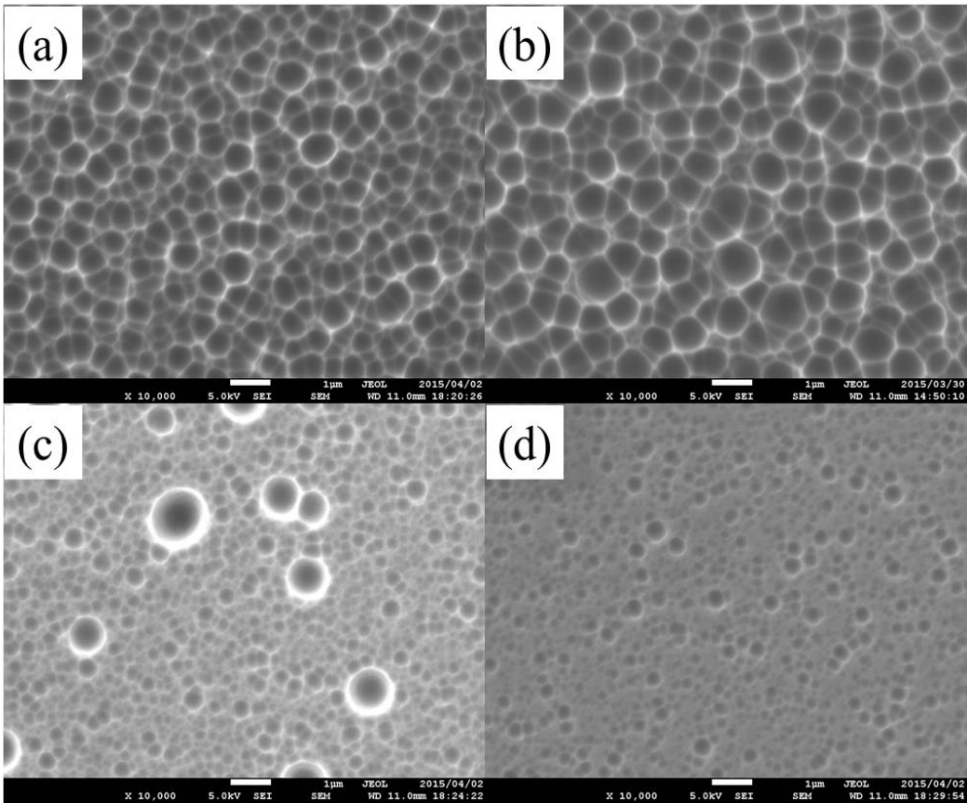

Fig 4.10 Surface morphology of XG glass substrate etched with pressure of (a) 4 Pa (b) 7 Pa (c) 10 Pa and (d) 15 Pa

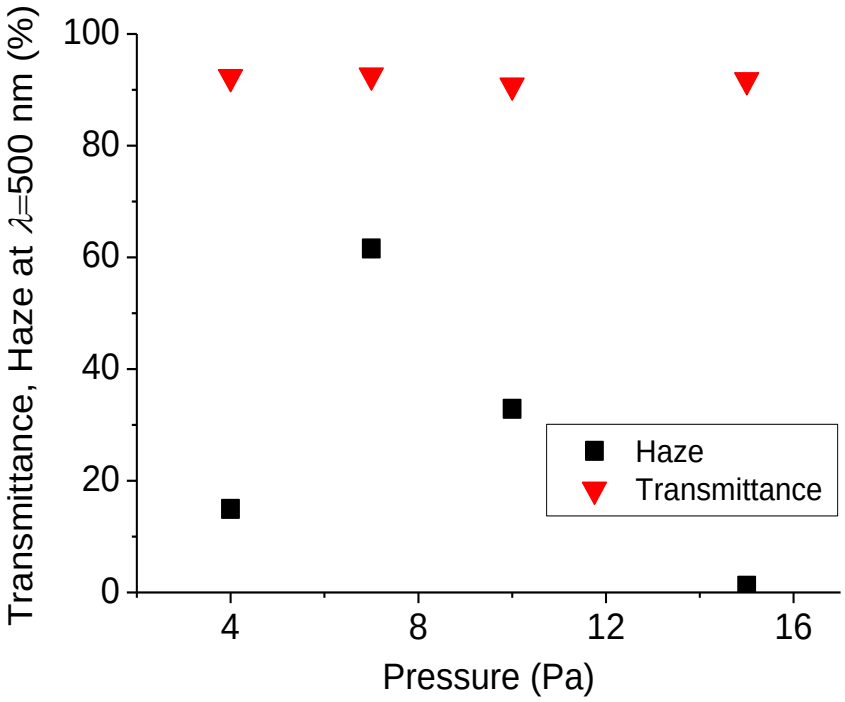

Fig. 4.11 Transmittance and haze of XG glass substrate etched with different pressure.

The effect of pressure on the surface morphology of etched glass substrate is investigated. The experimental condition is shown in Table 4.5. The pressure is changed from 4 Pa to 15 Pa. Figure 4.10 shows the SEM surface morphology of etched corning XG glass substrate with different pressure. All samples show crater-like surface morphology. With increasing pressure from 4 Pa to 7 Pa, the diameter of crater increases. However, the diameter of crater will decrease when the pressure is increased from 7 Pa to 15 Pa. In addition, the uniformity of crater size gets bad when the pressure is 10 Pa. Figure 4.11 shows the transmittance and haze ratio at λ=500 nm of etched glass substrate. The change of haze ratio with pressure shows a same tendency as that of crater diameter. The maximum haze ratio is obtained with the pressure of 7 Pa. All substrates show high transmittance of over 87 %.

4.4.1.4 Effect of wet etching treatment

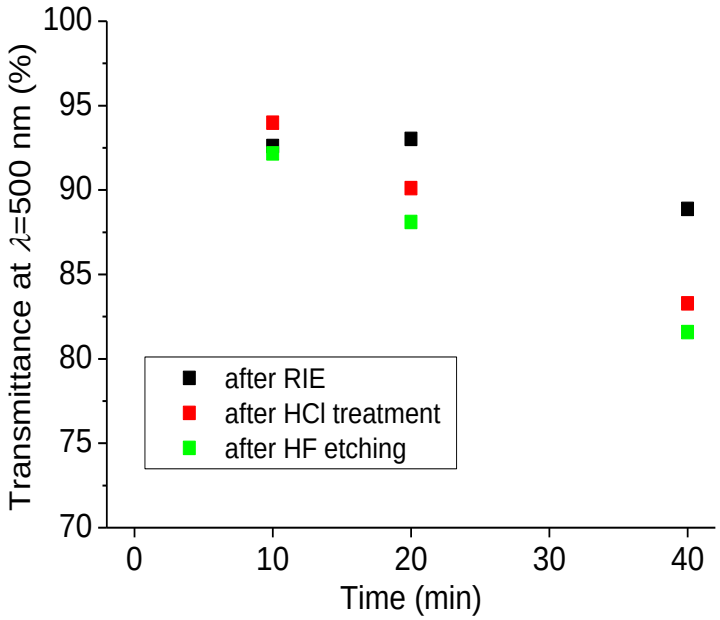

Fig. 4.12 Effect of wet etching treatment on the transmittance of RIE etched XG glass substrate.

The effect of wet etching treatment on the properties of RIE etched glass substrate is investigated. Table 4.6 exhibits the experimental condition before wet etching treatment. Figure 4.12 shows the effect of wet etching treatment on the transmittance of RIE etched XG glass substrate. It can be found that wet etching treatment would decrease the transmittance. This phenomenon gets more obvious when the RIE etching time increases. In the case of glass substrate etched with 40 min, the transmittance decreases by 6.3% after HCl treatment and decreases by 2.0% after HF etching.

Table 4.6 Experimental condition of glass substrate etching before wet etching treatment

Glass	XG
Pressure (Pa)	7
Gas	CF_4 (96%)+O_2 (4%)
Flow rate (sccm)	15
Power (W)	200
Etching time (min)	10, 20 or 40

Figure 4.13 shows the effect of wet etching treatment on the haze ratio of RIE etched glass substrate. The wet etching would increase the haze ratio a little when the glass substrate is etched with 10 and 40 min. In the case of glass substrate etched with 20 min, the haze ratio increases by 24.6% after HCl treatment and increases by 9.0 % after HF etching.

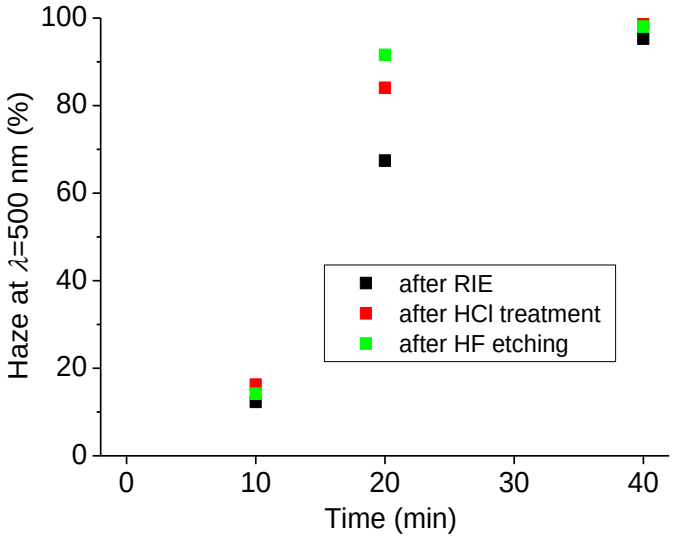

Fig. 4.13 Effect of wet etching treatment on the haze ratio of RIE etched XG glass substrate.

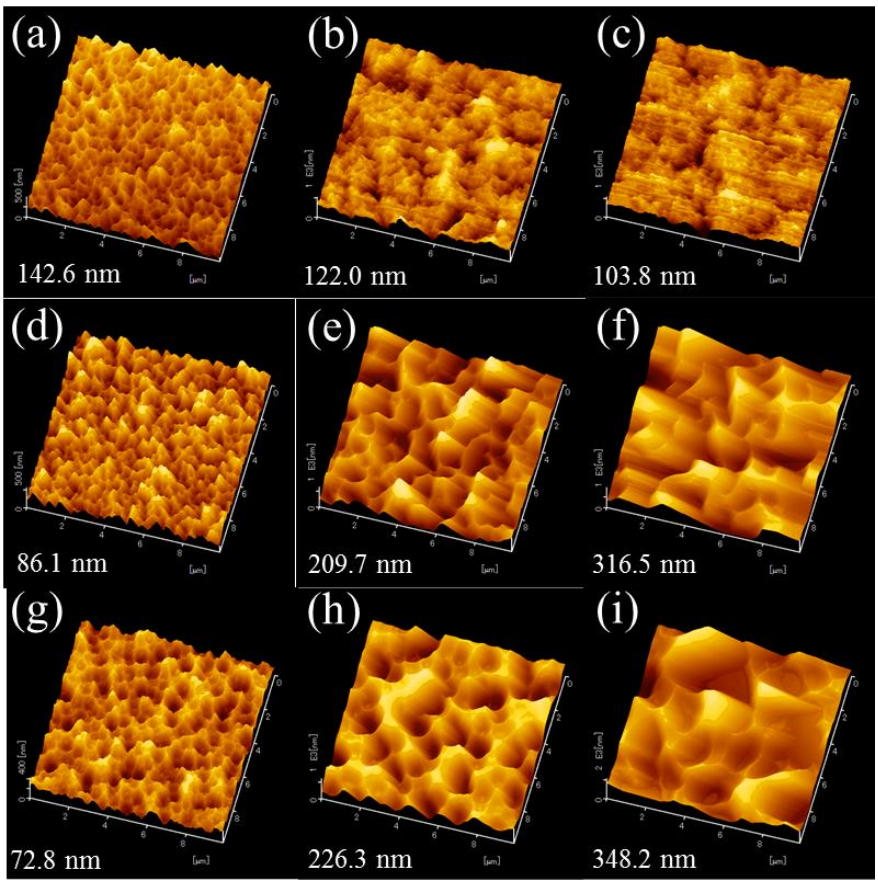

Fig. 4.14 DFM surface morphology micrograph of XG glass taken after RIE etching (RIE etching time (a) 10 min, (b) 20 min and (c) 40 min);taken after HCl treatment (RIE etching time (d) 10 min, (e) 20 min and (f) 40 min); taken after HF etching (RIE etching time (g) 10 min, (h) 20 min and (i) 40 min). The figure in each graph refers to the root-mean-square roughness.

The effect of wet etching treatment on the surface morphology micrograph of XG glass is shown in Fig. 4.14. It can be found that wet etching treatment decreased the surface roughness when the RIE etching time is 10 min, while it increased the surface roughness greatly when the RIE etching time is larger than 10 min. The gap in the surface roughness among the glass etched with different time is small before wet etching treatment. However, the gap gets very big after the wet etching treatment and the surface roughness increases obviously with increasing RIE etching time.

4.4.2 Characteristics of RIE etched corning 7059 glass substrate

Table 4.7 Properties of Corning 7059 glass substrate [18]

Chemical composition	50.2% SiO_2, 25.1% BaO, 13.0% B_2O_3, 10.7% Al_2O_3 and 0.4% As_2O_5
Density (g/cm^3) at 20°C	2.76
Strain point (°C)	593
Annealing point (°C)	639
Softening point (°C)	844
Hardness	~7 (scratch hardness)
Volume resistivity	12.9 (Ω·cm) (250°C)
Transmittance (thickness 0.7 mm)	> 90% (380-2200 nm)
Reflective index	1.5119 (546.1 nm) 1.5078 (643.8 nm)

In this section, the commercial Corning 7059 (abbreviated as 7059) glass substrate is used for RIE etching. 7059 glass is a low alkali technical sheet barium-borosilicate glass with good thermal shock resistance. This glass was originally developed for thin-film circuits of electronics industry, which require an extremely smooth substrate with special electrical properties. Further, the glass has a low level of alkali which is below 0.3%. This is very important for many electronic applications since alkali ions are known to be detrimental to performance and reliability of thin-film devices. Table 4.7 shows the properties of 7059 glass. It can be found that the hardness of 7059 glass is very small, compared to that of XG glass.

Table 4.8 Experimental condition of 7059 glass with changing etching time and pressure

Pressure (Pa)	4, 7 or 15
Gas	CF_4 (96%)+O_2 (4%)
Flow rate (sccm)	15
Power (W)	200
Etching time (min)	10, 20 or 40

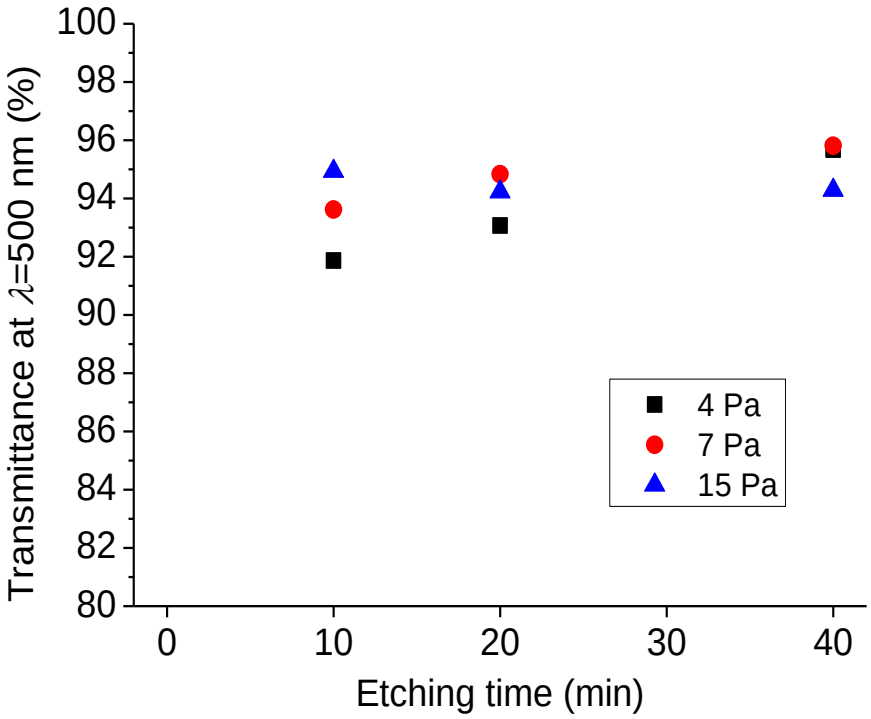

Fig. 4.15 Transmittance at λ=500 nm of 7059 glass etched with different time and pressure.

The effect of etching time and pressure on the surface morphology of etched glass substrate is investigated. The experimental condition is shown in Table 4.8. The etching time is changed from 10 min to 40 min, while the pressure is changed from 4 Pa to 15 Pa. Figure 4.15 shows the transmittance at λ=500 nm of 7059 glass etched with different time and pressure. All etched glass shows high transmittance of over 92%. When the pressure is 4 or 7 Pa, the transmittance increases gradually with increasing time. When the pressure is 15 Pa, the transmittance decreases gradually with increasing time. In addition, with the same etching time, the pressure seldom influences the transmittance.

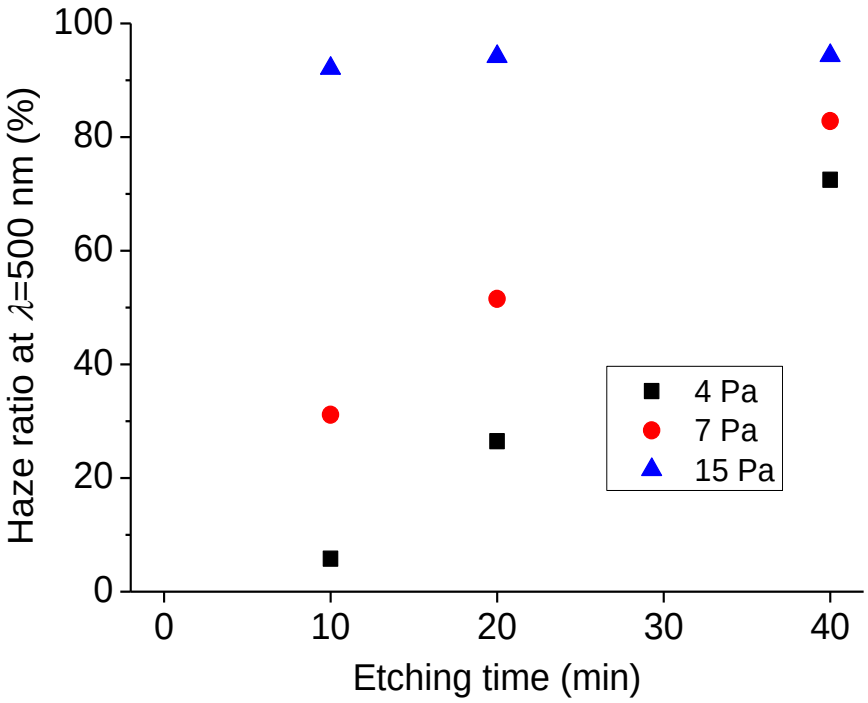

Fig. 4.16 Haze ratio at λ=500 nm of 7059 glass etched with different time and pressure.

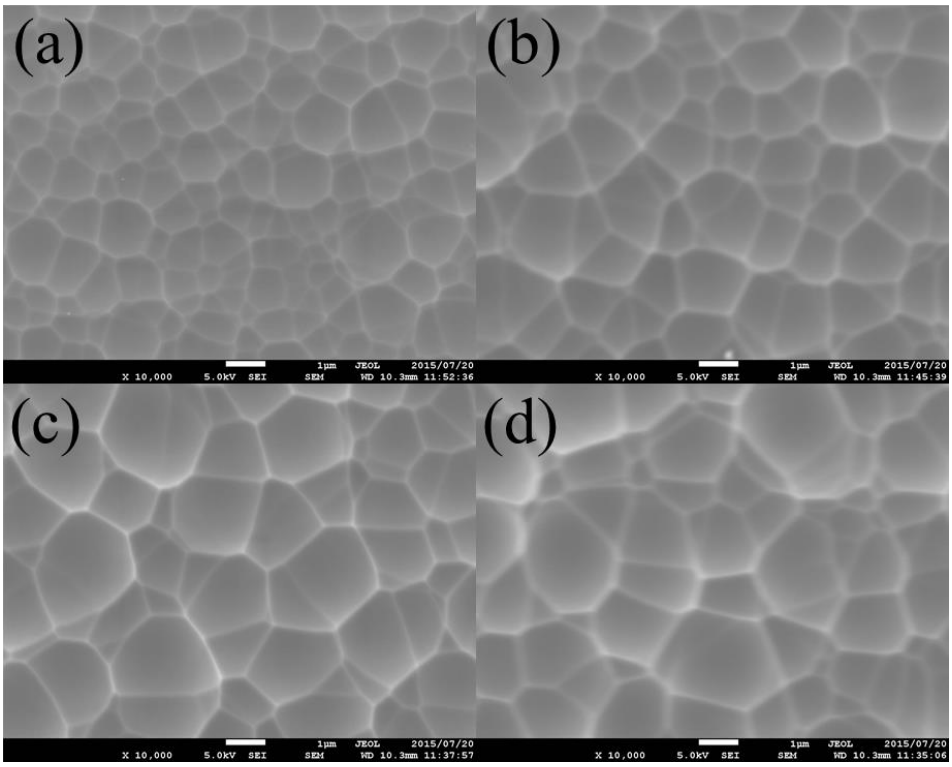

Fig. 4.17 SEM surface micrographs of 7059 glass etched with (a) 5 min (b) 10 min (c) 15 min and (d) 20 min (RF power is 250 W).

The effect of etching time and pressure on the haze ratio of 7059 glass is shown in Fig. 4.16. The haze increases greatly with increasing time when the pressure is 4 and 7 Pa, while it changes little with time when the pressure is 15 Pa. With the same etching time, haze ratio increases obviously with increasing pressure. Figure 4.17 shows the SEM surface micrographs of 7059 glass etched with different etching time. It can be found that all of the etched glasses show crater-like surface morphology. The diameter of crater increases with the etching time.

4.4.3 Characteristics of nanoimprinting patterned glass substrate

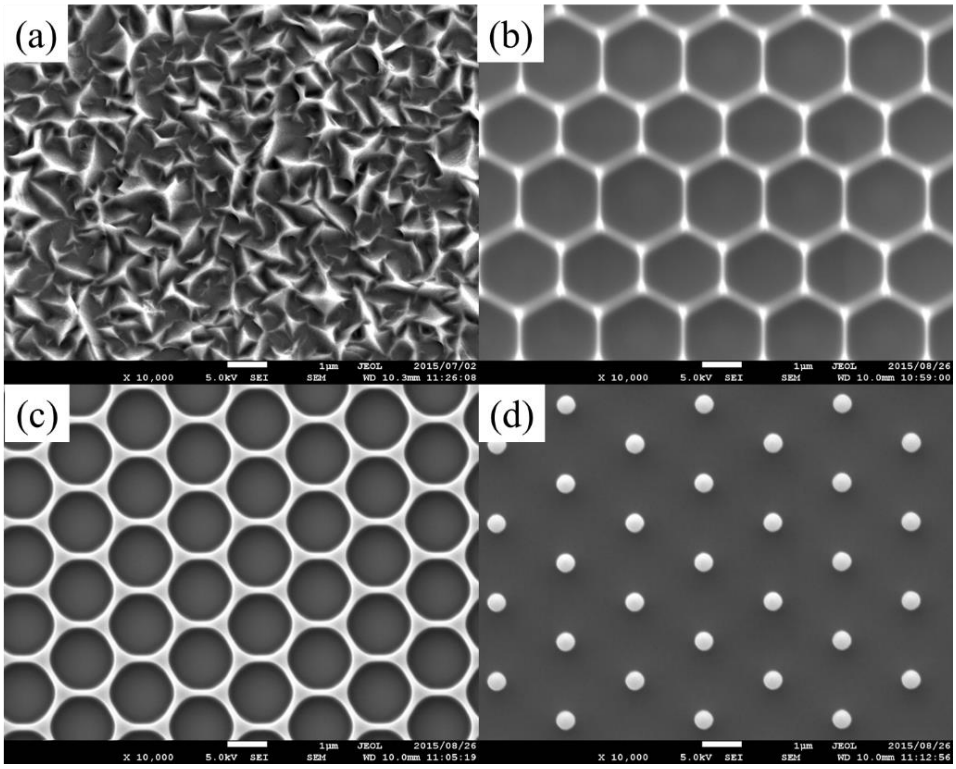

Fig. 4.18 Surface SEM micrographs of glass substrates imprinted with patterns of (a) pyramid (b) cone (P=2 μm) (c) hole (P=1.7 μm) and (d) pillar (P=2 μm).

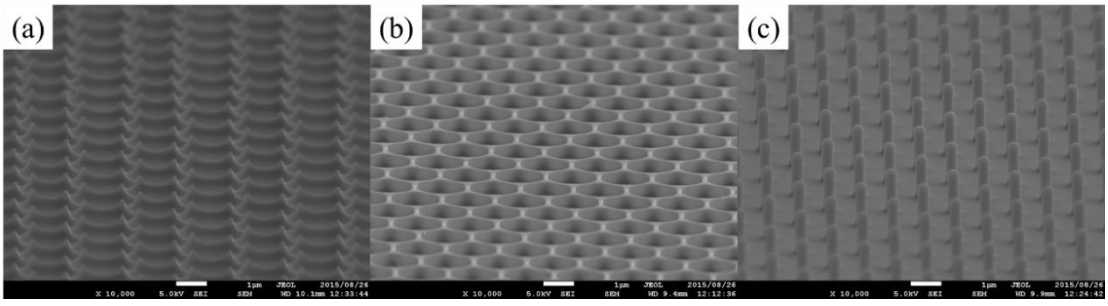

Fig. 4.19 SEM micrographs of glass substrates imprinted with patterns of (a) cone (P=2 μm) (b) hole (P=1.7 μm) and (c) pillar (P=2 μm) taken at a tilt angle of 15 degree.

Figure 4.18 shows the surface SEM micrographs of glass substrates imprinted with different patterns. Figure 4.19 shows the SEM micrographs of glass substrates

imprinted with different patterns taken at a tilt angle of 15 degree. It can be found that all of imprinting patterns are very regular and uniform. The dimensions of feature size on the substrates is almost identical with theses on the corresponding master mold.

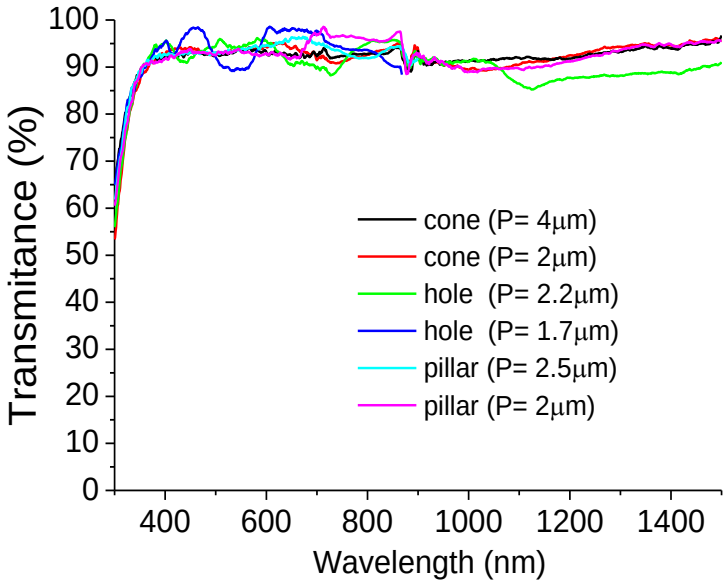

Fig. 4.20 Transmittance of imprinted glass substrate with different patterns.

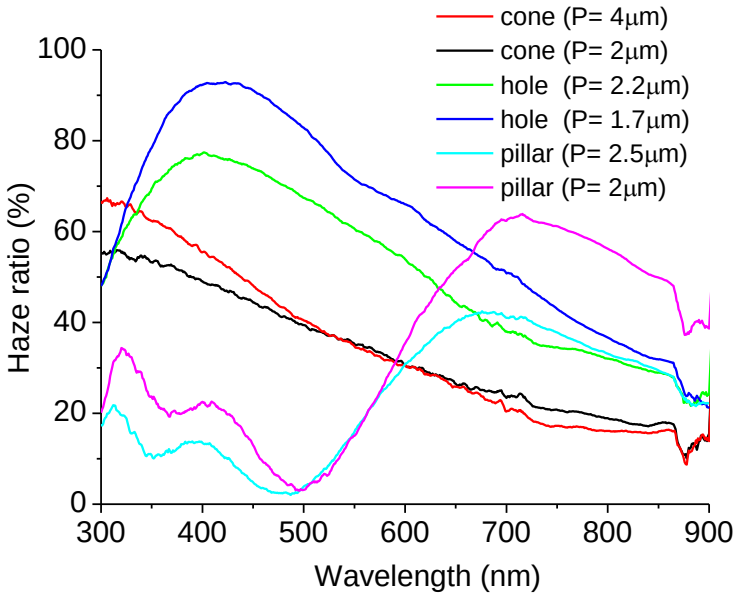

Fig. 4.21 Haze ratios of imprinted glass substrate with different patterns.

Figure 4.20 shows the transmittance of the imprinting patterned glass substrates. All of these substrates show high transmittance of over 90 %. Figure 4.21 shows the haze ratio of the imprinting patterned glass substrates. It can be found that all imprinting patterned substrates show large haze ratio. Substrates with cone pattern show an average haze ratio of about 16% at wavelength of 700-900 nm. Substrates with hole pattern show high haze ratio at broad wavelength region. Substrates with pillar pattern show low haze ratio at short wavelength, but they show large haze ratio at wavelength of larger than 500 nm. At wavelength of 700-850 nm, substrate with pillar (P=2 μm) shows the highest ratio with average values of over 40%. For substrates with cone pattern, with decreasing the period of feature size, the haze ratio increases at wavelength of 300-500 nm, while it decreases at wavelength of 700-900 nm. For substrates with hole and pillar patterns, the haze ratio increases with decreasing the period of feature size.

4.5 Characteristics of sol-gel AZMO/roughened glass substrate

In this section, we are going to coat sol-gel AZMO thin film on etched or patterned glass substrate. The electrical, optical and structural characteristics of the AZMO/etched or patterned glass substrate will be introduced. Optimum sol-gel process and moderate condition of etching or imprinting glass substrate was investigated for fabricating optically-rough and physically-flat TCO substrate.

4.5.1 Characteristics of sol-gel AZMO/RIE etched XG glass substrate

AZMO sol-gel precursor with three different solvent (2-Methoxyethanol (2-M),

ethanol (EtOH) and mixed liquor of 2-M and EtOH (50% 2-M + 50% EtOH)) was used to conduct spin-coating. The RIE etched XG glass is used as substrate. The characteristics of these AZMO/etched glass substrate would be introduced in order.

4.5.1.1 AZMO sol-gel precursor with EtOH as solvent

Firstly, EtOH was used as the solvent of sol-gel precursor. The XG glass substrate is etched with the condition used in section 4.4.1.1. Table 4.9 shows the details of sol-gel process. Fig. 4.22 exhibits the SEM surface micrographs of AZMO/ XG glass etched with different etching time. It can be found that wrinkle-like surface morphology is formed. The AZMO thin film gets discontinuous when coated on the XG glass substrate etched with time of larger than 10 min.

Table 4.9 Sol-gel process (I)

Mg/Zn ratio	0.10
Solvent	EtOH
Concentration	0.5 M
Coating times	16
1st annealing	650^{o}C $N_2$1h
2nd annealing	650^{o}C FG 5min
Film thickness	681 nm

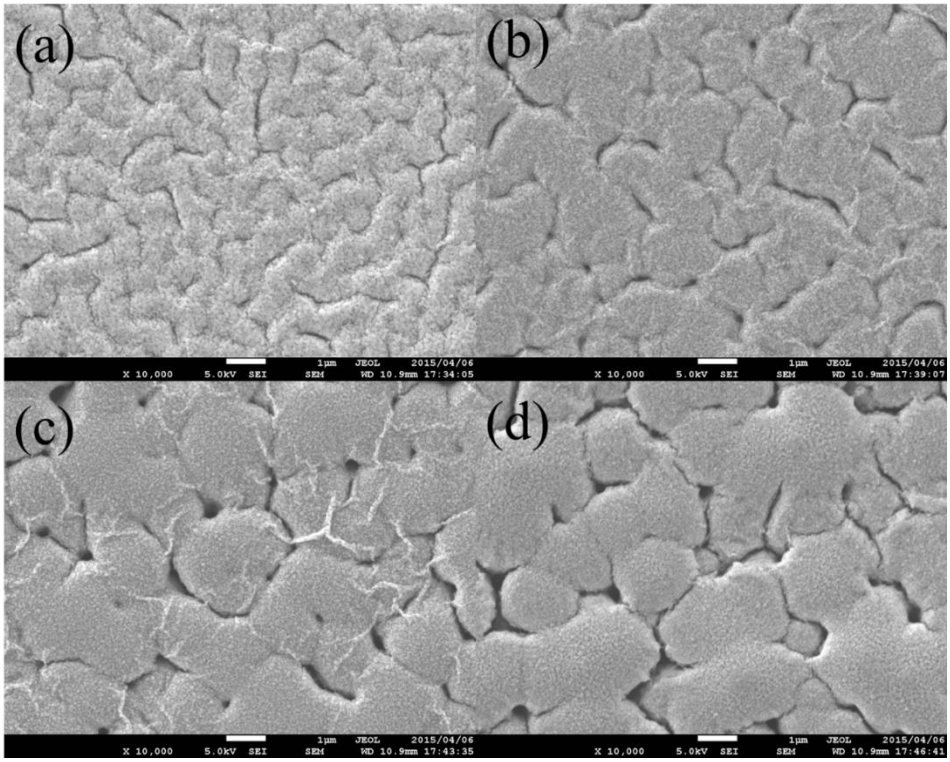

Fig. 4.22 SEM surface micrographs of AZMO (EtOH)/ XG glass etched with etching time of (a) 5 min (b) 10 min (c)15 min and (d) 20 min.

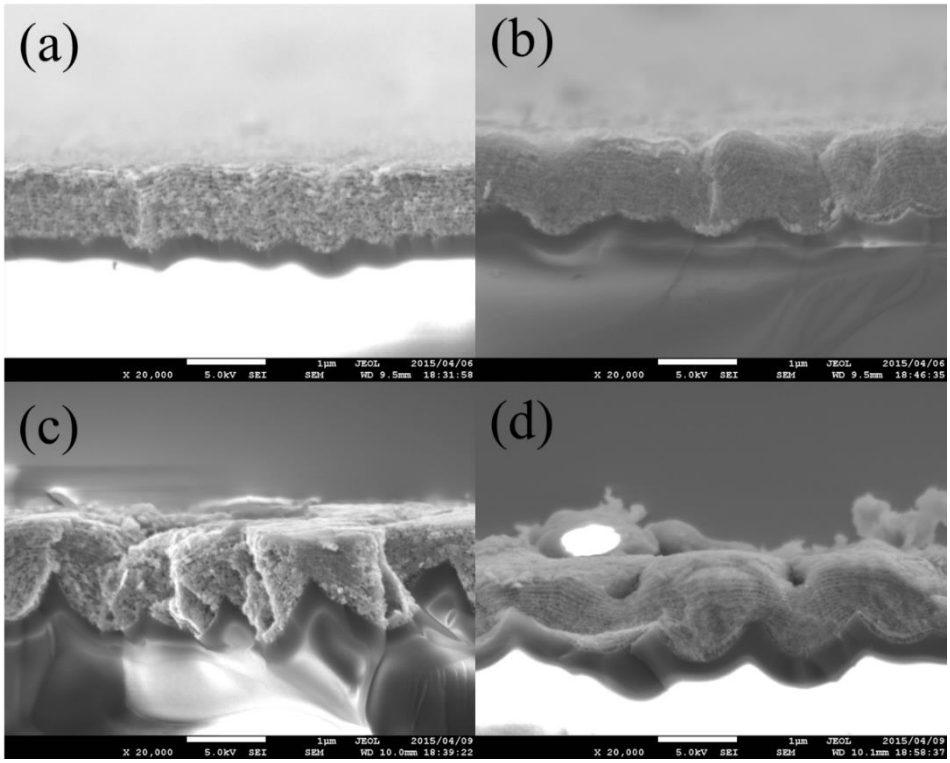

Fig. 4.23 SEM cross sectional micrographs of AZMO (EtOH)/XG glass etched with etching time of (a) 5 min (b) 10 min (c)15 min and (d) 20 min.

Figure 4.23 shows the SEM cross sectional micrographs AZMO (EtOH)/ XG glass etched with different etching time. It can be found that AZMO thin films adhere to the etched glass substrate well, but the surface is rough. The surface roughness increases obviously with increasing the roughness of etched glass substrate.

The optical, electrical and surficial properties of AZMO (EtOH)/etched XG glass is shown in Fig. 4.24. The haze ratio and surface roughness increases almost linearly with increasing etching time of XG glass substrate. All the substrates show high transmittance of over 85% at wavelength of 500 nm. In addition, all the substrates show sheet resistance of about 70 Ω/sq, regardless of the etching time of glass substrate.

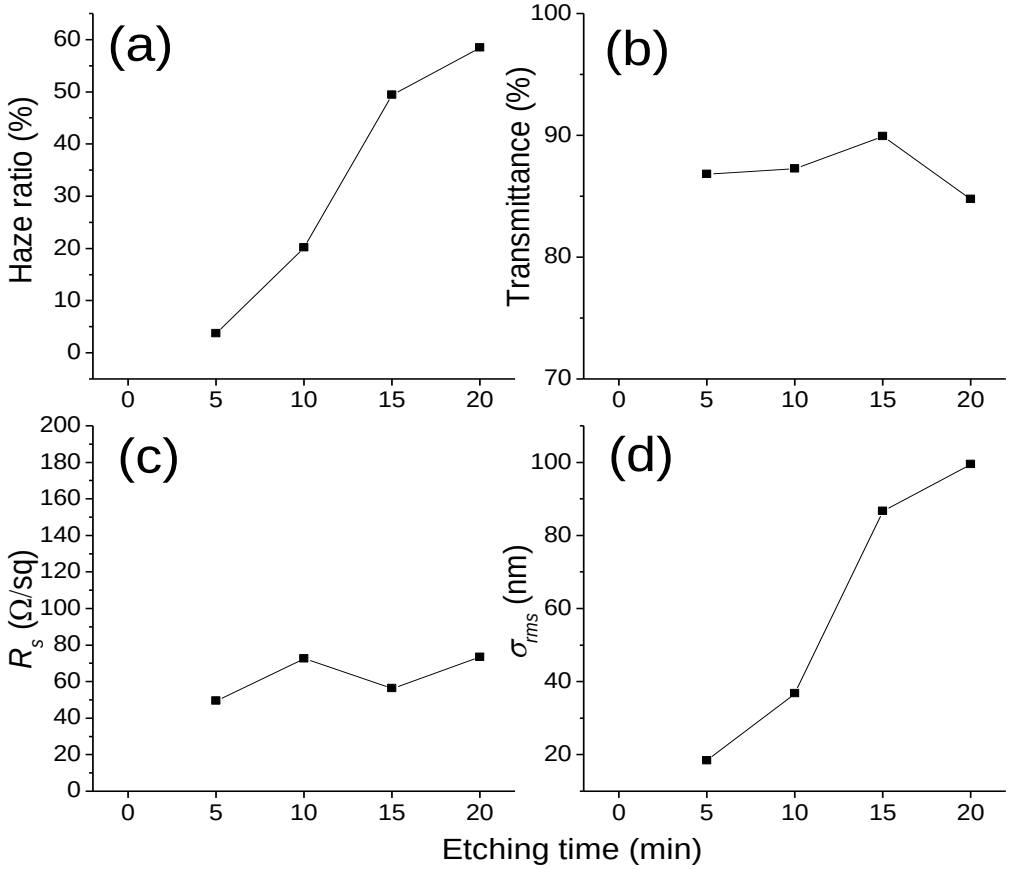

Fig. 4.24 (a) Haze ratio at λ=500 nm (b) transmittance at λ=500 nm (c) sheet resistance and (d) surface roughness of AZMO (EtOH)/XG glass etched with different etching time. The σ_{rms} refers to root-mean-square roughness.

4.5.1.2 AZMO sol-gel precursor with 2-Methoxyethanol as solvent

2-Methoxyethanol (2-M) was used as the solvent of sol-gel precursor. The XG glass substrate is etched with the condition used in section 4.4.1.1 except the RF power of plasma generation. The RF power of plasma generation is changed from 200 W to 250 W for making better uniformity. Table 4.10 shows the details of sol-gel process. Figure 4.25 exhibits the SEM surface micrographs of AZMO (2-M)/XG glass etched with different etching time. All AZMO thin films show more smooth surface morphology than that with EtOH as the solvent. However, the films still get discontinuous when coated on the etched glass substrate. Holes or channels appeared on the surface of AZMO/etched XG glass and their amounts gradually decreases with increasing the etching time of glass substrate.

Table 4.10 Sol-gel process (II)

Mg/Zn ratio	0.10
Solvent	2-M
Concentration	0.75 M
Coating times	20
1st annealing	650^{o}C $N_2$1h
2nd annealing	650^{o}C FG 5min
Film thickness	680 nm

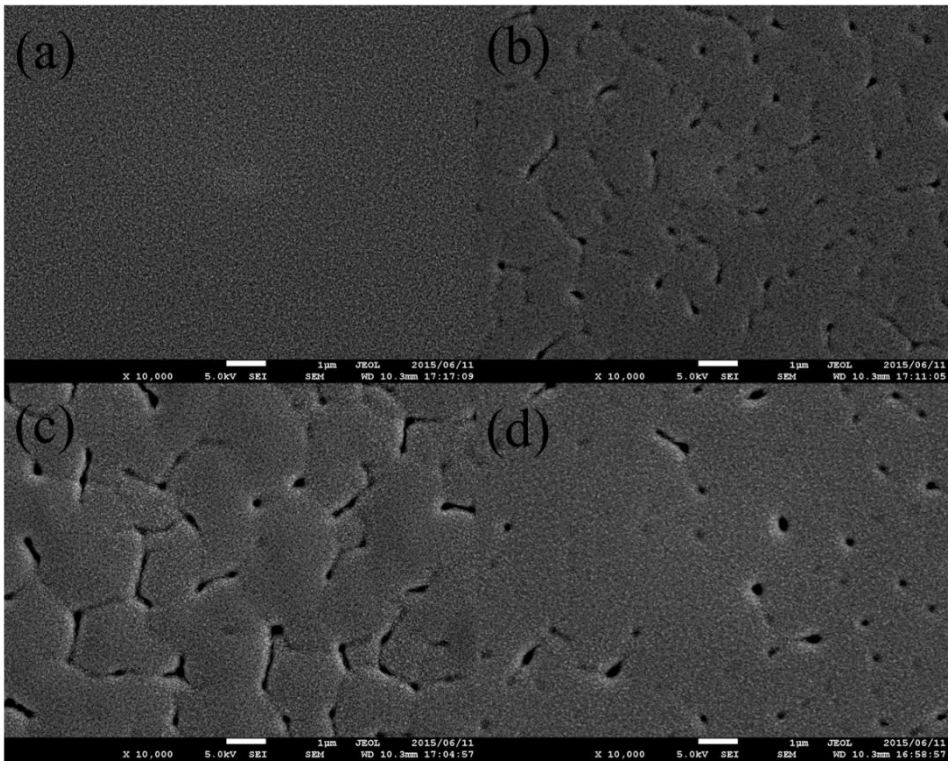

Fig. 4.25 SEM surface micrographs of AZMO (2-M)/ XG glass etched with etching time of (a) 0 min (b) 10 min (c)15 min and (d) 20 min.

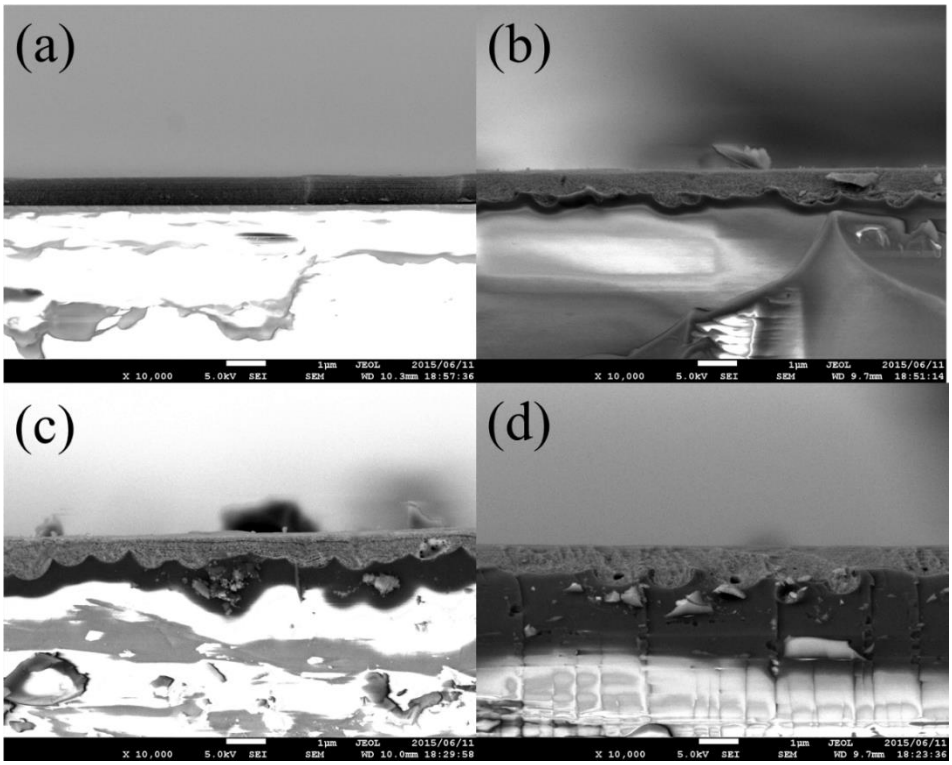

Fig. 4.26 SEM cross sectional micrographs of AZMO (2-M)/ XG glass etched with etching time of (a) 0 min (b) 10 min (c)15 min and (d) 20 min.

The SEM cross sectional micrographs of AZMO (2-M)/ XG glass etched with different etching time is shown in Fig. 4.26. All substrates show flatter surface than the AZMO (EtOH)/ etched XG glass. Furthermore, the vertical feature size of etched glass increases obviously with increasing etching time. As a result, the AZMO thin film cannot adhere well to the etched substrate with high roughness. In Fig. 4.26 (d), some holes appeared at the interface between the AZMO thin film and etched glass substrate.

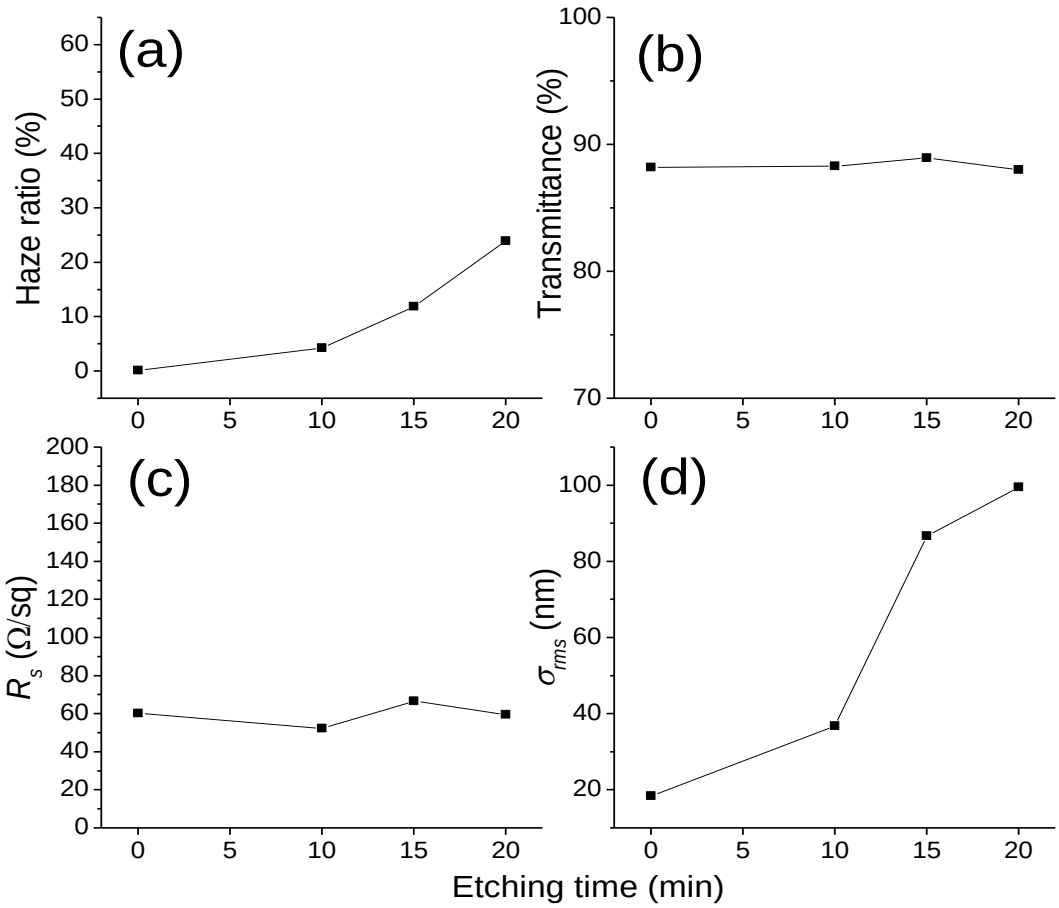

Fig. 4.27 (a) Haze ratio at λ=500 nm (b) transmittance at 500 nm (c) sheet resistance and (d) surface roughness of AZMO (EtOH)/XG glass etched with different etching time. The σ_{rms} refers to root-mean-square roughness.

The optical, electrical and surficial properties of AZMO (2-M)/etched XG glass is shown in Fig. 4.27. The haze ratio and surface roughness increases gradually with increasing etching time of XG glass substrate. However, the haze ratio get smaller than

that AZMO (EtOH)/etched XG glass with the same etching time. All the substrates show high transmittance of over 88% at wavelength of 500 nm. In addition, all the substrates show sheet resistance of about 60 Ω/sq, regardless of the etching time of glass substrate.

4.5.1.3 AZMO sol-gel precursor with 2-M and EtOH as solvent

Table 4.11 Sol-gel process (III)

Mg/Zn ratio	0.10
Solvent	50% 2-M + 50% EtOH
Concentration	0.75 M
Coating times	20
1st annealing	650^{o}C $N_2$1h
2nd annealing	650^{o}C FG 5min
Film thickness	1134 nm

The mixture of 2-M and EtOH (50% 2-M + 50% EtOH) was used as the solvent of sol-gel precursor. The XG glass substrate is etched with the condition used in section 4.4.1.1 except the RF power of plasma generation. The RF power of plasma generation is changed from 200 W to 250 W for making better uniformity. Table 4.11 shows the details of sol-gel process. Fig. 4.28 exhibits the SEM surface micrographs of AZMO (2-M + EtOH)/XG glass etched with different etching time. The AZMO thin film coated on the XG glass etched with 10 min shows wrinkle-like surface morphology. The surface of AZMO thin film coated on the XG glass etched with 15 or 20 min gets

smooth, but it is not as smooth as that with solvent of 2-M coated on the glass etched with the same time. The films still get discontinuous when coated on the etched glass substrate. Holes or channels also appeared on the surface of AZMO/etched XG glass and their amounts gradually decreases with increasing the etching time of glass substrate.

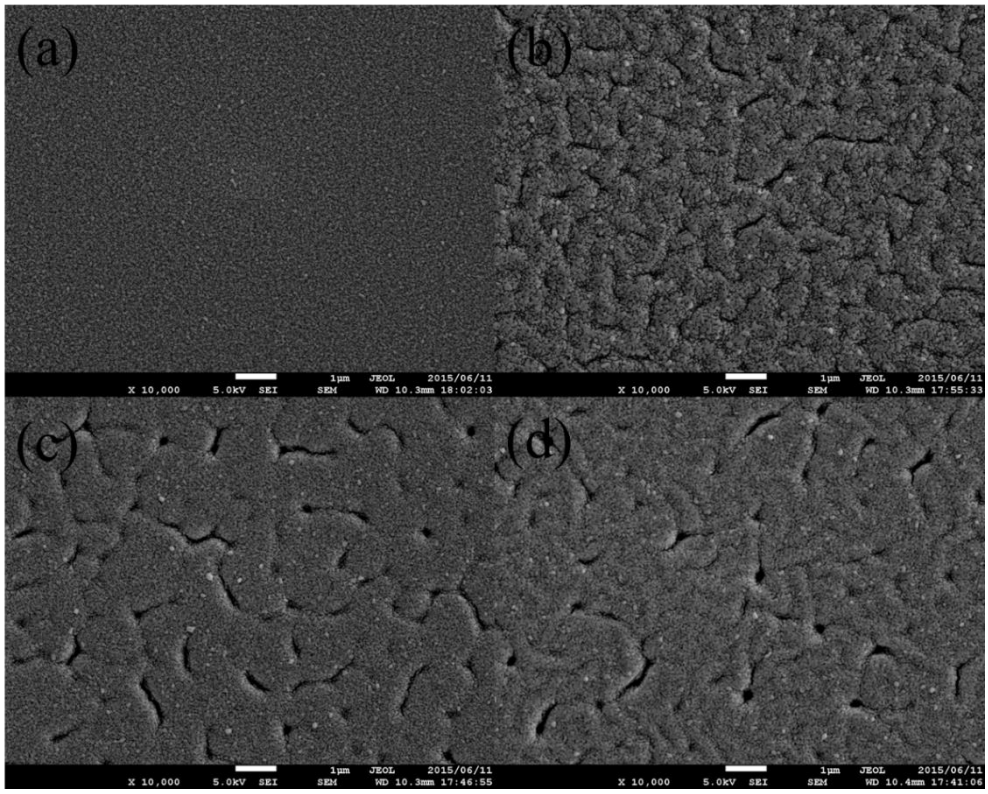

Fig. 4.28 SEM surface micrographs of AZMO (2-M + EtOH)/XG glass etched with different etching time (a) 0 min (b) 10 min (c)15 min and (d) 20 min.

The SEM cross sectional micrographs of AZMO (2-M + EtOH)/ XG glass etched with different etching time is shown in Fig. 4.29. All substrates show flatter surface than the AZMO (EtOH)/ etched XG glass, but their surface is not so flat as that of AZMO (2-M)/ etched XG glass. AZMO thin film adhere well to the etched substrate, compared to AZMO (EtOH)/ etched XG glass.

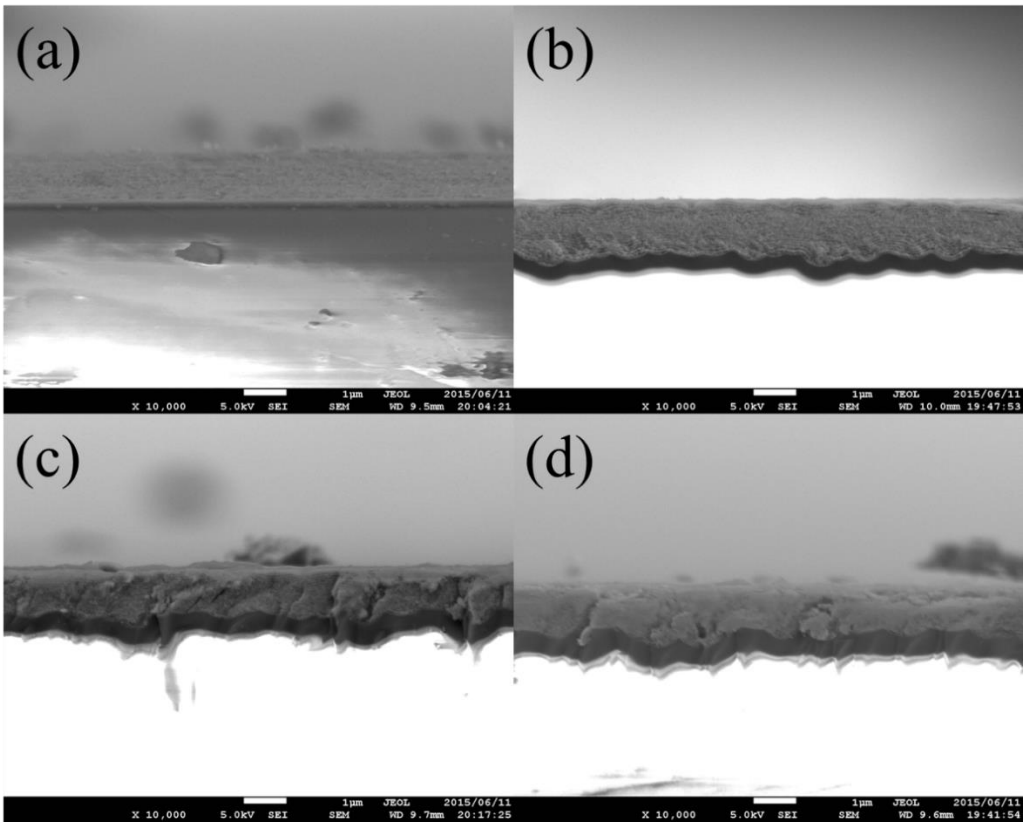

Fig. 4.29 SEM cross sectional micrographs of AZMO (2-M + EtOH)/XG glass etched with different etching time (a) 0 min (b) 10 min (c)15 min and (d) 20 min.

4.5.2 Characteristics of sol-gel AZMO/RIE etched 7059 glass substrate

AZMO sol-gel precursor with 2-M as the solvent was used to conduct spin-coating, because it can make the most smooth surface on the etched glass substrate. The RIE etched 7059 glass is used as substrate. The characteristics of AZMO/etched 7059 glass substrate will be introduced.

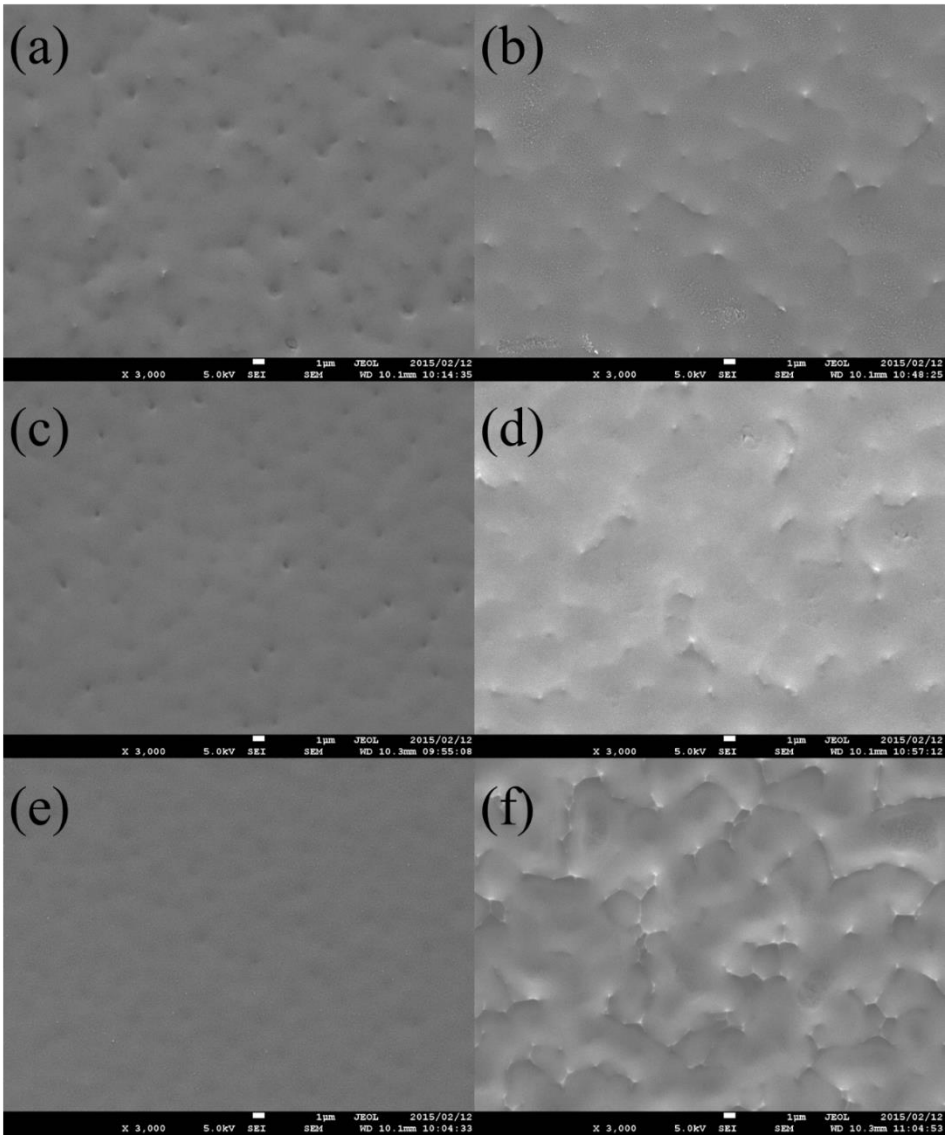

Fig. 4.30 SEM surface micrographs of AZMO / 7059 etched with (a) 7 Pa 10 min (b) 15 Pa 10 min (c) 7 Pa 20 min (d) 15 Pa 20 min (e) 7 Pa 40 min and (f) 15 Pa 40 min.

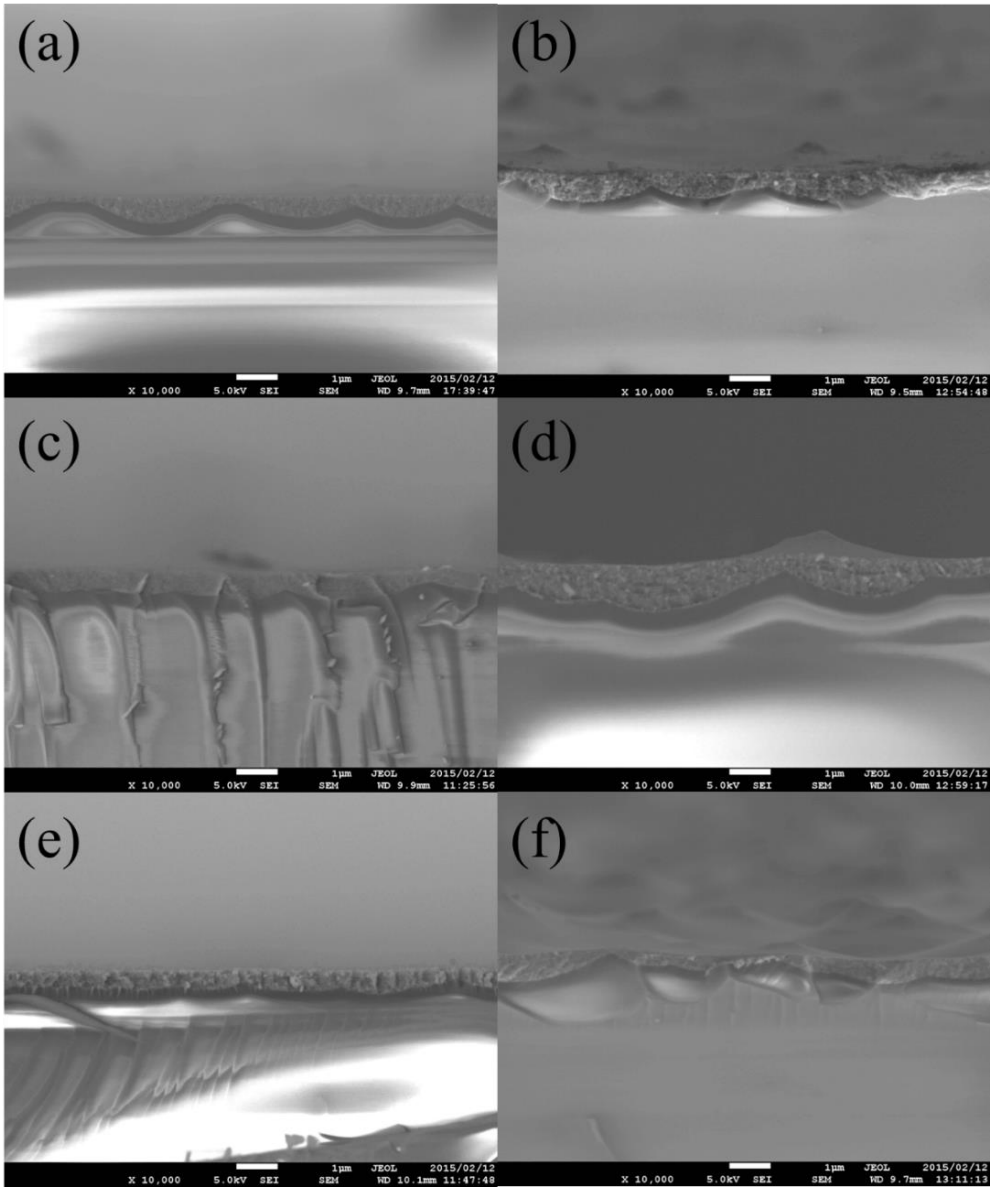

Fig. 4.31 SEM cross sectional micrographs of AZMO / 7059 etched with (a) 7 Pa 10 min (b) 15 Pa 10 min (c) 7 Pa 20 min (d) 15 Pa 20 min (e) 7 Pa 40 min and (f) 15 Pa 40 min.

The 7059 glass substrate is etched with the condition used in section 4.4.2. (the pressure is 7 Pa or 15 Pa). The coating of AZMO thin film is conducted with the condition shown in Table 4.10. Figure 4.30 shows the SEM surface micrographs of AZMO/7059 glass etched with different etching time and pressure. Continuous films are formed on all substrates, regardless of the etching time and pressure. When the pressure is 7 Pa, the surface tends to get smooth with increasing the etching time of

glass substrate. When the pressure is 15 Pa, with increasing the etching time of glass substrate, the surface roughness of substrate gets large. With the same etching time, 15 Pa would make a rougher surface roughness of substrate than 7 Pa.

The cross sectional SEM micrographs of AZMO/7059 glass etched with different etching time and pressure are shown in Fig. 4.31. It is more obvious that pressure of 7 Pa would make a flatter surface than that of 15 Pa if the etching time of glass substrate is same. In the case of 15 Pa pressure, the vertical feature increases apparently with increasing the etching time of glass substrate.

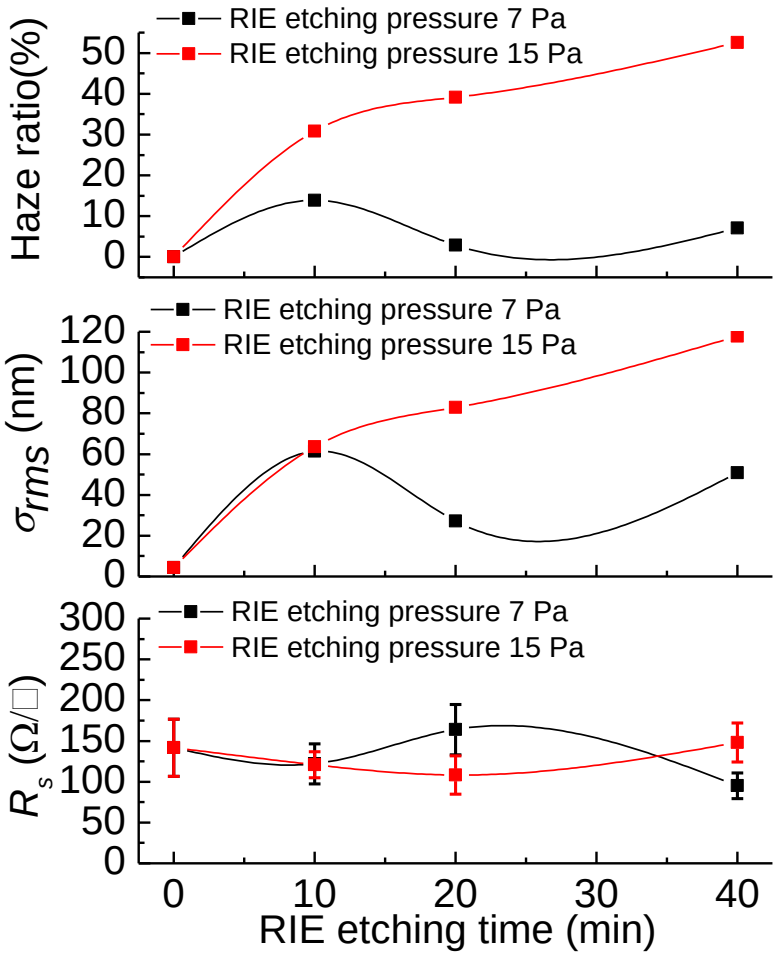

Fig. 4.32 Haze ratio at λ=500 nm, surface roughness and sheet resistance of AZMO/ 7059 glass etched with different etching time and pressure

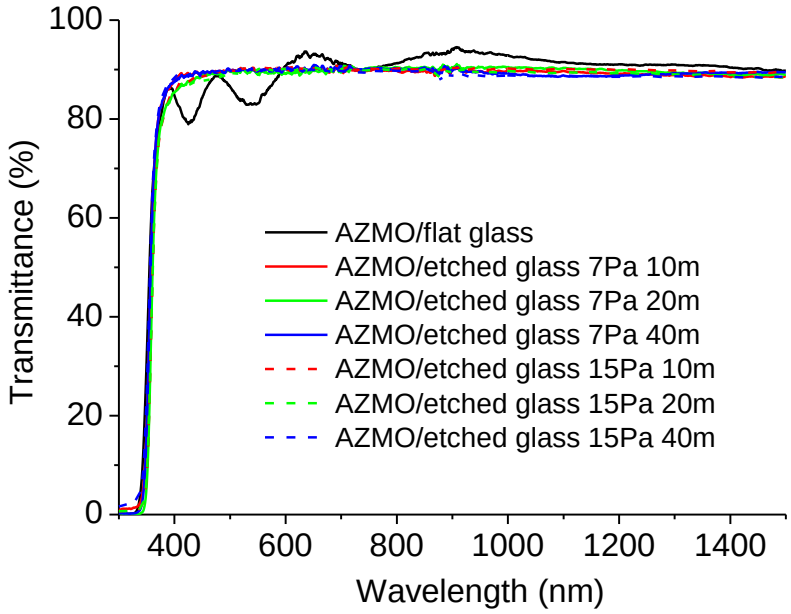

Fig. 4.33 Transmittance of AZMO/7059 glass etched with different etching time and pressure.

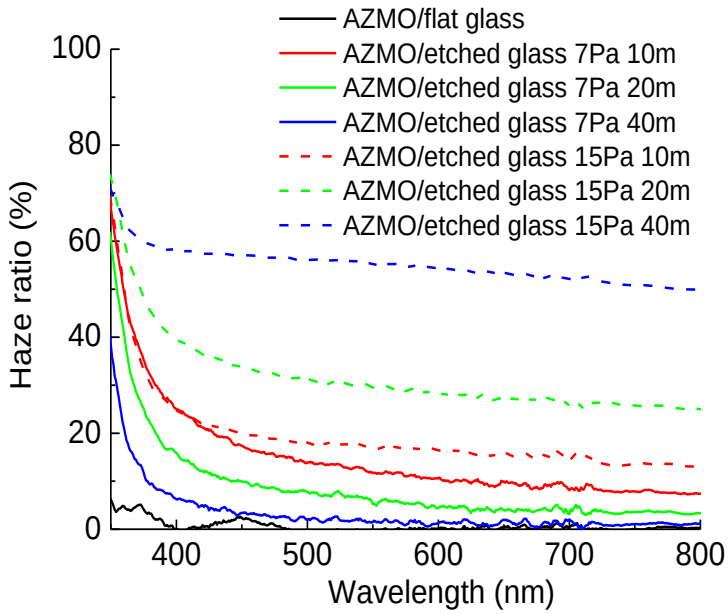

Fig. 4.34 Haze ratio of AZMO/ 7059 glass etched with different etching time and pressure.

Figure 4.32 shows the haze ratio at λ=500 nm, surface roughness and sheet resistance of AZMO/7059 glass etched with different etching time and pressure. With the same etching time, the AZMO/7059 glass etched with the pressure of 15 Pa makes

a larger haze ratio and surface roughness than that with pressure of 7 Pa. In the case of AZMO/7059 glass etched with the pressure of 15 Pa, the haze ratio and surface roughness increases gradually with increasing etching time of glass substrate. However, in the case of AZMO/7059 glass etched with the pressure of 7 Pa, the haze ratio and surface roughness get the maximum at etching time of 10 min and then decreases gradually with increasing etching time of glass substrate.

Figure 4.33 shows the transmittance of AZMO/etched glass substrate. All substrate shows high transmittance of over 85% at wavelength region from 380 nm to 1500 nm. The haze ratio at wavelength region from 350 nm to 800 nm is shown in Fig. 4.34. It clearly shows that the haze ratio of AZMO/etched 7059 glass increases apparently with increasing RIE pressure or etching time.

4.5.3 Characteristics of sol-gel AZMO/imprinting patterned glass substrate

At the beginning, AZO sol-gel precursor with 2-M as the solvent was used to conduct spin-coating. The glass substrate is imprinting patterned with the condition used in section 4.4.3. The coating of AZO thin film is conducted with the condition shown in Table 4.10 except the Mg addition.

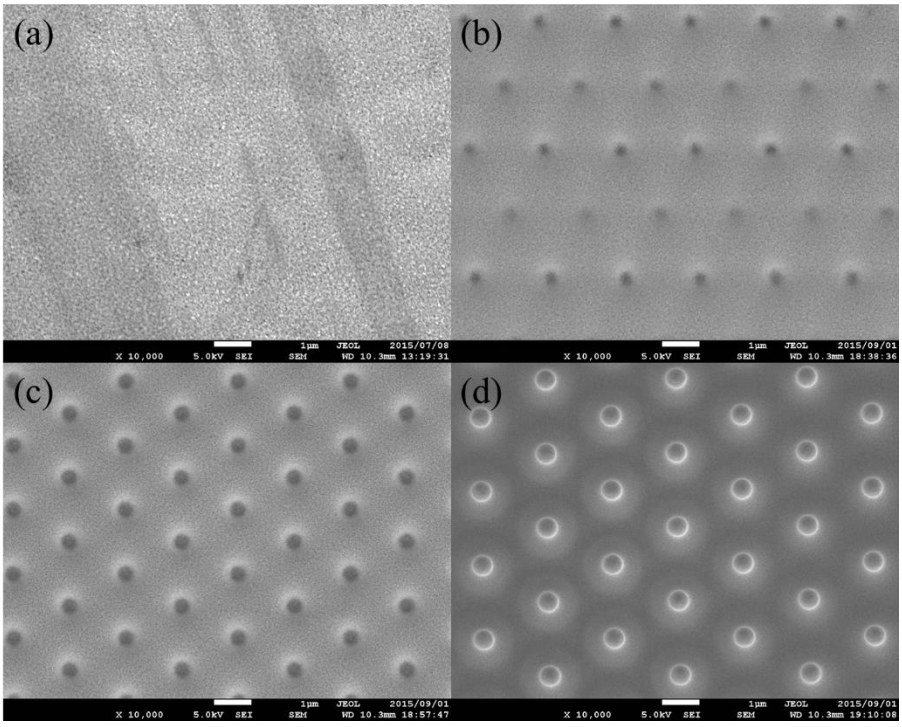

Fig. 4.35 Surface SEM micrographs of AZO/substrate imprinted with patterns of (a) pyramid (b) cone (c) hole, and (d) pillar.

Figure 4.35 shows the surface SEM micrograph of AZO/substrate imprinted with different patterns. It can be found that only the AZO/substrate imprinted with pyramid pattern shows flat surface. The AZO/substrate imprinted with cone pattern shows almost flat substrate.

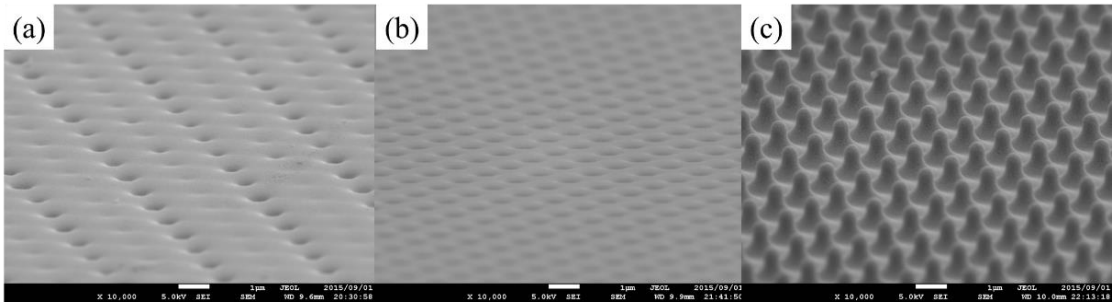

Fig. 4.36 SEM micrographs of AZO/substrate imprinted with patterns of (a) cone (P=2 μm) (b) hole (P=1.7 μm), and (c) pillar (P=2 μm) taken at a tilt angle of 15 degree.

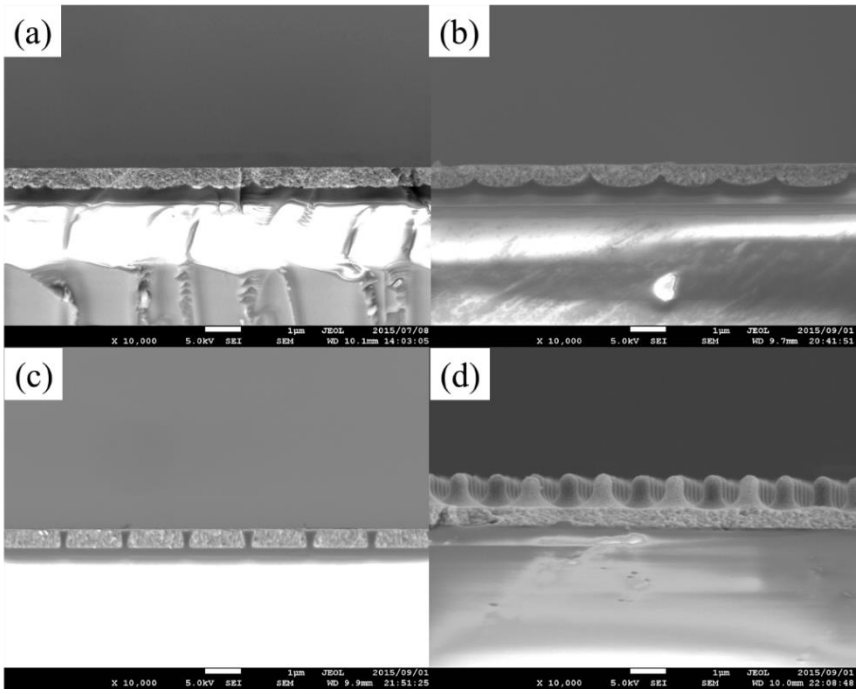

Fig. 4.37 Cross sectional SEM micrographs of AZO/substrate imprinted with patterns of (a) pyramid (b) cone (P=2 μm) (c) hole (P=1.7 μm), and (d) pillar (P=2 μm).

Figure 4.36 shows the SEM micrographs of AZO/substrate imprinted with different patterns taken at a tilt angle. It can be clearly observed that the surface of these substrate is almost flat, and the surface morphology follows the morphology of imprinting patterned substrates as shown in Fig. 4.19. The cross sectional SEM micrographs of AZO/substrate imprinted with patterns are exhibited in Fig. 4.37. From this view, AZO/substrates imprinted with pyramid, cone and hole patterns show almost

flat surface. The AZO/substrate imprinted with pillar pattern show periodic small hills on the surface.

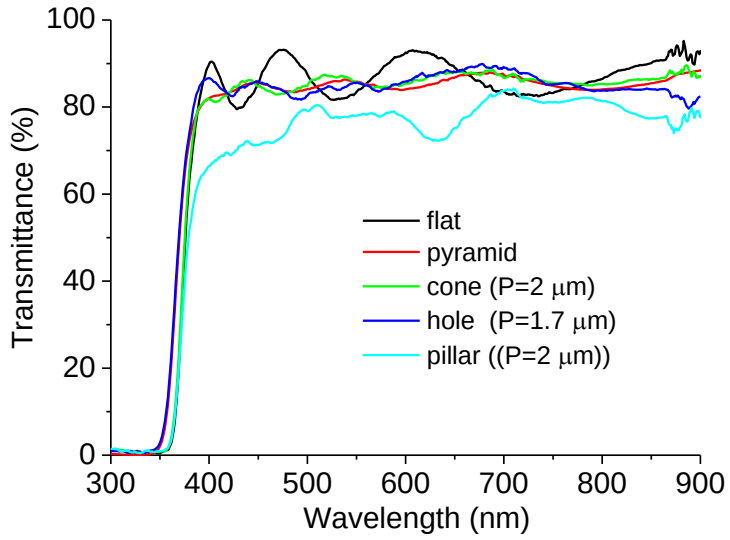

Fig. 4.38 Transmittance of AZO/substrate imprinted with different patterns.

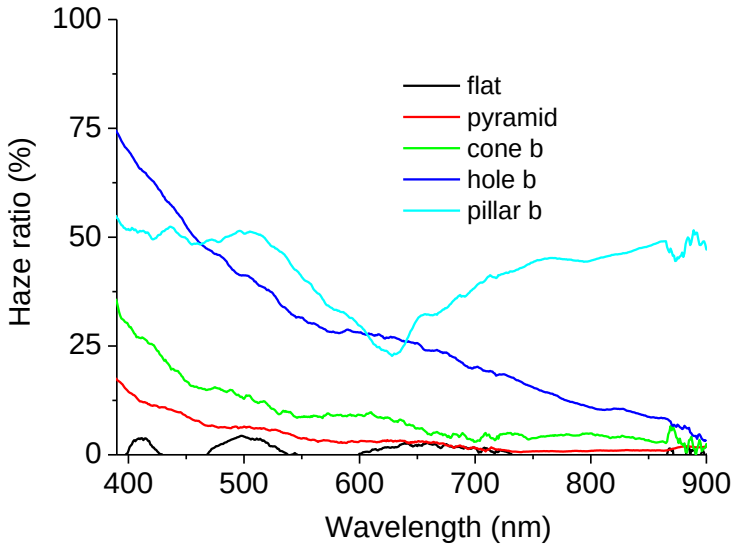

Fig. 4.39 Haze ratio of AZO/substrates imprinted with different patterns.

Figure 4.38 shows the transmittance of AZO/substrate imprinted with different patterns. All substrates except the substrate with pillar pattern show high transmittance of over 80 %. The haze ratio of AZO/substrates imprinted with different patterns is

shown in Fig. 4.39. AZO/substrates imprinted with hole and pillar patterns show high haze ratio. Interestingly, AZO/substrate with pillar pattern shows the highest haze ratio from wavelength of 650 nm and its haze ratio increases with increasing wavelength. AZO/substrate with pillar pattern shows higher haze ratio than AZO/substrate with pyramid pattern. Table 4.12 shows the properties of AZO/substrate imprinted with different patterns. All substrates show R_s of lower than 100 *Ω/sq*. The surface roughness (R_a and σ_{rms}) of substrates increases in the order of pyramid, hole (P=1.7 μm), cone (P=2 μm), and pillar (P=2 μm). At 800 nm, all substrates show high haze ratio of over 80%, and the haze ratio increases in the order of pyramid, cone (P=2 μm), hole (P=1.7 μm) and pillar (P=2 μm).

Table 4.12 Properties of AZO/substrate imprinted with different patterns.

Patterns	pyramid	cone (P=2 μm)	hole (P=1.7 μm)	Pillar (P=2 μm)
R_s (Ω/sq)	23.5	31.8	61.0	27.4
R_a (nm)	8.6	23.4	16.7	>100
σ_{rms} (nm)	10.9	34.3	21.6	>100
T at 800 nm (%)	84.1	85.4	83.8	81.4
H_T at 800 nm (%)	0.9	4.9	10.9	44.6

Note: R_a refers to the arithmetic average of absolute values of roughness. *T* refers to transmittance and H_T refers to haze ratio in transmission.

In order to reduce the surface roughness of AZMO/patterned substrates, coating of AZMO (Mg/Zn=0.10 mol. %) thin film on these patterned substrates was conducted by using 1. 25 M sol-gel precursor (20 times spin-coating), for increasing the film thickness. After two-step annealing, these AZMO/patterned substrates show sheet resistance of about 100 *Ω/sq*. Figure 4.40 shows the transmittance of AZMO/substrate

imprinted with different patterns. It can be found that all samples show high transmittance of over 75 % except the AZMO/substrate patterned with pillar pattern (P=2 μm). The AZMO/substrate patterned with cone pattern shows higher transmittance than the AZMO/etched XG glass substrate.

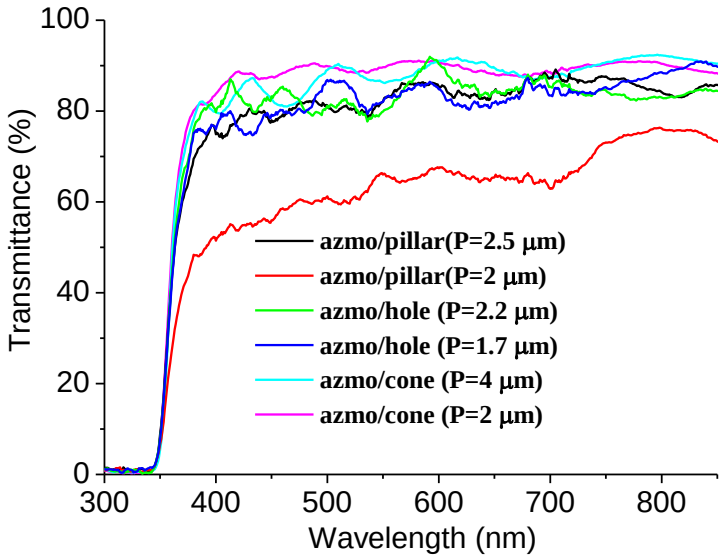

Fig. 4.40 Transmittance of AZMO/substrate imprinted with different patterns.

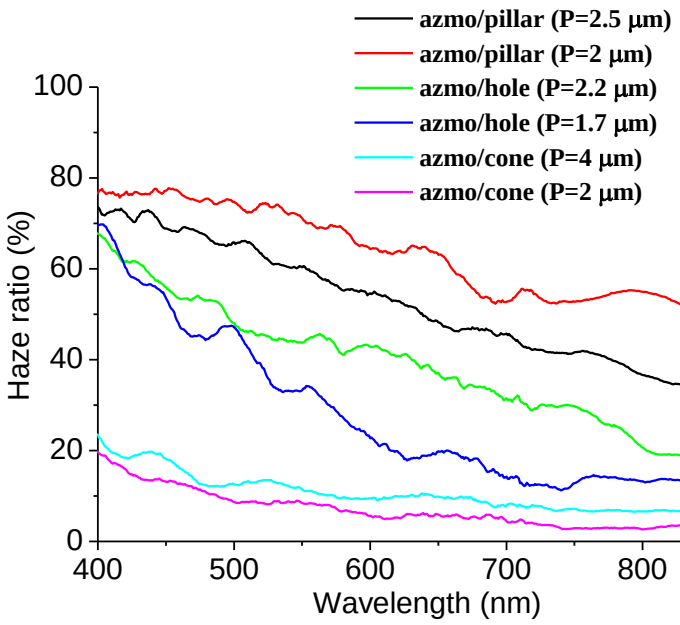

Fig. 4.41 Haze ratio of AZMO(1.25 M 20L)/substrates imprinted with different

patterns.

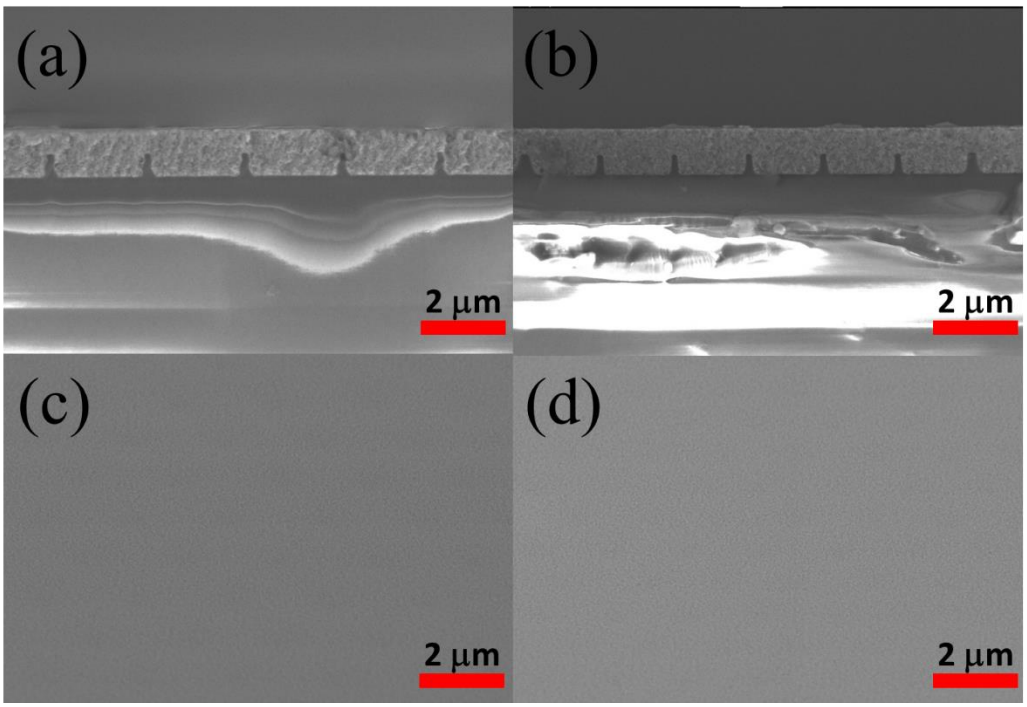

Fig. 4.42 SEM cross section micrograph of (a) AZMO(20L)/hole (P=2.2 μm) and (b) AZMO(20L)/hole (P=1.7 μm) and inclined surface (tile angle 30°) micrograph of (c) AZMO(20L)/hole (P=2.2 μm) and (d) AZMO(20L)/hole (P=1.7 μm).

The haze ratio of AZMO(1.25 M 20L)/substrates imprinted with different patterns is shown in Fig. 4.41. AZMO/patterned substrates show high H_T. The H_T is quite related to the shape and period of feature size on the pattern. The H_T increase in the order of AZMO/cone pattern, AZMO/hole pattern, and AZMO/pillar pattern. In the case of AZMO/pillar pattern, the haze ratio increases with the decrease in the period of feature size on the substrate. In the case of AZMO/hole and cone pattern, the haze ratio increases with the increase in the period of feature size on the substrate. AZMO/substrates with hole and pillar pattern show higher haze ratio than the AZMO/etched XG glass substrate. AZMO/substrate with hole pattern shows almost flat surface and becomes one very promising OR-PF substrate. AZMO/substrate with hole pattern (P=1.7 μm) shows an average H_T of 13.1 % at wavelength region of 700 nm-850 nm. This value is larger than that of the BZO (H_T =7.1 %, 1416 nm) substrate.

However, its surface roughness is still large. It indicates that adding solute concentration is not an effective method to reduce the surface roughness.

Increasing AZMO coating layer on hole patterned substrate was carried out to reduce the surface roughness. The hole pattern was selected due to the large haze ratio and achievable small surface roughness. The amount of AZMO coating layer was increased from 20 to 40. Figure 4.42 shows the cross section and inclined surface (tile angle 30^o) of AZMO/hole patterned substrates. It can be found that much flatter surface than AZMO(20L)/hole patterned substrates was obtained.

The effect of increasing coating layer on the DFM surface morphology of AZMO/hole patterns was investigated. The DFM observation confirmed that increasing coating layer from 20 L to 40 L effectively reduced the surface roughness from 21.6 nm to 4.1 nm. The AZMO(40L)/hole patterned substrate shows a similar surface roughness as the AZMO(40L)/flat glass substrate. In addition, increasing the period of feature size on the pattern increased the surface roughness a bit. The AZMO(40L)/hole(1.7 μm) patterned substrate shows a R_s of 47.0 *Ω/sq*, while the AZMO(40L)/hole(2.2 μm) patterned substrate shows a R_s of 34.3 *Ω/sq*.

The transmittance of AZMO/hole patterned substrates with different coating layers and period of feature size was measured. It was found that the AZMO substrates showed high transmittance than the conventional BZO (1416 nm) substrate. The AZMO/hole patterned substrates showed similar transmittance as the AZMO/flat glass substrate. Figure 4.43 shows the H_T in transmission of AZMO/hole patterned substrates with different coating layers and period of feature size, respectively. It can be found that increasing coating layer decreases the H_T. With 40 coating layers, increasing the period of feature size on the pattern would decrease the H_T a bit. The AZMO(40L)/hole (1.7 μm) patterned substrates show a bit larger H_T than the BZO (1416 nm) substrate at

wavelength region of 700 nm-850 nm.

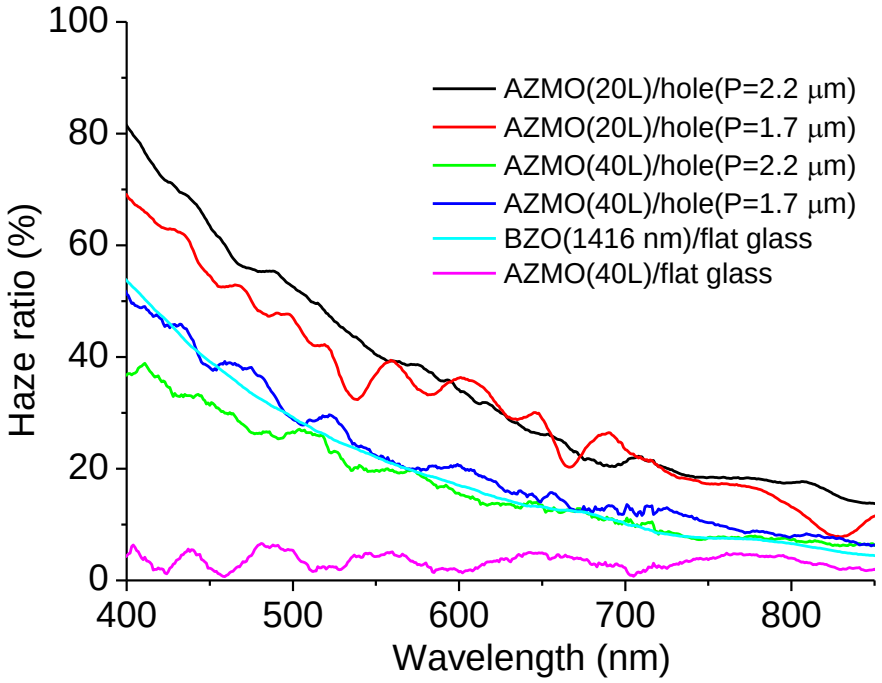

Fig. 4.43 Haze ratio in transmission of AZMO(0.75 M)/hole patterned substrates with different coating layers and period of feature size.

4.6 Summary

The fabrication of optically-rough and physically-flat TCO substrates was conducted by spin-coating sol-gel AZMO on roughened glass substrates. The glass substrates were roughened by reactive-ion etching and room nanoimprinting techniques.

In the part of RIE, RIE etching time, RF power of plasma generation, and pressure influenced the size of feature formed on the etched glass substrate greatly. All etched glass substrate showed crater-like surface morphology. The etched XG glass showed larger vertical feature than the RIE etched 7059 glass, resulting in larger haze ratio than that of latter. After the coating of AZMO thin film with the sol-gel precursor using different solvent on etched glass substrate, the 2-Methoxyethanol derived AZMO

thin film showed flat surface with small roughness on etched 7059 glass. A great amount of defect of holes and channel appeared on the surface of AZMO/RIE etched XG glass substrate due to the too large vertical feature size. In addition, in the case of RIE etched 7059 glass substrate, the surface of 7059 glass etched with pressure of 15 Pa was so rough that the surface roughness of AZMO/RIE etched 7059 glass got very large, although it showed a very large haze ratio.

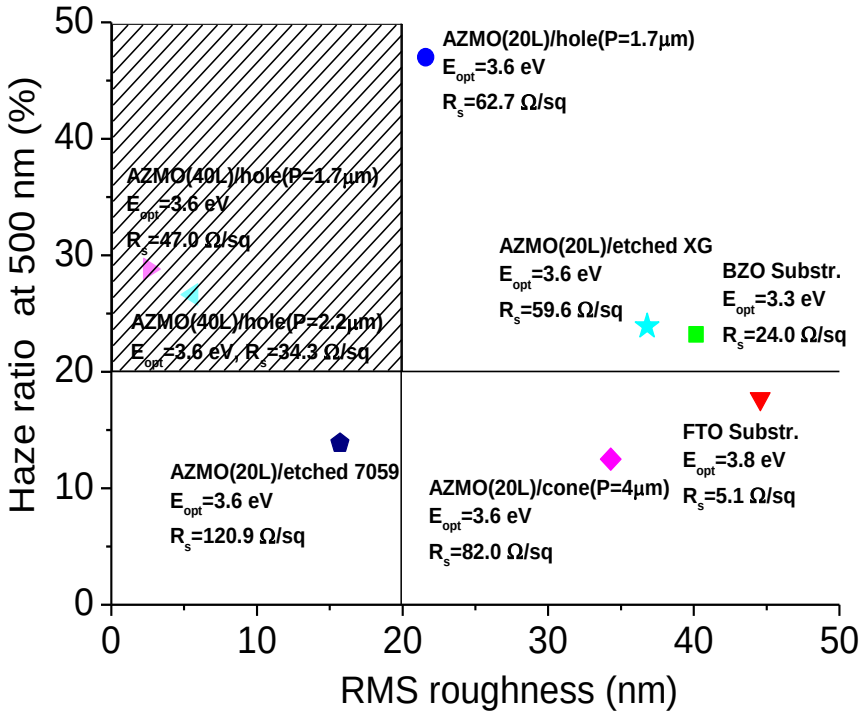

Fig. 4.44 Performance parameters of the OR-PF AZMO substrates developed in this thesis.

In the part of room-temperature nanoimprinting, a variety of periodic and uniform feature sizes were formed on the glass substrates. Substrates imprinted with hole and pillar patterns showed high haze ratio at long wavelength region, indicating good light-scattering behavior. It was attributed to the diffraction grating effect caused by the feature size on the patterned substrates. After AZMO coating, the AZMO/glass substrate patterned with hole and cone patterns showed flat surface and high haze ratio

at wavelength region of 700-850 nm.

Figure 4.44 showed the performance parameters of the OR-PF AZMO substrates developed in this thesis. The H_T at λ=500 nm was selected for comparison. All of these samples showed small RMS surface roughness and sheet resistance (R_s) of less than 100Ω/sq. An AZMO (20L)/RIE etched 7059 glass substrate (7 Pa 200W 10 min) and AZMO (20L)/cone patterned substrate showed smaller surface roughness, however, they showed lower H_T than BZO substrate. AZMO (20L)/RIE etched XG glass substrate showed a bit smaller surface roughness than BZO substrate, but its H_T was similar as BZO substrate. AZMO (20L)/hole (1.7 μm) patterned substrate showed larger haze than BZO substrate and it showed a surface roughness of about 22 nm. Only the AZMO (40L)/hole patterned substrates achieved our target values. They showed small roughness and large haze ratio simultaneously. An AZMO(0.75 M 40L Mg/Zn=10 mol. %)/substrate with hole pattern (P=1.7 μm) showed a RMS surface roughness of 2.6 nm, a R_s of 47.0 Ω/sq, and an average H_T of 9.5% at wavelength region of 700 nm-850 nm. This value of H_T was larger than BZO (1416 nm) substrate.

Reference

[1] Wikipedia, https://en.wikipedia.org/wiki/Sol-.

[2] D.J. Harrison, K. Fluri, K. Seiler, Z. Fan, C.S. Effenhauser, A. Mans, Micromachining a Miniaturized Capillary Electrophoresis-Based Chemical Analysis System on a Chip, Science 13 (1993) 895-897.

[3] D. Mikolas, R. Bojko, H.G. Craighead, F. Haas, D.A. Honey, H.F. Bare, Fabrication of aspheric high numerical aperture reflective diffractive optic elements using electron beam lithography, J. Vac. Sci. Technol. B 12 (1994) 20-26.

[4] C. Pierrat, T. Siegrist, J. deMarco, L. Harriott, S. Vaidya, Multiple-layer blank structure for phase-shifting mask fabrication, J. Vac. Sci. Technol. B 14 (1996) 63-68.

[5] S. Ronggui, G.C. Righini, Characerization of reactive ion etching of glass and its application in integrated optics, J. Vac. Sci. Technol. A 9 (1991) 2709-2712.

[6] Stainbrüchel, H. W. Lehmann, and K. Frick, J. Electrochem Soc.: Solid-State Sci. and Technol., (1985) 180-185.

[7] P.W. Leech, Reactive ion etching of quart and silica-based glasses, Vacuum 55 (1999) 191-196.

[8] X. Li, Deep reactive ion etching of Pyrex glass using SF_6 plasma, Sensors and Actuators A 87 (2001) 139-145.

[9] A. Hongsingthong, T. Krajangsang, I.A. Yunaz, S. Miyajima, M. Konagai, ZnO films with very high haze value for use as front transparent conductive oxide films in thin-film silicon solar cells, Appl. Phys. Express 3 (2010) 0511021-0511023.

[10] H. Wada, K. Nishikubo, P. Sichanugrist, M. Konagai, Improved light-trapping effect for thin-film silicon solar cells fabricated on double-textured white glass substrate, Canadian Journal of Physics 92 (2014) 920-923.

[11] S.Y. Chou, P.R. Krauss, P.J. Renstrom, Nanoimprint lithography, J. vac. Sci. Technol. B 14 (1996) 4129-4133.

[12] L.J. Guo, Nanoimprint Lithography: Methods and Material Requirements, Adv. Mater. 19 (2007) 495-513.

[13] C. Battaglia, K. Soderstrom, J. Escarre, F.J. Haug, D. Domine, Efficient light management scheme for thin film silicon solar cells via transparent random nanostructures fabricated by nanoimprinting, Appl. Phys. Lett. 96 (2010) 2135041-2135044.

[14] C. Battaglia, J. Escarre, K. Soderstrom, L. Erni, L. Ding, G. Bugnon, Nanoimprint lithography for high-efficiency thin-film silicon solar cells, Nano Lett. 11 (2011) 661-665.

[15] Y. Igaku, S. Matsui, H. Ishigaki, J. Fujita, M. Ishida, Room temperature nanoimprint technology using hydrogen silsequioxatne, Jpn. J. Appl. Phys. 41 (2002) 4198-4202.

[16] S. Matsui, Y. Igaku, H. Ishigaki, J. Fujita, M. Ishida, Y. Ochiai, H. Namatsu, M. Komuro, Room-temperature nanoimprint and nanotransfer printing using hydrogen silsequioxane, J. vac. Sci. Technol. B 21 (2003) 688-692.

[17] L. Delta Technologies, http://www.delta-technologies.com/products.asp?C=1.

[18]M.C. Gupta, T.A. Strasser, Electron-Beam-Deposited Corning 7059 Glass Thin Films For Waveguides, Proc. SPIE (1988) 44-45.

Chapter 5 Application of AZMO/glass substrate to hydrogenated amorphous silicon single junction solar cells

5.1 Introduction

In this chapter, AZMO thin film will be applied as the front transparent conductive layer in hydrogenated amorphous silicon (a-Si) single junction solar cells. Firstly, the effect of bandgap widening on the performance of a-Si solar cells will be investigated. Secondly, the development of textured $Zn_{1-x}Mg_xO$ transparent conductive layer will be conducted to improve the optical confinement of a-Si solar cells. Finally, the influence of optically-rough and physically-flat TCO substrate on the performance of a-Si solar cells will be discussed.

5.2 Fabrication process of a-Si single junction solar cells

The structure of the a-Si single junction solar cells with superstrate configuration used in this work is illustrated in Fig. 5.1. The glass substrate is flat or roughened glass substrate. The TCO thin film is mainly AZMO thin film. Boron doped ZnO (BZO) fabricated by the MOCVD method is also be used as the TCO layer for comparison. Antireflection layer is also used to reduce the optical reflection at the interface between TCO and p-a-SiC_x layer. Niobium pentoxide doped titanium or Aluminum doped ZnO fabricated by magnetron sputtering will be used as the antireflection layer. The p layer is p type silicon carbide (p-a-SiC_x:H) with an E_{opt} of

around 2.0 eV. The B_2H_6 is used as the donor impurity. The i layer is the i-a-Si:H. The n layer is n type microcrystalline silicon oxide (μc-a-SiO_x:H). The PH_3 is used as acceptor impurity. Back reflector is utilized to enhance the light absorption in the photovoltaic active layer. The BZO fabricated by MOCVD will be used as the back reflector. Ag and Al deposited by a thermal evaporation method will be used as the metal electrode. The detailed deposition process of antireflection layer, photovoltaic active layer, and back reflector will be introduced in order.

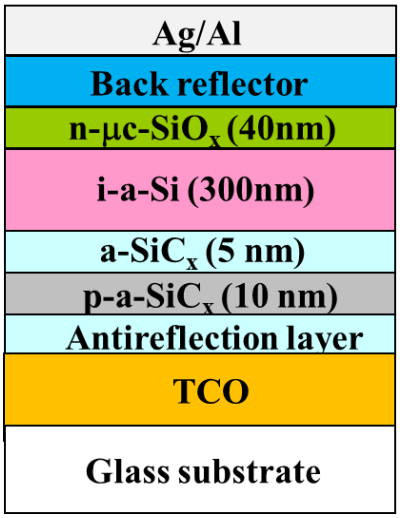

Fig. 5.1 Schematic of the cross sectional structure of a-Si single junction solar cells with superstrate configuration.

5.2.1 Deposition of antireflection layer

Niobium pentoxide doped titanium (TNO) or Aluminum doped ZnO (AZO) were deposited by radio frequency (RF) magnetron sputtering method as the antireflection layer. Figure 5.2 shows the schematic diagram of RF magnetron sputtering equipment used in this work. The TNO is deposited with target of 92 wt. % TiO_2 and 8 wt. %. The AZO is deposited with target of 99.5 wt. % ZnO and 0.5 wt. % Al_2O_3. Argon (Ar) will

be used as the gas. The gas flow rate was controlled by a mass flow controller (MFC). The chamber is evacuated by a pumping system, including a turbo molecular pump backed with an oil-sealed rotary pump. The pressure inside the chamber is around 10^{-5} Pa. The detailed deposition condition is listed in Table 5.1.

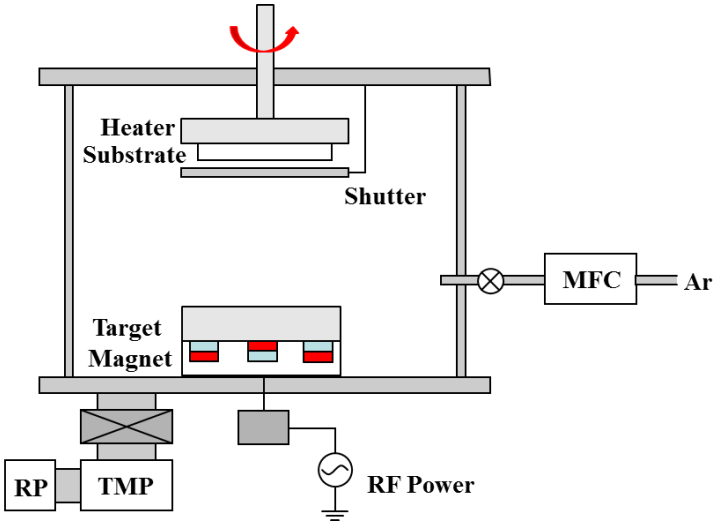

Fig 5.2 Schematic diagram of RF magnetron sputtering equipment used in this work.

Table 5.1 Deposition condition of AZO and TNO fabricated by magnetron sputtering

Target	Ar flow rate (sccm)	Pressure (Pa)	Temperature (°C)	Power (min)	Distance (nm)
AZO	10	0.4	200	100	100
TNO	10	1.0	200	90	100

Note: the distance refers to the distance between the substrate and target.

5.2.2 Deposition of photovoltaic active layer

The p-i-n a-Si single junction solar cells with superstrate configuration was fabricated by plasma enhanced chemical vapor deposition (PECVD) method. The

deposition equipment is a multi-chamber system as shown in Fig. 5.3. As shown in the figure, the equipment consists of four chambers, including a load lock chamber for loading sample, p-i-n chamber with VHF-PECVD (60 MHz) for depositing individual layer and a robot arm for transferring sample among these chambers.

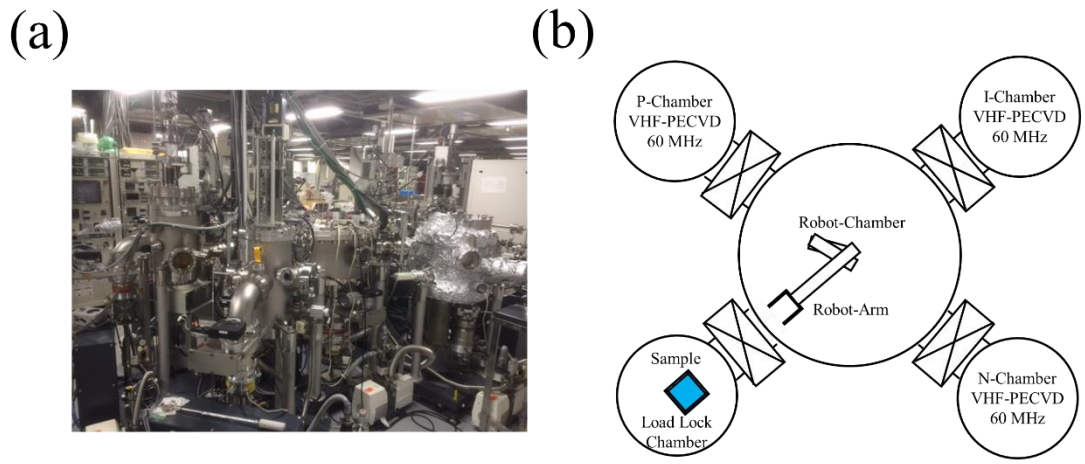

Fig. 5.3 Multi-chamber system for solar cell fabrication. (a) photograph (b) top view schematic diagram.

Figure 5.4 shows the schematic diagram of cross-section of VHF PECVD chamber used in this study. The chamber consists of two parallel-located electrodes, heater, a pumping system, pressure controller and VHF power supply. The substrate is attached to a ground and is heated by a heater. The substrate temperature of heater is monitored by using a thermocouple. The substrate is held on the upper electrode with surface downward. The silicon thin films will be deposited on the surface of substrate. The distance between two electrodes is adjustable. The chamber is evacuated by a pumping system, including a turbo molecular pump backed with an oil-sealed rotary pump, and the exhaust gases are properly treated by a gas scrubber. The pressure inside the chamber is around 10^{-6} Pa. The chamber pressure is measured by a Pirani gauge and

a diaphragm pressure gauge. The diaphragm pressure gauge is linked to a control gate value, monitoring a deposition pressure. During deposition, the gas flow rates of each chamber were controlled by a mass flow controller (MFC).

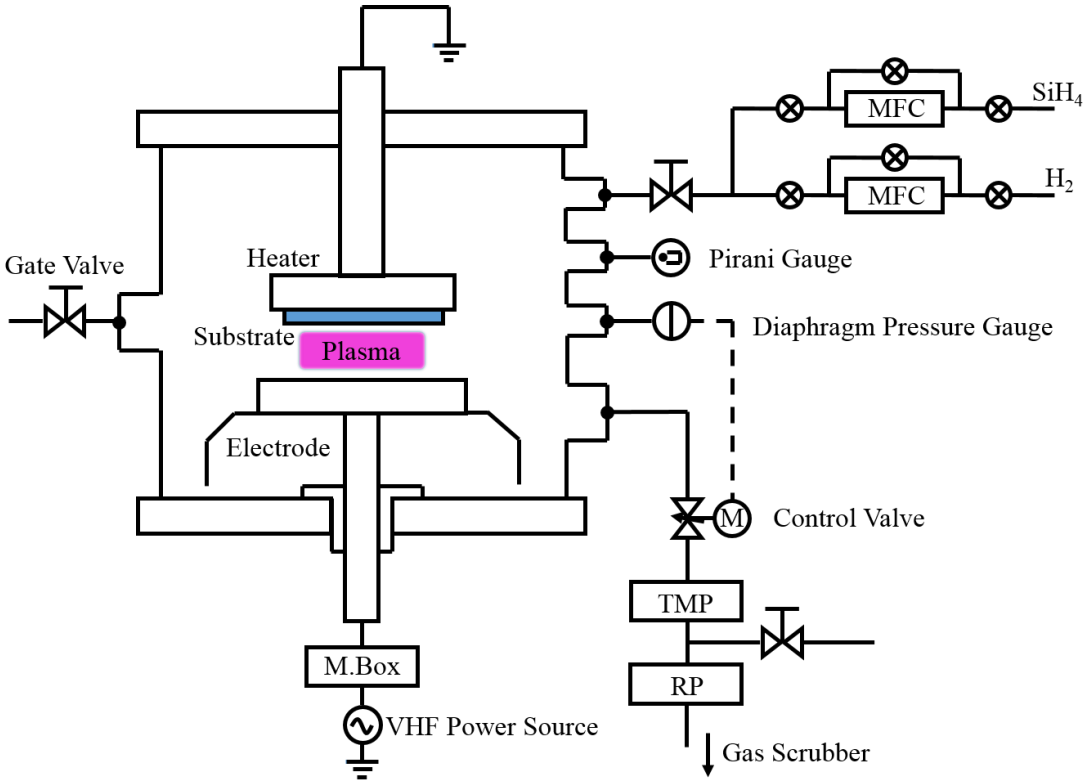

Fig. 5.4 Schematics of cross-section of VHF PECVD equipment used in this study.

As source gases, SiH_4, H_2, B_2H_6 (1% in H_2), PH_3 (1% in H_2), SiH_3CH_3 (MMS), CO_2 were used. The detailed deposition condition of each layer is shown in Table 5.2. Current density versus voltage (*J-V*) characteristics of solar cells were measured under 1-sun (AM 1.5, 100mV/cm^2). Quantum efficiency (*QE*) was measured under monochromatic light with constant photon numbers of 1×10^{14} s^{-1} at the wavelength range of 300-800 nm. *J-V* characteristics and *QE* measurement were carried out using a mask with an illumination area of 0.078 cm^2.

Table 5.2 Deposition conditions used for the fabrication of p-i-n a-Si solar cell.

Layer	Gas flow rate (sccm)						Pressure	Power	Temp.	Gap
	B_2H_6	MMS	CO_2	H_2	SiH_4	PH_3	(Pa)	(W)	(^oC)	(cm)
p-pure	8	2	-	180	10	-	26	10	180	2
p-buffer	-	1	-	180	10	-	26	10	180	2
i	-	-	-	10.5	8.43	-	20	1	180	2
n	-	-	9.5	300.5	3.33	10	200	15	180	2

Note: MMS refers to monomethylsilane.

5.2.3 Deposition of back reflector layer

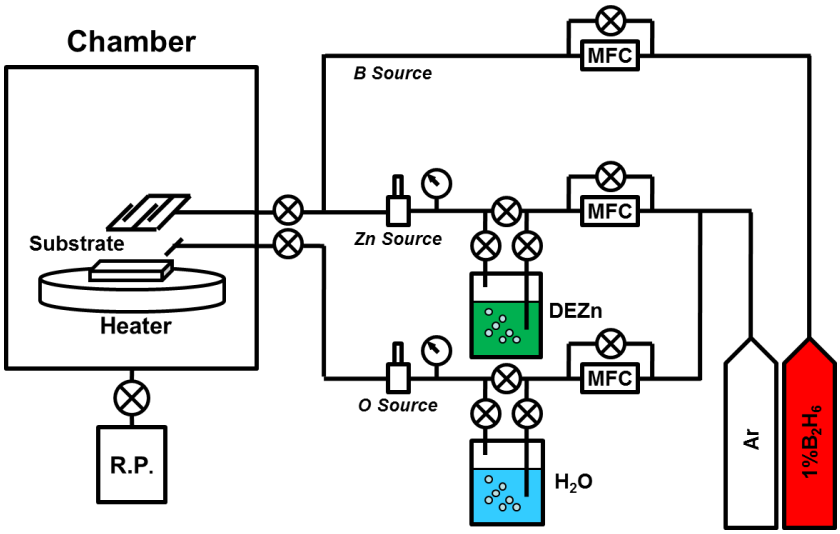

Fig 5.5 Schematics of MOCVD system used in this work.

Boron doped ZnO were deposited by MOCVD method as the back reflector layer. Figure 5.5 shows the schematic diagram of MOCVD system used in this work. Diethylzinc ($Zn(C_2H_5)_2$, DEZn) was used as the znic source. H_2O was used as the oxygen source. Ar was used as the carrier gas. 1% hydrogen diluted B_2H_6 was employed as dopant gas. The DEZn and H_2O are in bubbles, which are soaked in the temperature-controlled baths. The detailed deposition condition is shown in Table 5.3.

Table 5.3 MOCVD deposition condition used for the fabrication of BZO back reflector.

Deposition conditions	Values
Deposition pressure (Torr)	3
Depostion temperature (^{o}C)	155
DEZn bath temperature (^{o}C)	20
H_2O bath temperature (^{o}C)	40
Line pressure (atm)	1
B_2H_6 flow rate (sccm)	0.5
Ar flow for DEZn (sccm)	100
Ar flow for H_2O (sccm)	70
Deposition rate (nm/s)	~1

5.3 Characteristics of a-Si single junction solar cells deposited on flat AZMO/flat glass substrate

The widely recognized feature of sol-gel derived AZMO thin film is its flat surface morphology. So, at the beginning, the flat AZMO/flat glass substrate was used as the front transparent conductive layer in a-Si solar cells.

5.3.1 Effect of bandgap widening of TCO

Bandgap widening of front transparent conductive layer is conducted by changing the Mg/Zn ratio from 0 to 15 mol. %. It was expected to increase the spectral response of a-Si solar cells at short wavelength. The detailed information of the samples can be found in section 3.3.1.1. In this part, the EtOH was used as the solvent and Zn^{2+}

solute concentration is 0.5 M. These enabled lower resistivity and sheet resistance than the one shown in section 3.3.1.1. The E_{opt} was tuned from 3.42 eV to 3.62 eV and all films show flat surface with σ_{rms} of less than 10 nm.

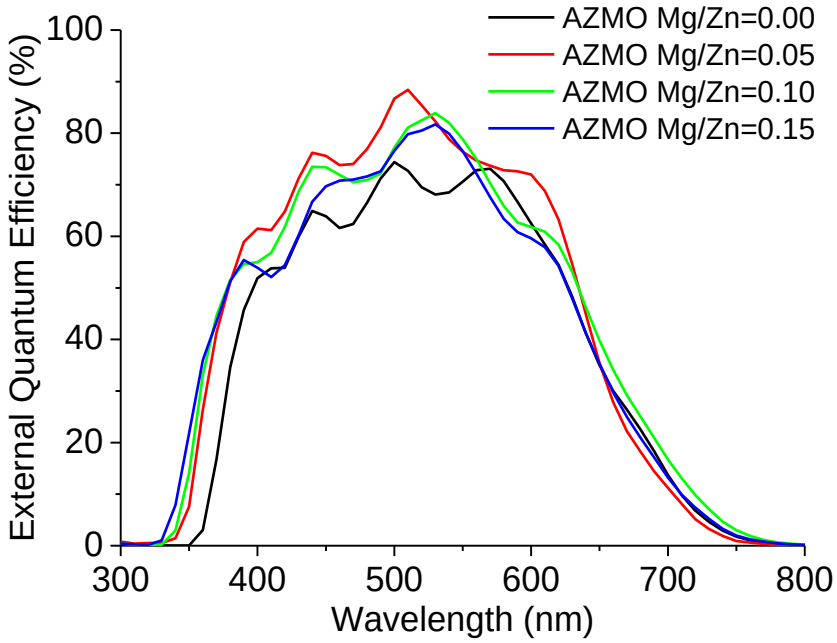

Fig. 5.6 External quantum efficiency of a-Si solar cells fabricated on the AZMO thin film with different Mg content.

The p-i-n a-Si solar cell with structure shown in Fig 5.1 was fabricated on these substrates. In this case, the thickness of BZO is 2000 nm. Figure 5.6 shows the external quantum efficiency of a-Si solar cells fabricated on the AZMO thin film with different Mg content. It can be found that all samples show wave-like curves, indicating that interference of incident light occurred at the interface between TCO and p-a-SiC_x layer due to the flat interface. It is very clear that bandgap widening of front transparent conductive layer indeed improved the spectral response at short wavelength region of around 350 nm. At wavelength region of 400 nm-600 nm, bandgap widening of front transparent conductive layer also increased the spectral response compared to AZO thin film. However, the spectral response contrarily decreases with widening the E_{opt} of front

electrode furtherly (Mg/Zn>0.10). The reason is not clear now. One possible reason is the enhanced recombination at the AZMO/p-a-SiC_x interface due to the downwards band bending caused by the bandgap widening of TCO [1]. In addition, the refection of these solar cells is so high that the external efficiency is low, especially at long wavelength region.

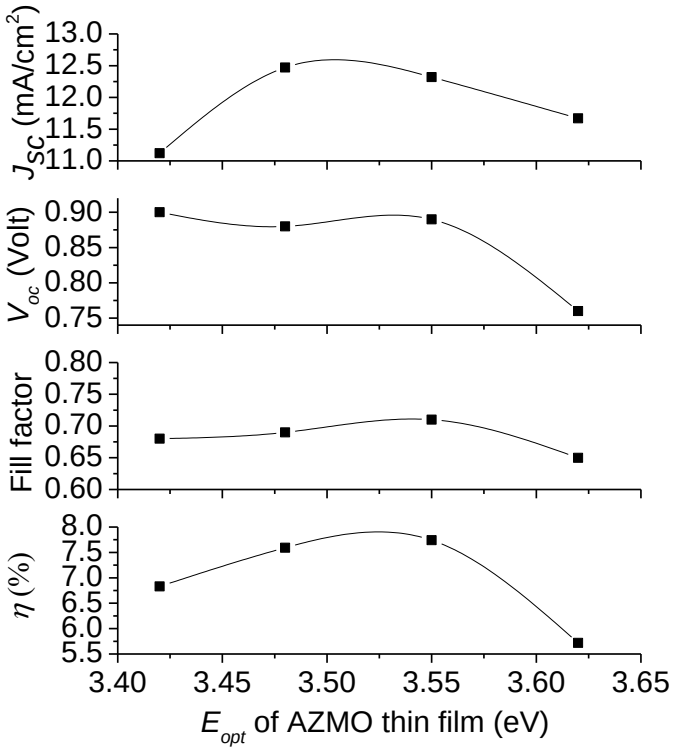

Fig. 5.7 Dependence of performance parameters on the E_{opt} of AZMO thin film.

The dependence of performance parameters on the E_{opt} of AZMO thin film is shown in Fig. 5.7. The short circuit current density (J_{sc}) and fill factor (FF) increases gradually when the E_{opt} of AZMO thin film changes from 3.42 to 3.55 eV, however it decreases when the E_{opt} of AZMO thin film is larger than 3.55 eV. The open circuit voltage (V_{oc}) keeps almost constant when the E_{opt} of AZMO thin film changes from 3.42 to 3.55 eV, however, it decreases when the E_{opt} of AZMO thin film is larger than 3.55 eV. As a result, with increasing E_{opt} of AZMO thin film, the conversion efficiency (η) increases gradually and then decreases. The maximum value was obtained with

using AZMO thin film with E_{opt} of 3.55 eV. The drop in J_{sc} is caused by the decrease in the spectral response at wavelength region of 400 to 600 nm as observed in Fig. 5.6.

There are two possible reasons for the decrease in V_{oc} and *FF*. First, it is the presence of electron injection barrier at the AZMO/ p-a-SiC_x interface, which is caused by the bandgap widening of front transparent conductive layer, that leads to the downwards band bending at the interface, resulting in the drop in V_{oc} an *FF*. Second, it is the roughened surface morphology, which is caused by the Mg addition induced increase in grain size (Fig. 3.9), that gives rise to the drop in V_{oc} and *FF*. Overall, the flat surface of AZMO thin film (E_{opt} = 3.42-3.55 eV) brought about a V_{oc} of around 0.90 V for a-Si solar cells. This value is comparable to that of a-Si solar cells deposited on the naturally textured SnO_2: F [2] and ZnO: B [3] substrate. Meanwhile, the flat surface of AZMO thin film (E_{opt} = 3.42-3.55 eV) also results in low J_{sc} due to the insufficient light-scattering. AZMO (3.55eV)/flat glass substrate enabled the highest η (7.74%) with a J_{sc} of 12.32 mA/cm^2, a V_{oc} of 0.89 V and a *FF* of 0.71. The value of *FF* is comparable to that in the published paper [4].

5.3.2 Effect of antireflection layer

The optical reflection of these solar cells fabricated in section 5.3.1 is very high due to the high optical reflection at the TCO/Si interface. It is caused by the flat surface of AZMO substrate and the significant difference between the refractive indices of AZMO and p-a-SiC_x. Therefore, antireflection layer is needed to reduce the optical reflection of solar cells. In view of the refractive indices at λ=500 nm of p-a-SiC_x (~4) and AZMO (~1.9), TiO_2 thin film (~2.7) is very good candidate [5, 6, 7, 8]. As a result, niobium pentoxide doped titanium (TNO) fabricated by RF magnetron sputtering was utilized as the antireflection layer between TCO and p-a-SiC_x layer. The deposition

condition was shown in Table 5.1. The thickness of TNO is changed by changing the deposition time.

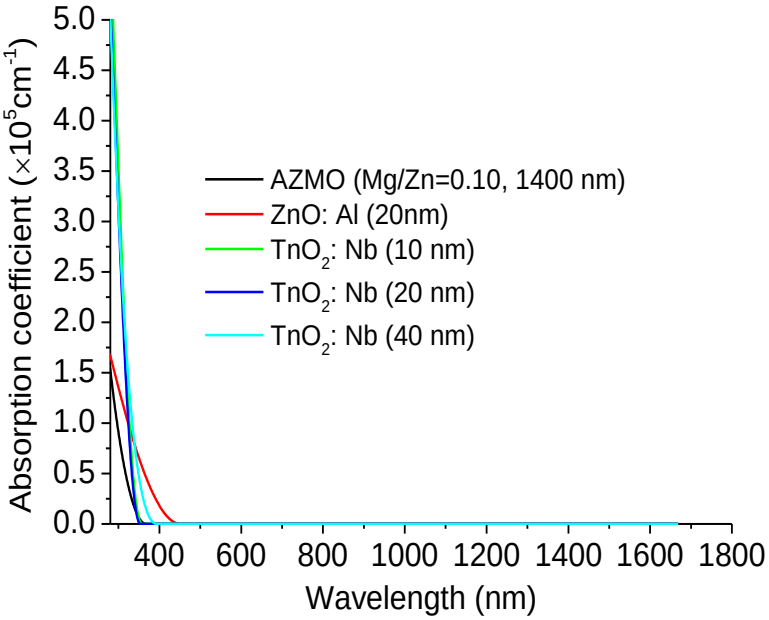

Fig. 5.8 Absorption coefficient of AZO and TNO thin films deposited by sputtering.

The dependence of the refractive indices of TNO thin film on film thickness was investigated. The refractive indices was measured by using an ellipsometer (J. A. Woollam Co.). It was found that the thickness influenced the n greatly. TNO with thickness of 20 nm showed the largest n, while the TNO with thickness of 40 nm showed the smallest n. Figure 5.8 shows the absorption coefficient of AZO and TNO thin films. It can be found that TNO shows larger absorption coefficient than AZO and AZMO thin film at short wavelength. The TNO with thickness of 40 nm shows larger absorption coefficient than thinner ones at wavelength of around 400 nm.

Then, the deposition of TNO thin film on the AZMO(1400 nm)/flat glass substrates was conducted. The transmittance, reflectance, and absorptance of AZMO/flat glass substrates coated with TNO of different thickness was measured. It was found that transmittance of TNO/AZMO/glass substrates decreases greatly with

increasing the thickness of TNO. It is caused by the increase in reflection and absorption with increasing film thickness. Another possible reason is the high reflection at the interface between TNO and air when measurement was done. Figure 5.9 shows the absorption of AZMO/flat glass substrates coated with TNO. It can be found that the absorption increases slightly with increasing the thickness of TNO.

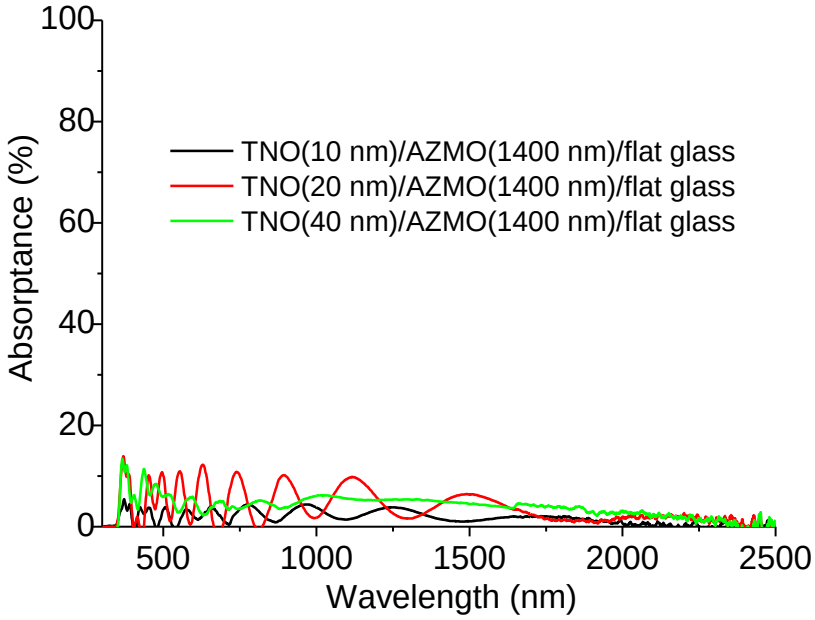

Fig. 5.9 Absorptance of AZMO/flat glass substrates coated with TNO.

The p-i-n a-Si solar cell with structure as shown in Fig 5.1 was fabricated on these substrates. In this case, the thickness of BZO is 2000 nm. Before the deposition of solar cells, another 10 nm AZO was deposited on the top of TNO/AZMO/glass substrates to avoid the hydrogen induced reduction [9]. The *J-V* curves of these solar cells are shown in Fig. 5.10. It can be found that the J_{sc} only get increased with 20 nm TNO. There is little improvement on J_{sc} with 10 nm TNO. The J_{sc} contrarily get decreased with 40 nm TNO. All solar cells show a high V_{oc} of about 0.91V and a *FF* of about 0.65. The solar cells with 20 nm TNO show the highest η due to the creation of

the largest J_{sc}.

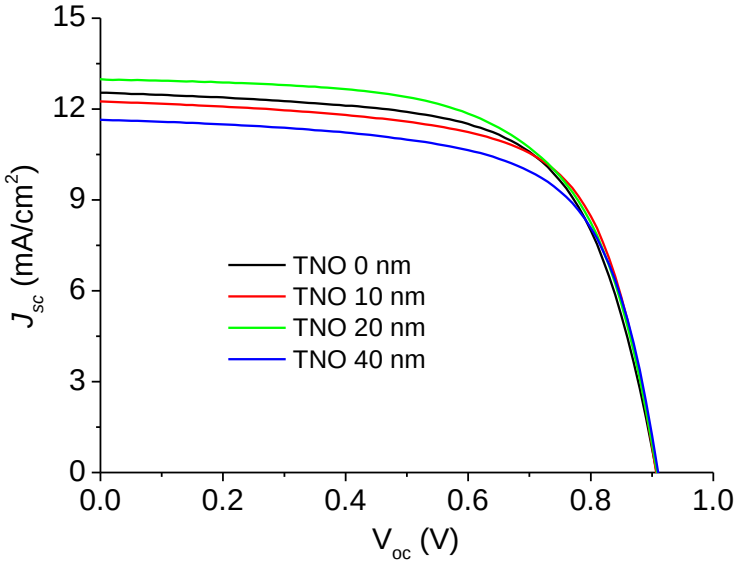

Fig. 5.10 *J-V* curves of a-Si solar cells deposited on the AZO/TNO/AZMO/flat glass substrates.

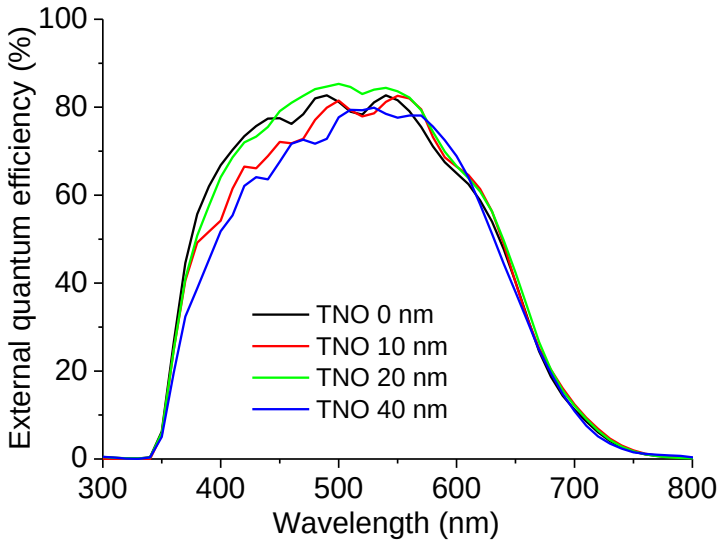

Fig. 5.11 EQE of a-Si solar cells deposited on the AZO/TNO/AZMO/flat glass substrates.

Figure 5.11 shows the EQE of a-Si solar cells deposited on the AZO/TNO/AZMO/flat glass substrates. It is obvious that the spectral response at wavelength 450-580 nm gets improved with 20 nm TNO. This should be attributed to

the antireflection effect of TNO at TNO/p-a-SiC_x interface. It caused the increase in J_{sc}. However, at the same time the spectral response at wavelength 350-450 nm gets decreased with 20 nm TNO. This might be caused by the absorption in the TNO and AZO layer. Employing 10 nm and 40 nm TNO as the antireflection layer decreases the spectral response at wavelength of 350-600 nm severely. This might be caused by the mismatching of refractive indices. In the case of 40 nm TNO, the absorptance is in the TNO layer was high as indicated in Fig. 5.9. The reflectance of these solar cells is shown in Fig. 5.12. One can find that the solar cells with 20 nm TNO show the lowest reflection at the wavelength region of 450-550 nm. This confirms the antireflection effect of TNO layer. Solar cells with 10 nm and 40 nm TNO show high reflection at short wavelength. This cause the low spectral response at short wavelength region as indicated in Fig. 5.11.

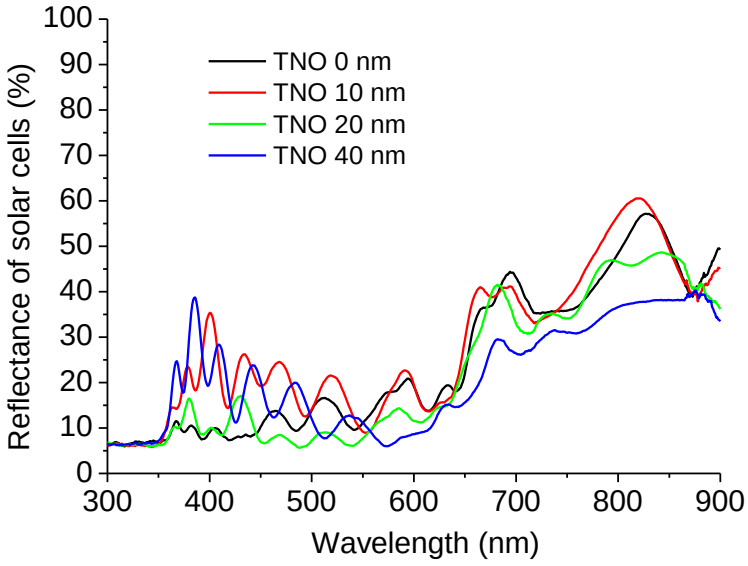

Fig. 5.12 Reflection of a-Si solar cells deposited on the AZO/TNO/AZMO/flat glass substrates.

5.4 Characteristics of a-Si single junction solar cells deposited on rough AZMO/flat glass substrate

Optical confinement is very important for thin-film solar cells in order to increase the short circuit density of device, because the photoactive layers are not thick enough to absorb the incident light sufficiently [10]. Rough surface morphology of textured transparent conductive oxide contributes a lot to improving optical confinement of thin-film solar cells through enhancing light-scattering [11]. Fluorine doped SnO_2/glass substrate [12] or boron doped ZnO/glass substrate [13] with growth induced pyramidal surface textures, which are deposited by chemical vapor deposition, scatter the incident light effectively and were widely used as the front electrode of thin-film Si solar cells. Etching ZnO films deposited by sputtering method with diluted HCl can make a crater-like morphology, and it effectively enhances the light-scattering in amorphous silicon (a-Si) solar cells. However, few research was proposed on the development of textured $Zn_{1-x}Mg_xO$ thin film, although it has been developed by many methods including pulsed laser deposition [14], magnetron sputtering [15], metal organic chemical vapor deposition [16], atomic layer deposition [17], and sol-gel process [18]. In view of bandgap widening and resistance to hydrogen-plasma reduction during fabrication process of solar cells, development of textured $Zn_{1-x}Mg_xO$ thin film is an urgent topic.

Consequently, in this section, efforts were made to develop textured $Zn_{1-x}Mg_xO$ thin film through sol-gel process, because sol-gel process enables the formation of surface texture for thin-film materials through the nonequilibrium solute precipitation and crystallization process during the drying procedure. Nagayasamy et al. [19] reported that ZnO thin film with spindle-like surface morphology was obtained by sol-gel process with increasing the Zn^{2+} solute concentration in precursor.

5.4.1 Experiments

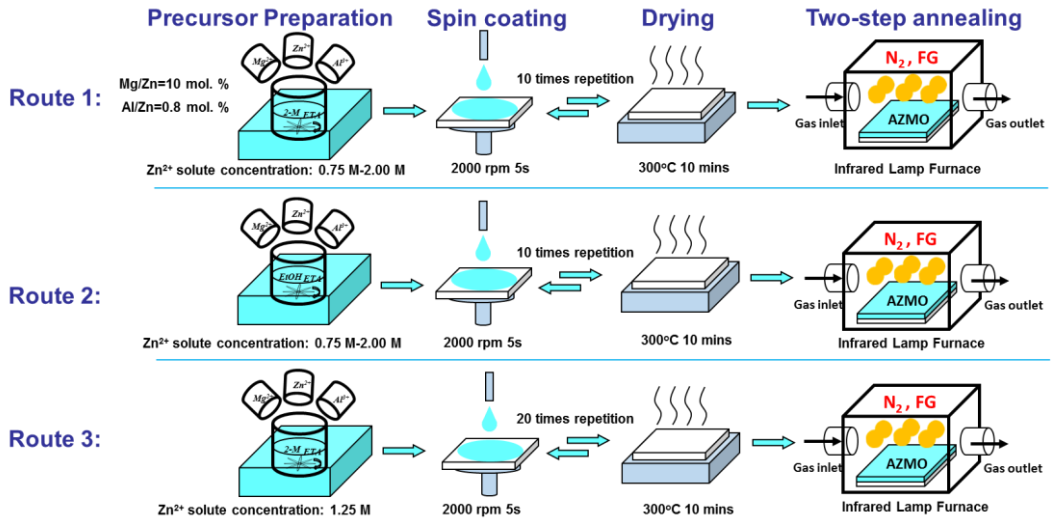

Fig. 5.13 Experimental methods to fabricate AZMO thin film with rough surface morphology.

AZMO thin films were fabricated by sol-gel process on flat glass substrate (Corning Eagle XG, 0.7-mm-thick) as mentioned in section 3.2.1. In order to control morphology, three routes were proposed as shown in Fig. 5.13. In route 1, 2-M was used as the solvent, and the Zn^{2+} solute concentration in sol-gel precursor was changed from 0.75 M to 2.00 M. In route 2, EtOH was used as the solvent, and the Zn^{2+} solute concentration in sol-gel precursor was changed from 0.75 M to 2.00 M. In these two case, the times of spin-coating was 10. In route 3, 2-M was used as the solvent, and the Zn^{2+} solute concentration in sol-gel precursor was fixed at 1.25 M. The times of spin-coating was 20. Finally, the films were firstly annealed in nitrogen at 650°C for 120 min and secondly annealed in forming gas (97% N_2 + 3% H_2) at 500°C for 5 min. For comparison, boron doped ZnO thin film was deposited by metalorganic chemical vapor deposition. The detailed deposition process is shown in Table 5.3.

These AZMO and BZO films coated glass substrate were applied as the front electrode in a-Si single junction solar cells with superstrate configuration. The structure

of these solar cells is shown in Fig. 5.1. In this case, no antireflection layer of TNO was used. Instead, one layer of Al doped ZnO thin film (20 nm) deposited by RF magnetron sputtering was inserted at AZMO/p-a-SiC_x layer. It is used to decrease the bandgap-widening induced downwards band bending at the interface TCO/p-a-SiC_x [20]. In addition, BZO with thickness of 100 nm was used as the back reflector.

5.4.2 Results and discussions

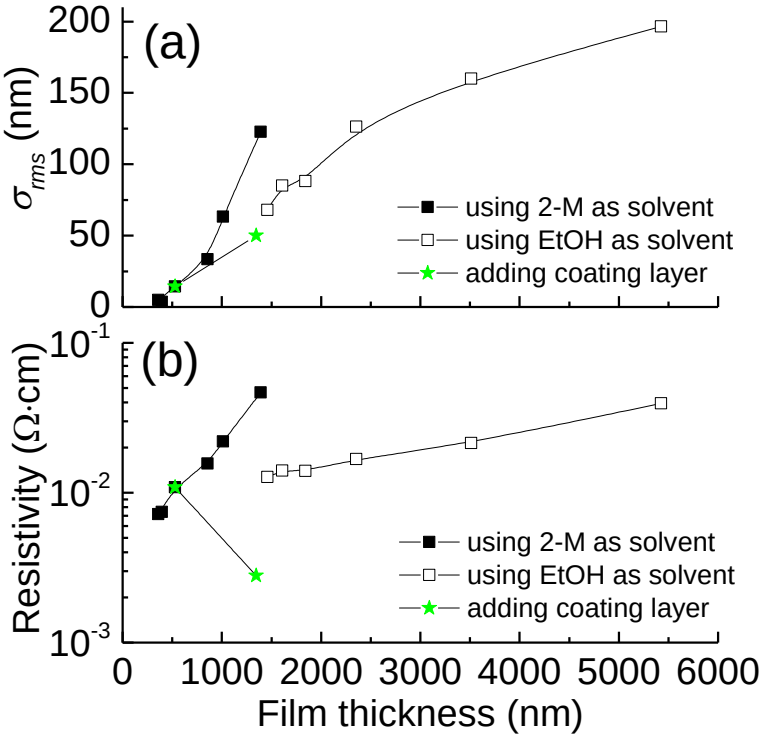

Fig. 5.14 Dependence of (a) surface roughness and (b) resistivity on the film thickness. The square symbol refers to increasing thickness through increasing the Zn^{2+} solute concentration, while the pentagon symbol refers to increasing thickness through adding coating layers.

Figure 5.14 shows the dependence of surface roughness and resistivity on the film thickness. The root-mean-square surface roughness (σ_{rms}) increases obviously with increasing film thickness. In the way that increases thickness through increasing the Zn^{2+} solute concentration, with the same Zn^{2+} solute concentration and coating layer, using EtOH as solvent can make a much rougher film than using 2-M as solvent,

because the former enabled a larger thickness of per coating layer than the latter with the same condition of spin-coating and annealing. Adding coating layer also clearly increases the σ_{rms}, but this increase in σ_{rms} is not pronounced. In terms of resistivity, only adding coating layer tends to decrease the resistivity, while increasing Zn^{2+} solute concentration would contrarily increase the resistivity regardless of the solvent. This indicates that using large Zn^{2+} solute concentration when preparing sol-gel precursor would deteriorate the resistivity of annealed sample.

Table 5.4 Performance parameters of the BZO and AZMO

Sample	BZO	AZMO1	AZMO2	AZMO3
Condition	-	1.25M/2-M/20L	0.75M/EtOH/10L	2.0M/2-M/10L
σ_{rms} (nm)	40.2	42.3	67.9	122.7
R_s (Ω/sq)	24.0	20.8	95.8	132.3
ρ ($\times 10^{-3}$ Ω·cm)	3.40	7.35	13.96	18.42
n ($\times 10^{19}$ cm^{-3})	4.0	4.4	5.6	3.4
μ ($cm^2 \cdot V^{-1} \cdot s^{-1}$)	21.1	19.3	10.5	10.0
H_T at 500 nm (%)	23.2	41.4	72.4	71.6
Thickness (nm)	1416	1345	1458	1392

Three samples with a similar thickness of about 1400 nm were selected from these samples shown in Fig. 5.14 for further discussion. The detailed information of these samples were listed in Table 5.4. The MOCVD deposited BZO thin film with similar thickness was also indicated for comparison. The AZMO1 was fabricated with using 1.25 M Zn^{2+} solute concentration and 20 coating layers with 2-M as solvent. The AZMO2 was fabricated with using 0.75 M Zn^{2+} solute concentration and 10 coating layers with EtOH as solvent. The AZMO3 was fabricated with using 2.0 M Zn^{2+} solute

concentration and 10 coating layers with 2-M as solvent. AZMO1 shows a similar σ_{rms} as BZO, while AZMO2 and AZMO3 shows larger σ_{rms} than BZO. All AZMO samples show larger haze ratio (H_T) in transmission at 500 nm than BZO. AZMO1 shows a similar resistivity as BZO. The resistivity of AZMO2 and AZMO3 is larger than AZMO1 and BZO. The AZMO samples show similar carrier concentration as BZO. AZMO2 and AZMO3 shows smaller Hall mobility than AZMO1 and BZO. AZMO1 enabled a sheet resistance (R_s) of 20.8 Ω/sq and a resistivity (ρ) of about 7.4×10^{-3} Ω·cm.

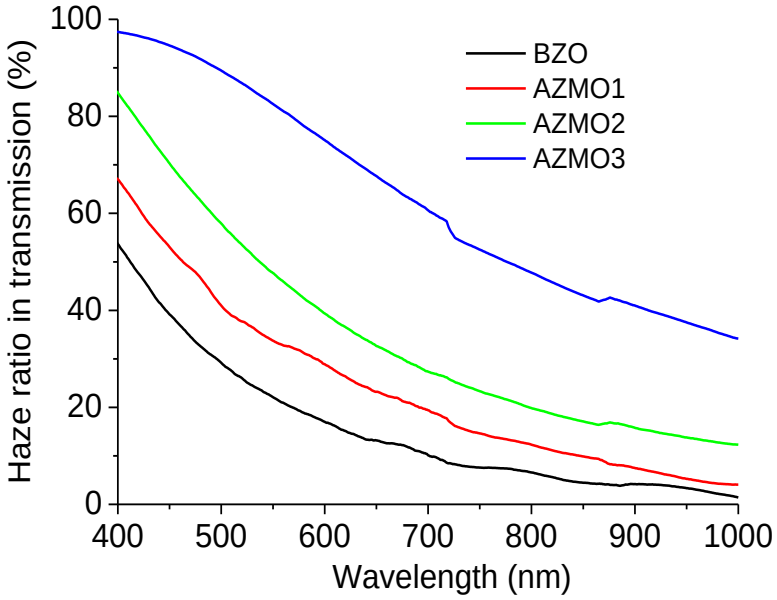

Fig. 5.15 Haze ratio in transmission of BZO and AZMO.

The SEM and DFM observation showed that the BZO showed pyramid-like surface morphology, while AZMO samples showed wrinkle-like surface morphology. AZMO2 and AZMO3 showed rougher wrinkle than AZMO1. The AZMO3 showed additional reticular texture compared to AZMO2. The wrinkle-like feature consists of nano-sized grains. This morphology was quite probably formed during the solvent evaporation and subsequent solute precipitation at the drying procedure. The transmittance, reflectance, and absorptance of BZO and AZMO samples were also

measured. The AZMO samples show higher transmittance and lower absorptance at short wavelength region of 350-400 nm relative to BZO due to the bandgap widening. Figure 5.15 shows the haze ratio in transmission of BZO and AZMO samples. AZMO samples clearly show larger haze ratio than BZO sample at wavelength region of 400-1000 nm. For AZMO samples, the haze ratio increases with the σ_{rms}. AZMO2 and AZMO3 exhibit larger haze ratio than AZMO1, implying that rough wrinkle morphology scatters incident light greater than slim wrinkle morphology.

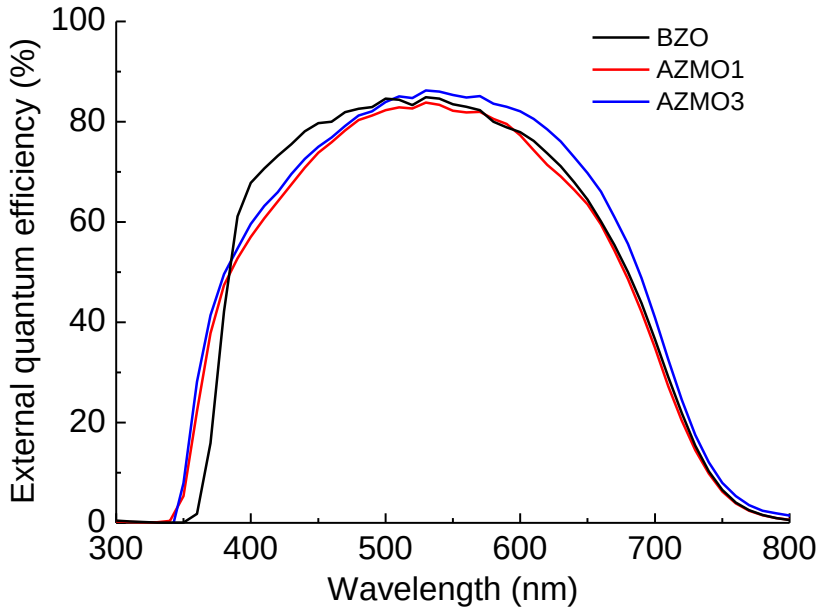

Fig. 5.16 External quantum efficiency of a-Si single junction solar cells with AZMO and BZO as the front conductive layer.

Figure 5.16 shows the external quantum efficiency of a-Si single junction solar cells with AZMO and BZO as the front conductive layer. It is obvious that the cells deposited on AZMO shows an enhanced spectral response at short wavelength of around 350 nm than that deposited on BZO due to the reduced optical loss in the front conductive layer through bandgap widening. At wavelength region of 380-500 nm, the spectral response of cells deposited on AZMO is weaker than that of cells deposited on

BZO. This is caused by the high reflection of AZMO thin film at this region. At wavelength region of 500-800 nm, the spectral response of cells deposited on AZMO1 is similar as that deposited on BZO and the spectral response of cells deposited on AZMO3 is greater than that of solar cells deposited on BZO due to the enhanced light-scattering.

Table 5.5 Performance parameters of a-Si solar cells deposited on BZO and AZMO substrates.

TCO	V_{oc}(V)	J_{sc}(mA/cm^2)	FF(%)	η(%)
BZO	0.87	14.7	0.73	9.23
AZMO1	0.87	14.8	0.53	6.84
AZMO2	0.64	14.2	0.44	4.03
AZMO3	0.33	15.7	0.34	1.78

The performance parameters of a-Si solar cells deposited on BZO and AZMO substrates are listed in Table 5.5. This increase in spectral response lead to the increase in short circuit current (J_{sc}) of solar cells. The solar cells deposited on AZMO3 shows the largest J_{sc} due to the strongest light-scattering. The solar cells deposited on AZMO1 and AZMO3 shows larger values of J_{sc} than that deposited on BZO. However, the open circuit voltage (V_{oc}) and fill factor (FF) of solar cells deposited on AZMO2 and AZMO3 with rough wrinkle morphology are much lower than that deposited on AZMO1 with slim wrinkle morphology and BZO with pyramidal morphology, resulting in bad conversion efficiency of solar cells. It indicates that too rough surface morphology would deteriorate the V_{oc} and FF of solar cells through deteriorating the growth quality of photoactive layers, as mentioned in the published literatures [21]. The

solar cells deposited on AZMO3 shows the worst conversion efficiency due to the largest σ_{rms} of TCO layer.

AZMO1 enabled the highest conversion efficiency among AZMO samples due to the moderate morphology of slim wrinkle. The solar cell deposited on AZMO1 substrate shows similar values of J_{sc} and V_{oc} as that deposited on BZO substrate. However, its value of *FF* is lower than that of solar cells deposited on BZO. There are two possible reasons. First, the σ_{rms} of AZMO1 (50.1 nm) is a bit larger than that of BZO (40.2 nm). This deteriorated the growth of photovoltaic active layer and decreased the *FF*. Second, the series resistance of solar cells deposited on AZMO1 (160.7 $\Omega \cdot cm^2$) is larger than that of solar cells deposited on BZO (55.9 $\Omega \cdot cm^2$). This also cause the decrease in *FF*. Consequently, much more elaborate morphology control of the AZMO thin film is needed for increasing the light-confinement in solar cells without deteriorating the V_{oc} and *FF* of solar cells.

5.4.3 Conclusions

Morphology control of sol-gel AZMO thin film was conducted for enhancing light-scattering. One wrinkle-like morphology was formed by controlling the solvent evaporation and solute precipitation during sol-gel process. Using solvent with large evaporation rate or increasing solute concentration can make rough wrinkle surface morphology. This AZMO substrates with rough wrinkle surface morphology shows larger haze ratio than the MOCVD derived BZO substrate with pyramidal surface morphology. However, it deteriorated the film crystallinity and electrical properties due to the nonequilibrium nucleation and growth. Employing this textured AZMO thin film as the front transparent conductive layer improved the spectral response of a-Si single junction solar cell at short and long wavelength simultaneously. Increasing coating

layer with moderate solute concentration proved to be a better method than utilizing large Zn^{2+} solute concentration to increase the surface roughness, because it enables better electrical properties of AZMO thin film and better performance of a-Si solar cells. AZMO with slim wrinkle morphology (optical bandgap=3.6 eV, thickness=1345 nm, σ_{rms}=42.3 nm, and R_s of 20.8 Ω/sq) suggests a potential to be the transparent conductive layer of thin-film solar cells.

5.5 Characteristics of a-Si single junction solar cells deposited on optically-rough and physically-flat TCO substrates

In this section, the deposition of a-Si single junction solar cells on optically-rough and physically-flat TCO substrates will be conducted. The effect of optically-rough and physically-flat TCO substrates on the performance of a-Si single junction solar cells will be investigated.

5.5.1 Characteristics of a-Si single junction solar cells deposited on AZMO/ RIE etched glass substrates

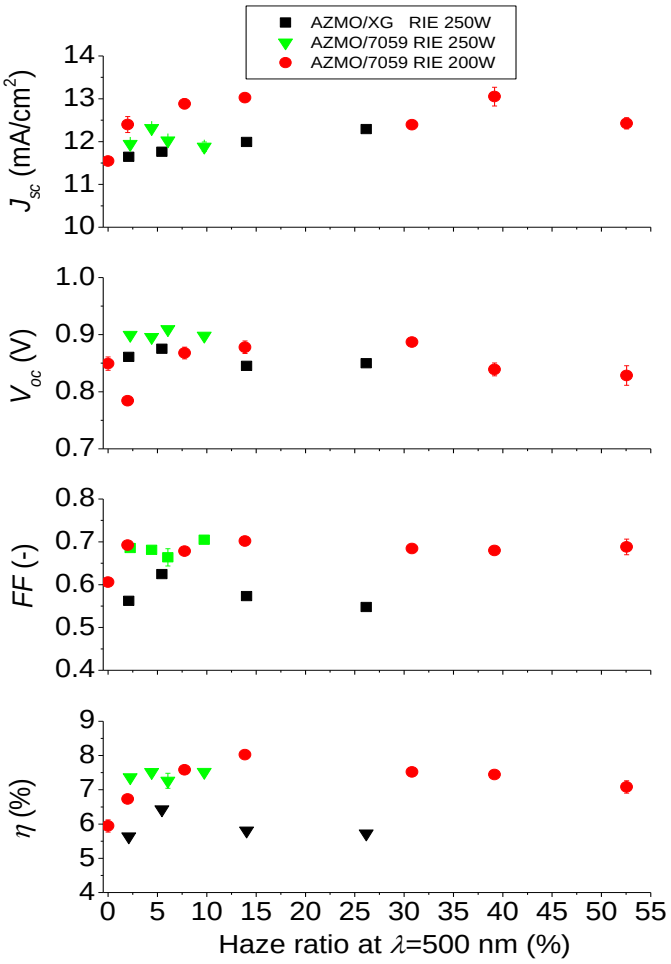

Fig. 5.17 Dependence of performance of solar cells on the haze ratio of AZMO/etched glass substrates.

Firstly, the effect of AZMO/etched glass substrates on the performance of a-Si single junction solar cells is investigated. The AZMO/etched glass substrates fabricated in sections 4.5.1 and 4.5.2 are used as the TCO substrates. The a-Si single junction solar cells is deposited with the structure shown in Fig. 5.1. In this case, one layer of Al doped ZnO thin film (20 nm) deposited by RF magnetron sputtering was inserted at AZMO/p-a-SiC_x interface, and no back reflector of BZO was used.

Figure 5.17 shows the relationship between the performance of a-Si solar cells and the haze ratio of AZMO/etched glass substrates. Three kinds of etched glass substrates were selected. Although they were fabricated by different conditions, the performance of solar cells deposited on these substrates show similar tendency. With increasing haze ratio, the conversion efficiency increases at first, and then decreases gradually. The solar cells deposited on AZMO/etched 7059 substrates show higher η than that deposited on AZMO/etched XG substrates. The solar cells deposited on AZMO/etched 7059 (RIE 200 W, 7 Pa, 10 min) shows the highest conversion efficiency (8.02%). The J_{sc} shows the a similar change tendency with haze ratio as conversion efficiency. The solar cells deposited on AZMO/etched 7059 (RIE 200 W, 15 Pa, 20 min) shows the largest J_{sc} (13.05 mA/cm^2). The V_{oc} seldom change with the haze ratio. The solar cells deposited on AZMO/etched 7059 (RIE 250 W, 7 Pa, 15 min) show the largest V_{oc} (0.91V). In addition, the solar cells deposited on AZMO/etched 7059 substrates show larger *FF* than that deposited on AZMO/etched XG substrates. The solar cells deposited on AZMO/etched 7059 substrates show *FF* of about 0.70.

Figure 5.18 shows the *J-V* curves of a-Si solar cells deposited on the AZMO/etched 7059 substrates. The data of solar cells deposited on BZO (2000 nm)/flat glass substrate is also indicated for comparison. Solar cells deposited on AZMO/etched substrates (RIE time $\leq$ 20 m) show better performance (larger J_{sc}, larger V_{oc}, and

larger *FF*) than solar cells deposited on AZMO/flat glass substrate. However, their performance is still worse than that of solar cells deposited on BZO substrates. Although their V_{oc} is similar to that of solar cells deposited on BZO, their J_{sc} and *FF* are lower than that of solar cells deposited on BZO, resulting in lower conversion efficiency.

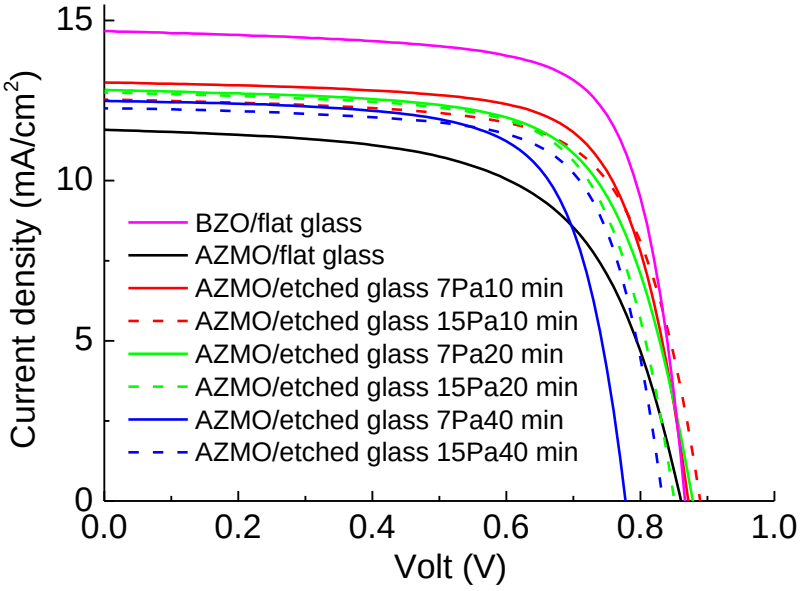

Fig. 5.18 *J-V* curves of a-Si solar cells deposited on AZMO/etched 7059 substrates.

Figure 5.19 shows the *EQE* of a-Si solar cells deposited on BZO and AZMO/etched 7059 substrates. Solar cells deposited on the AZMO/etched 7059 substrates show an improved spectral response at wavelength region of 350-600 nm relative to that deposited on AZMO/flat substrates. Compared to the solar cells deposited on BZO substrate, solar cells deposited on the AZMO/etched 7059 substrates show an improved spectral response at short wavelength of around 350 nm, but at wavelength of 600-800 nm their spectral response is not as good as that deposited on the BZO substrate. This indicates that the scattering behavior of AZMO/etched substrates is not as good as BZO substrate with pyramidal surface morphology.

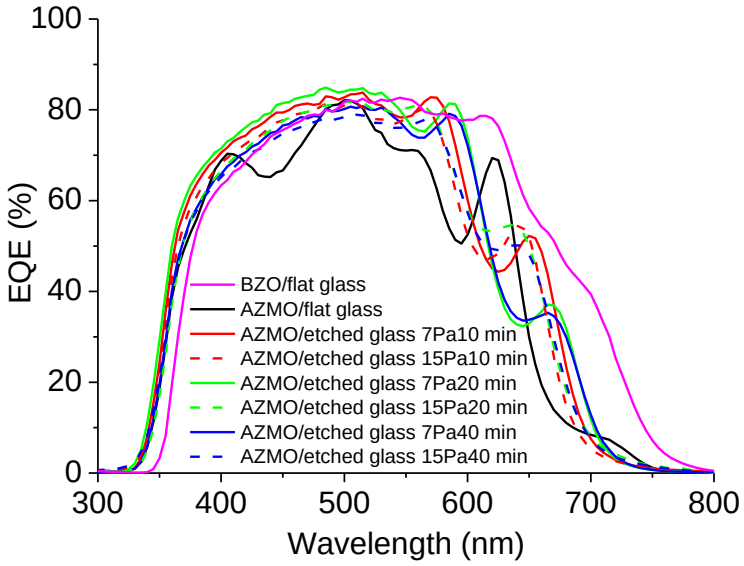

Fig. 5.19 *EQE* of a-Si solar cells deposited on BZO and AZMO/etched 7059 substrates.

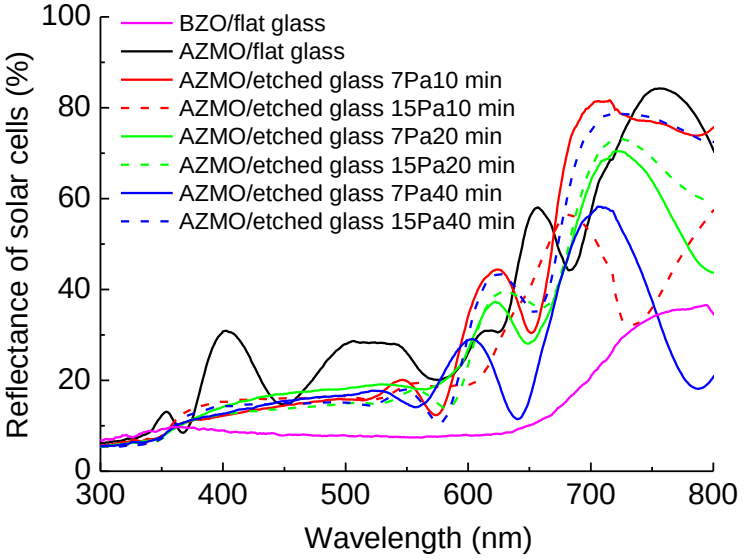

Fig. 5.20 Reflectance of a-Si solar cells deposited on BZO and AZMO/etched 7059 substrates.

Figure 5.20 shows the reflection of a-Si solar cells deposited on BZO and AZMO/etched 7059 substrates. Solar cells deposited on AZMO/etched 7059 substrates shows a lower reflection that deposited on AZMO/flat substrate. However, their

reflection is still much larger than that deposited on BZO substrate, especially at long wavelength region 600-800 nm. This high reflection cause the low spectral response of solar cell at long wavelength. In addition, the low reflection of solar cells deposited on BZO substrate is attributed to the nanoscale pyramidal surface morphology of BZO. It was reported that this pyramidal surface morphology played as an antireflection layer at the TCO/p-a-Si interface. At wavelength region of 600-700 nm, the wave-like curve reflects that there is strong light interference occurred in the solar cells deposited on the AZMO/etched glass substrate. This is caused by the formation of flat interface due to the flat surface of AZMO thin film. These results indicates that the light-confinement in the solar cells deposited on AZMO/etched glass substrate is not as good as that deposited on BZO with pyramidal surface morphology.

5.5.2 Characteristics of a-Si single junction solar cells deposited on AZMO /imprinting patterned glass substrates

The effect of AZMO/imprinting patterned glass substrates on the performance of a-Si single junction solar cells is investigated. The AZMO/ imprinting patterned glass substrates fabricated in section 4.5.3 are used as the front electrode. The a-Si single junction solar cells is deposited with the structure as shown in Fig. 5.1. In this case, one layer of Al doped ZnO thin film (20 nm) deposited by RF magnetron sputtering was inserted at AZMO/p-a-SiC_x layer, and a back reflector of BZO (1500 nm) was used.

Table 5.6 shows the performance parameters of a-Si solar cells deposited on AZMO(20L)/flat and patterned glass substrates. The AZMO(20L)/pyramidal or cone patterned substrate enables similar V_{oc} and *FF* as AZMO(20L)/flat glass substrate due to the flat surface. But no improvement on J_{sc} was found. It indicates that the scattering ability of these substrate is poor. In addition, the solar cells deposited on

AZMO(20L)/hole patterned substrates were totally short due to the contact problem during *J-V* and *QE* measurement. The reason is not clear. One possibility is that the structure of AZMO/patterned substrate is fragile and it probably collapsed when the tip of detector was pressed on the sample.

Table 5.6 Performance parameters of a-Si solar cells deposited on AZMO(20L)/ patterned glass substrates.

Pattern	TCO	V_{oc}(V)	J_{sc}(mA/cm^2)	*FF*(%)	η(%)	R_s (Ω·cm^2)	R_{sh} (Ω·cm^2)
none	AZMO(20L)	0.88	11.9	0.62	6.47	93.6	1.44×10^4
pyramid	AZMO(20L)	0.89	11.5	0.64	6.50	84.1	1.02×10^4
cone (P=4μm)	AZMO(20L)	0.90	11.6	0.63	6.54	89.1	0.71×10^4

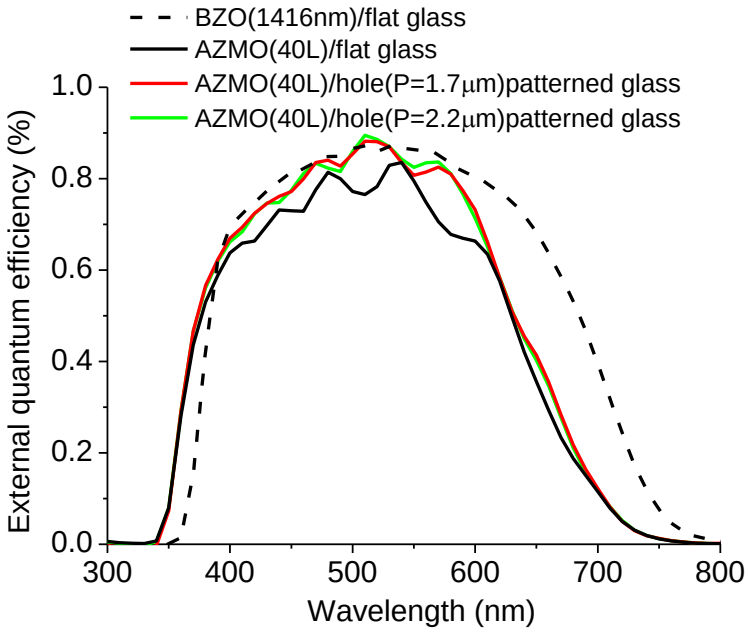

Fig. 5.21 External quantum efficiency of a-Si solar cells deposited on AZMO and BZO substrates.

Increasing coating layer of sol-gel AZMO on hole patterned substrate tends to strengthen the pattern structure and solved the contact problem during the measurement.

The short problem of solar cells was solved and moderate performance was obtained, when the a-Si solar cells were deposited on AZMO(40L)/hole patterned substrates. Figure 5.21 shows the external quantum efficiency of a-Si solar cells deposited on AZMO and BZO substrates. Compared with the BZO substrate, the AZMO substrate obviously improved the spectral response at wavelength region of 330-380 nm due to bandgap widening of TCO. However, the OR-PF substrate cannot make a spectral response of solar cells at wavelength region of 650-750 nm as large as BZO substrate due to the insufficient light-confinement. Compared with the AZMO/flat substrate, the OR-PF AZMO substrate improved the spectral response at wavelength region of 400-620 nm due to the enhanced light-scattering and antireflection effect.

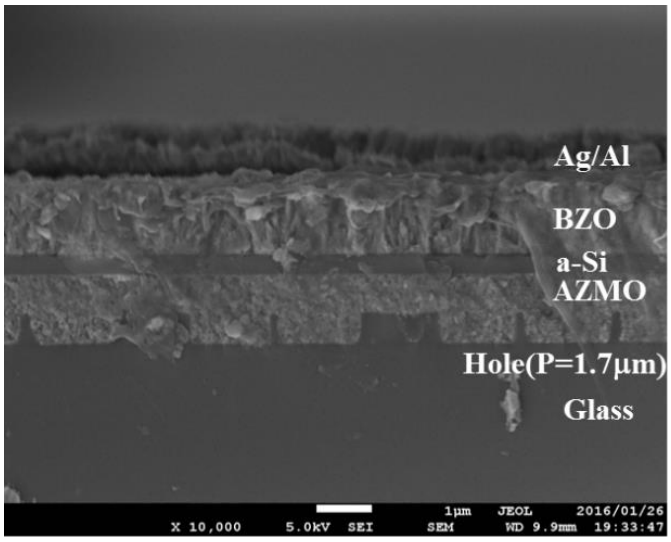

Fig. 5.22 SEM cross sectional micrograph of a-Si solar cells deposited on AZMO (40L)/ hole (P=1.7 μm) substrate.

Figure 5.22 shows the SEM cross sectional micrograph of a-Si solar cells deposited on AZMO (40L)/ hole (P=1.7 μm) substrate. It can be found that high quality of a-Si photoactive layer was obtained due to the flat surface of OR-PF AZMO substrate. Table 5.7 shows the performance parameters of a-Si solar cells deposited on AZMO substrate. The AZMO/hole patterned substrate enables similar V_{oc} and *FF* as

AZMO/flat glass substrate due to the small surface roughness. It also makes larger J_{sc} than AZMO/flat glass substrate due to the large haze ratio. In the case of OR-PF AZMO substrate, smaller period of feature size on the pattern enables a bit larger J_{sc} due to the increased H_T.

Table 5.7 Performance parameters of a-Si solar cells deposited on AZMO substrates

Glass	Pattern	TCO	H_T 500 nm (%)	η (%)	V_{oc} (V)	J_{sc} (mA/cm^2)	FF (%)
Flat XG	no	AZMO(40L)	0.23	6.64	0.82	12.1	0.67
Flat XG	hole(P=1.7um)	AZMO(40L)	28.8	7.38	0.82	13.2	0.68
Flat XG	hole(P=2.2um)	AZMO(40L)	26.6	6.59	0.82	13.1	0.61

Although it was demonstrated that the OR-PF AZMO substrate shows a bit larger H_T at wavelength region of 700-850 nm than BZO substrate in section 4. 5. 3, the solar cells deposited on the OR-PF AZMO substrate showed lower spectral response at wavelength region of 700-850 nm than BZO substrate. There are two possible reasons. First, BZO substrate can scatter the incident light into broader angle than OR-PF AZMO substrate. Usually, there are two parameters to characterize the scattering process at a rough interface: haze ratio and angular intensity distribution. Haze ratio in transmission defines the fraction of light that is scattered compared to the total intensity of light at the interface, while the angular intensity distribution defines the intensity distribution of scattered light as a function of the angle at which the scattered light propagates. It was found that the BZO shows stronger intensity of scattered light at each angle, especially at large angles. It means that BZO can scatter the incident light into broader angle than OR-PF AZMO substrate. This can intensify the light-confinement in the absorption layer and increase the spectral response at long wavelength. In the

case of OR-PF AZMO substrate, it scatters the incident light into narrow angle and the light is easy to get out of the solar cells, so the reflectance of solar cells is high and then the spectral response of solar cells at long wavelength is low.

Second, BZO substrate enables more multiply light-scattering in the solar cells than OR-PF AZMO substrate. In the case of BZO substrate, the morphology of photoactive layer will follow the rough surface of BZO substrate. So there are more rough interfaces than that in solar cells deposited on the OR-PF AZMO substrate. Therefore, multiply light-scattering occurs and the incident light path increases. As a result, the spectral response of solar cells deposited on BZO substrate at long wavelength is high.

5.6 Summary

Applying sol-gel derived AZMO thin film as the front electrode to a-Si single junction solar cells was conducted. Its effect on the performance of a-Si solar cells was investigated. Bandgap widening of TCO through increasing Mg/Zn molar ration in sol-gel precursor improved the spectral response at short wavelength, however, too wide bandgap (E_{opt} >3.55 eV) deteriorated the performance of solar cells through decreasing J_{sc}, V_{oc}, and FF. Solar cells deposited on AZMO with E_{opt}=3.55 eV (Mg/Zn=10 mol. %) showed the best performance. Employing 20 nm Nb doped TiO_2 thin film as the antireflection layer at the TCO/p-a-SiC_x interface improved the spectral response of a-Si solar cells at wavelength of 450-580 nm through reducing the optical reflection at the TCO/p-a-SiC_x interface. Roughening surface morphology via using solvent with large evaporation rate or increasing solute concentration improved the spectral response of a-Si solar cells at wavelength of 600-800 nm by enhancing the light-scattering.

Employing optically-rough and physically-flat AZMO substrate as front electrode improved the performance of solar cells deposited on AZMO substrates. The spectral response at short wavelength of around 350 nm was improved obviously due to the decrease in optical loss in front TCO layer via the bandgap widening of TCO. A V_{oc} of 0.92 V was obtained by using AZMO/ RIE etched 7059 (7 Pa 250 W 10 min) glass substrate due to the flat surface. A solar cell with η of 8.02 % (V_{oc}=0.88 V, J_{sc}=13.02 mA/cm^2, and FF=0.70) was obtained by using AZMO/RIE etched 7059 glass substrate (7 Pa 200 W 10 min). A J_{sc} of 13.2 mA/cm^2 was achieved with AZMO(40L)/hole (P=1.7 μm) patterned substrate. All of these suggest that the potential of OR-PF AZMO substrates for the front electrode of various thin-film solar cells.

References

[1] D. Rached, R. Mostefaoui, Influence of the front contact barrier height on the Indium Tin Oxide/hydrogenated p-doped amorphous silicon heterojunction solar cells, Thin Solid Films 516 (2008) 5087-5092.

[2] T. Matsui, A. Bidiville, K. Maejima, H. Sai, T. Koida, T. Suezaki, M. Matsumoto, K. Saito, I. Yoshida, M. Kondo, High-efficiency amorphous silicon solar cells: impact of depostion rate on metastability, Appl. Phys. Lett. 106 (2015) 0539011-0539015.

[3] H. Wada, K. Nishikubo, P. Sichanugrist, M. Konagai, Improved light-trapping effect for thin-film silicon solar cells fabricated on double-textured white glass substrate, Canadian Journal of Physics 92 (2014) 920-923.

[4] H. Park, J. Lee, H. Kim, D. Kim, J. Raja, J. Yi, Influence of SnO_2:F/ZnO:Al bi-layer as a front electrode on the properties of p-i-n amorphous silicon based thin film solar cells, Appl. Phys. Lett. 102 (2013) 1916021-1916023.

[5] D. Mardare, M. Tasca, M. Delibas, G.I. Rusu, On the structural properties and optical transmittance of TiO_2 r.f. sputterd thin films, Applied Surface Science 156 (2000) 200-206.

[6] N. Yamada, T. Hitosugi, N.L.H. Hoang, Y. Furubayashi, Y. Hirose, S. Konuma, T. Shimada, T. Hasgawa, Structral, electrical and optical properties of sputter-deposited Nb doped TiO_2 (TNO) polycrystralline films. , Thin Solid Films 516 (2008) 5754-5757.

[7] Y. Sato, H. Akizuki, T. Kamiyama, Y. Shigesato, Transparent conductive Nb-doped TiO_2 films deposited by direct-current magnetron sputtering using TiO_{2-x} target, Thin Solid Films 516 (2008) 5758-5762.

[8] C.M. Maghanga, G.A. Niklasson, C.G. Granqvist, Optical properties of sputter deposited transparent and conducting TiO_2: Nb films, Thin Solid Films 518 (2009) 1254-1258.

[9] T. Fujibayashi, T. Matsui, M. Kondo, Improvement in quantum efficiency of thin film Si solar cells due to the suppression of optical reflectance at transparent conducting oxide/Si interface by TiO_2/ZnO antireflection coating Appl. Phys. Lett. 88 (2006) 1835081-1835083.

[10] Y. Hishikawa, E. Maruyama, S. Yata, M. Tanaka, S. Kiyama, S. Tsuda, Optical confinement in high-efficiency a-Si solar cells with textured surfaces, Sol. Energ. Mat. Sol. Cells 49 (1997) 143-148.

[11] J. Muller, B. Rech, J. Springer, M. Vanecek, TCO and light-trapping in silicon thin film solar cells, Solar Energy 77 (2004) 917-940.

[12] H. Sakai, T. Yoshida, T. Hama, Y. Ichikawa, Effect of surface morphology of transparent electrode on the open-circuit voltage in a-Si:H solar cells, Jpn. J. Appl. Phys. 29 (1990) 630-635.

[13] K. Tabuchi, W.W. Wenas, A. Yamada, M. Konagai, K. Takahashi, Optimization of ZnO films for amorphous silicon solar cells, Jpn. J. Appl. Phys. 32 (1993) 3764-3769.

[14] K. Matsubara, H. Tampo, H. Shibata, A. Yamada, P. Fons, K. Iwata, S. Niki, Band-gap modified Al-doped $Zn_{1-x}Mg_xO$ transparent conducting films deposited by pulsed laser deposition, Appl. Phys. Lett. 85 (2004) 1374-1376.

[15] K. Maejima, H. Shibata, H. Tampo, K. Matsubara, S. Niki, Characterization of $Zn_{1-x}Mg_xO$ transparent conducting thin films fabricated by multi-cathode RF-magnetron sputtering, Thin Solid Films 518 (2010) 2949-2952.
[16] C. Li, F.Y. Meng, S. Zhang, J.Q. Wang, Effects of Mg content and B doping on structural, electrical and optical properties of $Zn_{1-x}Mg_xO$ thin films prepared by MOCVD, J. Cryst. Growth 312 (2010) 1929-1934.
[17] G. Luka, B.S. Witkowski, L. Wachnicki, K. Goscinski, R. Jakiela, E. Guziewicz, M. Godlewski, E. Zielony, P. Bieganski, E. Placzek-Popko, W. Lisowski, J.W. Sobczak, A. Jablonski, Atomic layer deposition of $Zn_{1-x}Mg_xO$:Al transparent conducting films, J. Mater. Sci. 49 (2014) 1512-1518.
[18] A. Singh, A. Vij, D. Kumar, P.K. Khanna, M. Kumar, S. Gautam, K.H. Chae, Investigation of phase segregation in sol-gel derived ZnMgO thin films, Semicond. Sci. Technol. 28 (2013) 0250041-0250048.
[19] N. Nagayasamy, S. Gandhimathination, V. Veerasamy, The effect of ZnO thin film and its structural and optical properties prepared by sol-gel spin coating method, Open Journal of Metal 3 (2013) 8-11.
[20] H. Park, J. Lee, H. Kim, D. Kim, J. Raja, J. Yi, Influence of SnO2:F/ZnO:Al bi-layer as a front electrode on the properties of p-i-n amorphous silicon based thin film solar cells, Appl. Phys. Lett. 102 (2013) 1916021-1916023.
[21] Y. Nasuno, M. Kondo, A. Matsuda, Effects of Substrate Surface Morphology on Microcrystalline Silicon Solar Cells, Jpn. J. Appl. Phys. 40 (2001) L303-L305.

Chapter 6 General conclusions and future prospects

6.1 General conclusions

In this thesis, novel optically-rough and physically-flat transparent conductive oxide (TCO) substrates were developed for thin-film solar cells with superstrate configuration. These substrates consist of a widegap $Zn_{1-x}Mg_xO$ transparent conductive thin film prepared by sol-gel process and glass substrates with rough surfaces prepared by reactive ion etching or nano-imprinting technique.

Firstly, $Zn_{1-x}Mg_xO$ thin films with wide bandgap and low resistivity were developed by sol-gel process. Resistivity of about 3.9×10^{-3} Ω·cm was achieved for a sol-gel $Zn_{1-x}Mg_xO$ thin film with an optical bandgap of 3.61 eV (Mg/Zn=10 mol. %, thickness=681 nm). Al doping contributed to the decrease in resistivity and the increase in optical bandgap. Annealing atmosphere in two-step annealing process played an important role in improving the electrical and optical properties of Al-doped $Zn_{1-x}Mg_xO$ (AZMO) thin film. It was found that the first step annealing in nitrogen increased carrier concentration, and the second step annealing in forming gas with a glass cover contributed to the improvement of Hall mobility. An optimum H_2 concentration in forming gas existed for decreasing the resistivity of AZMO thin film when the second annealing in forming gas was conducted without glass cover. This sol-gel AZMO thin film enables “physically-flat” concept on roughened substrates.

Secondly, conditions of reactive ion etching (RIE) of glass substrates and shapes of imprinting patterns were investigated in details to realize a scattering interface for fabricating “optically-rough” structure. In the part of RIE, moderate feature size on the substrate was obtained by controlling the etching time, RF power of plasma generation, and pressure. The etched Corning XG glass showed larger vertical feature than the

etched 7059 glass, resulting in large haze ratio at long wavelength. After coating sol-gel AZMO thin film with 2-Methoxyethanol as solvent, the AZMO/RIE etched 7059 glass substrate showed smooth surface and good scattering behavior. In the part of room-temperature nanoimprinting, the shape and period of feature size on the patterned substrate influence the optical properties of substrates greatly. Substrates imprinted with hole and pillar patterns showed high haze ratio at long wavelength region, indicating good light-scattering behavior. After AZMO coating, the AZMO/glass substrate patterned with a hole pattern showed a flat surface and a high haze ratio at long wavelength region. In terms of overall performance, the AZMO/hole patterned substrate shows high haze ratio and low surface roughness. AZMO(0.75 M 40L Mg/Zn=10 mol. %)/substrate with a hole pattern (period=1.7 μm) showed a root-mean-square surface roughness of 2.6 nm, a sheet resistance of 47.0 *Ω/sq*, and an average haze ratio of 9.5% at wavelength region from 700 nm to 850 nm. This value was larger than that of the typical ZnO: B substrate with pyramidal surface morphology, which was deposited by the metal organic chemical vapor deposition method.

Subsequently, these AZMO substrates were applied as the transparent conductive layer in hydrogenated amorphous silicon solar cells (a-Si) single junction solar cells with superstrate configuration. Bandgap widening of TCO through increasing Mg content improved the spectral response at short wavelength, however, too wide bandgap (E_{opt} >3.55 eV) deteriorated the performance of solar cells due to the decrease in J_{sc}, V_{oc}, and *FF*. Solar cells deposited on AZMO (E_{opt}=3.55 eV, Mg/Zn=10 mol. %)/flat glass substrate showed the best performance. Employing 20 nm Nb-doped TiO_2 thin film as the antireflection layer at the TCO/p-a-SiC_x interface improved the spectral response of a-Si solar cells at wavelength of 450-580 nm through reducing the optical reflection. Roughening surface morphology of AZMO thin film via utilizing the

nonequilibrium solute precipitation and crystallization process during the drying procedure improved the spectral response of a-Si solar cells at wavelength of 600-800 nm by enhancing the light-scattering, however, deteriorated the overall performance. When the optically-rough and physically-flat AZMO substrate was applied as the front electrode of a-Si single junction solar cells, the spectral response at short wavelength of around 350 nm was improved obviously due to the decrease in optical loss. A high V_{oc} of 0.92 V was obtained by using AZMO/RIE etched 7059 (7 Pa 250 W 10 min) glass substrate due to the flat surface. A solar cell with η of 8.02 % (V_{oc}=0.88 V, J_{sc}=13.02 mA/cm^2, and FF=0.70) was obtained by using AZMO/RIE etched 7059 glass substrate (7 Pa 200 W 10 min). A J_{sc} of 13.2 mA/cm^2 was achieved with AZMO(40L)/hole (period=1.7 μm) patterned substrate.

Overall, a novel optically-rough and physically-flat AZMO substrate was developed. This substrate showed low optical absorption, low surface roughness, high haze ratio in transmission at long wavelength region, and moderate sheet resistance, simultaneously. It was demonstrated that a-Si single junction solar cells fabricated on this substrate showed good device performance. These results indicate the potential of the optically-rough and physically-flat AZMO substrate for the front electrode of several types of thin-film solar cells.

6.2 Future prospects

The developed optically-rough and physically-flat (OR-PF) type TCO substrates would contribute to the development of other kinds of thin-film solar cells. These substrates would become a very promising substrate of perovskites solar cells, because their unique properties. At present, the sol-gel derived ZnO thin film has been applied into planar-hetero junction perovskite solar cells and improvement on the performance of solar cells was achieved [1]. Figure 7.1 shows the schematic of the perovskites solar cells with OR-PF type AZMO substrate. The OR-PF type AZMO substrate can further improve the performance of perovskites solar cells through reducing optical loss and enhancing light-scattering. In addition, it helps to achieve the fabrication of solar cells with chemical solution processes.

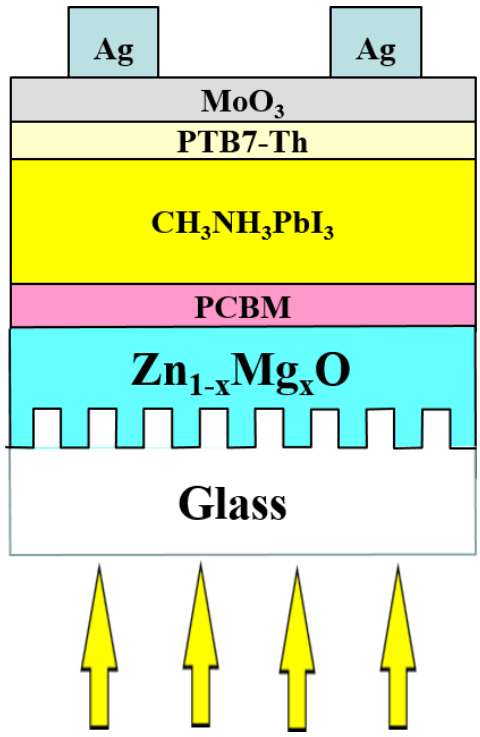

Fig. 7.1 Schematics of perovskites solar cells with optically-rough and physically-flat AZMO substrate.

$$\nabla \times E = -\frac{\partial B}{\partial t}$$

$$\nabla \times H = J + \frac{\partial D}{\partial t}$$

$$\nabla \cdot D = \rho$$

$$\nabla \cdot B = 0$$

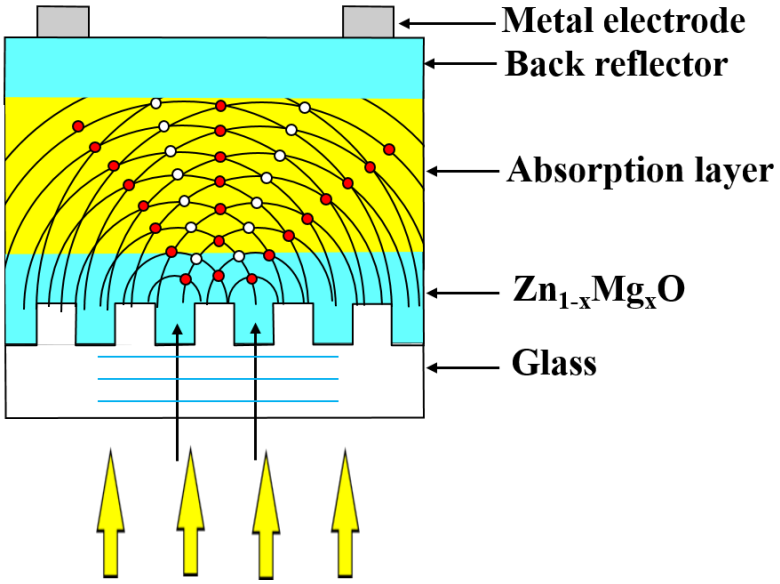

Fig. 7.2 Schematics of numerical simulation of the wave propagation in thin-film solar cells with Maxwell's equations.

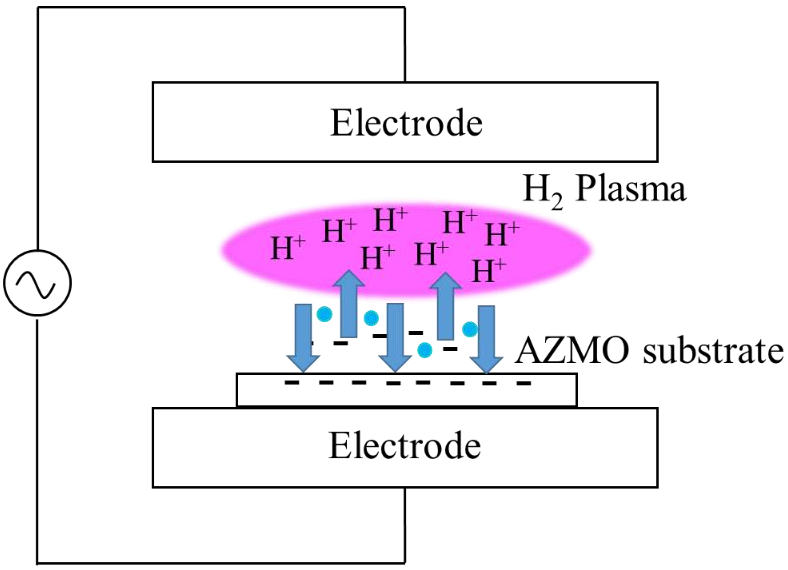

Fig. 7.3 Schematics of hydrogen plasma treatment on AZMO substrate.

Quantitative theories on the relationship between the shape of feature size on the patterned glass substrate and the optical wave propagation in the absorption layer needs to be founded. Numerical simulation of Maxwell's equations utilizing the finite-difference time-domain algorithm is a good method to investigate the wave propagation

in thin-film solar cells. Figure 7.2 shows the schematic of numerical simulation of the wave propagation in thin-film solar cells with Maxwell's equations. Then, precise control of shape of feature size (period and height) on the patterned glass substrate can be done, for enhancing the light absorption in the active layer.

Furthermore, in order to improving the conductive ability of AZMO thin film, decreasing the sheet resistance of sol-gel derived AZMO thin film to be less than 10 Ω/sq is another very important topic. Hydrogen plasma treatment is a very good method to reduce the resistivity of ZnO thin film [2]. Figure 7.3 shows the schematics of hydrogen plasma treatment on AZMO substrate. The hydrogen plasma treatment would increase the carrier concentration in AZMO thin film by hydrogen incorporation.

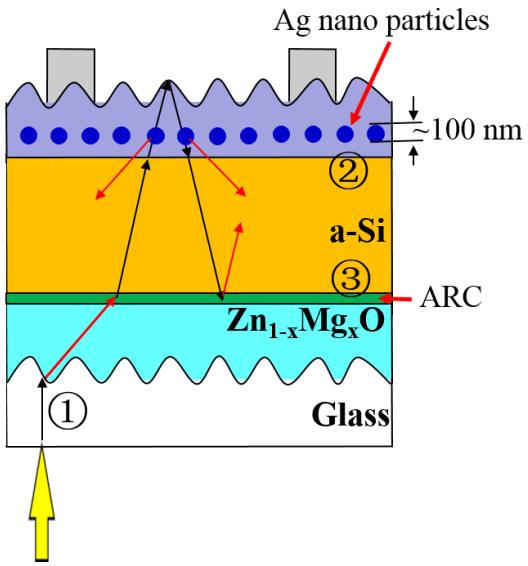

Fig. 7.4 Schematics of measures to improve the spectral response of thin-film solar cells deposited on OR-PF AZMO substrate.

Moreover, there are several measures to improve the spectral response of thin-film solar cells deposited on OR-PF AZMO substrate at long wavelength region. Figure 7.4 shows the schematics of measures to improve the spectral response of thin-film solar cells deposited on OR-PF AZMO substrate. First, optimizing the shape of feature size on pattern can broaden the scattering angle of incident light at the interface between

the TCO and glass substrate. Second, utilizing Ag particles as the plasmonic back reflector can enhance the light-scattering at rear side for λ=~700 nm [3]. Third, inserting an antireflection coating such as TiO_2 at TCO/p-a-SiC_x interface can reduce the optical reflectance at the TCO/p-a-SiC_x interface and enhance the total reflectance at the p-a-SiC_x/TCO interface. These measures can increase the spectral response at long wavelength and intensify the light-confinement in the absorption layer, then increase the J_{sc} of thin-film solar cells.

Reference

[1] J. Kim, G. Kim, T. K. Kim, S. Kwon, H. Back, J. Lee, S. H. Lee, H, Kang, and K. Lee, Efficient planar-heterojunction perovskite solar cells achieved via interfacial modification of a sol-gel ZnO electron collection layer, J. Mater. Chem. A. 2 (2014) 17291-17296.
[2] F. Wang, H. Chang, C. Tseng, C. Huang, H. Liu, Influence of hydrogen plasma treatment on Al-doped ZnO thin film for amorphous silicon thin film solar cells, Curr. Appl. Phys. 11 (2011) S12-S16.
[3] H. Tan, R. Santbergen, A. H. M. Smets, and M. Zeman, Plasmonic light-trapping in thin-film silicon solar cells with improved self-assembled silver nanoparticles, Nano Lett. 12 (2012) 4070-4076.

Acknowledgments

I would like to express my sincere gratitude to Associate Prof. Shinsuke Miyajima for giving me the interesting research topic and the opportunity to do Ph. D study in the Tokyo Institute of Technology. I am very grateful for his patient and continuous guidance and support throughout this study.

I would like to express my gratitude to Prof. Makoto Konagai for his kind guidance, comment, and advices on this study.

I am very grateful to Prof. Akira Yamada for his constructive advices and comments on this study.

I am very grateful to Prof. Mitsumasa Iwamoto, Prof. Shigeki Nakagawa, Associate Prof. Pham Nam Hai, and Dr. Yukimi Ichikawa for reviewing this thesis.

I am very grateful to Dr. Porponth Sichanugrist for his important contribution to this thesis by giving a lot of comments, guidance, and help on the fabrication of a-Si solar cells.

I would like to express my sincere thanks to Mr. Keiichi Nishikubo for his patient guidance on the operation of RIE equipment and Wet etching treatment.

I would like to express my sincere thanks to Dr. Chisato Niikura and Dr. Amartya Chowdhury for their patient guidance on the operation of PECVD equipment. I would like to express my special gratitude to Dr. Chisato Niikura for her patient discussion and guidance on the operation of room-temperature nanoimprinting process.

I would like to express my sincere thanks to Dr. Xianfeng Zhang and Dr. Shunsuke Kasashima for their patient guidance on the operation of MOCVD and SEM equipment.

I would like to express my sincere thanks to Yuki Takiguchi for his discussion and guidance on the operation of RF magnetron sputtering equipment.

I would like to thank all the people who supported me throughout my career in the Konagai and Miyajima, and Yamada laboratory.

I deeply appreciate secretaries at the laboratory, Kimiko Furukawa and Rie Mikado for their lots of warm and kind supports.

Last but not least, I would like to thank my family most sincerely for their invaluable support and encouragement.

List of Publications

Journal Papers

1. Lei Meng, Makoto Konagai, and Shinsuke Miyajima, "Effect of annealing atmosphere on the electrical and optical properties of sol-gel derived Al doped $Zn_{1-x}Mg_xO$ thin film", Thin Solid Films, 597, 144-150, 2015.

2. Lei Meng, Shinsuke Miyajima, and Makoto Konagai, "Effect of Al doping concentration on the electrical and optical properties of sol-gel derived $Zn_{0.87}Mg_{0.13}O$ thin film", Jpn. J. Appl. Phys. 54, 08KB091-08KB094, 2015.

3. Lei Meng and Shinsuke Miyajima, "Characteristics of naturally textured $Zn_{1-x}Mg_xO$ transparent conductive thin film fabricated by sol-gel process", Journal of the Electrochemistry Society, (submitted), 2016.

International Conferences

1. Lei Meng, Shinsuke Miyajima, and Makoto Konagai, oral presentation, "Development of transparent and conductive Al doped $Zn_{1-x}Mg_xO$ thin film by sol-gel process with two-step annealing", SPIE Optics + Photonics, Thin Films for Solar and Energy Technology VI, 91770G (October 16-22, 2014, San Diego, CA, United State).

2. Lei Meng, Shinsuke Miyajima, and Makoto Konagai, poster presentation, "Effect of Al addition on the electrical, optical and structural properties of sol-gel derived $Zn_{1-x}Mg_xO$ thin film", The 6th world Conference on Photovoltaic Energy Conversion, Thin Film Silicon Solar Cells, (November 23-27, 2014, Kyoto, Japan).

3. Lei Meng and Shinsuke Miyajima, poster presentation, "Morphology control of sol-gel derived $Zn_{1-x}Mg_xO$ transparent conductive layer for improving optical confinement of thin-film solar cells", 25th International Photovoltaic Science and Engineering Conference, Thin-film based Silicon Cells and Materials, (November 17-19, 2015, Busan, South Korean).

International Workshops

1. Lei Meng, Shinsuke Miyajima and Makoto Konagai, poster presentation, "Effect of Al addition on the electrical, optical and structural properties of sol-gel derived $Zn_{1-x}Mg_xO$ thin film", Korea-Japan Top University League Workshop on Photovoltaics (November 28-29, 2014, Miyazaki, Japan).

Domestic Conferences

1. Lei Meng and Shinsuke Miyajima, poster presentation, "Novel optically-rough and physically-flat $Zn_{1-x}Mg_xO$: Al substrate for superstrate-type thin-film solar cells", The 63rd Japan Society of Applied Physics Spring Meeting (March 19-22, 2016, Tokyo, Japan).